

Experimental and Theoretical Determination of the Transport Properties of $n\text{-Al}_x\text{Ga}_{1-x}\text{Sb}/\text{GaSb}$



This thesis is presented for the degree of Doctor of Philosophy

Supervisors:

Prof. Manus Hayne

Dr. Andrew J. Marshall

Laura A. Hanks MPhys

2019

Experimental and Theoretical Determination of the Transport Properties of $n\text{-Al}_x\text{Ga}_{1-x}\text{Sb}/\text{GaSb}$

Laura A. Hanks

July 2019

Abstract

The work in this thesis reports on the design, growth, fabrication, measurement and analysis of $n\text{-GaSb}/\text{Al}_{0.2}\text{Ga}_{0.8}\text{Sb}$ heterostructures. Initially a growth study was completed in order to minimise the native p -type GaSb defects (usually of $p \sim \times 10^{17} \text{ cm}^{-3}$) and to calibrate the n -type doping (achieved using Te). This growth study then informed simulations of the band structure and the transport properties via Schrödinger-Poisson and transport lifetime modelling, allowing an investigation for the design of a high mobility $n\text{-GaSb}/\text{Al}_{0.2}\text{Ga}_{0.8}\text{Sb}$ structure, to ensure correct confinement. The optimum designs from the simulation study were then grown and fabricated into 8-pad geometry non-gated Hall bars. The metallisation recipe researched further as initial recipes were deemed unsuitable. The resulting devices were then measured as a function of magnetic field and temperature to obtain the transport properties (mobility and carrier density).

It has been shown that an optimum set of growth conditions ($T_g = 475 \text{ }^\circ\text{C}$, $V/\text{III}=1.3$) reduces the p -type native defects resulting in a hole concentration of $5 \times 10^{16} \text{ cm}^{-3}$ at room temperature. Simulations of AlGaSb/GaSb heterostructures were completed, investigating the conduction band and the effect of the p -type defects. It was found that doping below the well is necessary for confinement in these structures. Both square and triangular quantum wells were grown on semi-insulating GaAs substrates with an interfacial misfit array to prevent strain. These samples were fabricated where the metallisation recipe Pd/In/Pd/Au was used, allowing cold temperature measurements. Measurements of the transport properties across a temperature range of (3-300) K at low field ($< 3 \text{ T}$) resulted in a peak mobility of $9030 \text{ cm}^2/\text{Vs}$, where background impurity scattering was shown to be the limiting scattering rate. High field measurements of a doped heterojunction resulted in Shubnikov-de Haas oscillations visible up to 100 K. As the first transport measurements of confined $n\text{-GaSb}/\text{AlGaSb}$, these results inform the direction of optimisation for high mobility devices in this material.

Declaration

I Laura A. Hanks, declare that the contents of this thesis titled “Experimental and Theoretical Determination of the Transport Properties of $n\text{-Al}_x\text{Ga}_{1-x}\text{Sb}/\text{GaSb}$ ” is my own independent research and work. Where there is exception to this specific reference has been made to the work of others. No part of this work has been submitted previously to any other academic institution or for any other degree of qualification. This thesis is submitted in partial fulfilment of the requirements for the degree of Doctor of Philosophy.

Date

Signature

Acknowledgements

I have been gifted with a particularly large support group throughout not just my PhD but my whole life and I have many people to thank for who I have become and what I have achieved.

I would like to dedicate this thesis to my parents Helen and Martin for always ensuring I got the best education I possibly could, and to my husband, Chris, for being my rock and who has never missed a chance to make me happy. Thank you to my parents for all the help throughout my life, the hours spent helping me catch up with my reading when I was behind, thank you for entertaining my fascination of solving maths problems as a hobby when I was younger Thank you also for always being there to remind me of what can be achieved when you just keep trying and always believing in me. To Chris, thank you for your unending, unyielding support through this PhD, for the many confidence boosters, cups of tea, and rants. Most importantly, reminding me how wonderful the world is, when you take the time to see it. You have made this stressful and chaotic time joyful. Your love, care and honesty has kept me focussed and calm...ish. Thank you to Insbey, the newest member of the family for being there for a calming cuddle.

I must also show gratitude to my primary supervisor Professor Manus Hayne for his guidance, support and encouragement throughout the PhD. You believed in me and most importantly acknowledged my hard work, thank you. You also sent me to many conferences and the ESONN summer school which both reignited my passion for traveling and for the wider aspects of physics outside my PhD. I can't ignore the help of my secondary supervisor Dr Andy Marshall who taught me almost everything I know about MBE growth, cleanroom processing and the incredible value of making mistakes and learning from them, particularly in the cleanroom. I would also like to thank Dr Leonid Ponomarenko for all his guidance, patience and insight, and for allowing me the use of his measurement set up.

I would like to thank the rest of Manus's research group for their friendliness and assistance throughout these last few years, Sam Harrison, Alex Robson, Peter Hodgson, Ofogh Tizno, Tom Wilson and Dominic Lane. In particular, thank you Tom for listening to me go on and on about wedding planning and the many times the research went wrong. These past couple of years would have been a lot less entertaining without you. Thank you also to his family Ellie and Merlin for their kindness and affection.

The department contains a wealth of wonderful people, ever eager to help and chat. Thank you to those who have done both on many an occasion, namely, Veronica Letka, Adam Craig, Xiao Collins, Alex Jones, Josh Chawner and Licia Ray. Josh, the many exciting card games have been a stress relief and will be sorely missed. Licia, thank you for your careful balance of support, witty remarks and honesty, I will never get bored of our chats.

My support has not just come from the department or my immediate family but also from particularly caring friends and extended family. Julie and Phil Gauterin and Gwenllian Evans have always shown particular enthusiasm, interest and encouragement in my education and research, and they have always had confidence that I will reach my goals, whatever they may be. To Lynda, Kevin, Jack, Lucy and Mick McIndo and to Jean Collins thank you for welcoming me into your family with such warmth. You have never lacked encouraging words. I would like to acknowledge my closest friends starting with Dr Marie Anderson, for her constant encouragement through this process and setting a perfect example that determination can get you anywhere. I would like to also acknowledge Rosie Hughes and Dan O'Neil for their reassurance, brilliant distractions and fun weekends. Life would not be nearly as exciting without you.

To all of the above, your support has seen me through the last few years and made it not just possible, but joyful both inside work and out. Thank you.

List of Publications and Presentations

Poster - L Hanks, A Marshall and M Hayne, GaSb/GaAlSb 2DEG Devices for Magnetotransport, UK Semiconductors 2016, Sheffield Hallam University, July 2016.

Poster - L Hanks, A Marshall and M Hayne, GaSb/GaAlSb 2DEG Devices for Magnetotransport, UK Semiconductors 2016, European School on Nanosciences & Nanotechnologies, Université Grenoble Alpes, August 2016.

Poster - L Hanks, A Marshall, L Ponomarenko and M Hayne, Al_{0.2}Ga_{0.8}Sb/GaSb 2DEG Heterostructure Devices for Magnetotransport, Advances in Quantum Transport in Low Dimensional Systems, University College London, September 2017.

Invited seminar talk - L Hanks, A Marshall, L Ponomarenko and M Hayne, Transport of Modulation-Doped Al_{0.2}Ga_{0.8}Sb/GaSb Heterojunctions, Cavendish Laboratory, University of Cambridge, October 2017.

Conference proceedings - L A Hanks, M Hayne, A R J Marshall and L Ponomarenko, "Transport of Modulation-Doped Al_{0.2}Ga_{0.8}Sb/GaSb Heterojunctions", *J. Phys.: Conf. Ser.*, vol. 964, p. 012006, 2018.

Poster - L Hanks, L Ponomarenko, A Marshall and M Hayne, Determination of Al_{0.2}Ga_{0.8}Sb/GaSb Transport Properties, International Symposium on Quantum Hall Effects and Related Topics, Max -Plank Institute for Solid State Research, June 2018.

Talk - L Hanks, A Marshall, M Hayne, Determination of Al_{0.2}Ga_{0.8}Sb/GaSb Transport Properties, UK Semiconductors 2018, Sheffield Hallam University, July 2018.

Poster - L Hanks, L Ponomarenko, A Marshall and M Hayne, Determination of Al_{0.2}Ga_{0.8}Sb/GaSb transport properties, High Magnetic Fields in Semiconductor Physics, Toulouse, July 2018.

Talk - L Hanks, A Marshall, M Hayne, Realisation and Transport Measurements of n-Al_{0.2}Ga_{0.8}Sb/GaSb, UK Semiconductors 2019, Sheffield Hallam University, July 2019.

Table of Contents

Abstract	ii
Declaration	iii
Acknowledgements	iv
List of Publications and Presentations	vi
Table of Contents	vii
List of Figures	xi
List of Tables	xx
Chapter 1 Introduction	1
1.1 Motivation	1
1.2 Thesis Structure	4
Chapter 2 The Physics of Semiconductor Structures	8
2.1 Electrical Properties of Semiconductors	9
2.1.1 Crystal Structure	9
2.1.2 Band Structure and Effective Mass	10
2.1.3 Carrier Distribution, States and Density	15
2.2 Transport in III-V Semiconductors	22
2.2.1 The Hall Effect Phenomenon and Measurement	22
2.3 Band Structure Engineering	25
2.3.1 Alloying	26
2.3.2 Heterostructure Band Alignment	27
2.3.3 Confined Band Structures	29
2.3.4 Carrier Density in 2D Structures	31
2.3.5 Strain and Lattice Mismatch	32

Chapter 3	Growth, Material Quality & GaSb Defects	37
3.1	Principles of Epitaxial Growth and Defect Formation	37
3.1.1	The Basics of Growth Kinetics	38
3.1.2	Antisite and Vacancy Formation	39
3.2	Parameters and Procedures of Molecular Beam Epitaxy	44
3.2.1	The MBE Machine	44
3.2.2	Parameters of Molecular Beam Epitaxy Growth	46
3.2.3	Growth and Preparation Procedures	48
3.2.4	Van der Pauw Method	49
3.3	Measurement of Defects and Doping in Bulk GaSb	52
3.3.1	Aims	53
3.3.2	Reducing Defects Through Growth: A literature review	53
3.3.3	Experimental Procedure	56
3.3.4	Measured Defect Reduction Through Improved Growth	57
3.3.5	Temperature Dependence of Antisite Defects	61
3.3.6	Doping Considerations for <i>n</i> -GaSb	67
3.4	Conclusions	75
Chapter 4	Fabrication of Semiconductor Devices	77
4.1	Fabrication Overview	77
4.2	Optical Lithography	79
4.3	Thermal Evaporation	83
4.4	Etching	86
4.5	Bonding	86
4.6	Mask Creation	87
4.7	Summary	89
Chapter 5	Characterising Metal-Semiconductor Interfaces	90
5.1	Contacting Theory	90
5.2	A Review of Contacting Materials for <i>n</i> -GaSb	93
5.3	Determining Contact Resistance	95
5.4	Characterization of Metal Contacts on <i>n</i> -GaSb	97

5.4.1	Aims for Contact Resistance	97
5.4.2	Recipes Tested	98
5.4.3	Ohmicity	102
5.4.4	Determination of Contact Resistance	103
5.4.5	Resistance Variation with Temperature	107
5.5	Conclusions	108
 Chapter 6 Designing Heterostructures Through Simulation		110
6.1	Input and Calculation Flow in nextnano	111
6.2	Schrödinger-Poisson Modelling Theory	113
6.2.1	Schrödinger's Equation and Numerical Implementation	114
6.2.2	Poisson's Equation and Numerical Implementation	115
6.3	Simulated Confinement in GaSb Heterostructures	117
6.3.1	The Effect of Defects on Heterostructure Design	118
6.3.2	Doping the Barrier of a Triangular Well	119
6.3.3	Doping the GaSb Buffer in the Triangular Well	123
6.3.4	Doping the Triangular Quantum Well	125
6.3.5	Square Quantum Well Design Investigation	127
6.3.6	Schrödinger-Poisson Summary	128
6.4	Transport Model Theory	130
6.4.1	Impurity Scattering	131
6.4.2	Phonon Scattering	133
6.4.3	Interface Roughness	135
6.5	Simulation of GaSb Heterostructure Transport Properties	136
6.5.1	Structural Variations in the Transport Model	138
6.5.2	Transport Properties of Simulated Al _{0.2} Ga _{0.8} Sb/GaSb Structures	140
6.6	Conclusion	147
 Chapter 7 Measurement of GaSb Transport Properties		149
7.1	Measurement Theory of Transport Properties	150
7.1.1	Measuring 2D Transport Properties	150

7.1.2	Multi-Carrier Fitting of Conduction	151
7.1.3	Carrier Dynamics at High field	153
7.2	Equipment and Set Up for Magnetotransport	156
7.3	Transport Measurements of $\text{Al}_{0.2}\text{Ga}_{0.8}\text{Sb}/\text{GaSb}$ Heterostructures	158
7.3.1	Magnetic Field Dependence of Resistance	159
7.3.2	Transport Properties of GaSb Heterostructures	165
7.3.3	High Field Measurements and Analysis	169
7.3.4	Revision of the Transport Model	173
7.3.5	Conclusions	173
Chapter 8	Conclusions and Further Investigations	176
8.1	Conclusions	177
8.2	Further Work	182
References		185
Appendix A:	Growth Rate Conversion Calculations	193

List of Figures

- Figure 1.1:** Simulated electron mobility as a function of sheet carrier density at 1 K for AlGaAs/GaAs (solid) and AlGaSb/GaSb (dotted) heterojunctions [15]. 4
- Figure 2.1:** **Left:** Examples of the standard Bravais lattices including the primitive cubic, the body-centred cubic and the face-centred cubic (fcc). **Right:** An example of a zinc blende structure where the dark atoms form one face centred cubic structure and the light atoms form another. Where the bottom left light atom is the equivalent to the bottom left corner of its fcc structure and the others are the face centred atoms that are held in that cubic unit cell. 9
- Figure 2.2:** **Left:** Simplistic band diagram commonly used when combining multiple semiconductors showing the conduction band edge E_c , the valence band edge E_v with a gap between them, E_g . **Right:** Parabolic band structure showing the conduction band, and the heavy hole and light hole bands (both of which make up the valence band). 10
- Figure 2.3:** **Top:** The probability densities of the bonding and antibonding states offset by an amount relative to the energy difference between them. As the separation decreases the difference in energy increases. The light blue indicates the bonding state and the dark blue indicates the antibonding state. **Bottom:** Formation of bands and a gap from bonding and antibonding orbitals as the atomic distance decreases, adapted from ref [21]. 11
- Figure 2.4:** Parabolic and non-parabolic dispersion relations for GaAs (green) and GaSb (blue), with the non-parabolic dispersion shown as dashed lines. 14
- Figure 2.5:** Full GaSb band diagram for the conduction and valence bands, reproduced from ref [11], annotated to point out the E_g for both Γ and L points. 14
- Figure 2.6:** The density of states for electrons against energy in 3D. 16
- Figure 2.7:** The Fermi Dirac distribution against energy with an indication of how the distribution changes with temperature. As temperature increases there is an increased likelihood of having occupied states in the conduction band. ... 17
- Figure 2.8:** Visualisation of carrier density calculation at 150K (left) and 300K (right), where the density of electrons increases with temperature due to the increased probability of occupation of electronic states in the conduction band. 18
- Figure 2.9:** A schematic diagram of the Hall effect, showing the movement of electrons, creation of the electric field and the direction of the Hall field. 22
- Figure 2.10:** A diagram indicating how semiconducting materials with different band gaps can be used to create confinement. 25
- Figure 2.11:** Band gap against lattice constant for all binary III-V semiconductors indicating the ternary alloy branches between the binary materials. Materials at similar lattice constants are lattice matched reducing strain [32]. 27

- Figure 2.12: Left:** Energy band gap between the valence band peak and the Γ , L and X points, and how this changes with aluminium fraction from GaSb to AlSb. **Right:** A graph showing how the band gap difference between GaSb and AlGaSb changes with aluminium fraction. The colours represent a change from a direct band gap at the Γ point, to indirect at L or X. 27
- Figure 2.13: Top:** A schematic diagram that illustrates the three types of heterojunction alignment, straddling, staggered and broken gap. **Bottom:** A scaled diagram indicating the types of alignments for a selection of III-V semiconductor materials when aligned using Anderson's rule. 28
- Figure 2.14:** The relationship between the de Broglie wavelength and effective mass, noting common III-V semiconductor compounds..... 29
- Figure 2.15:** An example of the wave-functions offset by their energy in a finite quantum well. 30
- Figure 2.16:** A triangular well created with the band bending from electrons being physically removed from their dopant ions (positioned at the green dashed line)..... 31
- Figure 2.17:** A figure showing how differing lattice constants in strained and relaxed states can form defects..... 32
- Figure 2.18: Left:** A plot showing the graphical solution of the Matthews and Blakeslee model [39] for a Al_{0.2}Ga_{0.8}Sb/GaSb heterojunction, the black line shows the $y=x$ line and the cyan line signifies the critical thickness calculation, where in equation 2.32 hc on the RHS is set to equal x . **Right:** The critical thickness for Al_xGa(1 - x)Sb against the alloy fraction x . The cyan line represents the Matthews and Blakeslee model highlighting the value used in this work for a 0.2 aluminium alloy fraction. The People and Bean model is shown in pink [43]..... 36
- Figure 3.1:** Schematic diagram of the surface processes that occur during epitaxial growth. 38
- Figure 3.2:** A schematic diagram of a selection of the native defects that could be created in a GaSb lattice, showing each atom (Sb in blue and Ga in green) with its associated outer electronic bonding. Donated free electrons are shown in orange with unfilled orbitals (holes) shown in yellow. Clockwise from the top left are a gallium vacancy, V_{Ga} , an antimony vacancy, V_{Sb} , a gallium antisite, Ga_{Sb} , and an antimony antisite, Sb_{Ga} 40
- Figure 3.3:** Schematic of the MBE machine, noting each chamber and with detailed annotation of the growth chamber. 44
- Figure 3.4: Left:** Pictures of RHEED patterns before deoxidisation where only a few bright spots are observed. **Right:** RHEED pattern observed once growth has begun, showing the three bright primary lines and two secondary lines between each of them ($a \ 3\times$). 45

- Figure 3.5:** A schematic diagram showing different configurations used when measuring electrical resistance in a van der Pauw geometry, where arrows indicate the current being set and voltage measured is shown by dot ended lines..... 50
- Figure 3.6:** How the correction factor f varies with the ratio of the two longitudinal resistances $R_{AB, CD}/R_{BC, DA}$ 51
- Figure 3.7:** Snake like defects that can occur from an uneven IMF. The defects are dislocations visible on the surface that originate at the junction between the GaAs and GaSb layers. **Left:** Optical microscopy image of the surface of the sample. **Right:** Beam exit x-section AFM showing the distinct layers of GaAs and GaSb where it is clearly seen that the dislocation starts at the junction (measured by Dr Alex Robson)..... 56
- Figure 3.8:** A graph of measured transport properties for carrier density and hole mobility for undoped GaSb grown under varying growth conditions, indicating the improvement of mobility with a decrease of carrier density. The error bars on this graph are from the spread of the repeated measurements. 57
- Figure 3.9:** Graphs showing the measured carried density and mobility at 300 K of undoped GaSb against growth temperatures with different symbols indicating different V/III ratios, V/III=1.3 (▲), 1.6 (●) and 2.2 (■).The light grey shaded regions indicate the limit of growth temperatures observed in this study to give milky vs shiny growth at a V/III ratio of 1.3. 58
- Figure 3.10: Top:** A schematic diagram of the variation of sticking coefficient with growth temperature. **Bottom:** A schematic diagram indicating the V/III ratios at which the Sb flux is too low and therefore causes defects (blue), optimal (green) and is too high and therefore causes defects (orange). R1 is a constant V/III ratio across temperature..... 60
- Figure 3.11:** A graph showing the measured carried density and mobility across growth temperature with lines for different measurement temperatures, 290 K, 80 K, 50 K..... 62
- Figure 3.12: Left:** A plot of the measured carrier density against temperature with data points and guides for the eye. **Right:** An Arrhenius plot of the measured carrier density which can be used to extract an activation energy, the transparent line indicates the linear fit in each case. 63
- Figure 3.13:** A fit of the measured carrier density from sample 505 with the data shown as points (▲) and two separate fits shown with the fit parameters given on the plot. One defect with two ionisation levels is shown in red (using equation 2.15), and two defects, one with two ionisation level, and one with one ionisation level, is shown in dashed black (using equation 2.14). 65
- Figure 3.14:** A graph of mobility against temperature for two unintentionally doped GaSb samples. Squares indicate the measured mobility for an MBE grown sample created in this work which is grown on a GaAs semi-insulating substrate followed by an IMF. The dashed line shows the mobility measured by Dutta *et al.* [9] for a sample grown from a melt. 67

Figure 3.15: A graph showing the measured carrier density at 300 K of doped GaSb at varying Te cell temperatures, producing both p and n -type carriers (points). The solid black line indicates the fitted line to calibration samples grown on InSb. The dashed line is an adjustment of the calibration line for growth rate in GaSb. The pink dashed line is a fit to the GaSb samples using equation 3.6 (see the text for further details). The undoped samples are shown for context.	69
Figure 3.16: A graph showing the measured carrier density relationship with measurement temperature. , indicating different activation behaviour for both p and n -type bulk GaSb.....	72
Figure 3.17: A schematic diagram indicating the electron states in a standard band diagram. Where the black line represents the Fermi-distribution and the blue shaded regions indicate the filled electron states.	73
Figure 3.18: The apparent carrier density calculated from the Hall coefficient against the ratio of electrons in the L-band to the Γ -band, which is analogous to temperature. Each line is for a set total carrier density with blue being a lower concentration and red being higher where equation 3.12 was used for this calculation.	74
Figure 4.1: A diagram indicating each of the processing steps involved in the creation of a Hall bar, with the final image (RHS), showing a microscope image of the processed Hall bars.	78
Figure 4.2: A figure showing the various results of exposure test, the correct or intended exposure test, under exposure (or under development), over exposure (or over development) and bad contacting.....	81
Figure 4.3: A diagram indicating the improved formation of a contact after lift off with the use of a bi-layer resist.	83
Figure 4.4: A schematic diagram of a thermal evaporator indicating the relevant components for metal evaporation as well as the sensor position.	84
Figure 4.5: A picture showing the chip carrier for a Hall bar used in the temperature dependent set up, shown to aid the bonding description.....	87
Figure 4.6: Contact and mesa mask unit cell design. The cell has three chips, each with three Hall bars surrounded by gold guidelines. The total repeated pattern has an area of 5 mm ² . The Hall bars and certain other features have been annotated for reference in this work in black.....	88
Figure 5.1: A figure showing a separate metal and semiconductor, then the band structure alignment after the joining of these two materials when $\phi_m < \chi_s$ and when $\phi_m > \chi_s$	91
Figure 5.2: A demonstration of transmission line measurement geometry and the graphical analysis that can be conducted.	96

Figure 5.3: A schematic diagram of the resistances involved in measuring a Hall bar for the determination of transport properties. The ideal current path is shown in green. 98

Figure 5.4: Example I-V characteristics for each metal recipe investigated shown at 300K. Black points indicate the measured points from a current voltage sweep and the red line indicates the fit line used to extract a resistance (see the text for further details). 101

Figure 5.5: A graph of voltage against current for a Schottky contact indicating the significant variation in resistance when it is taken from differing regions of the traces, whereas in a perfectly ohmic case all resistances are equal. . 102

Figure 5.6: Transmission line measurements for each annealed recipe using the low current region of each trace. The black crosses indicate the measured points, the red dots indicate the average of each spacer and the orange line is a linear fit. Each graph is annotated with the contact resistance, taken from half the y intercept of the fit line, and the halved average of all the points ($12R$). 104

Figure 5.7: A plot indicating how a current voltage measurement would change when two Schottky contacts are placed in series (left) and in parallel (right) with varying size resistors, the changing darkness of red signifies the increased magnitude of the resistor with the black line indicating no resistor in series. 105

Figure 5.8: A series of traces for In (left) and Pd/In/Pd/Au (right) for varying spacers (represented by varying colours), giving an indication that the indium recipe characteristic is governed by an in series varying resistance, and Pd/In/Pd/Au by an in parallel resistance. 105

Figure 5.9: Left: The resistance of annealed Pd/In/Pd/Au TLM pairs against spacer indicating the bimodal resistances. All contact pairs with a high resistance are indicated by red crosses, whilst those with lower resistance are indicated by black crosses. **Right:** R_2 against spacer indicating the ohmicity of each trace. These two plots together indicate there are two types of contacts created, relatively low resistance ohmic contacts, and high resistance Schottky contacts. 106

Figure 5.10: Contact resistance against temperature for each contacting recipe (all annealed) down to 77 K, where two recipes were highly resistive below 150 K, and two remained of reasonable resistance down to 77 K. 107

Figure 6.1: A schematic diagram indicating the changes that occur during a Schrödinger-Poisson calculation. **Left:** A simple well with its associated first wave function, the dashed line indicating a dopant plane. **Middle:** Poisson's equation solution for a simple well with a dopant plane. **Right:** The resulting Schrödinger solution of the changed well and the shifted wave function. 114

Figure 6.2: A schematic diagram indicating the condition in which a trial wave function is accepted as a solution. 115

- Figure 6.3:** **Left:** The charge distribution in the form of a histogram, where Z' is the depth into the structure. **Right:** A diagram illustrating the electric field strength from an infinite sheet of charge..... 116
- Figure 6.4:** The initial $\text{Al}_{0.2}\text{Ga}_{0.8}\text{Sb}/\text{GaSb}$ heterojunction structure proposed to achieve electron confinement, noting the doped and undoped (unintentionally doped) regions. 117
- Figure 6.5:** The same structures simulated with low and high defect concentration (blue and purple lines respectively). **Left:** A heterojunction with doping in the top and bottom barriers with an undoped well, where the RHS barrier is reduced due to doping. **Right:** A quantum well with n -type doping of concentration $1 \times 10^{17} \text{ cm}^{-3}$ in the top and bottom barriers and an undoped well. Both structures have spacers either side of the well. 119
- Figure 6.6:** Band diagrams for a $\text{Al}_{0.2}\text{Ga}_{0.8}\text{Sb}/\text{GaSb}$ structures doped only in the top cap with the Fermi level (dashed) set at 0 eV. The doped region is shaded grey. **Left:** Doping is too low, resulting in a sample that is p -type. **Right:** Doping is too high, where doping the top cap results in wave functions and occupied states in the barrier. 120
- Figure 6.7:** Band diagrams for an $\text{Al}_{0.2}\text{Ga}_{0.8}\text{Sb}/\text{GaSb}$ structure at 3 K with doped buffer and barrier regions. Outlined are the highest and lowest conduction band edge energies for the doping range investigated, shaded to indicate the variation of results between them. Similarly, the ground state wave functions for each structure with the highest and lowest doping are outlined. The dashed grey line at 0 eV indicates the Fermi level..... 123
- Figure 6.8:** Simulation results of the peak wave function position (depth into the heterojunction) against temperature. Only a few select doping concentrations are displayed for clarity. The dark blue lines indicate where the doping is equal in the barrier and buffer and the purple indicates where the barrier doping is greater than the buffer. The grey line shows the separation of the barrier and the well and thus approximately where the 2DEG should reside. 124
- Figure 6.9:** The ground-state wave functions against temperature for symmetrically doped heterojunctions with a doped well. These figures show the broadening of the wave function with higher doping levels. The junction is located at a depth of 120 nm. **Left:** Symmetric doping of $1 \times 10^{17} \text{ cm}^{-3}$. **Right:** Symmetric doping of $1 \times 10^{18} \text{ cm}^{-3}$ 125
- Figure 6.10:** **Left:** The band structure for an $\text{Al}_{0.2}\text{Ga}_{0.8}\text{Sb}/\text{GaSb}$ 25 nm quantum well with either side doped in the doping range ($1 \times 10^{17} - 1 \times 10^{18}$) cm^{-3} with spacers of 20 nm and 50 nm either side of the well. The shaded grey area indicating the region below the Fermi level. **Right:** A focus on the quantum well showing the ground state energy (light blue dashed) the second energy state (purple dashed) and the L band (pink solid). 127
- Figure 6.11:** **Left:** A charged impurity scattering electrons. **Middle:** The conservation of energy for a scattering event with a scattering angle of Θ [36]. **Right:** The scatter due to a charged plane of dopant ions. 131

- Figure 6.12: Left:** The variation in the ground state energy for a quantum well with a subtraction of 3 monolayers (orange dashed) from a well width of 15 nm (red dashed) and the same variation for a 30 nm well width (light and dark blue dashed) **Right:** A schematic diagram showing an extreme case of how the well width can vary across a structure with a line indicating the approximate midpoint of the well and thus likely the wave function peak. 135
- Figure 6.13:** A diagram that describes the different parameters of interface roughness. L is the roughness extent, Δ is the rms average roughness and $\Delta(\mathbf{r})$ the probability function [109]. 136
- Figure 6.14: Left:** The mobility for each well width dependent scattering rate against well width at 300 K for a GaSb quantum well. The green dashed line indicates the optical phonon scattering rate used by Ridley *et al.* [123] and the green solid line is the optical phonon as calculated by nextnano. **Right:** A graph showing the mobility due to the interface roughness variation with the roughness parameters at a well width of 20 nm. The colours represent the mobility and the scale is shown on the colour bar. The solid lines show contours of constant mobility and the dashed lines are lines of constant ΔL 139
- Figure 6.15: Left:** A standard transport model for a undoped heterojunction indicating how changing the doping concentration in the range $1 \times 10^{17} \text{ cm}^{-3}$ to $5 \times 10^{17} \text{ cm}^{-3}$ affects each scattering rate, and the associated mobility, directly and indirectly (through carrier density and kf). Each scattering mechanism is labelled, and regions are shaded to signify the change with doping concentration. The RHS is shaded to indicate the temperature at which the S.P. solver showed that the states deviated to the bulk. **Right:** A transport model isolating the effect of a change in the remote ionised impurity density using only the remote ionised impurity scattering rate, investigating the effect on the total mobility with carrier density and well width fixed. **Bottom:** A schematic of the structure simulated. 142
- Figure 6.16: Left:** The calculated mobilities for a heterojunction with a doped (solid line) and undoped (dashed) well with doping concentration $5 \times 10^{17} \text{ cm}^{-3}$. The grey shaded region at high temperature is to signify the region where the undoped well may have bulk states (i.e. not confined to the well). **Right:** The transport model for the full range of doping considered ($1 \times 10^{17} \text{ cm}^{-3}$ to $5 \times 10^{17} \text{ cm}^{-3}$) for a uniformly doped structure indicating the significance of the ionised impurity scattering. The range of calculated mobilities for the equivalent undoped well structures is shown in grey. **Bottom:** A schematic diagram of the structure simulated where the doped region varies as described above. 144
- Figure 6.17: Left:** A standard transport model indicating how changing the doping concentration in the range $1 \times 10^{17} \text{ cm}^{-3}$ to $7 \times 10^{17} \text{ cm}^{-3}$ affects the mobility of a square quantum well. Regions are shaded to signify the change with doping concentration. The mobility due to scattering from remote ionised impurities is not visible on this scale. **Right:** A schematic diagram of the structure that was simulated where the doped region varies as described above. 145

Figure 6.18: The total mobility for each structure design with the full doping range shown.	146
Figure 6.19: The final structures to be grown and measured informed by the simulations performed in the chapter.	148
Figure 7.1: The behaviour of each resistivity (ρ_{xx} and ρ_{xy}) when a sample has a single carrier of mobility μ_1 and carrier density n_1 (red solid), and when the sample has two carriers with equal density and the second carrier has a lower mobility (green dashes). Left: longitudinal resistivity against magnetic field. Right: transverse resistivity against magnetic field.	153
Figure 7.2: A diagram indicating the physical effects that occur at high fields depicted both classically and quantum mechanically.	153
Figure 7.3: A diagram indicating the physical effects that occur at high fields which result in an oscillating resistance trace, there these oscillations are periodic in $1/B$	155
Figure 7.4: A schematic diagram of the set up for a Hall measurement on a Hall bar using two lock-in amplifiers. The left lock-in amplifier supplies a low frequency oscillating voltage across a large resistor R to generate a current, and measures the longitudinal voltage. The right lock-in measures the transverse voltage.	157
Figure 7.5: The longitudinal and transverse resistivities measured against magnetic field for a square quantum well structure.	159
Figure 7.6: The measured longitudinal and transverse resistivities for a square quantum well (open circles), and a fit to the data using the two-carrier fit equations given in the previous section (lines). For clarity only a small selection of temperatures are shown, with a reduced number of points for each temperature.	160
Figure 7.7: The mobility and carrier density for a square quantum well structure where a single carrier is assumed (dots) and where a two carrier fit was carried out (diamonds and squares). The high mobility carrier (squares) was assumed to be the carrier in the ground state of the QW (the 2DEG).	160
Figure 7.8: Schematic diagrams showing the increase in carrier density with energy level. Left: A GaSb/AlGaSb quantum well with calculated energy levels using an infinite square well approximation. Blue lines indicate levels in the Γ -band with purple lines indicating levels in the L-band. The dashed black line indicates the Fermi level which was calculated from the measured carrier density. Right: The density of states (top) and carrier density (bottom) against energy with faint lines indicating the energy of the states. The carrier density in the first state just before the onset of occupancy in the second state, and at the calculated Fermi level, are labelled.	162
Figure 7.9: The longitudinal and transverse resistivities measured against magnetic field for a doped heterojunction structure.	163

- Figure 7.10:** The mobility and carrier density for a doped heterojunction structure where a single carrier is assumed (dots) and where a two carrier fit was carried out (diamonds and squares). The high mobility carrier (squares) was assumed to be the carrier in the ground state of the QW (the 2DEG). 163
- Figure 7.11:** The transport model for a 25 nm square quantum well structure where each line is labelled and the total mobility (black) is expected to align with the data which is shown for comparison (crosses). **Left:** The transport model using expected parameters. **Right:** The transport model where the parameters have been adjusted to ensure a fit to the low temperature data. 166
- Figure 7.12:** The transport model for a doped heterojunction where each line is labelled and the total mobility (black) is expected to align with the data which is shown for comparison (crosses). **Left:** The transport model using expected parameters. **Right:** The transport model where the parameters have been adjusted to ensure a fit to the low temperature data. 168
- Figure 7.13: Top:** Measured longitudinal resistivity for the doped heterojunction against magnetic field, across measurement temperature. **Bottom:** The longitudinal resistance against magnetic field, with a parabolic background subtracted. 169
- Figure 7.14:** Shubnikov-de Haas oscillations observed from the doped heterojunction plotted against $1/B$ to show the periodic nature of the oscillations. **Inset:** Fan diagram where the peaks and troughs of the oscillations (half integer and integer indexes respectively) are plotted against $1/B$ to find the peak frequency or fundamental field, BF 170
- Figure 7.15:** A plot of Shubnikov-de Haas oscillation amplitude dampening against temperature for different B -field values corresponding to resistance peaks and minima for the doped heterojunction. The dampening factor was fit to the extracted points and an effective mass was obtained and given in the legend..... 171
- Figure 7.16: Left:** Dingle plots the doped heterojunction at various temperatures where the data is free fit (solid line) and fit with a set intercept of 0 (dotted), each line is offset by 1 for clarity. **Right:** The quantum lifetime against temperature where the coloured circles indicate the free fitted lines from the Dingle plot, with the associated error from the fitting. The black squares indicate the quantum lifetime extracted from the Dingle plot when the intercept is set to 0. 172

List of Tables

Table 3.1: The formation enthalpies of the common defects found in GaSb given in eV [52].	41
Table 3.2: A table showing the growth condition variations used in the growth study. Where multiple V/III ratios are given, these correspond to multiple growths. The highest and lowest temperature in the table resulted in milky growths and thus won't be shown further.	57
Table 3.3: Activation energies (E_1) for GaSb samples grown with different growth temperatures using different temperature regimes. The error given is the std from the variance of the fit.	64
Table 4.1: The standard lithography recipe used in this work for both contacts and mesa masks, where the acceleration is the initial acceleration until the speed is reached.	82
Table 4.2: Dimensions of all Hall bar designs created on the Hall bar mask, labelled following the mask shown in Figure 4.6. The smallest aspect ratio is defined as the aspect ratio between neighbouring contacts.	88
Table 5.1: A table showing the contact recipes tested and their associated annealing recipes.	99
Table 5.2: A table showing resistance calculated over different ranges for each contacting recipe to 2 significant figures, and the ratio R_{Point}/R_{HighV} , to 1 decimal place. All values taken at 300 K.	103
Table 5.3: A table showing the extracted TLM contact resistances and the halved average resistances for each metallisation recipe at 300 K, given in $k\Omega$.	107
Table 6.1: A table indicating the parameters used in the S.P. solver calculations for $Al_{0.2}Ga_{0.8}Sb$ /GaSb structures. In the table α and β represent the material parameters for a change in band gap with temperature, and ϵ_r represents the relative permittivity.	118
Table 6.2: A table indicating the summarised Schrödinger-Poisson results from the confinement study for an $Al_{0.2}Ga_{0.8}Sb$ /GaSb heterojunction with a doped barrier and an undoped buffer, where each structure has a background acceptor concentration of $5 \times 10^{16} \text{ cm}^{-3}$ due to native defects.	122
Table 6.3: A table summarising the design options to be investigated using the transport model.	129
Table 6.4: A table to indicate the parameters used for the transport model, including the reference each value was acquired from.	137
Table 7.1: A table indicating the low temperature transport properties for each structure measured in this work, the carrier shown below is the high mobility carrier in all cases.	165

Table 7.2: A table showing the model parameters required to fit the mobility of an undoped square quantum well, at low temperature, in a transport model. It is shown that unphysical changes to parameters other than background impurity concentration are required to fit the data given the expected background impurity concentration. Fit 2 was used to fit the data in Figure 7.11..... 167

“I was taught that the way of progress was neither swift nor easy.”

- Marie Curie

Chapter 1

Introduction

1.1 Motivation

Over the last few decades, electron transport in nanostructures has been heavily investigated, particularly in materials such as silicon and gallium arsenide (GaAs). Over a period of 10 years the mobility of GaAs/AlGaAs heterojunctions increased by a factor of 1000, and research has since branched out into many other materials. However, a relatively similar material, gallium antimonide (GaSb), has yet been relatively untouched. Though the mobility of bulk GaSb has been investigated, no significant research into electron mobility has yet been performed on GaSb/AlGaSb two-dimensional electron gases (2DEGs). GaSb has a lower effective mass and a higher dielectric constant than GaAs, both advantageous for high mobility devices. Unfortunately, it also has a high native *p*-type background and has an interesting *n*-type band structure, with low lying L and X minima which can contribute to conduction. This work aims to further the knowledge of transport properties in confined *n*-type GaSb systems through investigation of both simulation and experimental work. This work also aims to further the understanding of the complications of creating a confined *n*-GaSb electrical device.

GaSb has been known and well-studied in the III-V semiconductor field as an optoelectronic material. The emerging material has proven significant in the semiconducting world, particularly in the areas of infra-red photonic detectors and long wavelength lasers [1-3]. However, detailed knowledge of the electrical properties of GaSb is relatively limited. Investigations into bulk transport properties started in the 1960s, though interest then waned, however, recently there has been a resurgence in interest in GaSb for with confined hole transport for topological insulators [4], as well as added interest in high magnetic field transport measurements in *p*-type GaSb [5]. Despite the

lack of depth of investigations into the electron based transport properties in GaSb, there has been research into various fundamental properties which will aid this work, such as the growth condition dependence of the native p -type defects found in GaSb [6-8] and the unusually high p -type nature created from low tellurium doping levels [9]. Further, research has shown that there is a particularly low-lying L-band in GaSb, where this has been shown to have a potentially significant impact on the measured Hall coefficient across temperature for bulk n -GaSb[10]. Nonetheless, confined electrical properties and electrical devices in n -GaSb based systems is a field that is under researched, where research in this area could unlock a wealth of potential applications [11].

As an understanding to the potential benefits that GaSb can unlock, it is worth comparing to the historical improvements seen in GaAs/AlGaAs systems, a comparatively similar III-V semiconductor. These comparisons not only highlight the similarities between GaSb and GaAs, but show the potential improvements possible in GaSb due to many advantageous physical properties. One of the principle reasons for the extensive research into GaAs, besides the low effective mass, is the fact that its alloy, AlGaAs is well lattice matched, reducing the strain in these systems. Whilst AlGaSb is less well lattice matched, the change in lattice constant for small aluminium fractions is still small, especially when compared to the more extreme III-V InSb, where strain and the associated defects are often a limiting factor in many practical heterostructures[12]. Further, recent developments into the growth of GaSb, particularly at Lancaster University, have shown that interfacial misfit arrays (IMFs) can be employed to effectively eliminate any strain between grown GaSb epilayers and a GaAs substrate, allowing for microns of unstrained growth. This allows the implementation of a defining feature of GaAs based systems in a material system where the electron effective mass is $\sim 42\%$ lower ($m_{\text{GaAs}}^* = 0.067 m_0$, $m_{\text{GaSb}}^* = 0.039 m_0$)[13].

Extending this comparison, since the invention of molecular beam epitaxy (MBE) by J. R. Arthur and A. Y. Cho in the late 1960s, GaAs based systems have improved in low temperature mobility from $\sim 10^4$ cm²/Vs in the late 1970s to $\sim 10^7$ cm²/Vs in the late 1990s. The highest reported mobility has been achieved in a GaAs two-dimensional electron gas (2DEG), with a maximum mobility of $\sim 35 \times 10^6$ cm²/Vs [14]. Many of these improvements have been achieved through improved understanding of growth conditions, the growth kinetics on the sample surface and dedicated MBE machines, as well as improvements in heterostructure design to reduce carrier scattering. On this first point, many of the improvements in understanding developed for GaAs are also directly applicable to GaSb, and further, many growth trials have previously been undertaken to

explain various experimental observations in GaSb. These include an inherent p -type background, believed to come from native defects, the formation of which are unavoidable in GaSb, though the density of which can be improved upon. Similarly, the understanding gained in the design of GaAs based heterostructures can be applied to GaSb, though again careful consideration has to be taken to account for the high p -type background. This is a research area that could be greatly expanded upon, with at this time, no strong confirmation of electrical measurements and analysis of confined n -GaSb based systems.

Expanding this point further to again highlight the advantageous properties of GaSb, a significant limiting factor of the mobility for many GaAs samples is the remote ionised impurities scattering, the mobility equivalent of which has a dependence of ϵ_r^2/m^* , where ϵ_r is the relative permittivity and m^* is the effective mass [14, 15]. For both these material parameters GaSb is favourable compared to GaAs for high mobility samples ($\epsilon_r = 15.7$ for GaAs and $\epsilon_r = 12.9$ for GaSb). These favourable parameters sparked interest from a number of research groups, as such Takeda *et al.*[6]. Takeda *et al.* investigated the possibility of improved mobility in AlGaSb/GaSb structures from AlGaAs/GaAs through simulation, focusing on the mobility produced from remote ionised impurities scattering at low temperature. Shown below in Figure 1.1 is a simulation completed by Takeda *et al.* showing the mobility associated with remote ionised impurities scattering at a temperature of 1 K. The simulation shows the mobility is greater for GaSb than GaAs across a wide range of carrier densities, giving promise to high mobility devices made from confined GaSb structures. This simulation however is limited to just remote ionised impurities. However, at the time this work was produced GaSb was a relatively unknown material, and therefore important factors were overlooked, such as the native defects present in GaSb. These defects are significant and typically result in a p -type concentration of $\sim 10^{17} \text{ cm}^{-3}$. Therefore, remote ionised impurities are not the only scattering mechanism that needs to be considered at low temperature.

Though these defects are significant in concentration, which will increase scattering and lower mobility, as mentioned previously, GaSb does not suffer from significant strain like other III-V materials such as InSb. Introduction of interfacial misfit arrays between GaAs and GaSb, allows for the growth of GaSb on GaAs substrates for many microns without significant strain build up.

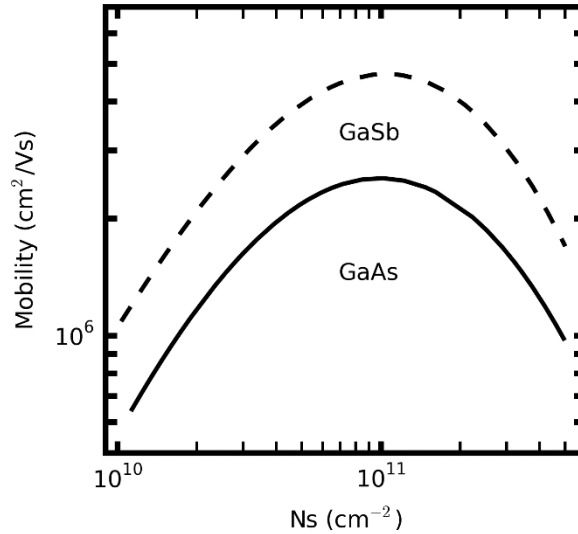


Figure 1.1: Simulated electron mobility as a function of sheet carrier density at 1 K for AlGaAs/GaAs (solid) and AlGaSb/GaSb (dotted) heterojunctions [15].

The production of high mobility structures leads to devices which can be used for low power consumption, high speed technologies such as in communications and sensing [16]. Historically, GaAs, being well researched and optimised for these applications. However, there has been a trend in recent years towards higher lattice constant, lower band gap materials for the production of high electron mobility transistors (HEMTs), in which the antimonides are next in line. GaSb is far behind the curve for these applications and is currently not well researched for even fundamental electrical properties[17].

The work presented here aims to help rectify this by performing detailed simulations of GaSb based structures to create designs for high mobility structures, growing, fabricating and measuring these AlGaSb/GaSb structures, and extracting and analysing their transport properties, relating these back to back to the initial simulations.

1.2 Thesis Structure

This thesis describes the design, growth, fabrication, measurement and analysis of $\text{Al}_{0.2}\text{Ga}_{0.8}\text{Sb}/\text{GaSb}$ heterostructures, where the devices processed are non-gated Hall bars and the measurements are aimed at obtaining the transport properties of these structures. Overall this thesis is a guide to the process of going from physical concept to reality. As such, each chapter (where relevant) contains background theory, implementation and results, where each chapter represents one step in the process towards the measurement of the transport properties of $\text{Al}_{0.2}\text{Ga}_{0.8}\text{Sb}/\text{GaSb}$ heterostructures.

Chapter 1 discusses the motivation for this work and where n -GaSb/AlGaSb structures fit into the field of transport measurements with regards to the more established GaAs/AlGaAs. The improvement in the mobility of GaAs heterostructures over time is also discussed to give an historical perspective of the possible improvements that can be made given sufficient time and with a focussed research effort.

Chapter 2 gives an overview of the general background theory that is necessary for the rest of this thesis, however theory specific to only a single chapter is discussed in that chapter. The theory outlined includes the electronic properties of crystals, such as crystal structure and band structure formation, the Fermi-distribution and the density of states, and the use of these to calculate the carrier density of doped and undoped systems. Basic transport theory is also outlined focussing primarily on the Hall effect, with the further concepts of transport lifetime and scattering discussed in Chapter 7. This chapter then moves onto band structure engineering and the formation of 2DEGs through alloying and layering of materials. The implications of confinement on the previously stated theory are then discussed. Finally, the practical realisation of confined structures is discussed in the form of strain within crystal structures, and lattice mismatch between dissimilar crystal compositions.

Chapter 3 explains the use of epitaxial growth in this work and the challenges that come from the native defects in GaSb. Not only is the theory behind molecular beam epitaxy (MBE) explained, but also the standard procedure of how to use an MBE machine to practically realise GaSb based heterostructures. Following this, a literature review is given, describing the nature of the defects in GaSb, with this influencing the subsequent growth study performed in this work to improve the quality of GaSb growth. This growth study varied different growth parameters (such as flux ratios and growth temperatures) in an attempt to reduce the native defects and improve mobility in bulk GaSb as a building block to creating high mobility $\text{Al}_{0.2}\text{Ga}_{0.8}\text{Sb}/\text{GaSb}$ heterostructures. This section also includes a tellurium doping calibration study, with samples presenting with an unusual correlation between carrier concentration and cell temperature (doping level) at low cell temperatures. Both n -type and p -type samples were investigated across a range of measurement temperatures.

Chapter 4 moves on from growth to the fabrication of Hall bars, where standard processing procedures are described. The theory behind each procedure is discussed and the processing recipe outlined. The procedures include optical lithography, metallisation

via thermal evaporation, etching and electrical bonding. The lithography mask used was created specifically for this work and so the design process of the mask is also described.

Chapter 5 outlines the difficulties of the metallisation of *n*-type GaSb to create low resistance contacts, as well as the investigation performed into achieving ohmic contacts for *n*-GaSb. There does not exist in the literature a standard metallisation for ohmic contacts to *n*-GaSb, despite many research groups attempts, and as such, a literature review is given to highlight the range of possible metallisation recipes previously attempted. The metallisation of *n*-GaSb is discussed at length as creating ohmic contacts to this material has proven difficult in practice. As such, the theory behind ohmic contacting and the investigation into varying contacting recipes is presented. Simple characterisation measurements were obtained for each metallisation recipe to obtain a practical solution to contacting *n*-GaSb, where the aim was to find a reasonable contacting resistance across the temperature range being used for transport measurements (3-300) K.

Chapter 6 describes the simulations undertaken to appropriately design an $\text{Al}_{0.2}\text{Ga}_{0.8}\text{Sb}/\text{GaSb}$ heterostructure to achieve two-dimensional confinement of electrons. The first section of the chapter provides the practical design considerations for the heterostructures and how these considerations were accounted for in the simulations that were undertaken. Following this, the theory behind a Schrödinger-Poisson solver, used to analyse the band structure of the heterostructure, is given. The band structure simulation results for various $\text{Al}_{0.2}\text{Ga}_{0.8}\text{Sb}/\text{GaSb}$ structures are presented, where the results include investigations into the dependence of the confinement in the heterojunctions when parameters such as the dopant and defect concentrations are varied. Subsequently, transport modelling theory is discussed, with the predicted transport properties (mobility and individual scattering rates) of $\text{Al}_{0.2}\text{Ga}_{0.8}\text{Sb}/\text{GaSb}$ quantum wells and heterojunctions shown. There is a further look into the electron scattering behaviour in these structures where square and triangular quantum wells are compared. From these studies, a set of viable structures are selected to be grown and measured, with the measured results from these structures displayed in chapter 7.

Chapter 7 presents the measured transport data for an $\text{Al}_{0.2}\text{Ga}_{0.8}\text{Sb}/\text{GaSb}$ square quantum well and two $\text{Al}_{0.2}\text{Ga}_{0.8}\text{Sb}/\text{GaSb}$ heterostructures, designed in the previous chapter. The chapter begins by describing the equipment set ups used to perform electrical measurements. The low *B*-field data is analysed, including through two-carrier fitting, and the electron mobilities and carrier densities are extracted for the square quantum well

and the heterojunctions. Comparisons are again drawn between the heterojunctions and quantum wells with a transport model used to analyse the principle scattering mechanisms in each structure. Subsequently, high-field, Shubnikov-de Haas measurements are presented and analysed, with these confirming the presences of a 2DEG, as well as allowing extraction of a carrier density, effective mass and quantum lifetime. Discrepancies between the predicted and measured mobilities are also discussed.

Chapter 8 summarises the body of research and results presented in this work, and suggests possible areas of study for future endeavours, including further studies into the growth, metallisation and high temperature behaviours of *n*-type GaSb based materials.

“Anyone who is not shocked by quantum theory has not understood it.”

- Niels Bohr

Chapter 2

The Physics of Semiconductor Structures

In the modern-day world, we are surrounded by semiconductor structures, from the light emitting diode to the field effect transistor and have a good understanding of their electrical properties. The key to the success of the semiconductor is the control and the variety. Rather than being simply conducting or non-conducting they require an input such as temperature or voltage in order to conduct and the input required is dependent on the exact composition of the semiconductor. This allows a host of (semi)conductive material to be created with different properties each suitable for a different application by simply adding a bit more of a particular element.

In this chapter the physical and electronic structures of bulk semiconductors will be explained, followed by a brief summary of electron transport. After which, there will be an explanation of combining semiconductor materials in order to create electron confinement, from which some of the strengths of semiconducting materials will become clear. Overall this chapter introduces the background knowledge required to understand the rest of the thesis, but more relevant theory to the specific results will be given in the following chapters. The theory in the first two parts of this chapter is required for understanding bulk materials, which are investigated for material quality in Chapter 3. The overall aim of this thesis is an investigation into transport of electrons in AlGaSb/GaSb structures, the engineering of which is discussed in the latter section. From this base knowledge, structures were created, where Chapter 6 and 7 discuss the simulation and measurement of these confined structures. This chapter will discuss semiconductors in general, however, with particular reference to III-V semiconductors and specifically GaSb.

2.1 Electrical Properties of Semiconductors

2.1.1 Crystal Structure

Semiconductors have a crystalline structure where a regular array of atoms is formed. Binary semiconductors (a semiconductor created from two atomic species) will alternate each atom to create a regular structure where each atom of an atomic species is surrounded by the other atomic species. The outer electrons of each atom bond the structure together; the group III atom donates three electrons to bonding and the group V donates five electrons to bonding etc. This bonding is in general covalent (sharing of electrons), however there is some ionicity due to the electronegativity¹ difference of the group V and III atoms resulting in a greater distribution of electrons around the group V atom [18].

Crystals can form a few different types of crystalline structure each made up of the same repeated shape, a unit cell. The Bravais lattice describes the shape of the unit cell with the most common being face-centred cubic, primitive cubic or body-centred cubic as seen in Figure 2.1 (left).

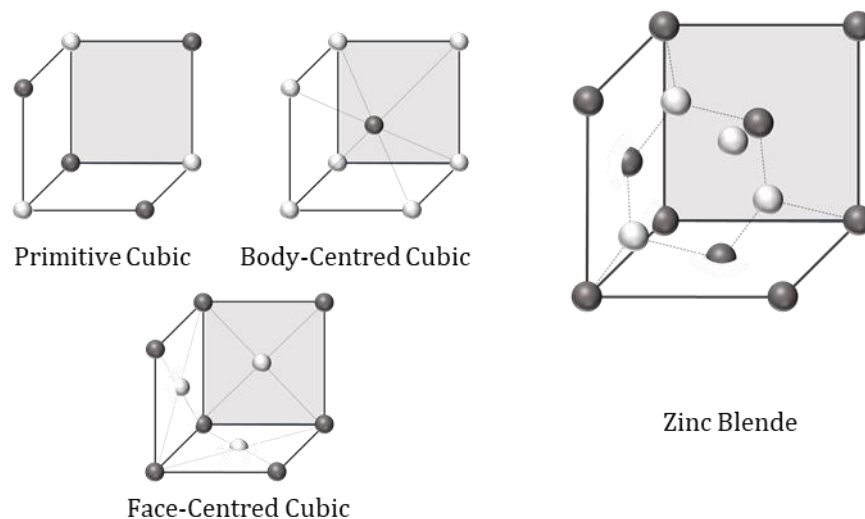


Figure 2.1: Left: Examples of the standard Bravais lattices including the primitive cubic, the body-centred cubic and the face-centred cubic (fcc). **Right:** An example of a zinc blende structure where the dark atoms form one face centred cubic structure and the light atoms form another. Where the bottom left light atom is the equivalent to the bottom left corner of its fcc structure and the others are the face centred atoms that are held in that cubic unit cell.

¹ The power of an atom in a molecule to attract electrons to itself.

In general, III-V semiconductors such as GaSb and GaAs have a zinc blende structure. This structure consists of two face-centred cubic lattices (fcc) combined, where the group three atom forms one fcc and the group V atom creates another. Each atom is bonded to four nearest-neighbour atoms of the alternative species, this could also be described as a face-centre cubic with two atoms offset from each other in each atomic slot [19, 20]. When growing a semiconductor crystal, the structural integrity of the crystal is key. When combining materials, an important property to note is the lattice constant, a_0 , which is the width of the unit cell; in cases where the unit cell is not cubic a material may have more than one lattice constant in each direction [19].

In order to describe the electronic properties, reciprocal or momentum space is often used by redefining the crystal lattice in that space. In this space, the electron energy states can easily be associated with an electrons wave-like nature, where the reciprocal lattice in k -space defines the allowed energy states for the electrons through the associated momentum. The spacing between the allowed states is equal to $2\pi/L$, where L is the length of the crystal. This concept can be a difficult one, but the real importance is that the periodic nature of the crystal is maintained in momentum space and so much like the unit cell, only the repeated element of the space needs to be observed.

2.1.2 Band Structure and Effective Mass

The band structure of a semiconductor is simply a description of the energy states in the crystal that electrons may occupy.

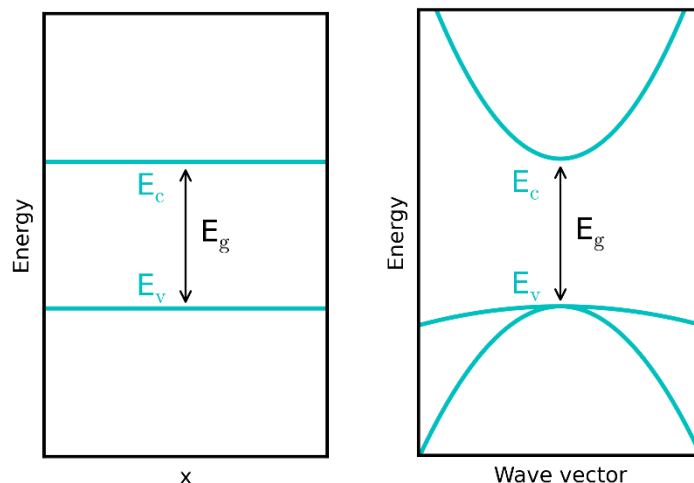


Figure 2.2: **Left:** Simplistic band diagram commonly used when combining multiple semiconductors showing the conduction band edge E_c , the valence band edge E_v , with a gap between them, E_g . **Right:** Parabolic band structure showing the conduction band, and the heavy hole and light hole bands (both of which make up the valence band).

Some energy states are so high that they will never be occupied and some so low that they are consistently occupied. The energy states are closely packed and form what are called bands shown on an energy diagram. The simplest band structure diagram can be displayed as a valence band and conduction band, where at 0 K all states are filled up to the valence band edge. Between the bands is an energy band gap where energy states are forbidden. The size of the band gap is the obstacle electrons have to overcome in order to conduct. The upper limit of the band gap is given by the conduction band, which has an edge at the lowest unfilled state. This is for intrinsic semiconductors where doping and dopant states are not considered, doping is considered in more detail later in the chapter. In the conduction band the electrons are free, and not bound to an individual atom.

The bands originate from the states of orbiting electrons, where the outer electrons can be described by their state, such as $4p^1$ for Ga and $5p^3$ for Sb. When two atoms are brought close together the states of the separate atoms begin to merge and form what are called bonding and antibonding states. In a bonding state the electron probability density is nonzero between the atoms and is found at a lower energy, it is these states that form the valence band. The antibonding state is solely focused on each atom with zero-electron distribution between them, these states are what form the conduction band.

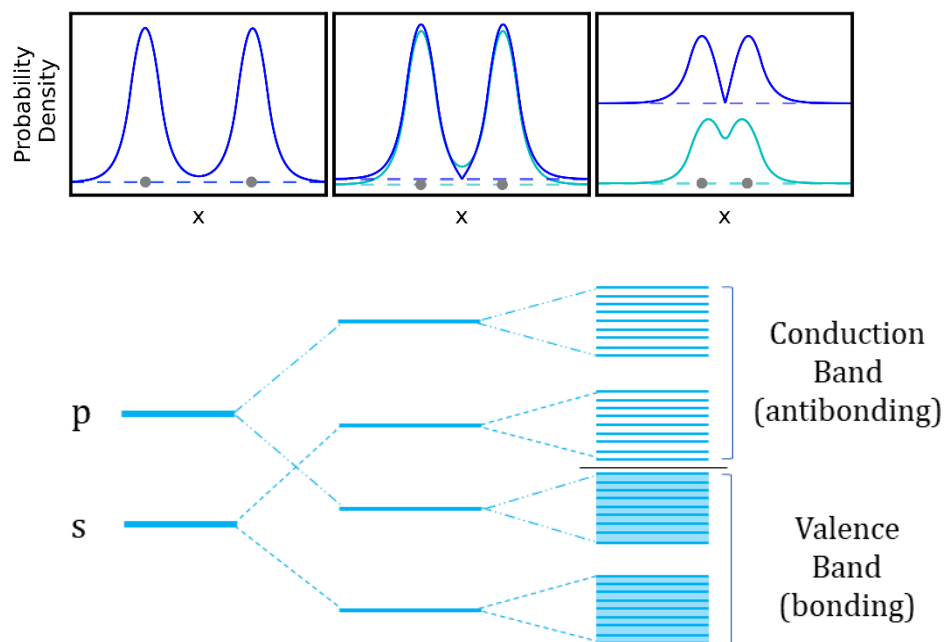


Figure 2.3: Top: The probability densities of the bonding and antibonding states offset by an amount relative to the energy difference between them. As the separation decreases the difference in energy increases. The light blue indicates the bonding state and the dark blue indicates the antibonding state. **Bottom:** Formation of bands and a gap from bonding and antibonding orbitals as the atomic distance decreases, adapted from ref [21].

These states are at different energies due to the Pauli exclusion principle, and only one spin up electron and one spin down electron can fill each state. This is just a simple case with a couple of atoms but can be readily extended to a full crystal structure where both the valence and conduction bands have a high density of states in each and are separated by an energy gap[22].

The above is a qualitative description of the tight-binding model, where the crystal potential is strong, and electrons are mostly bound to atoms. The tight binding model is mathematically stated in a number of standard texts such as “*Band Theory and Electrical Properties of Solids*” [23]. There are a few other models that can be used to describe the formation of a band structure such as the free and nearly-free electron models, where weak crystal potentials are assumed, and the model starts from a formed crystal and introduces the electrons. Despite approaching the situation from a completely different point of view, all these models arrive at similar band structures, with a periodic nature and approximately parabolic relation of energy in \mathbf{k} (reciprocal space)[23].

Reciprocal space, where the dimensions are expressed in the wave vector k , is often used to help describe the energy of the electrons in the crystal. In one dimension the wave vector k is related to real space by $k_x = n_x 2\pi/L_x$, where L_x is the length of the crystal and n_x is an integer number. The electron probability density in a crystal spreads across all real space, making real space an inconvenient variable when evaluating electron movement. The wave vector k is related to the spatial frequency of an electron’s probability density, making it a more convenient coordinate.

The simplified parabolic dispersion relation (E vs k) for a semiconductor is suitable for many cases and can be determined with equation 2.1

$$E = \frac{\hbar^2 k^2}{2m_e}, \quad \mathbf{2.1}$$

where k is the wave vector, E is the energy of the state and m_e is the electron mass and where the electron mass is proportional to the curvature of this E - k relationship. Equation 2.1 is the free electron case, however when we consider an electron travelling in a crystal, the potential of the crystal must also be considered. Mass is a quantity that is in general a resistance to acceleration and thus an effective mass, m^* , is used to more accurately describe the movement through the crystal lattice. The crystal lattice itself will exert a force on the electron as it moves and thus the effective mass will be crystal, and therefore material, dependent. The effective mass is defined by the curvature of the respective energy band and, can be expressed by

$$\frac{1}{m^*} = \frac{1}{\hbar^2} \frac{\partial^2 E}{\partial k^2}. \quad 2.2$$

In the crystal, the energy, E , of the conduction band will be given by

$$E = E_g + \frac{\hbar^2 k^2}{2m_e^*}, \quad 2.3$$

where the top of the valence band is equal to 0 and the valence dispersion energy is defined as $E = -\hbar^2 k^2 / 2m_h^*$. In the valence band a different effective mass has been stated, this represents the effective mass of a hole. The hole is a quasi-particle which is defined as the absence of an electron when an electron is excited to the conduction band. A hole moving in the valence band is considered to be a positively charged particle as it behaves in the opposite manner to the electron.

In certain semiconductors the dispersion relationship is non-parabolic, leading to an energy-dependent effective mass. Equation 2.1 is simply a first approximation and the second order equation becomes

$$E \left(1 + \frac{E}{E_g} \right) = \frac{\hbar^2 k^2}{2m^*}, \quad 2.4$$

with the effective mass for a non-parabolic band defined as

$$m^*(E) = m^* \left(1 + \frac{2E}{E_g} \right) \quad 2.5$$

where $1/E_g$ is considered the non-parabolicity factor. Therefore, as the band gap reduces the effect of non-parabolicity increases [24]. With the k vector for both parabolic and non-parabolic bands being dependent on carrier density, the physical significance of non-parabolicity is a resulting carrier density dependent effective mass.

By using the quadratic formula the non-parabolic energy E can be found for a range of k -vectors and the non-parabolic effective mass can be extracted. It is shown clearly here that the effect of non-parabolicity only comes into play for GaSb at a k of $\sim 0.05 \, 2\pi/a_0$, shown in Figure 2.4.

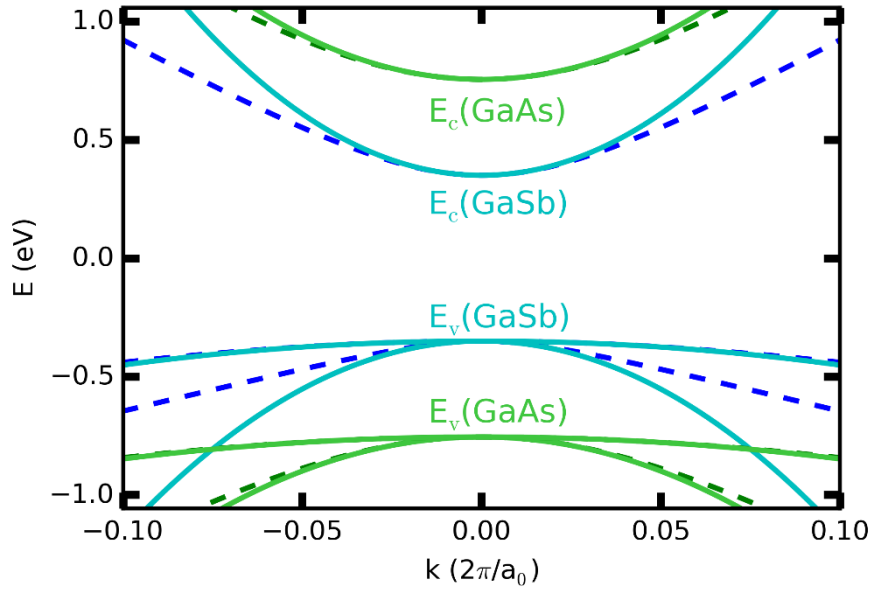


Figure 2.4: Parabolic and non-parabolic dispersion relations for GaAs (green) and GaSb (blue), with the non-parabolic dispersion shown as dashed lines.

Above where we have discussed the conduction and valence bands, we are describing a single direction in the crystal, usually this is satisfactory. However, in reality the crystal structure is a 3D entity, and there are differing conduction band-edges relating to these directions.

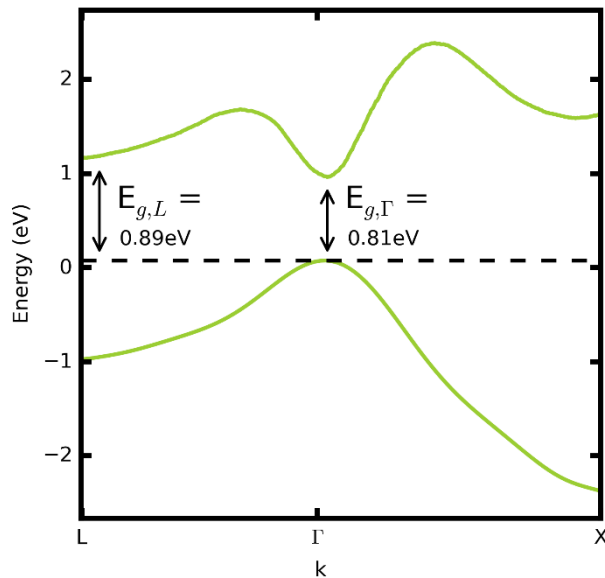


Figure 2.5: Full GaSb band diagram for the conduction and valence bands, reproduced from ref [11], annotated to point out the E_g for both Γ and L points.

The Γ -band edge is the most symmetric point in the crystal and is generally the bottom of the conduction band. The implication of the varying band edge in our case is that the band

edge at the L point (the L-band edge) in GaSb is lies close in energy to Γ -band and thus electrons with a high enough energy may conduct in the L-band where the effective mass is higher. This will affect the transport of electrons, as a higher mass results in lower mobility electrons.

All of the above structures are assumed to be at 0 K. The bands, however, are temperature dependent and the change given by the material parameters α and β in the Varshni equation, where the energy gap can be empirically found to equate to

$$E_g(T) = E_g(0 \text{ K}) - \frac{\alpha T^2}{\beta + T}, \quad 2.6$$

where for GaSb $\alpha = 4.2 \times 10^{-4} \text{ eVK}^{-1}$, $\beta = 140 \text{ K}$ and $E_g(0 \text{ K}) = 0.81 \text{ eV}$, resulting in a band -gap of $E_g(300 \text{ K}) = 0.73 \text{ eV}$ [13].

Now that the distribution of the states has been well defined, the final part in the electrical model of semiconductors is a description of what role the charge carriers actually play. The Fermi level is the level or energy state at which there is a 50% probability of that state being occupied. This is a practical description as it is temperature dependent, where higher states will have an increased probability of being occupied at high temperatures. If the Fermi level lies in or close to the conduction band the structure is n-type (from donors) and electrons are the majority charge carriers. If it lies within the band gap no conduction occurs without external input such as temperature. If it lies in the valence band the structure is p-type (due to acceptors) and holes are the majority carriers. A more fleshed out explanation of the description of carriers and Fermi level will be given in the next section.

2.1.3 Carrier Distribution, States and Density

The concentrations of electrons in the conduction band and holes in the valance band are calculated by combining two fundamental tools, the density of states (DOS), determining where the states lie, and the Fermi distribution, which determines the probability that the states will be filled. We will start by describing the DOS in three dimensions, after which the Fermi distribution will be explained, and, by combining these two models, the calculation for carrier density can be found. The inclusion of dopants will also be discussed, and how to address them mathematically.

2.1.3.1 Density of States in 3D

The density of states (DOS) is the number of energy states per unit energy per unit volume. From this calculation, the availability of energies that carriers can have, can be found. In three dimensions the density of states is found to be:

$$g_{3D}(E) = \frac{1}{2\pi^2} \left(\frac{2m^*}{\hbar^2} \right)^{\frac{3}{2}} \sqrt{E - E_g}. \quad 2.7$$

This equation is derived mathematically in many standard texts (see refs[19, 25, 26]), however, to understand its context, the derivation will briefly be described qualitatively.

The density of states is derived by isolating an arbitrary space or shape in k -space, finding the number of states in that volume and dividing by the volume and energy. This shape tends to be a spherical shell so that the magnitude is equal in all directions. The k states are separated by $2\pi/L$ in every direction and thus a regular grid can be created, relating k -space to real space with the crystal length L . The k -states that fall within that spherical shell can be then counted, resulting in the number of states per volume per energy.

Equation 2.7 can be integrated between two energies to find the volume density of available states, where $E=0$ is taken to be the valence band edge. Figure 2.6 shows a continuous distribution of increasing number of states with energy for GaSb. The density of states can also be calculated for reduced dimensions, the uses of which will be discussed later in this chapter.

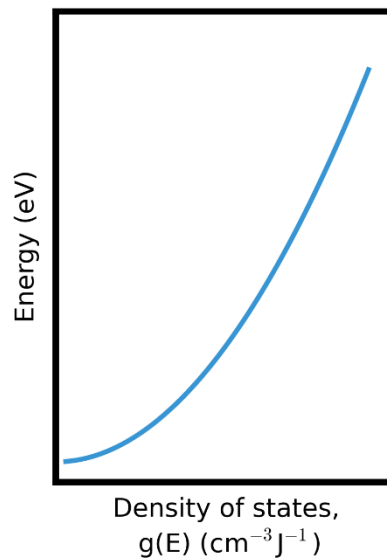


Figure 2.6: The density of states for electrons against energy in 3D.

The Pauli exclusion principle states that no two electrons can have the same quantum numbers, and so two electrons can only occupy the same state if they have opposing spin, and thus a factor of two has been included in the density of states to account for spin.

2.1.3.2 Fermi-Dirac Distribution

The Fermi-Dirac distribution is a probability density function which allows the probability of an energy state being occupied to be calculated against temperature. As shown in Figure 2.7, at very low temperatures (3 K) there is a sharp step, where, up to the Fermi level the probability of a state being occupied is ≈ 1 , and above it the probability is ≈ 0 . The Fermi level here lies in the mid gap where there are no states, if there were states here, they would be occupied. As temperature increases this sharp step softens and the probability of states being occupied in the conduction band increases. Therefore, even with a Fermi level at mid gap, there will be a small probability of occupied states in the conduction band as the temperature increases. It should be pointed out again that the Fermi level is the point where the Fermi distribution, the probability of a state being occupied, is 50%, meaning all the states above this have a lower probability of being occupied.

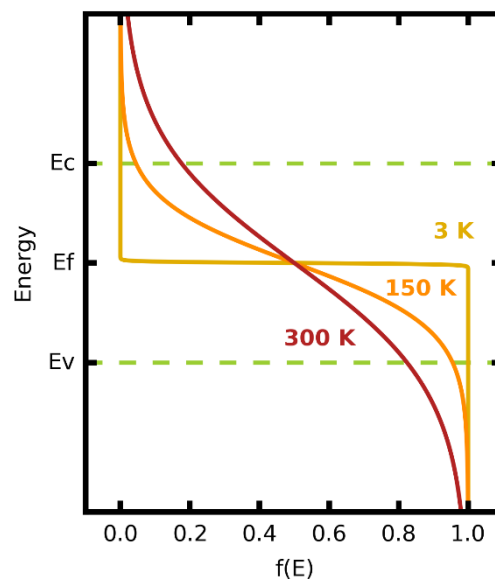


Figure 2.7: The Fermi Dirac distribution against energy with an indication of how the distribution changes with temperature. As temperature increases there is an increased likelihood of having occupied states in the conduction band.

Holes follow the inverse distribution, where at 0 K the probability is equal to 1 above the Fermi level. The Fermi level at mid gap means no conduction, fitting with the definition of an intrinsic semiconductor, where no conduction can occur without stimulus, such as temperature.

Formally, the Fermi Dirac distribution describes the probability that a fermion will occupy an energy state, E_i , at a given temperature T , mathematically given by equation 2.8. Where E_f is the Fermi level and k_b is the Boltzmann constant

$$f(E_i) = \frac{1}{e^{(E_i - E_f)/k_b T} + 1} \quad 2.8$$

The probability of a state being occupied by a hole is given by $1 - f(E)$.

2.1.3.3 Carrier Density

So now we have an understanding of the distribution of the energy states across the energy spectra (DOS) and an understanding of the probability that those states will be filled (Fermi-Dirac distribution). From these two distributions we can determine the density of electrons in the conduction band and equivalently the density of holes in the valence band, given by equations 2.9 and 2.10. The density of electrons is given by

$$n = \int_{E_c}^{\infty} g_c(E) f(E) dE, \quad 2.9$$

where $g_c(E)$ represents the density of states in the conduction band and $f(E)$ represents the Fermi distribution. This expression states that given a region of energy, the density of states across that energy times by the probability of those states being occupied gives us a density of electrons. The visual realisation of this can be seen in Figure 2.8.

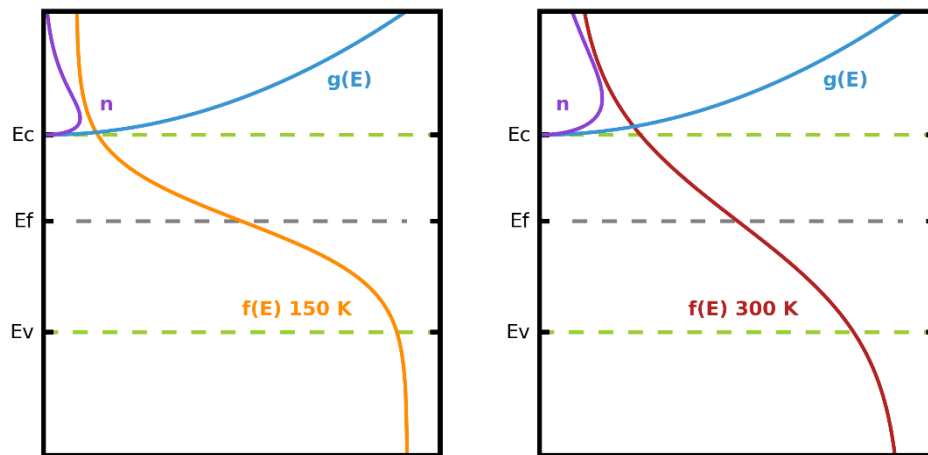


Figure 2.8: Visualisation of carrier density calculation at 150K (left) and 300K (right), where the density of electrons increases with temperature due to the increased probability of occupation of electronic states in the conduction band.

Equally, the hole concentration in the valence band is be given by

$$p = \int_{-\infty}^{E_v} g_v(E)(1 - f(E))dE. \quad 2.10$$

In the above we have been describing the case where there are no impurities or charged defects and the structure is simply intrinsic; intrinsic carrier concentrations tend to be very low.

To calculate an intrinsic concentration equation 2.11 tends to be used where N_c is known as the effective density of states in the conduction band and N_v is known as the effective density of states in the valence band, which are both derived from the Fermi-Dirac distribution. With intrinsic semiconductors there is charge neutrality, where, in a perfect crystal, each electron in the conduction band will leave a hole in the valence band, meaning that the intrinsic carrier density, n_i is equal to the number of electrons, and also the number of holes ($n_i=n=p$), then

$$n_i^2 = N_c N_v \exp(-E_g/k_b T),$$

$$N_c = 2 \left(\frac{2\pi m_e^* k_b T}{h^2} \right)^{\frac{3}{2}}, \quad 2.11$$

$$N_v = 2 \left(\frac{2\pi m_h^* k_b T}{h^2} \right)^{\frac{3}{2}}.$$

Using equation 2.11 an intrinsic carrier density of $1.54 \times 10^{12} \text{cm}^{-3}$ for GaSb is found at 300 K. It is easy to see how calculations of material parameters quickly become complicated when temperature dependence is incorporated. It is often assumed that the parameters are temperature independent which is often not the case.

It should be noted here that there is a subtle shift in the Fermi level with temperature for an intrinsic semiconductor, as there is a higher probability of occupied states in the conduction band, the 50 % probability of occupation is increased. The significance of this shift is very dependent on the material, but usually the Fermi level remains approximately midgap [27, 28] as typically $k_b T \ll E_g$ and $N_v/N_c \approx 1$:

$$E_f = \frac{E_g}{2} + \frac{k_b T}{2} \ln \left(\frac{N_v}{N_c} \right). \quad 2.12$$

In the case of GaSb at 300 K $E_f = E_g/2 + 58$ meV and thus is approximately midgap, where E_g for GaSb is 730 meV.

2.1.3.4 Doping Considerations

Often semiconductors are doped to increase the number of electrons or holes. Donor doping is achieved by putting an impurity atom with an extra electron in its outer shell into the crystal. For example in III-V semiconductors, group 6 elements in the periodic table are used as donor atoms (Te, Se, S) and tend to replace the group V atom. Group 4 elements can be used but tend to be amphoteric (can act as either acceptor or donor). This is due to them either replacing the group V atom and introducing a hole or group 3 and introducing an electron. Despite the amphoteric nature they are still commonly used in systems such as GaAs, where the preferred site of the silicon is determined by the temperature the GaAs is grown at, and there is a wide temperature range at which growth can be achieved. In GaSb there is a narrower range of temperatures and thus silicon acts as an acceptor.

When donor-impurities are introduced into the system a state is created just below the conduction band and electrons are easily promoted to the conduction band from it, even at low temperature. The donor-like nature tends to be associated with the purposeful doping, however any impurities could be an acceptor or a donor in a crystal, and in some cases defects in the crystal can also display this behaviour, such as in GaSb. If the state is very close to the conduction band they are named shallow donors. These new states imply that there is a higher probability of finding an electron in the conduction band than in the intrinsic case and thus the energy at which there is a 50 % probability of a state being filled (the Fermi level), is pushed up towards the conduction band. The extent of the movement is dependent on the number of donor atoms. The reverse is also true for acceptor impurity atoms creating states near the valence band and pushing the Fermi level down near the valence band [26]. The above equation, 2.12, is therefore no longer applicable and a new equation dependent on carrier density must be used.

The calculations in the previous section are based on the assumption that the Fermi level is firmly within the band gap (over $2k_bT$ away from either band). However, as stated above, with increased doping this is no longer the case. For semiconductors with a low m_e/m_h ratio such as GaSb and InSb these assumptions are invalid for only a small concentration of dopants and so the calculations should be treated carefully.

As intrinsic concentrations are quite low in comparison to the number of dopants added, materials with shallow dopants are approximated to have a number of electrons equal to

the dopant ions, or holes equal to acceptor ions. If both acceptors and donors are present and neither are of negligible concentration, the materials are called compensated. This means that a proportion of the electrons created by the donor atoms get trapped by the acceptor states of the acceptor atom, neutralising the acceptor atom without creating a charge carrier. Compensated material where the intrinsic carrier concentration is negligible is approximated to have a number of carriers equal to the difference in donor and acceptor atoms; electrons where donors are in the majority and holes where acceptors are in the majority. Though it is no longer the case that the numbers of electrons and holes are equal as in the intrinsic case, charge neutrality can still be applied in any equilibrium system where the sum of all the positively and negatively charged particles equals zero. This can be used to find carrier concentrations in doped semiconductors, or more accurately the number of ionised dopant atoms from a measurement of carrier concentration [29]. Charge neutrality states that

$$N_D^+ + p = N_A^- + n, \quad \mathbf{2.13}$$

where n is the number of electrons in the conduction band, h is the number of holes in the valence band, N_D^+ is the number of positively charged donor atoms (where the electron has been ionized) and N_A^- is the number of negatively charged acceptor ions.

How close the states lie to their respective bands also plays a large role in the number of carriers created. Before carriers become freed from their dopant atom (activated) they require an amount of energy equal to the energy difference between the state and the conduction band (the ionisation energy). Shallow dopants are close enough to the band that at 300 K they are almost all ionised. However, this is not always the case and the number of electrons created from the donors, n_d , can be calculated by

$$n_d = N_D^+ = N_D \left(\frac{1}{1 + g_d e^{\frac{(E_f - E_d)}{k_b T}}} \right), \quad \mathbf{2.14}$$

where g_d is the degeneracy factor, which is 2 for donors and 4 for acceptors (as the valence band is split into the heavy-hole and light-hole bands) and E_d is the ionisation energy. In the situation where an acceptor has more than one energy level the degeneracy and the thermalisation factor $g_d \exp((E_f - E_d)/k_b T)$ is replaced with a summation over all the levels:

$$n_d = N_D^+ = N_D \left(\frac{1}{1 + \left(\sum \left\{ g_d e^{\frac{(E_d - E_f)}{k_b T}} \right\} \right)^{-1}} \right). \quad 2.15$$

In reality, distinguishing the number of electrons that come from the dopants is difficult through measurement and what is actually measured is the total number of electrons, which in a compensated material is given by

$$n \approx \frac{N_D - N_A}{2N_A} \left(N_c \exp \frac{E_d - E_c}{k_b T} \right), \quad 2.16$$

which is found through a rather long rigorous treatment of the activation and Fermi-Dirac distribution [27, 30].

2.2 Transport in III-V Semiconductors

The subject of all electronics is the movement of electrons (or holes). The transport properties of semiconductors, both bulk and in heterostructures, is then of course of much interest in the creation of devices. Much can be said on this topic in terms of both measurement and physics, below is a brief summary of both, followed by more rigorous discussions in relevant chapters. Above we have discussed physical interpretation of carrier density, the measurement of which is discussed in the following section.

2.2.1 The Hall Effect Phenomenon and Measurement

The Hall effect occurs when a conductive material with a flow of charge carriers, I_x , is subjected to a magnetic field, B_z , which is applied perpendicularly to the direction of flow of the charge carriers.

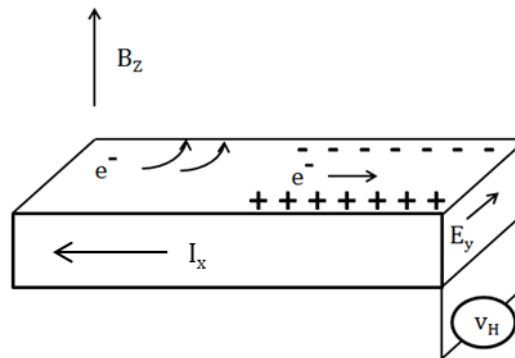


Figure 2.9: A schematic diagram of the Hall effect, showing the movement of electrons, creation of the electric field and the direction of the Hall field.

A force, the Lorentz force, acts on the electrons due to the magnetic field, changing their direction. The movement of charge carriers to one side creates a charge difference between the sides of the sample and thus produces an electric field, E_y , known as the Hall field. The electric Hall field counteracts the magnetic field effect and so the flow of charge carriers continues to flow as before, see Figure 2.9. When the forces are equal and opposite they give equation 2.17, where q is the charge of an electron (or hole) and v is its velocity [31], where,

$$F_{Lorentz} = (B_z \times v)q = qE_y = F_{EField} . \quad 2.17$$

Due to the charge separation across the sample, a measurable potential difference, the Hall voltage, V_H , is produced. Utilising this phenomenon, carrier concentration and carrier mobility can be extracted from measurements of voltage in differing orientations.

There are subtle differences in the calculation of these properties depending on the structure and geometry which is being measured, which will be explained where relevant in the results chapters of this thesis. For now it will simply be said that for bulk semiconductor material, measuring the Hall voltage can be used to determine the carrier concentration of that material, n as shown in equation 2.18, where t is the thickness of the sample, I_x is the current and q is the charge of the carrier.

$$V_H = \frac{I_x B_z}{qnt} . \quad 2.18$$

In addition to the carrier concentration, from the sign of the Hall voltage the type of the majority charge carriers can be found (electrons, n , or holes, p). Combining the Hall voltage with the longitudinal voltage and associated resistivity, ρ_{xx} , the carrier mobility, μ , can be extracted, where

$$\mu = \frac{V_H t}{B_z I_x \rho_{xx}} . \quad 2.19$$

The mobility is the average speed at which a charge carrier will travel with respect to the electric field that is being applied to it, which is the case for any electrical current. Measurements of mobility allow us to understand the ease at which an electron can travel through the material and as such can be thought of as a material quality factor when comparing like for like samples. The transport properties are dependent on one another through resistivity and are related by equation 2.20, such that

$$\mu = \frac{1}{\rho_{xx} n e}, \quad 2.20$$

where e is the magnitude of the charge of the electron. This is, of course, a simplified view of the Hall effect as there may be more than one current path, more than one carrier type and there may be inhomogeneities in the sample.

The above relates physically measurable quantities (V_H, ρ_{xx}) with material dependent parameters (n, μ). However, a more detailed derivation of the mobility can show how this also relates to the physical scattering processes (through the momentum relaxation time), where this gives a further understanding of material quality, independent of the effective mass. If we return to think about the force on an electron, we can see that the force of the electric field accelerates the electron. However, it is not always simply the case shown in equation 2.21,

$$\mathbf{F} = q\mathbf{E} = m\mathbf{a} = m^* \frac{d\mathbf{v}}{dt}, \quad 2.21$$

and in fact this is only true initially. Understandably this “speed” will be highest when the charge carrier travels in a straight line in the direction indicated by the electric field, which of course won’t always be the case. When a charge carrier differs from its ballistic path, it is due to a scattering mechanism which can take the form of anomalous charged impurities, phonons or defected material. These collisions act against the electrostatic force that is accelerating the electrons, and the average time for the velocity of the carrier to be randomised by these collisions is given by τ , the transport lifetime, and so incorporating this scattering term into equation 2.21 gives the force to be

$$\mathbf{F} = q\mathbf{E} - m \frac{\mathbf{v}}{\tau} = m^* \frac{d\mathbf{v}}{dt}. \quad 2.22$$

This equation always holds, where after the initial acceleration due to the electric field the electron will scatter and reach a steady velocity called the drift velocity. This is in fact an average as the scattering of the electrons will accelerate the carrier in differing, randomised directions, but in general do not completely change the direction of flow. The resulting acceleration is then zero and the mobility can be defined as the ratio of the magnitude of the velocity to the magnitude of the electric field, giving

$$\mu = \frac{v}{E} = \frac{\tau e}{m^*}. \quad 2.23$$

These scattering mechanisms reduce the mobility of the charge carrier and so are preferably minimised to create high speed devices. The scattering mechanisms are limitations of the mobility, and so it is often said that the mobility of a structure is “background impurity limited” or “interface roughness limited”. The mobility of like for like structures can therefore be an estimation of the density of defects and anomalies in the structures. At room temperature however, mobility is generally limited by phonons, which have a strong temperature dependence, unlike most other scattering mechanisms. The extent of knowledge that can be unlocked from mobility and the associated scattering mechanisms will be discussed in much greater detail in chapters 6 & 7.

The above derives the equations for bulk material, however this work is also interested in the investigation of transport properties in confined structures, in particular AlGaSb/GaSb heterojunctions. By combining particular materials, a conducting electron channel can be created. The creation of these structures requires knowledge of not just the individual materials but how they combine; this is called band structure engineering.

2.3 Band Structure Engineering

The basis of many quantum mechanical structures is the use of one or more quantum wells being used to confine electrons or holes. Though this at first seems like an abstract concept it is rather easily achieved in the world of semiconductors by sandwiching a material with a narrower band gap between two materials with higher band gaps. The lower band gap material allows the electrons to reside at a lower energy, making this material a preferable conduction path, with the higher band gap materials being less preferable. Thus, allowing the confinement of the electron. In fact, any system where the electrons are confined in a direction is a quantum well, and this can be created by a few methods. As a quantum well has multiple materials it is defined as a heterostructure; where two different semiconductor materials meet is defined as a heterojunction.

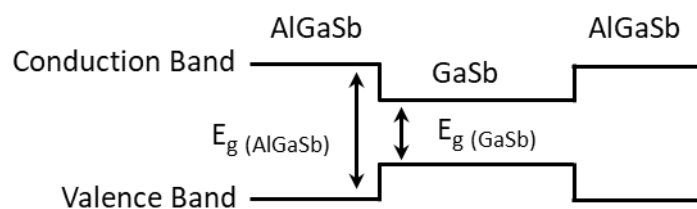


Figure 2.10: A diagram indicating how semiconducting materials with different band gaps can be used to create confinement.

First, we must find the materials with differing band gaps, in many cases alloying is used for the barriers where the binary is subtly changed by introducing small fractions of another material. Then the alignment of the material's conduction and valence bands should be considered, firstly undoped, then with doping considerations, and thirdly the effects of restricting the motion of the electrons should be explored. Finally, construction of such material systems should be addressed. Lattice materials, much like any other system, can be subject to stresses and strain.

2.3.1 Alloying

The alloying of binary heterostructures introduces a world of variety to the properties of the semiconductors. The binary semiconductor GaSb has a band gap of 0.7 eV and a lattice constant of 6.1 Å. By introducing some aluminium, to replace the group III atom gallium, the structure is subtly changed to $\text{Al}_x\text{Ga}_{1-x}\text{Sb}$ and the band gap and lattice constant are increased, where x is the fraction of Al. For example, for an Al fraction of 0.2, the bandgap would increase from 0.73 eV (GaSb) to 0.90 eV. The properties of a tertiary structure such as this are given by Vegard's law, which is essentially a linear interpolation between two binaries, in this case AlSb and GaSb. In some cases, a linear relationship is just a first approximation and is quite inaccurate and so a bowing parameter, b , must be included where

$$E_{g(\text{AlGaSb})} = xE_{g(\text{AlSb})} + (1 - x)E_{g(\text{GaSb})} - bx(1 - x). \quad 2.24$$

When $b = 0$, this equation reduces to the simple linear case. Having alloys that are lattice matched to the binary material is advantageous as it does not introduce strain into the system, which can change properties and disturb the structural integrity of the system; see section 2.3.5 Strain and Lattice Mismatch. A visual representation of III-V binary materials and the properties of the connecting alloys is given by Figure 2.11.

As the aluminium percentage is increased all of the parameters will steadily shift toward AlSb, meaning we can essentially choose the energy difference between our quantum well material and barrier material and be able to fine tune confinement for various applications.

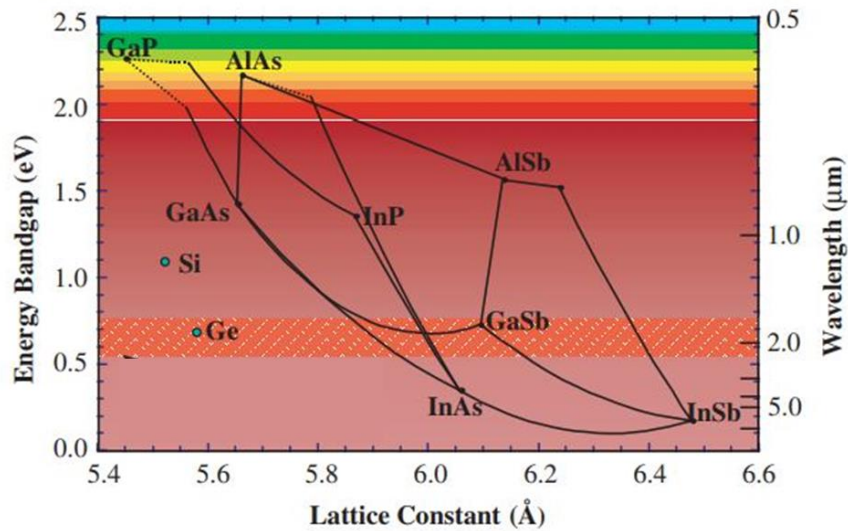


Figure 2.11: Band gap against lattice constant for all binary III-V semiconductors indicating the ternary alloy branches between the binary materials. Materials at similar lattice constants are lattice matched reducing strain [32].

Below in Figure 2.12, the bandgap difference can be seen between $\text{Al}_x\text{Ga}_{(1-x)}\text{Sb}$ and GaSb as the Al fraction increases. Interestingly there is a crossing point at 0.2 where the low lying L band in GaSb becomes the lowest conduction band minima creating an indirect band gap. Indirect band gaps are named as there is a change in momentum between the conduction band minima and the valence band. There is a further cross over with the X band at 0.56 Al fraction [33].

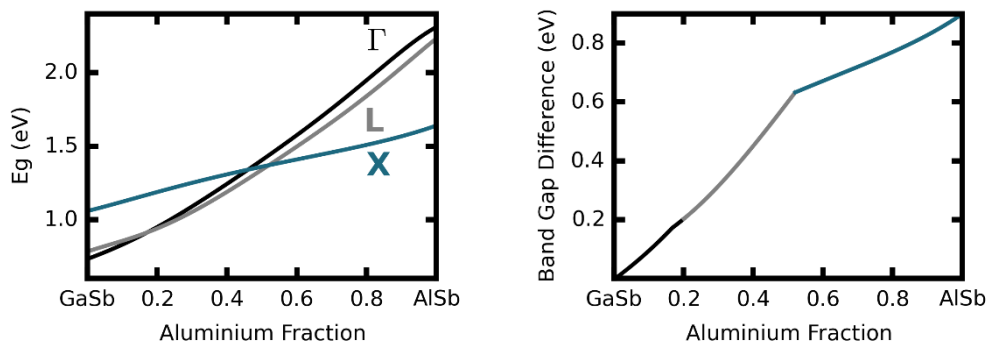


Figure 2.12: **Left:** Energy band gap between the valence band peak and the Γ , L and X points, and how this changes with aluminium fraction from GaSb to AlSb. **Right:** A graph showing how the band gap difference between GaSb and AlGaSb changes with aluminium fraction. The colours represent a change from a direct band gap at the Γ point, to indirect at L or X .

2.3.2 Heterostructure Band Alignment

When creating heterostructures the alignment of conduction bands should be well understood as different materials align in various ways and therefore there may be

different confinement for electrons and holes in an individual structure. There are three classifications of semiconductor alignments, type I (straddling), where one band gap is completely enclosed within another, type II (staggered), where the conduction band of one material lies within the band gap of the other and type III (broken gap), where there is no overlap of band gaps between the materials, see Figure 2.13.

One method of finding the alignment of two materials is by assuming the vacuum level is uniform across the structure and using the electron affinity, χ , to align the materials. This is Anderson's rule, where for materials A and B

$$\Delta E_c = \chi_A - \chi_B$$

and

$$\Delta E_v = (\chi_A + E_{g,A}) - (\chi_B + E_{g,B}),$$

2.25

where ΔE_c is the offset in the conduction band and ΔE_v is the offset in the valence band, see 2.17. Therefore, as semiconductors are not centrally aligned, the band offsets between the materials for both the conduction and valence band are required to appropriately predict the confinement for the structure. Using the above equations, in the case of this work AlSb/GaSb is considered to be a straddled gap with a conduction band offset of 0.46 eV and valence band offset of 0.44 eV at 300 K [13].

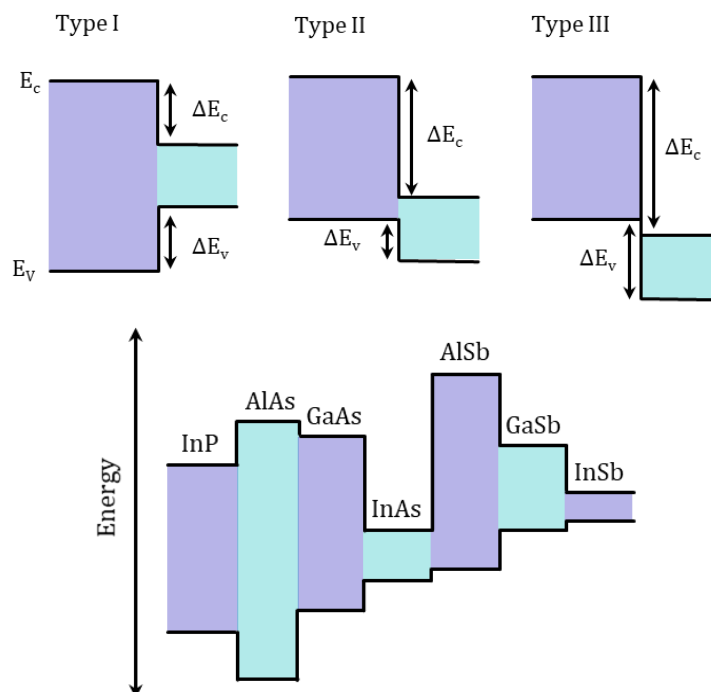


Figure 2.13: Top: A schematic diagram that illustrates the three types of heterojunction alignment, straddling, staggered and broken gap. **Bottom:** A scaled diagram indicating the types of alignments for a selection of III-V semiconductor materials when aligned using Anderson's rule.

2.3.3 Confined Band Structures

Though a potential well can be formed when any lower band gap material is placed between two materials of a higher band gap, quantum effects only occur when the well width is of the order of the de Broglie wavelength, creating a quantum well. The de Broglie wavelength is given by

$$\lambda = \frac{h}{\sqrt{(2m^*k_B T)}}, \quad 2.26$$

where h is Planck's constant (6.62607×10^{-34} Js) and k_B is Boltzmann's constant (1.3806×10^{-23} m²kgs⁻²K⁻¹). When the well width is of the order of the de Broglie wavelength quantum mechanical effects of confinement become significant and thus the particle confined can no longer be treated classically. Figure 2.14, shows that for an increase in effective mass a thinner quantum well is required for quantum effects to occur.

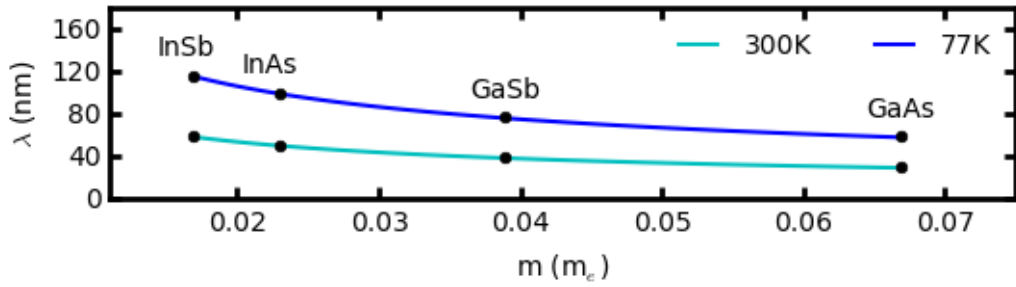


Figure 2.14: The relationship between the de Broglie wavelength and effective mass, noting common III-V semiconductor compounds.

At this length scale the particles within the well will become confined in that direction, but have free movement in the other directions, this is called two-dimensional (2D) confinement. One-dimensional (1D) and zero-dimensional (0D) confinement are also possible by further restricting the directions of travel for the particles.

The particles can be modelled by the Schrödinger equation, which describes the motion of a particle in any potential, in this case an electron in a confined conduction band. From the Schrödinger equation the energy of the electrons in the well and the wave-functions can be found. The wave function is a description of the quantum state, such that when its modulus is squared, it gives the probability density of the electron as a function of position. In one-dimension the Schrödinger equation is given by

$$-\frac{\hbar^2}{2m^*} \frac{\partial^2}{\partial z^2} \psi(z) + V(z) \psi(z) = E \psi(z), \quad 2.27$$

where ψ is the wave-function of the solution, E is the confinement energy and V is the potential. However, when there is more than one electron, as is the case with heterostructures, this probability density is used to describe a charge density. The potential profile would then be describing the conduction band (quantum well) of that structure.

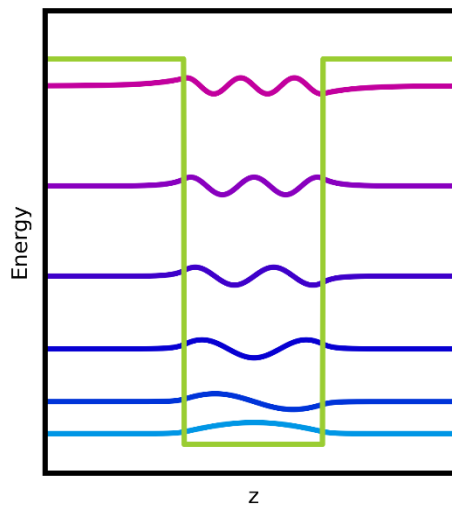


Figure 2.15: An example of the wave-functions offset by their energy in a finite quantum well.

In Figure 2.15, when considering the ground state wave function, the peak of the probability density (where most of the electrons reside) is at the centre of the symmetric well, indicating this is where the majority will be positioned.

In cases where there are free charges (e.g. where structures are doped) the Schrödinger equation individually will not accurately predict the wavefunctions or energy's of the electrons due to corresponding changes in the band structure due to the charge. The Schrödinger equation then determines the states that exist and thus the corresponding spatial density of charge. The Poisson equation is then used to evaluate the effect on the band structure of this distribution of charge. Where there is movement of charge in a structure such as in modulation doping, where the positive dopant ions are physically removed from the electrons they provide, there will be band bending. This comes from the electric field created between different areas of charge which will then have a perturbation on the potential well. This band bending can be manipulated in order to create confinement from a single heterojunction by creating a triangular well. As the doping is increased, as is the band bending, this can extend as far as to create a confinement and unwanted states within the dopant plane.

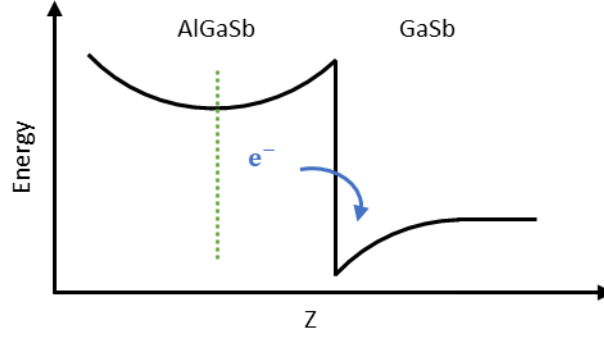


Figure 2.16: A triangular well created with the band bending from electrons being physically removed from their dopant ions (positioned at the green dashed line).

2.3.4 Carrier Density in 2D Structures

As the dimensionality of electron movement is reduced to 2D, the 3D density of states no longer applies. There is a recalculation where an area is evaluated, instead of a volume, in k -space, resulting in

$$g_{2D}(E) = \frac{m^*}{\pi\hbar^2} \Theta(E - E_i), \quad 2.28$$

which is independent of energy. As the energy levels in the quantum well are now quantised the Heaviside function, Θ , should be included, where E equals 1 when $E \geq E_i$ and 0 otherwise, where E_i represents the energy levels, creating a step-like relationship with energy. This adjustment to a two-dimensional density of states carries through to the carrier concentration, typically expressed in cm^{-2} ,

$$n_{2D}(E) = \int_{E_c}^{\infty} g_{2D}(E) f(E) dE. \quad 2.29$$

At $T=0$ K the upper bound of the integral is equal to E_f allowing the carrier density to be easily calculated, and rearranged to give an equation for the Fermi energy, E_f , as

$$E_f = \frac{\pi\hbar^2}{m^*} n_{2D}. \quad 2.30$$

When related to equation 2.1 this gives a simple relation for the Fermi wave vector k_f where $k_f = \sqrt{2\pi n_{2D}}$. It is seen that by this relation that for a 2D carrier density of $4 \times 10^{12} \text{ cm}^{-2}$, $k_f = 0.05 \ 2\pi/a_0$. When this is related to Figure 2.4, it is observed this carrier density would result in significant non-parabolic effects.

2.3.5 Strain and Lattice Mismatch

When physically creating heterostructures from growing one crystal lattice on top of another, strain from lattice constant mismatch must be considered. When two different materials are grown, the second material (epilayer) attempts to maintain the material lattice separation of the first material (substrate or lower epilayer), this produces strain in the lattice. It must be noted that the atomic volume must remain constant and so for a strained epilayer, if the lattice constant is smaller in the interface plane, it will be larger in the growth direction [34]. Once the second material reaches a particular thickness, the critical thickness, the lattice separation of the epilayer returns (relaxes) to its natural state by creating defects (misfits) as seen in Figure 2.17. This relaxation causes defects in the structure and therefore changes the conductive properties of the lattice. Thus, the critical thickness is something that is crucial to know when designing heterostructures in order to ensure the structure isn't relaxed. The strain developed from one material trying to adhere to another's lattice constant can be calculated, and will often change standard material parameters such as effective mass, and therefore mobility[35].

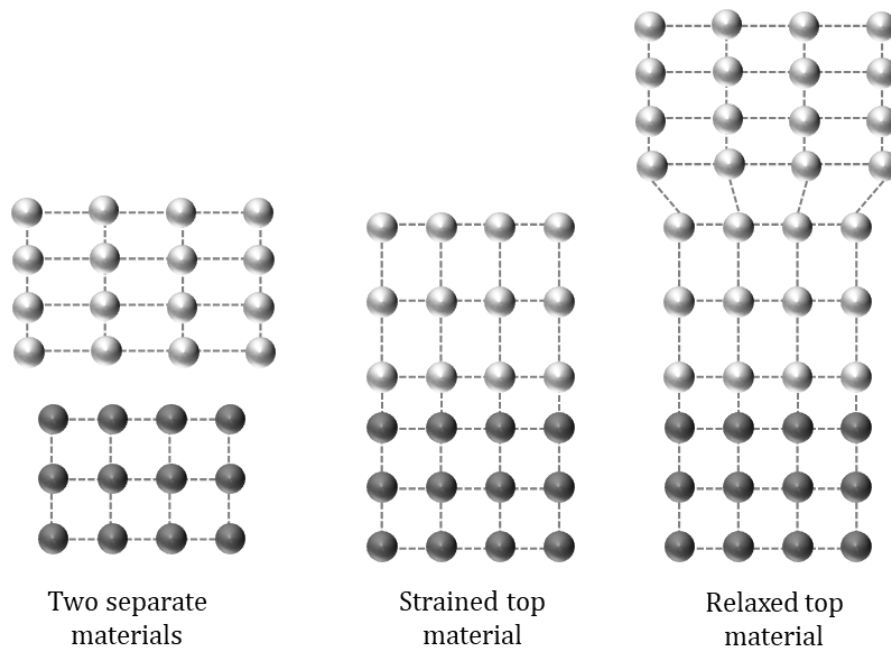


Figure 2.17: A figure showing how differing lattice constants in strained and relaxed states can form defects.

There are a number of structural defects that are created in growth, in general for this work we consider only two of them, 60° dislocations and 90° dislocations. The 90° (edge) dislocations are created through a missing bond and are parallel to the interface of the two materials. By breaking a bond, the 90° dislocation relieves strain in the system but does not affect further up in the sample, see **Figure 2.17** right, 60° dislocation not shown. This is due to it being energetically favourable to relieve strain through the breaking of a

bond rather than a consistent mismatch throughout the interface. The edge dislocation can be thought of as a series of missing bonds (90° dislocations) where the space above it creates a regular lattice and the space below it creates a different regular lattice. These dislocations can be preferable as the measured part of a given sample tends to be above these strained interfaces. Far more detrimental to the measured part of the sample is the 60° dislocation. These dislocations thread through the sample at 60° from the interface, moving upwards towards the measured layers of the sample. These dislocations can be linked where a misfit or edge dislocation doesn't go through the entire sample but instead "turn upwards" into 60° dislocations before reaching the end of the sample edge. As suggested, the dislocations along the growth direction are problematic if they are formed through the measurement space of the sample [36].

"The 60° (threading) dislocations are formed on the $(\bar{1}11)$ plane from the energy stored in strained atoms, these dislocations are more problematic as they effect the measurement space higher up the structure" [37].

The lattice mismatch, f , can be calculated by equation 2.31, where a_1 equals the lattice spacing of the substrate, or the underlying epilayer, and a_2 represents the second material [38]

$$f = \frac{1}{2} \frac{|a_1 - a_2|}{(a_1 + a_2)}. \quad \mathbf{2.31}$$

AlSb/GaSb interfaces only have a lattice mismatch of 0.7% which reduces to 0.13% for Al_{0.2}Ga_{0.8}Sb/GaSb, which is the barrier-well interface used in this work. This work uses a GaAs substrate, where the GaSb/GaAs interface has a lattice mismatch of 7.8%. This is very high and produces a large number of defects [38].

To avoid the threading dislocations being carried through the sample into the active region of the sample, interfacial misfit (IMF) array formation can be used. This is a method of reducing the defects created, by carefully controlling growth to generate a regular array of misfit dislocations in an individual layer at the interface. It has been suggested in the literature for many years that it is expected that when a threading dislocation from the substrate hits an interface, if the epilayer is strained, the threading dislocation would just continue as the structure of both the substrate and the epilayer are the same. However, if the epilayer is relaxed, it would be expected to terminate at the interface as above the interface (above the first monolayer of epilayer) the atom positions are determined purely by the epilayer atomic bonding, creating a pseudo-substrate of the epilayer. When f is high a 2D network of arrays would be expected; IMF's are the reality of this statement [34, 39].

As the atoms are tetrahedrally bonded, the surface of the crystal during growth forms one atomic species layer then another. To form an IMF, GaAs is grown and then the As is dissociated from the surface, leaving a gallium layer. The sample is then held in a Sb rich environment allowing for a single atomic layer transition from GaAs/GaSb. Within the interface there will still be periodic misfits or dangling bonds, however they are in the plane of the interface and so do not carry through the sample. There are still 60° dislocations in the sample that carry through, but these are greatly reduced in quantity [40-42]. In the GaSb/GaAs heterostructures with an IMF, the GaSb will be relaxed, meaning the lattice is not strained and has an unperturbed lattice constant, with very few vertical defects. Without an IMF the dislocation density of GaSb/GaAs structures are of the order of 10^9 cm^{-2} , while Huang *et al.* reported the same structure (with an IMF) produces a defect density of 10^5 cm^{-2} [1, 42]. With this method GaSb can be freely grown for microns on GaAs without concern of significant defect generation due to strain.

As this work studies heterostructures the mismatch and strain between the barrier (AlGaSb) and binary material (GaSb) should be considered with particular note of the critical thickness to ensure the designed structures do not go beyond this.

Models of lattice dislocations are often hinged on the use of Burgers vectors, b . These vectors represent the extent and direction of a distortion caused by a dislocation in the lattice and are found by drawing a loop around the distortion to evaluate it, the full explanation of these are outside the scope of this thesis, however a basic understanding is helpful for critical thickness models.

There are two models that can be used to calculate the critical thickness, one is the Matthews and Blakeslee model [39] and the other is the People and Bean model [43]; both were calculated for heterostructures designed in this work. The Matthews and Blakeslee model determines the critical thickness by focusing on the balance of forces between the tension in the threading dislocations with the force of the misfit strain caused from non-matching lattice constants. Eventually through continued growth, it is energetically favourable to release the strain through a production of a misfit at the interface and a propagating dislocation through the material.

The Matthews and Blakeslee model for critical thickness is given by the equation 2.32 and assumes a number of threading dislocations already exist in the grown material [8, 39].

$$h_c = \left(\frac{1}{4}\right) \left(\frac{b}{2\pi f}\right) \frac{1 - \nu \cos^2 \alpha}{(1 + \nu) \cos \lambda} \left(\ln \left(\frac{h_c}{b}\right) + 1\right), \quad 2.32$$

where h_c is the critical thickness, f is the natural misfit, b is the magnitude of the Burgers vector and ν is Poisson's ratio which is equal to the ratio of transverse to longitudinal strain in a structure. The angles α and λ (both =60° for GaSb) are defined as the angle between the dislocation line and its Burgers vector, and the angle between the slip direction and the direction in the film plane. The factor of $\frac{1}{4}$ given at the beginning of the equation is to adjust for a single heterojunction. Whereas the derivation by Matthews and Blakeslee was for a multi-layered system where the strain is shared between all layers, this factor changes to a half when a quantum well is considered [39].

People and Bean, however, do not assume a starting number of threading dislocations and calculate the critical thickness through assuming misfit dislocation creation occurs only through energy balancing of strain and defect creation [43]. They argued that the previous Matthews and Blakeslee model was not suitable for the small mismatch percentage ($\leq 0.5\%$) in $\text{Ge}_x\text{Si}_{1-x}/\text{Si}$ structures and adjusting it accordingly to better predict the critical thickness, they proposed the critical thickness is given by

$$h_c = \left(\frac{1-\nu}{1+\nu}\right) \left(\frac{1}{16\pi\sqrt{2}}\right) \left(\frac{b^2}{a(x)}\right) \left(\left(\frac{1}{f^2}\right) \ln\left(\frac{h_c}{b}\right)\right), \quad 2.33$$

where $a(x)$ is the lattice constant of the epilayer. They further compare their experimental results to both their adjusted theory and the Matthews and Blakeslee theory and conclude that Matthews and Blakeslee underestimate the critical thickness with any mismatch below 1.4 % [43]. All of the misfit percentages in this work are below 1.4 % and so should follow the People and Bean model, however, the critical thickness for GaSb/AlSb, with a mismatch of 0.65 % was calculated and compared to the range reported in Dutta *et al.* [44], this range being (10.0-17.0) nm. The Matthews and Blakeslee model resulted in 17.4 nm, a far closer estimate than People and Bean, which resulted in a critical thickness of 360 nm.

The Matthews and Blakeslee model was used as it was the closest to the experimental value, despite the misfit percentage being quite close to the applicable mismatch range quoted in People and Bean. The critical thickness calculated for a 20 % aluminium concentration was 120.4 nm and so the $\text{Al}_{0.2}\text{Ga}_{0.8}\text{Sb}$ barrier will not exceed this value as it is within the limits of both models.

These equations were solved graphically, as shown in Figure 2.18, where a $y=x$ line is plotted to extract a cross over point with the RHS of equations 2.32 or 2.33. In this case h_c

is set to x and where these lines cross is equivalent to the critical thickness given by equations 2.32 or 2.33.

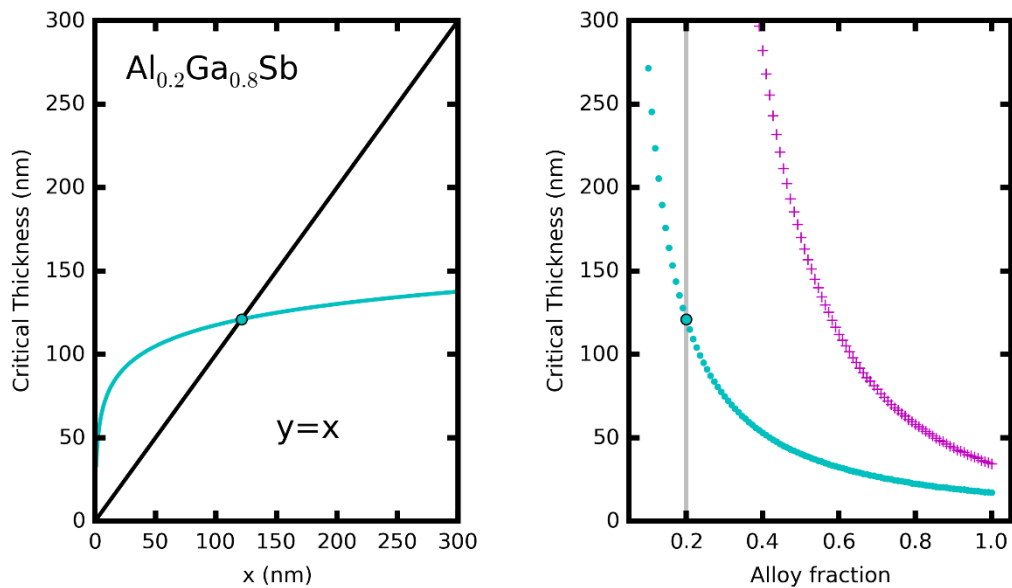


Figure 2.18: Left: A plot showing the graphical solution of the Matthews and Blakeslee model [39] for a $\text{Al}_{0.2}\text{Ga}_{0.8}\text{Sb}/\text{GaSb}$ heterojunction, the black line shows the $y=x$ line and the cyan line signifies the critical thickness calculation, where in equation 2.32 h_c on the RHS is set to equal x . **Right:** The critical thickness for $\text{Al}_x\text{Ga}_{(1-x)}\text{Sb}$ against the alloy fraction x . The cyan line represents the Matthews and Blakeslee model highlighting the value used in this work for a 0.2 aluminium alloy fraction. The People and Bean model is shown in pink [43].

The desire to grow below the critical thickness is to reduce the accumulated strain and any related defects. However, defects can form in many ways, some completely unrelated to strain and dependent purely on the growth kinetics. Such defects are prominent in GaSb and are discussed at length in the next chapter.

“Crystals are like people, it is the defects in them which tend to make them interesting!”

- Colin Humphreys

Chapter 3

Growth, Material Quality & GaSb Defects

All material in this work was grown by molecular beam epitaxy (MBE), and although MBE is a very well-established growth method, good GaSb growth for the purpose of electrical devices is still relatively unknown. Optoelectronic systems, where research based on GaSb is predominantly focused, is a well-studied area in Lancaster University Physics department. These samples however do not require exact and detailed understanding of doping compared to samples produced for electrical transport studies, and so further investigations of basic GaSb growth were necessary for this work.

In this chapter, first, the physical principles behind growth of crystals via MBE, and the complications of such will be discussed, with particular note of the native GaSb defects. A literature review of many of the various studies performed into GaSb native defects, which are the source of many complications for creating high mobility structures in GaSb, will also be discussed. Following this, the practical implementation of relating growth parameters, such as temperatures, times and valve positions, to more intuitively physical parameters, such as growth rates, layer thicknesses and V/III ratios will be illustrated. With the aid of these sections the results of growth studies into the native defect concentration as a function of these physical parameters, as well as the possible doping levels achievable, are presented.

3.1 Principles of Epitaxial Growth and Defect Formation

Epitaxial growth is the process by which many semiconductor crystals are grown. Ordered arrays of atoms are deposited on top of each other, one single atomic layer (monolayer) at a time. The atomic layers deposit such that the deposited crystal assumes

the crystal structure of the underlying material or substrate. This can be achieved through many methods such as metal organic vapor deposition (MOVPE) or liquid phase epitaxy (LPE), with each method having its own advantages. Of these, molecular beam epitaxy (MBE) is the most precise due to providing the more control of the interfaces between materials [45, 46].

3.1.1 The Basics of Growth Kinetics

Epitaxial growth such as MBE, involves many chemical and physical processes but can easily be outlined. Quite simply, a substrate is placed into a high vacuum growth chamber and heated. The desired growth materials, such as gallium and antimony, are heated in cells (Knudsen cells) to evaporation temperatures. Once suitably heated, the shutters to the cells are opened and a flux of particles is obtained on the surface of the substrate. Though growth materials such as gallium evaporate as molecules, these are in general also “cracked” to produce individual atoms or dimers (two atoms), and so when growth kinetics of the surface are discussed, atomic deposition is considered.

The atoms arrive and deposit onto the hot surface where various processes occur, including adsorption or incorporation of the beam atoms to the substrate, and migration or desorption of the adsorbed atoms. The surface itself can be described as a series of sites, which can react differently with the non-bonded atoms on the surface. These sites include layer step edges, and vacancies.

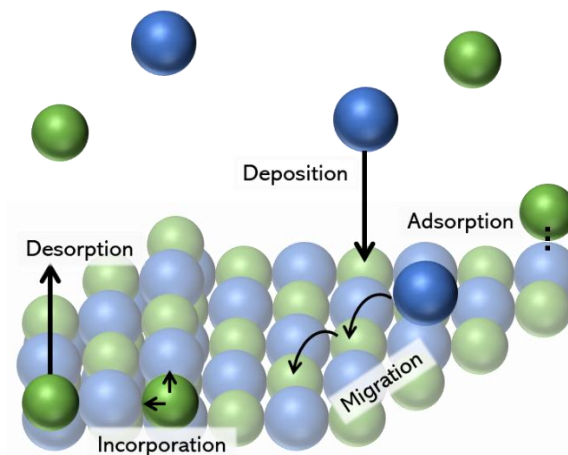


Figure 3.1: Schematic diagram of the surface processes that occur during epitaxial growth.

Several parameters such as the temperature of the substrate or flux atoms, and flux of depositing materials must be taken into consideration during growth, but here we will outline the importance of the sticking ratio (or sticking coefficient). The sticking ratio can

simply defined as the ratio of “*the number of atoms adhering to the substrate surface to the number of atoms arriving there*” [45, 47].

The atoms in the beam have an energy distribution upon arriving at the surface, which is dependent on the temperature of the Knudsen cell where the material originated. In order to fully incorporate into the crystal, an atom must first adhere (physically bond) to the surface through Van der Waals forces (physisorption), before incorporating (chemically bonding) to the surface (chemisorption). Once physically bonded, if there are no appropriate sites available, the atom will migrate across the surface until a site is found. The atoms with the highest energy will simply desorb from the surface (having overcome the Van der Waals forces), thus reducing the sticking coefficient.

The conversion of these atoms from being physisorbed to chemisorbed depends on the chemisorption sticking coefficient which is species, substrate orientation and atomic spatial distribution dependent. Mathematically, it is proportional to the probability of having vacant sites in the appropriate state, which is a function of the monolayer coverage of the surface. The physisorption however, is not dependent on the local environment, but the more global substrate temperature [45].

In general, group III atoms have a high sticking coefficient close to unity, where almost every atom arriving at the surface sticks. Group V atoms however have a lower sticking coefficient, only sticking if it is energetically favourable due to group the III elements creating appropriate sites. As such, the group III element controls how fast the lattice is grown and beam fluxes of group V elements may be much greater than group III fluxes in order to achieve an appropriate stoichiometric growth, where there is a regular array of alternating group III and V atoms [48].

There are few ways (modes) in which atomic layers can form during epitaxy, monolayer formation (Frank-van der Merwe), nucleated island formation (Volmer-Weber) and monolayer then nucleated formation (Stranski-Krastanov). In the case of the GaSb growth performed in this work, the depositing atoms are weakly bonded to each other compared to the substrate. Therefore they form monolayer islands which grow and spread to form a complete monolayer, i.e. Frank-van der Merwe growth mode [38, 45, 49].

3.1.2 Antisite and Vacancy Formation

All crystal defects can act as scattering mechanisms for any charge carrier, impairing the mobility. The rate of this scattering of the charge carrier will be greater if the defect is charged. The aim of this work, in short, is to reduce the scattering of the charge carriers

and increase the mobility, through improved material growth quality and reduction of defects. Point defects form from non-stoichiometric growth of a lattice, with native point defects named as they consist only of the atoms expected in the crystal (i.e. they do not contain any atoms of a foreign species). Antisites form where the constituent atoms are positioned in the opposing site, for example a gallium antisite (Ga_{Sb}) and an antimony antisite (Sb_{Ga}) consist of a gallium atom in an antimony site and antimony atom in a gallium site respectively. The misplaced atom is noted, with the subscript indicating the site. Similarly, an absence of an atom is a vacancy, such as V_{Ga} . There are also cases where interstitials occur (atoms between sites), but for GaSb these are not significant [11]. A schematic diagram of the formation of the native defects present in GaSb is shown in Figure 3.2, including the formation of the antisites (Ga_{Sb} , Sb_{Ga}) and the vacancies (V_{Ga} , V_{Sb}).

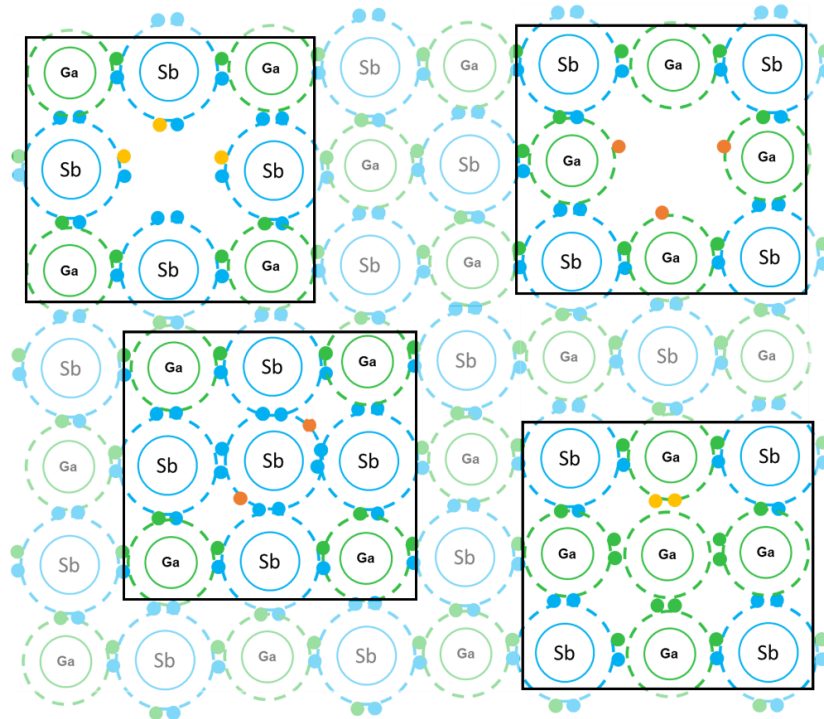


Figure 3.2: A schematic diagram of a selection of the native defects that could be created in a GaSb lattice, showing each atom (Sb in blue and Ga in green) with its associated outer electronic bonding. Donated free electrons are shown in orange with unfilled orbitals (holes) shown in yellow. Clockwise from the top left are a gallium vacancy, V_{Ga} , an antimony vacancy, V_{Sb} , a gallium antisite, Ga_{Sb} , and an antimony antisite, Sb_{Ga} .

Impurity defects occur through the addition of other elements via unwanted atoms in the MBE chamber (primarily excess carbon). This contribution is again small due to the relatively clean nature of the MBE chamber, and for GaSb, the native defects are the biggest contribution by a significant margin.

The Gibbs free energy of the system is given by the enthalpy and entropy of the system and the system as a whole works toward the Gibbs free energy being minimised (as this

is energetically favourable). The enthalpy term is dependent on both the defect type (antisite or vacancy), and the species (gallium or antimony) and is a positive factor linearly dependent on the concentration of defects, i.e. a higher enthalpy acts to increase the Gibbs free energy. The entropy of the system is a measure of the randomness created by introducing any defect into the system and is dependent on the ratio of the number of defects to the total number of atoms. The entropy term is only weakly dependent on the species and is a negative factor in the Gibbs free energy, i.e. a higher entropy minimises the Gibbs free energy. The combination of these factors ensures that there will always be defects present in any given material system, however the concentration of these can vary widely [50].

The Gibbs free energy is minimised when the concentration of the defects is large enough that the enthalpy required to create the defects is comparable to the entropy created. Above this concentration, too much energy is required to create any more defects. Due to the enthalpy term being the main species dependent factor, when investigating the primary defects of a material system, the formation enthalpy for each defect is the primary term compared[50, 51].

It should be noted that the concentration of the native defects is also dependent on the temperature and pressure of the beam flux, as well as the entropy and enthalpy (formation enthalpy). A lower formation enthalpy for a defect implies a lower level of energy required to create that defect and therefore a higher concentration of said defect. Shown below are the formation enthalpy energies for GaSb calculated by Van Vetchen *et al.* It should be noted that ΔH_{GaSb} is amongst the lowest of all formation enthalpies calculated by Van Vetchan, who investigated a host of III-V and II-VI semiconductor material systems [52],[51].

Table 3.1: The formation enthalpies of the common defects found in GaSb given in eV [52].

Material	ΔH_{GaSb}	ΔH_{SbGa}	$\Delta H_{\text{V}_{\text{Ga}}}$	$\Delta H_{\text{V}_{\text{Sb}}}$
GaSb	0.08	0.32	2.03	2.56

It is clearly shown in the above table that Ga_{Sb} defects in particular are easily formed and will therefore be found in significant concentrations. To properly understand the significance of the low values found in GaSb, it should be noted that in GaAs $\Delta H_{\text{As}_{\text{Ga}}} = \Delta H_{\text{Ga}_{\text{As}}} = 0.35$ eV and $\Delta H_{\text{V}_{\text{As}}} = \Delta H_{\text{V}_{\text{Ga}}} = 2.59$ eV, all significantly higher than the GaSb counterparts.

This large difference in formation enthalpy energies gives rise to a large difference in the number of each defect observed, where the formation of these defects can be understood by the nature of each of the constituent atoms. Sb's low sticking coefficient creates antimony vacancies which are energetically unfavourable (as seen in Table 3.1). These vacancies undergo the more energetically favourable reaction[53-55]



These defects can contribute significantly to electrical conduction and can in fact be the main electrical contribution to a semiconductor's carrier concentration. When the above reaction occurs, the donor type defect V_{Sb} converts to two accepting type defects [54]. However, once the defect is formed it must also be ionised to have an electrical effect, and therefore if the ionisation energy of the defect is large then it might not significantly contribute electrically. This is the case for both of the vacancy defects in GaSb[11].

The states of the Ga_{Sb} antisite, however, lie closer to the valence band edge. With low formation enthalpy and doubly-ionising nature, the Ga_{Sb} is the controlling electronic contribution of any grown, undoped (unintentionally doped), GaSb crystal. The resulting p -type concentrations are commonly as large as $1 \times 10^{17} \text{cm}^{-3}$ [7, 56-58].

The origin of the many defect species in GaSb have only recently become known in the semiconductor community, despite the high concentrations of defects in GaSb being common knowledge among those performing MBE growth. In 1964 Baxter *et al.* proposed that a defect of doubly accepting nature was present in GaSb, with a shallow ionisation energy of 30 meV [59]. 15 years later Allegre and Averous attributed an observed PL transition to a residual acceptor and identified this as a $\text{V}_{\text{Ga}}\text{Ga}_{\text{Sb}}$ complex [60]. In 1985 Lewandowski *et al.* investigated single crystal GaSb, determining that the defect responsible for the p -type conduction must be an antisite, but it was not clearly defined whether that antisite was part of a complex or not [58]. They suggested that the antisite was similar to that found in GaAs and originated from an antimony vacancy following the reaction stated in equation 3.1. In 1999 interest was growing to understand the origin and formation of these defects and, in particular, how to reduce them through the use of growth trials. The details of how these growth trials, and those implemented in this work, were performed will be explained in full in section 3.2.4, however at this time, the full explanation of the defects remained relatively unknown.

In 2001, Ling *et al.* used positron annihilation spectroscopy specifically to investigate the defects in GaSb [61]. This method targets vacancy defects, however, with knowledge of the defect formation, further information can be inferred from the results. At this time

there were very limited works using this method on GaSb. There was also little effort to tie in the defects observed in this work with those observed from growth results that had been stated previously. Ling *et al.* stated that the V_{Ga} defect can be removed via annealing while the hole concentration remains unchanged, attributing the unintentional hole concentration solely to the Ga_{Sb} defect. A year later, Hakala *et al.* theoretically studied all the native defects and their formation enthalpies, including complexed defects (multiple atoms forming a defect) and independent defects. They concluded the low formation energy required to create Ga_{Sb} , as well as the low ionisation energy, proves that this is the origin of residual acceptor observed[56]. Hakala *et al.* further showed that the GaSb defect concentration was orders of magnitude greater than the V_{Ga} concentration across most growth conditions. Further to these calculations, in recent years research groups have looked experimentally into the formation enthalpies and all ionisation energies of defects under varying growth conditions [6-8, 62]. However, so far there have been limited attempts to correlate experimental and theoretical results. This is mainly due to a disconnect between the conditions idealised on the surface in a theoretical simulation and the practical conditions used to create that surface. Clearly defects are inevitable, and in the case of GaSb they are also in large quantities as many research groups have demonstrated.

A further defect that needs to be considered in this work is the tellurium complex. It has been reported that small concentrations of tellurium, whilst typically a dopant, may actually increase the *p*-type background. This has been observed in GaSb grown in this work, as shown in section 3.3.6 [9]. The unusual behaviour has been reported to be due to a Te complex that forms with the Ga_{Sb} antisite, creating a triply accepting defect. When Te does not find such a site, it acts as a usual donor. Despite reports of this unusual behaviour little work has been undertaken to fully describe this defect and the behaviour seen since the original proposal of the Te complex from Dutta *et al.* [9]. This is another incentive to optimize the reduction in antisite defects as even an attempt to compensate (neutralise) out the unintentional *p*-type doping will require a significant concentration of tellurium atoms, some of which will be complexed, causing an increased acceptor concentration. This undesirably high level of dopant and defects (point charges), drastically increases the scattering of any charge carrier, leading to a reduced electrical mobility.

3.2 Parameters and Procedures of Molecular Beam Epitaxy

Growth of semiconductor materials requires good knowledge of both growth kinetics and the safe operation of the machines used for growth, such as a molecular beam epitaxy (MBE) machine. Understanding of material growth is truly the building block upon which many semiconductor devices are created, and as such it is a diverse and deep topic, much of which is outside the scope of this PhD. This section will outline the procedures necessary to undertake this work including the preparation of samples, the creation of recipes and the use of the MBE machine.

All samples in this work were grown by myself using Lancaster University's Veeco GENxplor MBE system. Training and supervision were initially performed by Dr. Andy Marshall before I undertook sole responsibility for my use of the MBE machine and the creation of recipes.

3.2.1 The MBE Machine

The relevant components for common use of the MBE machine are shown in the annotated diagram below, with special detail given to the growth chamber.

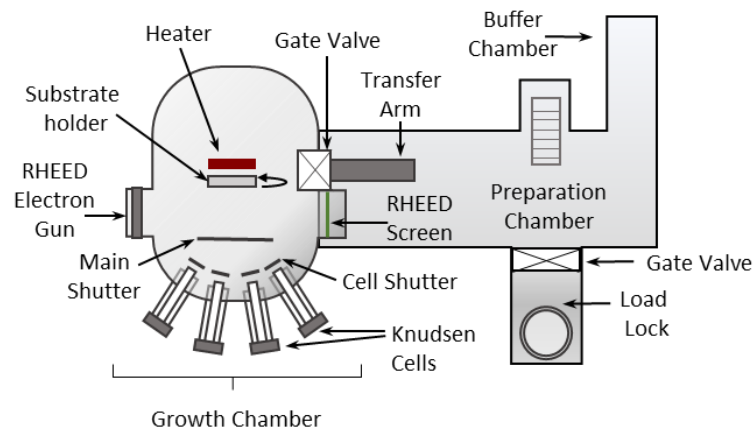


Figure 3.3: Schematic of the MBE machine, noting each chamber and with detailed annotation of the growth chamber.

In the order of loading a sample into the growth chamber: firstly, the load lock is used to move samples in and out of the MBE machine. The load lock is separated by a gate valve to protect the preparation chamber from contamination. This chamber's pressure is controlled by two pumps and a controlled flow of gaseous nitrogen. The preparation chamber stores the samples until they are ready to be moved out of the machine or are ready to be grown on. The outgas or buffer chamber allows for a thermal cycle which removes contaminants before growth, venting off the particles. A transfer arm is used to move the samples around the machine.

The growth chamber is separated from the rest of the MBE machine by a gate valve which is kept closed as much as possible to maintain an ultra-high vacuum of $\sim 10^{-9}$ Torr. The substrate holder (which rotates during growth) is placed centrally in the chamber with the substrate heater directly above the sample (the temperature is measured by a thermocouple). The Knudsen cells are positioned under the substrate and are where each element used during epitaxial growth is housed. Each Knudsen cell has a shutter and a valve for control of the flux, and the temperatures of these cells are elevated before growth, creating the gaseous form required for MBE. There is also a main shutter between the substrate and all the Knudsen cells to further protect the substrate from undesired elements contacting the surface, and to aid in the formation of sharp interfaces.

The MBE machine contains a reflection high-energy-electron diffraction (RHEED) gun and detector, used to monitor the surface during growth. This method of monitoring involves directing a beam of electrons at the surface of the sample at a shallow angle [45]. The resulting diffraction pattern is used as an estimation of the construction of the grid like surface of the lattice. If the surface is amorphous due to oxide, the RHEED pattern is diffuse which no clear features. When the oxide is being removed a spotted pattern starts to form from a rough surface, this can also be the case with Volmer-Weber growth as well as Stranski-Krastanov growth or poor-quality growth. A streaky lined pattern appears from good quality crystalline growth[38]. The intensity of the RHEED pattern away from the central line can be monitored to track the coverage of the monolayer being deposited, with each peak in intensity representing a smooth complete layer. Each material has a distinct RHEED pattern, related to the surface growth of the crystal structure from the incoming atomic species.

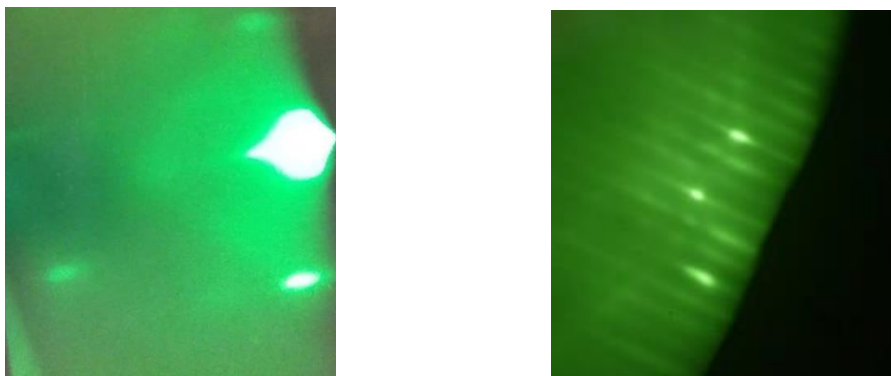


Figure 3.4: **Left:** Pictures of RHEED patterns before deoxidisation where only a few bright spots are observed. **Right:** RHEED pattern observed once growth has begun, showing the three bright primary lines and two secondary lines between each of them (a $3\times$).

There tends to be 3 primary bright lines (two equidistant from the central line) and between each of these lines are a number of fainter secondary lines. In the case where there is 1 secondary line, the pattern is called a “2×”, in the case where there are 3 it is called a “4×”. When growing GaAs alternating 2× and 4× patterns can be seen, with this called a “2×4” pattern. When growing GaSb a “1×3” pattern can be seen (i.e. no secondary lines, followed by 2 secondary lines).

3.2.2 Parameters of Molecular Beam Epitaxy Growth

There are many practical factors to obtaining good quality crystal growth, the cell temperature, the substrate temperature, the valve position and the time each layer is growing, are the fundamental parameters required for any growth. From these, more intuitive “*kinetic*” growth parameters can be found, such as the growth rate, V/III ratio, thickness and doping concentration (where appropriate)². A good understanding of both are required as the latter set of parameters are independent of the specific MBE machine, but the practical parameters are subject to differences such as the remaining volume of a material in a cell etc.

The rate of the growth of any III-V material is controlled by the temperature of the group III element and therefore the flux of that element, where this is due to the group III having a consistently higher sticking coefficient than the group V element. The group III flux is controlled by setting the temperature, whereas the group V element is heated to a specific growth temperature and the flux is controlled by the valve position³. The growth rate used as a standard throughout this work is 1 monolayer per second (ML/s), as is common in MBE grown III-V material, where this is often also used as a maximum growth rate. From the growth rate and the length of time that the shutter is open, a thickness in monolayers can be obtained, which is converted to μm by simple multiplication of the monolayer thickness (half the lattice constant a_0). The correlation between temperature and growth rate is obtained through empirical measurement. It should be noted here that there are many calibrations carried out for growth rate, however, to calibrate for all possible materials to grow would be very time consuming. Therefore equation 3.2 is used as a conversion from the actual growth rate as calibrated for gallium on GaAs to the gallium growth rate for GaSb, such that

² Each parameter is compared with calibrations that are routinely carried out at Lancaster University.

³ Group III elements are only not controlled in this fashion as there would be significant accumulation on the valves.

$$R_{\text{GaSb}} = R_{\text{GaAs}} \times \frac{a_{\text{GaSb}}^2}{a_{\text{GaAs}}^2}, \quad 3.2$$

where R_{GaSb} is the growth rate for gallium on GaSb, where a full explanation of this formula is given in appendix A. Similarly, R_{GaAs} is the growth rate for gallium on GaAs and the lattice constants are given by a_{GaSb} and a_{GaAs} . This equation can also be easily modified to convert the growth rates between any two binary crystals that share an element.

It would be intuitive to think that the V/III ratio (the ratio of the number of group V atoms arriving at the surface compared to the group III atoms) should equal one, given that there is ideally an equal distribution incorporated into the crystal at the surface. However, as mentioned previously, each element has a distinct sticking coefficient which governs the number of incoming atoms that stay adhered to the surface, with this value very dependent on the temperature of the substrate. It is therefore not simply a case of finding the right V/III ratio for the specific material being grown, but this must also be determined at each given substrate temperature. This also raises the possibility that there may be defects that only form under certain conditions, or defects that increase in concentration under certain conditions. It is for this reason that a range of growth parameters require investigation to be certain of finding the optimal conditions (a growth trial). When growing III-V materials, group V atoms tend to have lower sticking coefficients, and so the standard V/III ratio used in growth is more often between 1 and 5 for substances such as GaAs and GaSb [34, 63-65]. It is also standard practice to maintain a flux of group V on the surface even when not actively growing. If the substrate is heated above a material dependent growth temperature⁴ the flux prevents desorption from the surface and hence a Ga rich top layer.

In the case of alloys, such as AlGaSb the calculation of the growth rate should be split proportionally with the alloy fraction of the elements. For example, if a growth rate of 1 ML/s is desired for a sample with an aluminium percentage of 20 % (i.e. $\text{Al}_{0.2}\text{Ga}_{0.8}\text{Sb}$), to achieve this would require setting the temperature to achieve a rate of 0.2 ML/s for aluminium and 0.8 ML/s for gallium.

Doping flux is purely dependent on the rate of deposition and not the crystal material. However, factors such as the incorporation of the dopant, and the activation of that dopant in the crystal, must also be considered. Both of these values vary between dopant and crystal materials, creating a large discrepancy between the concentration measured at the

⁴ For GaSb an Sb flux is maintained above a substrate temperature of 424 °C.

same dopant temperature and the same rate for different material systems. Due to a low ionisation level, tellurium doping levels, the n-type dopant for the MBE machine used, are calibrated on InSb.

Once each of the kinetic parameters have been converted to practical parameters, they are input into the MBE machine recipe program (Molly 2000) which performs the recipe automatically. Though the crux of growth is described above, there are also many niche details required, including ensuring the cells have sufficient time to reach their set temperature, and knowing which materials have a hotter cell base or cell tip (both temperatures have to be set during growth). Although switching between actual and set temperatures rarely happens, the actual temperature is required for comparing work or for switching size and material of substrate. This is calculated by the transition temperatures and deoxidisation temperature. These details are not difficult to account for, but they are numerous. As part of this work, to assist in accurate completion of growth recipes a piece of software was created using python to produce recipes.

3.2.3 Growth and Preparation Procedures

A semi-insulating GaAs substrate wafer is taken out of the package and cleaved to the appropriate size (often a quarter of the wafer)⁵. It is then placed between two metal plates in a wafer holder, and to secure it in place, a ring the size of the inset of the holder is squeezed into position and pushed down. The ring applies force on the perimeter keeping the plates from shifting ensuring the wafer is held in place. The wafer holder is then tilted to ensure that the wafer does not move. During growth the wafer is spun, and if it is not secure in the wafer holder, it can shift in the holder resulting in non-uniform growth. On occasion the plates can bow from frequent use and thermal distortion which will increase the likelihood of the wafer moving during growth.

Once secured, the wafer holder is put into the wafer stack (which holds up to 3 wafer holders) with this placed into the load lock of the MBE machine. The load lock is then evacuated using a backing pump and a vacuum pump to lower the pressure, and the wafers outgassed, which further reduces the pressure in the load lock. The outgassing process bakes and cools the whole stack for approximately 20 mins to remove any contaminants from the surface. Once the wafers are sufficiently clean and the load lock

⁵ At each step in the procedures the wafer and wafer carriers are handled with tweezers and with minimal contact time to ensure minimal contaminants on the surface of the wafer.

pressure is reduced to that of the prep chamber, the wafer stack is moved into the prep chamber and then the load lock is once again sealed off.

The wafer holder is then placed into the internal outgas which subjects the sample to another thermal cycle and the particles that desorb from the surface are vented off. Once the pressure is low enough, the wafer holder is moved through the prep chamber into the growth chamber ready for growth⁶. The wafer stand position should be set to 0° before putting the wafer in for the wafer to be held correctly in place. The growth chamber is then shut and the wafer set to turn, usually at a speed of 10 rpm. All windows to the growth chamber should also be shut and the substrate heater that controls the substrate temperature, lowered.

It is important during preparation to ensure all the cells that are being used in the growth are sufficiently heated by the time they are used in the recipe to ensure the correct flux is being obtained.

The initial step of any growth is to deoxidise the surface, on a GaAs substrate this happens at 580 °C and can be observed using RHEED. Once the oxide has been removed a thin layer of the substrate material is grown, where in the case of GaAs, when this begins to grow the pattern switches to an alternating pattern of 2×4. If the pattern is diffuse at all or is not easily distinguishable, this indicates an uneven surface and therefore not a good starting point for growth. The deoxidisation procedure is well known for GaAs, and as such is the start of the recipe. However, when using another substrate material, it is important to follow this procedure manually. This is achieved by increasing temperature in steps until a clear RHEED pattern is observed.

Once the substrate is prepared, the structures are grown using a recipe which automatically changes the cell temperatures and valve positions. Once the structure is grown the sample is removed through the load lock, then the sample is generally cleaved and measured. In the case of transport measurement, this is achieved using the van der Pauw method and the Hall effect to determine the carrier density and mobility.

3.2.4 Van der Pauw Method

When calibrating the dopant concentration achieved for a given Knudsen Te cell temperature, it is standard procedure to use the van der Pauw method to check the carrier

⁶ The valve between the prep chamber and the growth chamber is kept closed at all times except when moving a sample in or out, this is to maintain vacuum quality and cleanliness in the growth chamber.

density and thus the doping concentration. This method can also be used to extract the mobility. Utilising the Hall effect described in chapter 2, the samples can be measured using a van der Pauw geometry to determine the resistivity. This method allows for a quick determination of the transport properties as only simple procedures are necessary. Indium solder is dotted on each corner of samples of 1 cm², where two of these contacts pass current and the other two measure voltage. The biggest advantage of the van der Pauw measurement method is that it can be implemented on almost any size of sample (for an arbitrary shape). However, for the van der Pauw method to be accurate, a set of rules must be followed. The contacts must be on the edges of the sample and sufficiently small [23, 66]. The sample must also be continuous between contacts (no holes in the samples) and of uniform thickness.

The van der Pauw method of determining the sample properties involves electrically measuring the resistance of the sample in multiple configurations and is based on the ratio of change in resistance between them.

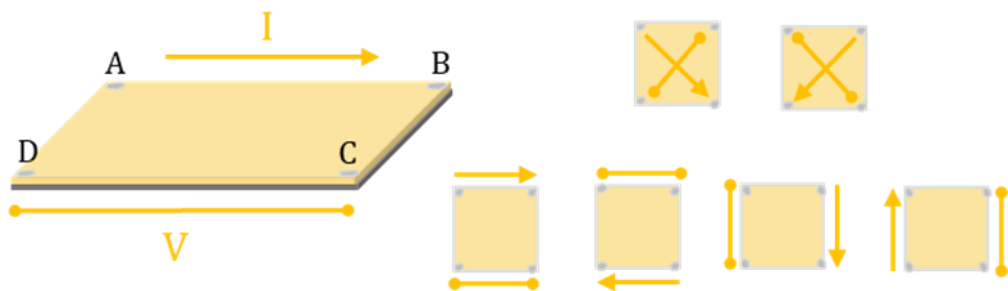


Figure 3.5: A schematic diagram showing different configurations used when measuring electrical resistance in a van der Pauw geometry, where arrows indicate the current being set and voltage measured is shown by double ended lines.

For example, in Figure 3.5, there are 4 longitudinal resistances (i.e. $R_{AB,CD}$ or $R_{BC,AD}$ and their reverse current counterparts) that can be measured, where using this notation the first two subscript letters indicate the direction of current flow, and the second two indicate the voltage difference being measured.

Using the van der Pauw equation (equation 3.3), the longitudinal resistivity of the sample can be calculated by averaging the resistance along two orthogonal sides (i.e. the side and top edge). Generally, each orientation is repeatedly measured and averaged before the combinations of orientations are averaged. The resistivity is then given by

$$\rho = \frac{\pi t}{\ln(2)} \frac{R_{AB,CD} + R_{BC,DA}}{2} f, \quad 3.3$$

where t represents the thickness of the sample and f is a function of the ratio of $R_{AB,CD}/R_{BC,DA}$ or the inverse (whichever is greater). This f function gives a percentage correction factor to account for geometry of the sample, which could be due to the sample not being perfectly square [66]. When extracting transport properties such as the mobility ($\mu \propto \rho$), it is important to include the correction factor so as to not overestimate the mobility. A plot of how this f -factor varies as a function of the resistance ratio is shown in Figure 3.6.

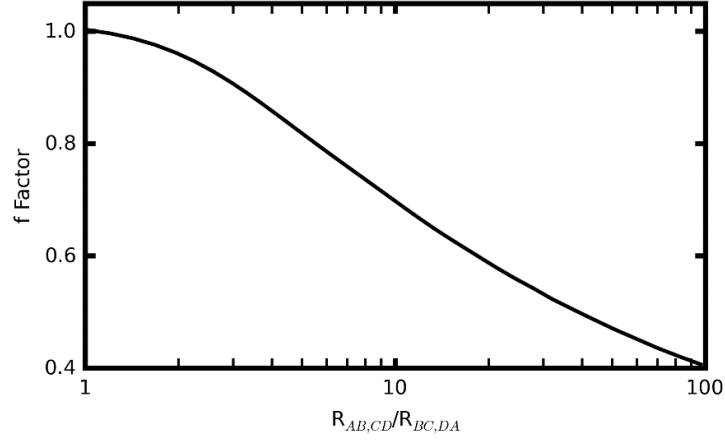


Figure 3.6: How the correction factor f varies with the ratio of the two longitudinal resistances $R_{AB,CD}/R_{BC,DA}$.

The f -factor must satisfy the following equation

$$\cosh\left(\frac{\left(\frac{R_{AB,CD}}{R_{BC,DA}}\right) - 1}{\left(\frac{R_{AB,CD}}{R_{BC,DA}}\right) + 1} \frac{\ln(2)}{f}\right) = \frac{1}{2} \exp\left(\frac{\ln(2)}{f}\right), \quad 3.4$$

where more details are given in ref [66]. It is generally accepted that even though the f -factor can be used for all ratios, that once a ratio is above 3, the sample has too distorted a geometry. There may also be an issue with the bonding and the sample should be re-bonded and re-measured [23].

The resistance associated with the Hall voltage is then measured, where each configuration is measured with no magnetic field, and then with a set magnetic field, in this case (0.25 ± 0.01) T. To find the carrier density, equation 3.5 is used, where the necessary transverse resistance (the average of $R_{AC,BD}$ and $R_{BD,AC}$) is measured such that

$$R_{AC,BD} = \frac{V_{AC,BD}(B) - V_{AC,BD}(B = 0)}{I_{AC,BD}}. \quad 3.5$$

Using the transport equations for bulk materials given in chapter 2, these electrical measurements can be used to determine the carrier density and mobility. Though the van

der Pauw method is an easy to use method, it is not without fault. The disadvantages of the method include the fact that there is no redundancy amongst contacts, with all 4 contacts required to achieve the measurement. If a single contact fails or is unreliable, this method will fail. Similarly, this method is sensitive to the size and position of the contacts, errors for such problems are outlined in ref [66]. The measurements of all orientations can also be time consuming [23].

The room temperature set up for this measurement included a Keithley 2400 sourcemeter, a Keithley 2700 multimeter and an electromagnet. The samples were bonded to a chip board created for this set up, and the field was routinely checked using a gaussmeter.

3.3 Measurement of Defects and Doping in Bulk GaSb

The work of this thesis ultimately aims to measure the transport properties of $n\text{-Al}_{0.2}\text{Ga}_{0.8}\text{Sb}/\text{GaSb}$ structures. In terms of growth, this is a seemingly simple structure, particularly in the case of a heterojunction. Complications become apparent though due to the high concentration of native defects created during growth of GaSb. These defects are present irrespective of growth method, or the substrate (i.e. they are not the result of strain). However, as has been evidenced in the literature as described previously, the concentration of the defects can be changed (though not eliminated) through varying the specific growth conditions.

A heavily defected material would of course have a large amount of scattering which would result in undesirably low mobility devices. However, these defects are also p -type which causes further complications. This is often referred to as “unintentionally doped” as although no external doping has been included, the carrier concentrations achieved are comparable to those of typically doped samples. This unintentional doping complicates the confinement in a single heterojunction as this confinement is solely reliant on the doping in the top cap (see section 2.3.3). The intended n -type doping originating from the Te atoms must now overcome a high p -type background to ensure an n -type device. Doping of the confined region should ensure n -type conduction is achieved, however this is not desirable as the dopant atoms in close proximity to the charge carriers would increase scattering and lower the mobility further. This concept is explored more fully in chapter 6, however for now it is clear that the reduction of defects would make confinement simpler, and would reduce the scattering. The reduction in scattering would therefore increase the mobility in the final devices.

3.3.1 Aims

There have been many studies into the effects on carrier density of the native defects in undoped GaSb and how to reduce their density through improved growth. However, a commonly accepted standard growth condition is not yet widely accepted, with wide variations used in the literature. It is clear from the theory given in section 3.1 that complete removal of defects, particularly the gallium antisite defect (Ga_{Sb}) is highly unlikely due to the small energy required for creation. However, some adjustable growth conditions may kinetically promote this reaction, detrimentally increasing the defect concentration.

This growth study aims to reduce the unintentional p -type carrier concentration in GaSb and as a result, obtain higher mobility (better quality) samples through variation of growth conditions. The carrier concentration of the undoped GaSb will be used as a measure of the concentration of defects. Prior to this study, the standard growth conditions used in Lancaster Physics Department were a V/III ratio of 2.2 and a growth temperature (T_g) of 505 °C, resulting in a high unintentional p -type carrier concentration of $9 \times 10^{16} \text{ cm}^{-3}$ and corresponding mobility of $350 \text{ cm}^2/\text{Vs}$ at 300 K. These conditions stem from growth trials from the works of Huang *et al.* [42] to produce high quality interfacial misfit arrays (IMFs) between GaAs and GaSb. The aim of the growth study performed in this work was to find the best growth condition of bulk GaSb to minimise the p -type defects, allowing the production of high quality $\text{Al}_{0.2}\text{Ga}_{0.8}\text{Sb}/\text{GaSb}$ 2DEG structures. Simultaneously it is desired to achieve an increase in mobility, with this used to quantify material quality. Whilst an improved growth condition minimising the number of defects should correspondingly increase the mobility, this will be examined through this study.

3.3.2 Reducing Defects Through Growth: A literature review

There have been frequent reports of differing GaSb growth studies, however, a quantitative review of growth conditions is difficult due to the inherent nature of growth. Parameters such as beam equivalent pressure ratio⁷ which are often reported, are not transferable to different MBE machines due to their dependence on the geometry of the Knudsen cells with respect to the substrate. The growth temperature is more transferable, provided sufficient information is given to deduce the actual temperature from the set temperature reported (e.g. transition temperatures and deoxidisation temperatures). Even given similar growth systems, different research groups often compensate for the

⁷ A ratio of the flux pressure for each beam rather than the growth rate ratio stated in this work.

large lattice mismatch between GaAs and GaSb (7.8 %) in different ways. This ultimately leads to measurements of slightly varied structures and as such, the conditions in each study aren't always directly comparable given the large number of uncontrolled variables. Nevertheless, a qualitative review of the many seemingly conflicting growth methods used to reduce defects is given below.

In 1986 Lee *et al.* [8] produced several undoped GaSb samples by MBE, varying both V/III ratio and temperature. They initially stated there was no simple correlation between the growth conditions and the electrical results (carrier density and mobility). However, the minimum V/III ratio required at each growth temperature to obtain a shiny reflective surface (i.e. reasonable quality growth) was deduced. From this it was suggested that a minimum Sb flux is required for improved transport properties, but there was no preferable growth temperature. Though the 77 K results were shown, only 300 K results were compared numerically, and this was stated to be due to significant carrier freeze out. It has since been suggested that at increased V/III ratios, Sb₄ aggregates causing vacant Sb sites and thus Ga_{Sb} accepting defects, confirming Lee's deduction [6, 8]. It should be noted here that, from converting the set temperature to actual temperature, Lee *et al.* investigated the higher temperature, high V/III ratio, range of parameters.

A decade later, Bosacchi *et al.* [7] studied a range of growth parameters, presenting the hole concentration as a function of growth temperature (T_g) and Sb₄/Ga beam equivalent pressure ratio (BEPR). For each BEPR, there was a dip in carrier concentration at a growth temperature of 450 °C whilst a BEPR of 8 (the highest that they reported) consistently gave lower a carrier concentration (defect density) as compared to reduced BEPR ratios. This particularly low defect concentration was at a level of $6 \times 10^{14} \text{ cm}^{-3}$ at 77 K. However, Bosacchi *et al.* also stated that the mobility at 77 K bared little correlation to carrier concentration or growth conditions. The explanation given that the samples were very clean and of high quality, with phonons therefore still dominating at this temperature.

They explained their low defect "sweet spot" of $T_g = 450 \text{ °C}$ with the dissociation properties of Sb. As temperature increases, Sb₄ is more easily dissociated in order to be incorporated into the lattice. The production of a Sb rich environment (higher V/III) would result in a lower concentration of Ga_{Sb} defects. However, as temperature increases the re-evaporation of Sb from the surface of the sample also increases, creating an antimony vacancy, V_{Sb}, which would result in a higher concentration of Ga_{Sb} defects.

At this point there are conflicting results stating that both a higher (Bosacchi *et al.*) and a lower V/III ratio (Lee *et al.*) are required for improved transport properties in GaSb. Though Bosacchi's insight into the multiple processes involved during growth of GaSb begins to unravel the complexities of defect creation.

Four years later Xie *et al.*[6] conducted a similar study with the use of Sb₁ and Sb₂. A mixture of the individual atom and diatomic molecule of Sb can be created from a Sb₄ source, where a cracker is used to heat the molecules to a high enough temperature that Sb₄ breaks down to smaller molecules. The higher the temperature the more the molecule is broken down (ie the higher the sb 1 ratio), Xie *et al.* reported that a cracker temperature above 950°C allows for a mole fraction of Sb₁ of greater than 90%. The motive behind the use of a different species of Sb was that Sb₄ has low surface mobility and the molecules cluster together creating Sb vacancy defects, and in turn, antisite defects. With the improved surface mobility of Sb₂, they hoped to reduce these defects. Though the results were comparable to that of Sb₄, they also point out that to minimise the defects there is a balance of requiring sufficient antimony on the surface to fill sites, whilst not having an excess such that the Sb agglomerates. This growth window was improved when using Sb₂ but not significantly. However, they do not tie this trend to any particular growth conditions or parameters. They found a decreasing mobility with growth temperature, with a minimum carrier concentration at a growth temperature of 440 °C. They also stated that they did not see agglomerations with increases in V/III ratio (at 550 °C), nor did they observe any change in transport properties when varying the V/III ratio. This was attributed to the increased surface mobility of Sb₂, and provided that the antimony flux was high enough, the vacant sites would be filled and the transport properties would be unaffected.

Xie *et al.* discussed Sb₄ flux whilst also discussing Bosacchi *et al.* and Lee *et al.* and the contradicting results they provide. This disagreement of a higher (Bosacchi *et al.*) and a lower V/III ratio (Lee *et al.*) is again explained with a balance of the Sb flux. As the Sb₄ flux increases, this promotes the clumping of Sb, leading to V_{sb}, whilst a lower flux may not produce enough Sb to create an ideal lattice, however through the use of Sb₂, the aggregation is not as likely, opening up the growth window.

The inherent issues for growth are that the method of creating an Sb rich environment in the growth chamber does not necessarily result in an Sb rich environment in the growth kinetics when incorporating into the lattice. This confusion can lead to seemingly contradictory results. Thus, an effort to bring together knowledge of growth kinetics,

defect formation and MBE methodology is required to paint a full picture of the relation between growth conditions and transport properties.

3.3.3 Experimental Procedure

All structures were grown using molecular beam epitaxy (MBE) on semi-insulating GaAs substrates with an IMF layer between the GaSb/GaAs junction to minimise threading dislocations. This is achieved by first growing a thin GaAs layer and then desorbing the As. Following this, an Sb rich environment is created and GaSb grown, creating a distinct interface between the two materials. In the samples studied here, GaSb was grown to a thickness of 2.2 μm at a rate of 1 ML/s, with the growth temperature ranging from 415 $^{\circ}\text{C}$ to 505 $^{\circ}\text{C}$ (above and below this temperature range samples were found to be milky) and V/III flux ratios of 1.3, 1.6 and 2.2 All samples were grown in the same growth run to ensure consistency between samples of the non-varied parameters. A thickness of 2.2 μm was chosen as this is representative of the future heterostructures. Whilst using thicker buffers can reduce threading dislocations in the measurement space, this is of diminishing returns. The growth temperatures given in this work are the actual temperature, rather than the set temperature. Each sample was checked by RHEED during growth to ensure a good surface morphology after the IMF layer, where a 3×1 pattern can be clearly seen from uniform growth of GaSb. The samples were also investigated in an optical microscope upon completion of growth to inspect for any snake like defects from uneven IMF, which can be seen in Figure 3.7 below.

After growth, the samples were cleaned, cleaved and measured using the van der Pauw method (3.2.4) to extract a carrier density and mobility, with each resistance measurement repeated 4 times and averaged.

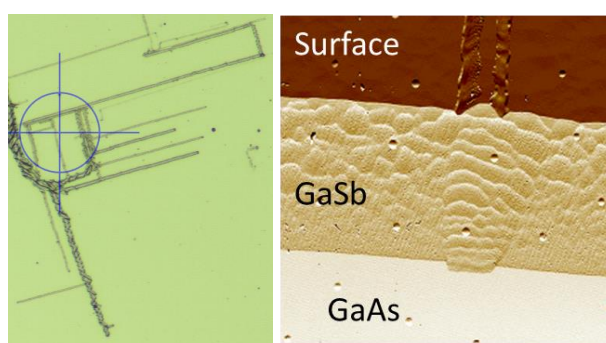


Figure 3.7: Snake like defects that can occur from an uneven IMF. The defects are dislocations visible on the surface that originate at the junction between the GaAs and GaSb layers. **Left:** Optical microscopy image of the surface of the sample. **Right:** Beam exit x-section AFM showing the distinct layers of GaAs and GaSb where it is clearly seen that the dislocation starts at the junction (measured by Dr Alex Robson).

3.3.4 Measured Defect Reduction Through Improved Growth

The growth study mainly focused on the growth temperature however there was also a brief investigation into V/III ratio. There was some attempt to work within the ranges of the above literature in order to resolve the lack of agreement between them. A table of the full range of growth conditions used in this study is given in Table 3.2.

Table 3.2: A table showing the growth condition variations used in the growth study. Where multiple V/III ratios are given, these correspond to multiple growths. The highest and lowest temperature in the table resulted in milky growths and thus won't be shown further.

T_g (° C)	V/III Ratio
380	1.3
410	1.3
450	1.3
475	1.3, 1.6, 2.2
505	1.3, 1.6, 2.2
520	1.3

The electrical properties such as the carrier density and the mobility of each sample were then determined. The mobility was taken as a material quality factor as the mobility is directly correlated with the defect concentration.

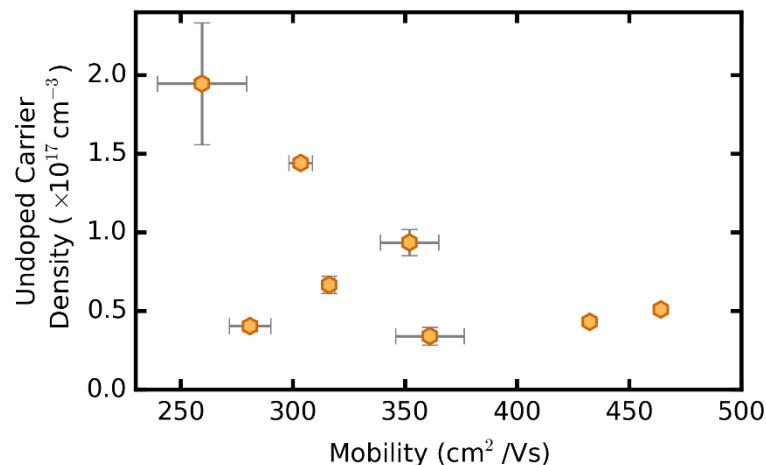


Figure 3.8: A graph of measured transport properties for carrier density and hole mobility for undoped GaSb grown under varying growth conditions, indicating the improvement of mobility with a decrease of carrier density. The error bars on this graph are from the spread of the repeated measurements.

As these samples are undoped, the p -type carrier density primarily originates from the native defects in the GaSb, and as such is taken as a measure of defect concentration. It should be made clear, however, that the carrier concentration is a measure of the net resulting charge carriers and as such can be a function of both accepting and donor defects in varying quantities.

As Figure 3.8 shows, there are a wide range of carrier densities and corresponding mobilities possible, with a number of samples showing a low carrier density and high mobility. Specifically, the sample to the far right of this graph has the highest mobility measured (high crystal quality) whilst also having a significantly reduced carrier density, with values of $p = 5 \times 10^{16} \text{ cm}^{-3}$ and $\mu = 465 \text{ cm}^2/\text{Vs}$.

Analysing these results further to examine trends with specific growth conditions (i.e. with temperature and with V/III ratio), the carrier density and mobility are shown again in Figure 3.9 as a function of these variables.

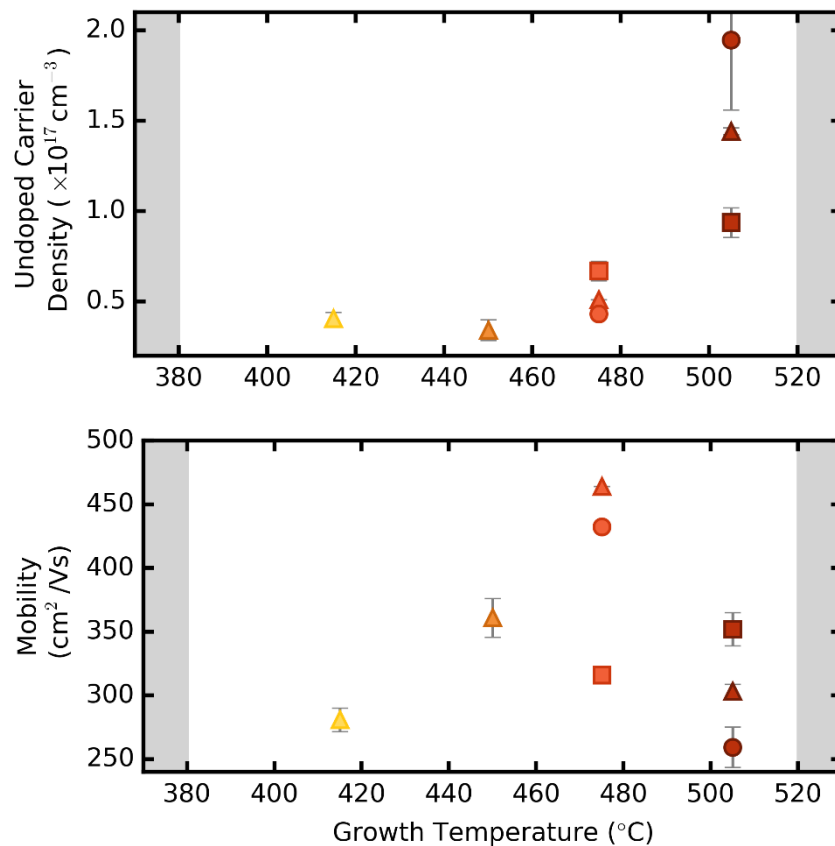


Figure 3.9: Graphs showing the measured carried density and mobility at 300 K of undoped GaSb against growth temperatures with different symbols indicating different V/III ratios, V/III=1.3 (\blacktriangle), 1.6 (\bullet) and 2.2 (\blacksquare). The light grey shaded regions indicate the limit of growth temperatures observed in this study to give milky vs shiny growth at a V/III ratio of 1.3.

It is clearly seen that a reduction in growth temperature yields a reduction in carrier density, whilst at the highest temperature, there is significant difference in the carrier density achieved with the various V/III ratios. The mobility however seems to peak at a particular (lower) growth temperature (475 °C). Therefore, there is not one continuous discernible trend as reported in the literature [6, 7], but there appears to be instead an optimal growth condition with no significant dip in carrier concentration at a particular temperature, as observed by Xie *et al.* and Bosachi *et al.*

From this growth study, the optimal growth condition is to grow at 475 °C substrate temperature at a V/III ratio of 1.3, which obtains a low carrier density of $5 \times 10^{16} \text{ cm}^{-3}$ and the highest mobility of $465 \text{ cm}^2/\text{Vs}$.

It can also be seen in Figure 3.9 that at the highest growth temperature (505 °C) a higher V/III ratio is preferable with a lower carrier density from defects and higher mobility. At 475°C however, the lowest V/III ratio is preferable. Again, these seem like contradictory statements, much like the contradiction of Bossachi *et al.* and Lee *et al.* At decreasing temperatures, the lowest V/III ratio results in a smaller carrier density but also a lower mobility. These seemingly different situations can be understood when considering the growth kinetics and the defects that form.

When considering the creation of defects, the growth kinetics and associated properties should be considered with respect to the atoms, as well as the environment created in the growth chamber.

The temperature of the Sb Knudsen cell flux is kept constant (530°C) as the flux rate, and correspondingly the V/III ratio, are calibrated at this temperature. However it is the difference in the temperatures of the substrate and the Sb atoms arriving at the surface that determines the physisorption sticking coefficient which leads to antisite defects (see section 3.1.2). It is known that sticking coefficients change with growth temperature, but the full nature of this relationship for Sb in GaSb is not well reported in the literature. However, for tertiary materials such as GaAsSb, it has been shown that the sticking coefficient decreases linearly with an increase in growth temperature [67]. Kinetically, this can be explained by considering that at high temperature, Sb is more likely to re-evaporate from the surface [6], creating a lower sticking coefficient.

Similarly, for any given temperature, the sticking coefficient may also vary with the V/III ratio. As such, a low V/III ratio could produce an insufficient Sb flux, causing defects, whilst a high V/III ratio may also result in agglomerations, producing defects. In this way, a

middle V/III ratio is optimal [6] [7, 8]. Further, it could then be suggested from the results presented in Figure 3.9 that this optimal V/III ratio changes with temperature due to the varying sticking coefficient.

Figure 3.10 aids in the understanding of the description given above of how the growth of GaSb varies with temperature, where this figure schematically illustrates the variation of optimal V/III ratios across growth temperature.

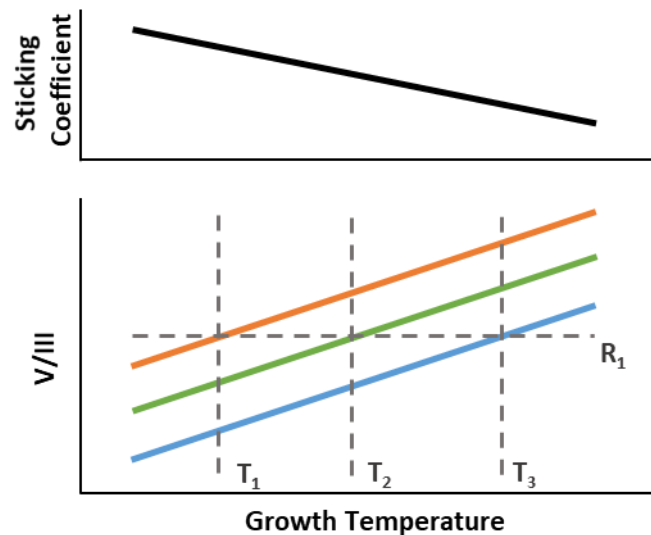


Figure 3.10: Top: A schematic diagram of the variation of sticking coefficient with growth temperature. **Bottom:** A schematic diagram indicating the V/III ratios at which the Sb flux is too low and therefore causes defects (blue), optimal (green) and is too high and therefore causes defects (orange). R_1 is a constant V/III ratio across temperature.

Figure 3.10 shows how the sticking coefficient varies as a function of temperature, and how for a given V/III ratio, this ratio can be too low, optimal, or too high depending on the growth temperature. Varying the V/III ratios much beyond these limits will result in milky growth. It is clear from the diagram that a given V/III ratio, R_1 , can cross each of the growth conditions indicated as the growth temperature is varied. At the lowest temperature T_1 this ratio is too high despite it being too low at T_3 and optimal at T_2 .

An explanation of these trends with regards to the movement of incoming atoms on the growing surface can be understood by considering the temperature dependence of the sticking coefficient. At hotter temperatures, the sticking coefficient is low and the Sb atoms have energy to migrate on the surface to find the appropriate sites. Once the initial V_{Sb} have been overcome (i.e. the vacancies filled), any increase in V/III ratio may show little correlation to the transport properties as excess Sb will not stick. This relates to the generally accepted rule of growing with a high V/III ratio when growing GaSb.

This is a possible explanation for the trends observed in Figure 3.9 at a growth temperature of 505 °C, where the temperature is sufficiently high that even at the higher V/III ratios, Sb agglomerations do not form. As the flux ratio is reduced however, this leads to the creation of V_{Sb} , and therefore Ga_{Sb} and V_{Ga} , leading to increased defect concentrations and a lower mobility.

Moving towards the 475 °C growth temperature, it is believed that the sticking coefficient is higher, with a comparably lower V/III giving a lower defect concentration and higher mobility. Increasing the Sb flux at this temperature could result in Sb agglomerations and further V_{Sb} defects, resulting in Ga_{Sb} defects. As the temperature is lowered again (below 460 °C) it is possible that the antimony sticking coefficient is sufficiently high that Sb_{Ga} defects are produced. These are donor defects which would compensate the accepting defects, leading to a lower measured p -type carrier density, yet a lower mobility, as seen in Figure 3.9.

The exact dependencies of these relationships with temperature (and hence the gradients of the lines in Figure 3.10) are not known. In fact, it is not even known if the relationship is linear across temperature, however, it can be stated that, once an optimal V/III ratio is found to reduce the defect concentration at a particular growth temperature (i.e. sufficient to fill vacant sites but not so much as to agglomerate), this optimal V/III ratio has a proportional relationship with growth temperature. Whether there is an optimal growth temperature would need further investigation as this would require knowledge of a specific balance of defects formed at each temperature.

Whilst it would obviously be beneficial to determine these relationships more accurately, and therefore to determine an optimal temperature dependent V/III ratio, this would require significant time and effort, and as such is beyond the scope of this work. For this work, the requirement was to achieve an improvement over the current standard, with this achieved.

Alternatively, works by Ichimura *et al.* [68] and Hakala *et al.* [56] provide an insight into theoretical simulation of defects with changing growth conditions, but this theoretical field currently does not have much correlation with measured experimental data.

3.3.5 Temperature Dependence of Antisite Defects

To further understand the nature of these defects the temperature dependencies of a select few samples were measured. These measurements again exploited the van der Pauw method, along with a helium cryostat to achieve cold temperature results, with

extended magnetic field dependence measurements covering a field range of ± 0.6 T. Complete details of the measurement apparatus are given in chapter 7 where a more detailed and extensive investigation is performed into the temperature and field dependence of reduced dimensionality (2D) *n*-type samples. The samples measured here were all grown with a V/III ratio of 1.3 and with growth temperatures of 450 °C, 475 °C or 505 °C. In the above section it is seen that there is a decrease in carrier density with growth temperature and a peak in mobility at $T_g = 475$ °C.

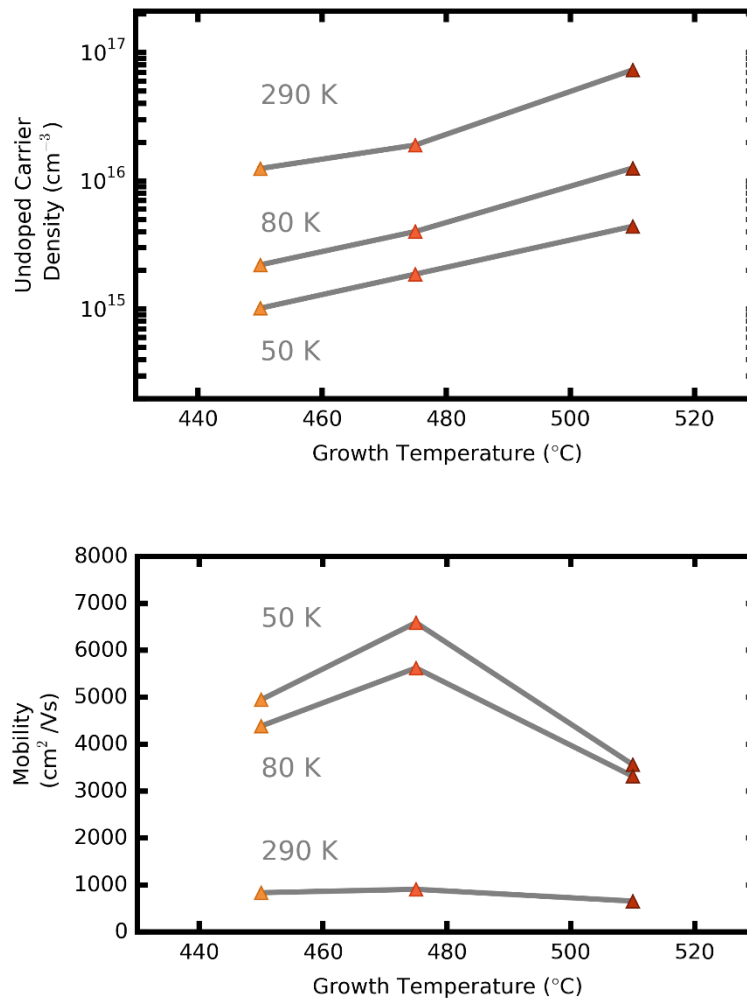


Figure 3.11: A graph showing the measured carried density and mobility across growth temperature with lines for different measurement temperatures, 290 K, 80 K, 50 K.

It can be seen from Figure 3.11 that the trends observed at room temperature are also seen as measurement temperature is reduced. A reduction in growth temperature results in a measured reduction in carrier density, and a peak in mobility at a growth temperature of $T_g = 475$ °C. The mobility peaks at a temperature of 55 K for all growth temperatures, with peak mobilities of 4950 cm²/Vs, 6590 cm²/Vs and 4080 cm²/Vs for growth

temperatures of 450 °C, 475 °C and 505 °C respectively. Above this temperature, the mobility is limited by scattering from phonons, whilst below this temperature it is likely limited by background impurity scattering [9]. The robustness of this trend with temperature reinforces the argument that there are some compensating defects in the lower growth temperature samples.

As these defects can be treated as a dopant, an activation energy can be deduced. Initially, this can be treated rather simply by plotting the high temperature regime (above 50 K) on an Arrhenius plot. On this plot the x axis is $1000/T$ and the y axis is the natural log of carrier density. The gradient of the resultant plot then gives an activation energy. To avoid confusion the samples will henceforth be named after their growth temperature.

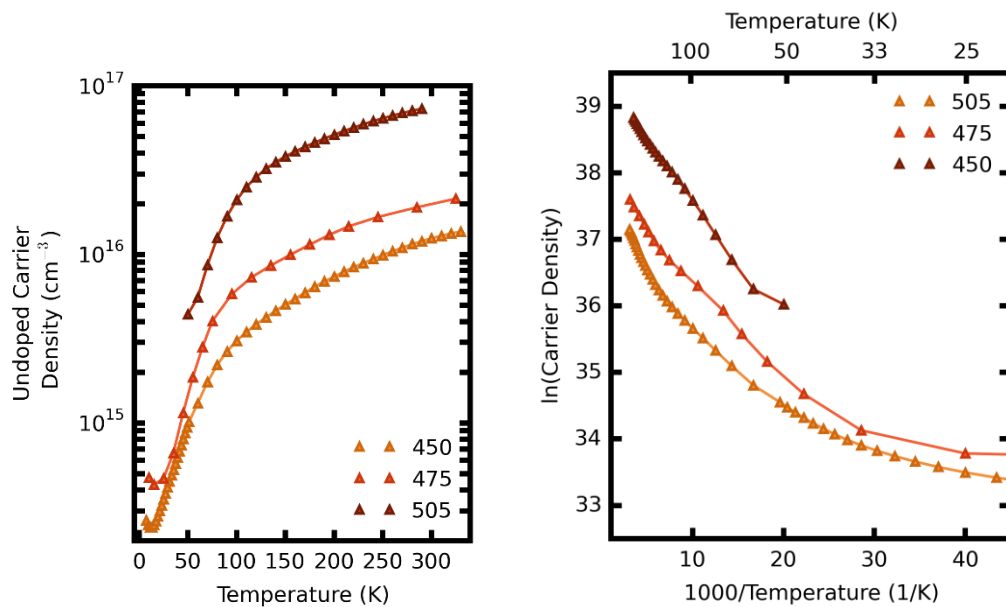


Figure 3.12: Left: A plot of the measured carrier density against temperature with data points and guides for the eye. **Right:** An Arrhenius plot of the measured carrier density which can be used to extract an activation energy.

All three samples show a steady decrease in carrier concentration with temperature until approximately 100 K where the gradient changes to a sharp decrease in concentration. The Arrhenius plot highlights the similarity of the gradients of 505 and 475 at high temperature (>150 K) but the gradients of these samples diverge as the temperature decreases.

The gradient can be found for temperatures between 50 K and 300 K, with the activation energies of each sample given in Table 3.3. The error given is the standard deviation (std) from the covariance of the fit. However, it is apparent that although this linear fit is

reasonable for the high growth temperature sample (505), this becomes less reasonable for the two lower growth temperature samples. The temperature range was thus split into three regimes, where the 450 °C sample shows a significant change in gradient, and the activation energies recalculated. Table 3.3 shows the activation for all three samples when various temperature ranges are considered.

Table 3.3: Activation energies (E_1) for GaSb samples grown with different growth temperatures using different temperature regimes. The error given is the std from the variance of the fit.

T_g (°C)	E_1 (meV) (50 – 300) K	E_1 (meV) (< 50) K	E_1 (meV) (50 – 150) K	E_1 (meV) (150 – 300) K
450	13.7 ± 0.6	5.2 ± 1.1	11.8 ± 0.4	27.8 ± 0.3
475	13.1 ± 0.4	4.0 ± 0.2	12.4 ± 0.6	19.6 ± 0.4
505	16.5 ± 0.2	-	16.5 ± 0.4	20.0 ± 0.4

In the high temperature region (> 150 K) it is seen that samples 475 and 505 have very similar activation energies. This would indicate the same defects providing the p -type carriers, with sample 450 then containing a defect with a deeper ionisation level. However, once the lower temperature region is considered (between 50 K and 150 K), the activation energy of sample 505 changes slightly, with the other two samples changing more significantly. In this temperature region samples 450 and 475 now have comparable activation energies indicating a similar defect. In the lower temperature limit (<50 K) the sample 505 could not be analysed and both 450 and 475 again gave comparable results with energies of 5.2 meV and 4.0 meV respectively.

The smaller change in activation energy of sample 505 across temperature indicates a dominating contribution from a single defect, with perhaps a smaller contribution from other defects or a single defect with multiple ionisation levels. At high temperature this dominating contribution is also seen in sample 475 but then as the temperature decreases below 150 K a different dominating effect occurs with a different activation energy which is similar to sample 450. Sample 450 does not have a suitable straight-line fit in any region below 150 K suggesting multiple process competing throughout the temperature range.

To more accurately determine the nature of carrier activation of these samples, a least squares fit of multiple defects was implemented. This model used the dopant activation (equation 2.14) for a single ionisation state dopant, and the equivalent for a dopant which considers multiple ionisation levels (equation 2.15) in combination to fit the data. Both

accepting, and donor defects were investigated with a two-level ionisation defect assumed to be the Ga_{Sb} antisite. The degeneracy factors were assumed to be 2 for donors and 4 for acceptors (as explained previously). The concentration of the dopants and the energy levels were free fitting parameters.

A reasonable fit was achieved to sample 505 above 50 K for a p -type defect with two activation levels, with energy levels of 25.7 meV and 72.6 meV. A better fit to the data at lower temperatures was achieved when this defect was considered in combination with another accepting defect with an activation energy of 29.8 meV, however, it could be argued that this better fit is simply due to the increased number of fitting parameters. Other combinations of defects were modelled however unphysical parameters were required to obtain a fit. The error from the fit was no more than ± 0.1 meV in each case for all energies stated here.

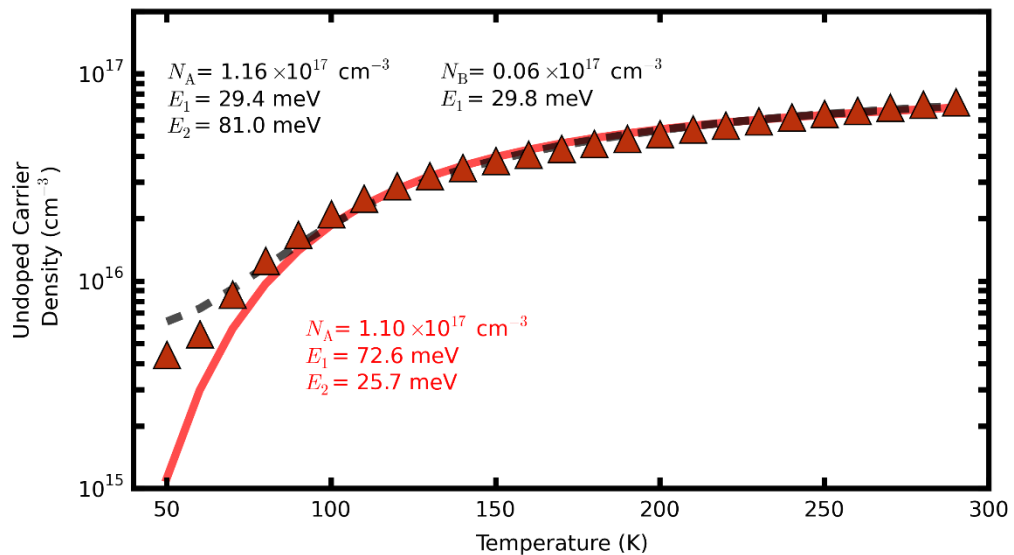


Figure 3.13: A fit of the measured carrier density from sample 505 with the data shown as points (▲) and two separate fits shown with the fit parameters given on the plot. One defect with two ionisation levels is shown in red (using equation 2.15), and two defects, one with two ionisation levels, and one with one ionisation level, is shown in dashed black (using equation 2.14).

Following the same procedure, a good fit to sample 475 was obtained for a doubly accepting dopant with activation energies of 25.3 meV and 72.4 meV, which are comparable to sample 505's 25.7 meV and 72 meV. As with sample 505, other combinations of defects required unphysical parameters to fit the data or a fit that didn't appropriately match the trend below 100 K. Finally, a fit to sample 450 across the temperature range (50-300) K could not be achieved with reasonable parameters for

combinations of up to 3 defects, and thus, no particular defect can be confirmed as a majority contribution.

The similarity of the activation energies of samples 505 and 475, with a doubly ionisable acceptor, suggests that the main contribution for both these samples is in fact from Ga_{Sb} antisite defects. Where each sample has a variation in the concentration as expected from the results discussed in section 3.3.4. Further, the activation energy of the first level achieved from the fitting performed here, is comparable with the literature values for the first level of this defect, which are 23-31 meV [7, 9, 69]. However, the secondary energy level found to be 73-81 meV in this work deviates from the literature (94 meV) [7, 9] when it is freely fit. The higher-level value given in the literature was determined from PL measurements, and was used as set parameter when fitting the transport measurements to determine the lower activation energy in both works. To investigate the significance of this difference, the second activation level in the fitting performed here was subsequently fixed at an energy of 94 meV. With the fit now adjusting just the other activation levels, the other activation levels increased by only a maximum of 0.7 meV in all cases.

The low growth temperature sample (450) however may have many competing contributions to the carrier concentration and thus cannot be fit sufficiently with the current model. This reinforces the argument suggested above from the room temperature measurements, where growth temperatures below 450 K (at a V/III ratio of 1.3) introduce defects other than the well-known Ga_{Sb} antisite. Though this statement and the nature of these defects, or even the number of different types, cannot be confirmed without further study. It is also understood that there are likely many temperature dependent processes occurring in all samples, and as such, this is far from a full picture of the unintentional dopants in GaSb.

It could also be considered that the GaAs substrate with an IMF, as used in this work, has a contribution to the electrical effects. To investigate this, the measured mobility across temperature was plotted alongside the mobility measured from a GaSb sample grown from a melt (Figure 3.14, data taken from ref [9]).

The sample measured by Dutta *et al.* used the vertical Bridgman technique from a stoichiometric melt. As such, their sample contained no GaAs substrate, and can be used to examine the effect of this substrate and the MBE growth quality. It can be seen that these two measured mobilities are very comparable and thus it is confirmed that the IMF has little negative consequence on the mobility across temperature. An alternative sample measured by Dutta *et al.*, grown from a gallium rich melt, had a peak mobility at ~ 7000

cm^2/Vs , comparable to the MBE grown samples measured here when grown at higher growth temperatures. This further proves the hypothesis that the Sb sticking coefficient decreases at higher growth temperatures.

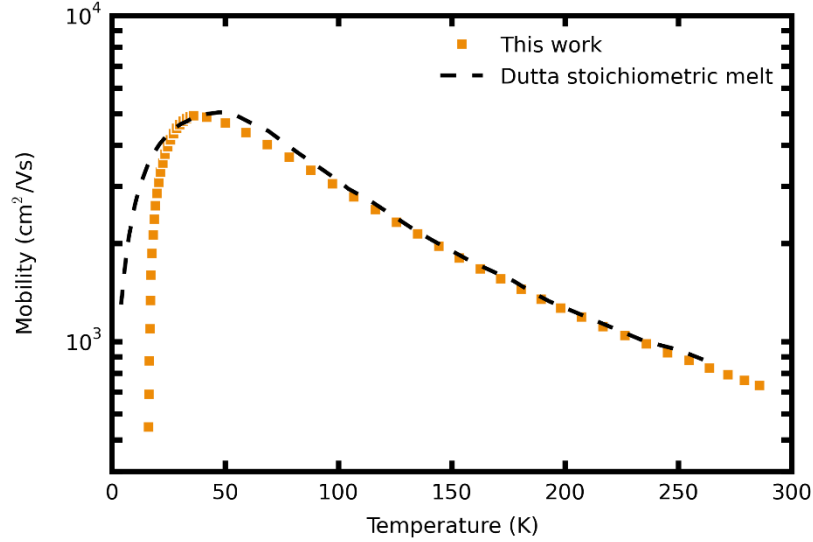


Figure 3.14: A graph of mobility against temperature for two unintentionally doped GaSb samples. Squares indicate the measured mobility for an MBE grown sample created in this work which is grown on a GaAs semi-insulating substrate followed by an IMF. The dashed line shows the mobility measured by Dutta *et al.* [9] for a sample grown from a melt.

Though a full description of the nature of the defects across growth temperature is far from complete, it can certainly be said that the sample grown at 475 °C with a V/III ratio of 1.3 gives the highest mobility across temperature and a low hole concentration. These growth conditions will be used for the growth of heterostructures, described further in the subsequent chapters. With further understanding of reduction of the p -type defects, the challenges of doping GaSb can now be explored.

3.3.6 Doping Considerations for n -GaSb

The n -type doping in GaSb was investigated, and in this work the dopant of choice is tellurium. However, doping GaSb proves a more complicated task compared to other materials; this is not just due to the inherent accepting concentration. The investigation of this bulk n -type doping may allow some further understanding to be used in the 2D structures. The doping in these $\text{Al}_{0.2}\text{Ga}_{0.8}\text{Sb}/\text{GaSb}$ structures is mainly used for doping the top barrier of $\text{Al}_{0.2}\text{Ga}_{0.8}\text{Sb}$ but could also be used to compensate the acceptor concentration. Though this is not ideal in the quantum wells where the electrons are conducting, though it may be necessary to achieve the appropriate confinement. This will be explored thoroughly in chapter 6.

Generally, there are two main factors that contribute to achieving a given doping concentration, ionisation and incorporation. The ionisation energy for a dopant is the amount of energy an electron requires to enter the conduction band (for a donor) or holes to enter the valence band (for an acceptor), where the shallower (closer to the band) this level is, the more easily the carriers will enter the band. A larger (deeper) ionisation energy will likely mean that not all electrons (or holes) will be activated at room temperature and as such, there will be a significant drop in carriers at a relatively high temperature. This ionisation energy is unique to the dopant species and the material it is introduced into.

The incorporation is the number of atoms that will bond permanently into the lattice. The higher the incorporation, the easier it is to achieve a given doping level practically, however the incorporation can saturate, introducing a limitation on how high a material can be doped. However, in our case the inherent acceptors in GaSb will also first have to be compensated (neutralised), before the electrons from Te can then be used as the main carrier concentration. This is further complicated by reports of an accepting Te complex with the Ga_{Sb} antisite [70].

A series of bulk *n*-type GaSb samples were prepared as in section 3.3.3 to provide a doping calibration, where these samples were investigated with increasing Te Knudsen cell temperature. Tellurium doped *n*-InSb samples are used to calibrate the doping concentration for materials grown in the MBE machine. Tellurium is a particularly shallow dopant in InSb allowing the assumption that the dopant is 100 % ionised at room temperature and thus indicative of the total dopant concentration deposited [71]. The InSb samples were consistently grown at 1 $\mu\text{m/hr}$ and were measured using the same method as the GaSb samples. An empirical formula relating the measured resultant carrier density to the Te cell temperature can be formed from this data. When doping in a different material, this carrier concentration is taken as a representative of the expected doping, though there will, of course, be a minor correction for growth rate, where the InSb calibration samples were grown at a constant 1 $\mu\text{m/hr}$ growth rate, whilst the GaSb samples were grown at 1.097 $\mu\text{m/hr}$ (1ML/s). This increased rate allows less Te atoms to incorporate as the bulk material is growing faster. This difference in rate purely stems from the difference in the size of monolayers between the two crystals and the conversion of the growth rate units.

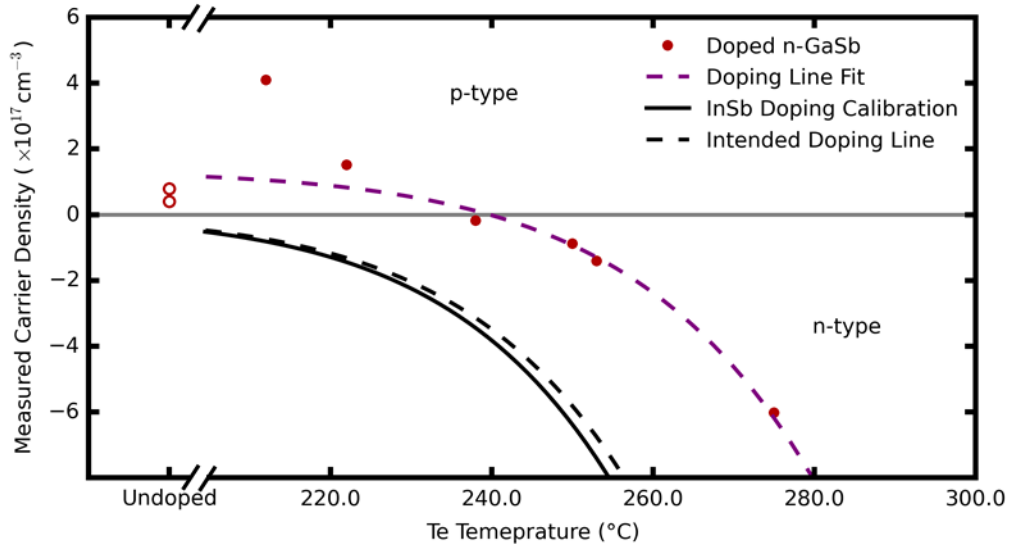


Figure 3.15: A graph showing the measured carrier density at 300 K of doped GaSb at varying Te cell temperatures, producing both *p* and *n*-type carriers (points). The solid black line indicates the fitted line to calibration samples grown on InSb. The dashed line is an adjustment of the calibration line for growth rate in GaSb. The pink dashed line is a fit to the GaSb samples using equation 3.6 (see the text for further details). The undoped samples are shown for context.

Figure 3.15 shows the measured carrier density with the increasing tellurium cell temperature, where it can be seen that the simple adjustment for the growth rate isn't satisfactory to describe the measured carrier density in GaSb. Here positive numbers represent *p*-type carriers and negative numbers represent *n*-type carriers. The solid line represents the carrier concentration measured in Te-doped InSb, used as the calibration, which can be approximated as the dopant atom concentration due to the low ionisation energy. Comparing to GaSb, as shown above, undoped GaSb is naturally accepting. However, when the Te cell temperature is increased to an appropriate low doping concentration for InSb (212 °C, $7 \times 10^{16} \text{ cm}^{-3}$), an increased acceptor concentration is found. The Knudsen cell temperature must be further increased until approximately 238 °C before GaSb switches to an electron concentration of $3 \times 10^{16} \text{ cm}^{-3}$. The measured doping line at this temperature is approximately a tenth of what would be expected from the InSb calibration. Even once the samples become *n*-type a high Te cell temperature is required to be able to sufficiently dope GaSb. This can be attributed in part to the ionisation energy difference for Te in both materials. In InSb the Te ionisation level is very shallow ($<0.7 \text{ meV}$) [71]. In GaSb, the activation is reported to be theoretically as high as $\sim 3 \text{ meV}$ [72], however, these values are too small to be significant across most temperatures as 3 meV is equivalent to a $k_b T$ at a temperature of $\sim 35 \text{ K}$. The incorporation is assumed to not vary significantly.

The initial increase of acceptor concentration with a small Te flux is attributed to the Te complex which has been reported previously, though scarcely. Dutta *et al.* investigated this unusual effect by low doping GaSb [9], where these samples were still *p*-type and were investigated through photoluminescence (PL) and transport measurements. The results of these measurements concluded that a small Te flux produced a Te complex with the Ga_{Sb} antisite defect creating a triply ionisable acceptor, producing an even greater accepting concentration. In theory, once all the antisites have been complexed with Te, for a further increase in Te, these acceptors become neutralised by the separate Te dopant atoms and finally the material becomes *n*-type.

It is a very simple model to suggest that all initial Te atoms become complexed and all subsequent Te atoms become donors. A more accurate picture is that as Te is incorporated into the crystal, a proportion will complex with the antisites if there are any within a migration length of the Te atom. However, many will not complex and will act as the donors they are intended to be. Therefore, determining the exact number of accepting defects in an *n*-type material becomes difficult.

To convert from a carrier concentration in InSb, n_{InSb} , to a carrier concentration in GaSb, n_{GaSb} , at a particular cell temperature, further care has to be taken. Analysing the difference between the two materials yields

$$n_{\text{GaSb}} = an_{\text{InSb}} + b, \quad 3.6$$

where the parameters a and b are fitting parameters with values of 0.39 and $1.3 \times 10^{17} \text{ cm}^{-3}$ respectively. A fit of equation 3.6 to the data is seen in Figure 3.15. These values are determined from comparison between the InSb and GaSb based calibration samples. It should be noted that, as above, both the carrier densities are negative numbers in this equation. The gradient value, a , can be attributed to any difference in incorporation or activation of Te in GaSb compared to InSb, and also in the proportion of Te complexes created. The y offset value, b , here can be considered as an offset which is attributed to the acceptors in the GaSb samples (both native and Te complex). Thus, it is theorised that *n*-type GaSb has up to $1.3 \times 10^{17} \text{ cm}^{-3}$ holes in any given sample.

This number seems rather large, however, a sanity check can be completed. The number of native acceptor ions (with 2 levels) N_A , can be assumed to be

$$N_A = \frac{p_{un}}{N_1 + N_2}, \quad 3.7$$

where p_{un} is the measured hole density in the undoped GaSb samples and N_1 and N_2 represent the proportion of each energy level ionised in the defect in the undoped samples at room temperature.

If all the acceptors in an n -doped sample are ionised, the number of holes due to the native defects (assuming no Te complexes) will be double the number of acceptors ($2N_A$) giving, in comparison to the measured undoped carrier density,

$$p_{n-native} = 2 N_A = \frac{2 p_{un}}{N_1 + N_2}, \quad 3.8$$

Here N_1 and N_2 still represent the proportion of carriers for each energy level that is ionised in the undoped sample. Similarly, if all the holes in the sample originate from the Te complexes, the hole concentration will equal

$$p_{n-Te} = 3 N_A = \frac{3 p_{un}}{N_1 + N_2}, \quad 3.9$$

as there are now 3 energy levels. It can reasonably be assumed that due to their respective ionisation levels, that the shallower level is all ionised in the undoped sample ($N_1 = 1$), and that N_2 will fall within the range 0 and 1. More specifically, out of the total number of holes, there will be a combination of some holes originating from Te complexed with the antisites, and some from antisites themselves. This is seen more clearly here,

$$p_n = p_{n-Te} b + (1 - b)p_{n-native}, \quad 3.10$$

$$p_n = \frac{3 p_{un}}{1 + N_2} - \frac{b p_{un}}{1 + N_2}, \quad 3.11$$

where b is a factor representing the percentage of holes originating from the Te complex defect (0 to 1). This model puts p_n within the limits of p_{un} and $3p_{un}$, where b and N_2 range from 0 to 1. The undoped samples result in a hole concentration of $(3.0 \times 10^{16} - 7.0 \times 10^{16}) \text{ cm}^{-3}$, putting p_n in the range of $(3.0 \times 10^{16} - 2.0 \times 10^{17}) \text{ cm}^{-3}$. As our offset is $(1.3 \times 10^{17} \pm 0.2) \text{ cm}^{-3}$, it falls within the higher end of this range. This is a very simplistic model; however, it justifies the magnitude of the hole concentration found in n -type GaSb.

It should also be mentioned that the concentrations of these defects are dependent on the growth conditions used. This is of no surprise, given that the concentration of antisite defects that the Te complexes to changes with growth conditions also. This Te acceptor is said to lie nearer to the valence band than the lowest level of the native acceptor [9]. It becomes quickly apparent that the part tellurium plays in doping GaSb is not simple or well understood in combination with the defects of GaSb.

The aim in this work is to use doping to create appropriate confinement for the charge carriers, and as such we need to not only be able to accurately dope the sample, but ensure that the dopants behaviour across temperatures produces the desired band structure. To aid our understanding of what can be expected, *n*-GaSb samples were measured across temperature. The carrier concentration across a full measurement temperature range of (3-300) K was investigated and compared for both a doped and undoped sample with the same growth conditions. Sample 475 was chosen as the undoped sample, with a doped counterpart grown with a Te cell temperature of 250 °C, resulting in a room temperature electron carrier concentration of $1.5 \times 10^{17} \text{ cm}^{-3}$.

As tellurium is a relatively shallow dopant in GaSb, the measured carrier concentration across temperature could be expected to remain constant until a very low temperature where there will be a decrease. Alternatively, if the ionisation level is deeper, activation behaviours similar to those seen in the *p*-type defects above could be expected. Interestingly, in *n*-GaSb neither of these effects are observed.

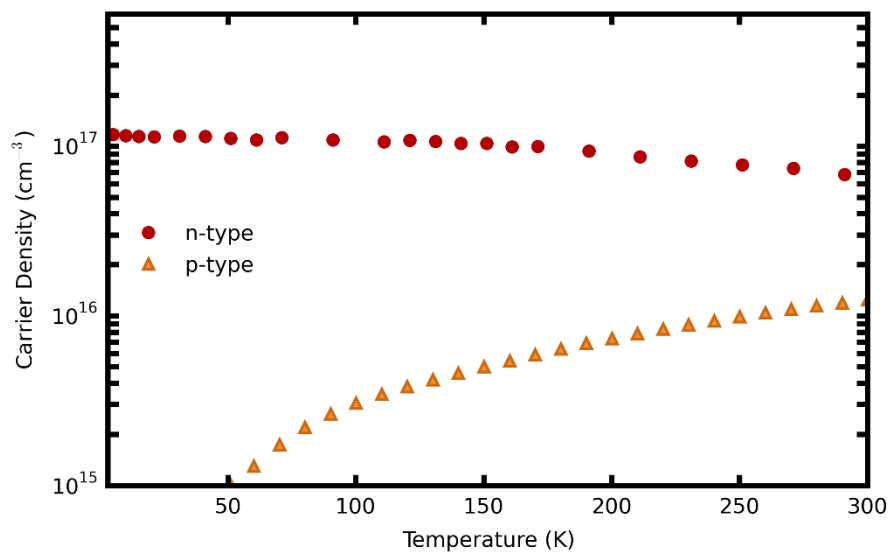


Figure 3.16: A graph showing the measured carrier density relationship with measurement temperature, indicating different activation behaviour for both *p* and *n*-type bulk GaSb.

Unlike most measured carrier densities in semiconductors observed against temperature, *n*-type GaSb increases with a decreasing temperature. It can be seen here that at room temperature the carrier density is measured to be $6.5 \times 10^{16} \text{ cm}^{-3}$, whereas at 3 K the carrier density has increased to $1.2 \times 10^{17} \text{ cm}^{-3}$.

It is tempting to assume that because the *p*-type carrier density in the undoped sample is decreasing, this would occur in the *n*-type sample. Then, as the *n*-type contribution is

expected to be unchanging, the p -type contribution decreasing would create the appearance of an increasing n -type concentration with decreasing temperature. However, this is not possible in an n -type semiconductor as all (or nearly all) of the acceptors are ionised.

Consider the band diagram shown in Figure 3.17. The valence band is full of states which are used for bonding. When electrons fill these states, they become stationary (i.e. do not conduct). Unfilled states represent holes which are then free to move. The probability of a state being filled is of course given by the Fermi-distribution. An acceptor however is put into the system as an atom or ion with an empty state, this is an unionised acceptor. To create a hole, an electron from the valence band has to fill the empty state of the acceptor, occupying the empty state. Thus, an ionised acceptor gives a hole, as expected. The Fermi level in an n -type semiconductor is close to the conduction band and thus there is a high probability of the acceptor states being ionised. This is true across the full temperature range and as such, an explanation for the apparent increase in carrier density with decreasing temperature is still required.

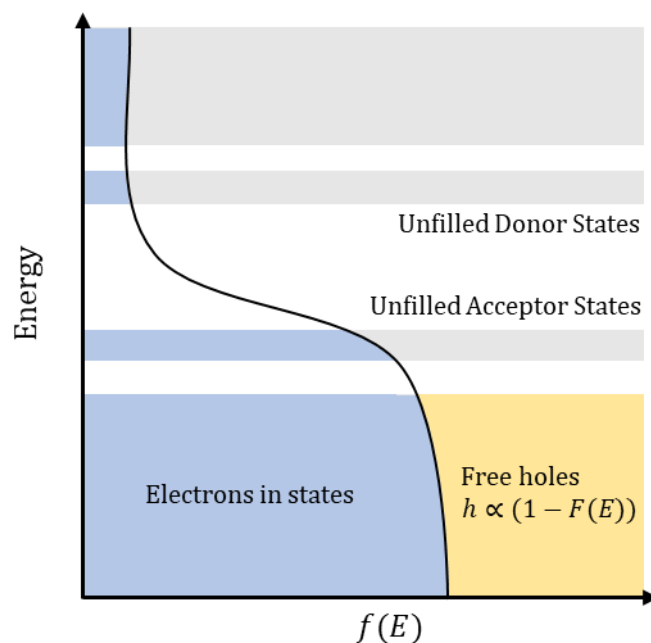


Figure 3.17: A schematic diagram indicating the electron states in a standard band diagram. Where the black line represents the Fermi-distribution and the blue shaded regions indicate the filled electron states.

This unusual observation has been reported before by Sagar *et al.* [10] and is said to behave in a similar way to germanium. The apparently increasing carrier concentration with decreasing temperature is seen from a change in distribution of electrons from the low-lying L band to the Γ band (in Ge). Sagar *et al.* gave an equation for a Hall coefficient from which the carrier density can be extracted, for a multi-band sample,

$$R_H = \frac{(n_L + n_\Gamma b^2)}{e(n_L + n_\Gamma b)^2}, \quad 3.12$$

where $b = \frac{\mu_\Gamma}{\mu_L}$.

It is seen here that there are a mix of carrier densities and mobilities from the Γ -band, n_Γ and μ_Γ , and L band, n_L and μ_L , when the Hall coefficient is measured (in GaSb). The L-band has a high effective mass and thus a low mobility by comparison to the Γ -band. If it is assumed that the sample has a single carrier, the Hall coefficient R_H , is assumed to equal $-1/ne$. By setting the total carrier concentration (the sum of n_Γ and n_L) to be constant across temperature, and simply investigating the ratio of electrons in the bands, the above observed trend can be seen. Figure 3.18 shows the carrier concentration (assumed to be from a single carrier), against the ratio of the number of electrons that are in the L-band to the Γ -band n_L/n_Γ . When this ratio is decreased (analogous to temperature decreasing as the Γ -band is at a lower energy) there is a decrease in R_H . The decrease in R_H leads to an apparent increase in carrier density when it is assumed single carrier. This figure was produced using Sagar *et al.*'s value of $b = 5$ [10].

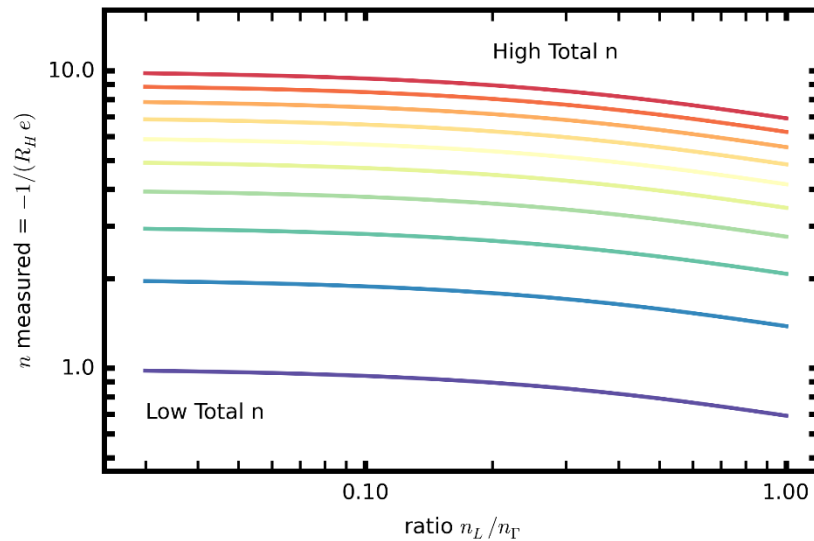


Figure 3.18: The apparent carrier density calculated from the Hall coefficient against the ratio of electrons in the L-band to the Γ -band, which is analogous to temperature. Each line is for a set total carrier density with blue being a lower concentration and red being higher where equation 3.12 was used for this calculation.

Sagar *et al.* investigated the band separation by measuring the Hall coefficient as a function of varying pressure and temperature. Changing the pressure changes the energy levels of the Γ and L bands at differing rates relative to the valence band, and as such the bands move together in energy as the pressure is increased. By measuring the Hall coefficients against pressure, a separation of 80 meV was found between the bands.

However, this separation seems large to have such a significant effect on the carrier density, despite the increased effective mass in the L band giving an increased density of states. A relatively large proportion of the electrons would have to be in the L-band at room temperature to observe such a significant change. This was not further investigated; however, it is by no means a complete model and this should be considered in further work.

3.4 Conclusions

This chapter gave an overview of the physical creation and characterisation of samples via MBE, discussing the physical practicalities of MBE growth and electrical measurement. The associated growth kinetics, which are integral to the creation of defects were also discussed, where these defects are prominent in GaSb growth and are responsible for an unavoidably high p-type background. The presence of these defects increase scattering and thus the concentration should be minimised.

A growth study of unintentionally doped GaSb was completed to obtain a reduced hole concentration (and therefore reduced defects) and an increased mobility (used as a material quality factor). The growth temperature range considered was (380-520) °C as these were the bounds for growth temperature to obtain a shiny (as opposed to milky) surface for a V/III ratio of 1.3. A limited range of V/III ratios were also experimentally tested for growth temperatures of 505 °C and 475 °C. All samples consisted of 2.2 µm of GaSb grown on a semi-insulating GaAs substrate with an IMF layer to create a relaxed GaSb epilayer. This growth method was found to give a very comparable mobility to melt grown GaSb. It was found that reducing the growth temperature reduced the hole concentration, however, this did not necessarily correspond to a significant increase in mobility. The optimal growth parameters were found to be a growth temperature of 475 °C and a V/III ratio of 1.3. The trends in carrier density and mobility against growth temperature were explained by consideration of the formation of defects, with the highest growth temperature resulting in a high concentration of antisite defects, and the lower temperatures also having an increased concentration of defects, but of both accepting and donor nature. The optimal growth condition was found to be in a sweet spot where there are a reduced number of antisite defects but no other species of defect are created. The creation of different defects across substrate temperature was determined to be primarily due to the sticking coefficient of Sb and how this decreases with temperature. Low-temperature transport measurements confirmed the trend is continued across a full temperature range (3-300) K. Activation analysis with a simple defect fitting model further supported this theory, however the lowest growth temperature measurements

indicated the presence of many defects that would require a more complex model to correctly identify the differing defect species.

Donor doped GaSb was also investigated across a range of Te cell temperatures and across a range of measurement temperatures. It was found that a low flux of Te resulted in an increased acceptor concentration consistent with a tellurium-antisite complex, creating a triply ionisable accepting defect. Once the Te flux was increased, the donor atoms began neutralising the acceptors, and then when further increased, the sample became *n*-type. A conversion from an InSb doping calibration to GaSb was found. From which it was extrapolated that there are possibly up to $1.3 \times 10^{17} \text{ cm}^{-3}$ minority hole carriers in a given *n*-type GaSb sample, where these originate from the Te complexes and GaSb native defects.

The temperature dependence of an *n*-type GaSb carrier concentration was also investigated giving an unusual trend of an increasing carrier density with decreasing temperature. This has been attributed to distribution of electrons in the low-lying L-band. As the mobility in the L-band is much lower than in the Γ -band, and by nature of the measurement of the carrier density and mobility being entwined, the Hall coefficient decreases with temperature. When this Hall coefficient is assumed to be single carrier, the resulting carrier density appears to increase with decreasing temperature. However, the separation of the Γ and L band is stated to be 80 meV and thus it is unusual to expect a significant proportion of electrons in the L band, though this is required in order to observe this significant difference.

With the information acquired from this chapter, confined structures can be grown. However, to measure these samples via Hall bar devices they must first be fabricated using standard techniques. These techniques will be explored in the next chapter.

Chapter 4

Fabrication of Semiconductor Devices

Whether it is on a production scale or a research scale, device fabrication is the bridge between the creation of quantum structures and the ability to integrate those structures into a circuit and measure the phenomena occurring within the structure. Once grown a wafer is cleaved it is brought into the cleanroom for cleaning and device fabrication. All Hall bars presented in this work were processed in Lancaster University’s Quantum Technology Centre which consists of class 1000 and class 100 cleanrooms. A class of cleanroom is defined in American standard 5295 by the maximum number of particles that are 0.35 μm or larger in a cubic foot of air [16]. Fabrication of these devices includes UV photolithography, to define the shape of the contacts and mesa, thermal evaporation, to deposit the contacts and etching to electrically isolate each Hall bar. The design of the Hall bar geometry and therefore lithography mask was an 8-pad non-gated geometry. Each of these steps of the processing will be described in detail and finally, a summary will be given, stating exact parameters and processing flow used in this work.

4.1 Fabrication Overview

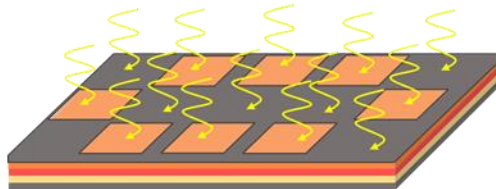
The monitoring of device creation is essential to see the progress through fabrication. At each fabrication step the samples were inspected through an optical microscope and records kept. Monitoring is an opportunity for further understanding of features created on the devices and how to improve device quality. Often, the finer details of processing, such as correct storage or handling, are left undescribed but can greatly improve device quality. In general, the grown surface shouldn’t be handled, and the sample only be handled by the edges to prevent any contamination. Equally, tweezers should always be cleaned between uses. The full fabrication procedure is shown below in Figure 4.1.



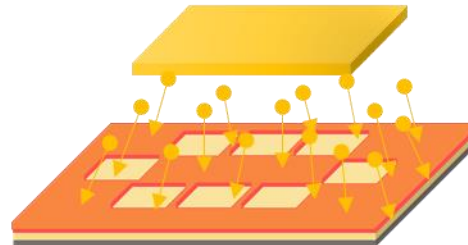
1. The sample is cleaved and cleaned.



2. Bi-layer positive resist is deposited and baked to harden.



3. UV light is shone through a mask to make the exposed resist soluble. It is then developed, leaving the desired pattern in the resist.



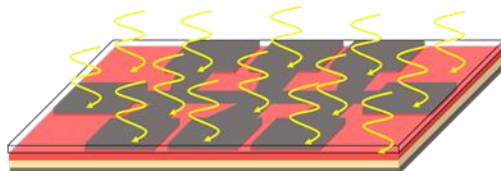
4. Thermally evaporated metal is deposited on to the sample.



5. The resist and any excess gold on top is removed leaving a contacting pattern.



6. A single layer of positive resist is deposited and baked to harden.



7. Step 3 is repeated with an alternative mask pattern designed to create the Hall bar shape.



8. The sample is placed in acid where the material is etched to the substrate for isolation.



9. Finally the resist is removed and the sample is then cleaved to a suitable size for the chip carrier.

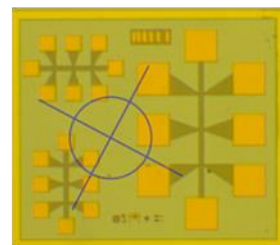


Figure 4.1: A diagram indicating each of the processing steps involved in the creation of a Hall bar, with the final image (RHS), showing a microscope image of the processed Hall bars.

Once the samples were grown, they were cleaved into an appropriate size ($\sim 1 \text{ cm}^2$) and were cleaned thoroughly. Initial cleaning was carried out by the ultrasonic bath for 5 minutes on a low power in a beaker of acetone, followed by a rinse of acetone upon completion to rid the surface of any unwanted particles. This process was then repeated with isopropyl alcohol (IPA) and the sample was then dried with gaseous N_2 . The Hall bar contact pattern was defined using optical lithography.

This process was performed using a bi-layer resist consisting of MicroChem LOR-3A lift-off resist, Shipley Microposit S1813, a purpose made quartz mask and a SUSS MicroTec MJB4 mask aligner. Following lithography, metal contacts were deposited using a Moorfield Minilab thermal evaporator. After lift-off of the residual metal and removal of excess resist, the second lithography step was performed. In this case, only an individual layer of positive resist (S1813) was used to define the Hall bar shape, before etching to isolate each device using hydrofluoric acid.

4.2 Optical Lithography

Optical lithography, or photolithography, is the method by which a pattern is defined. This defined pattern can then be used in device fabrication to define contacts when coupled with metal deposition or a mesa when coupled with etching. This is a basic but essential processing step to know and understand as it is the prelude to most other processing methods.

A sample must undergo a dehydration bake of 1 minute at $100 \text{ }^\circ\text{C}$ after having had any contact with solvent such as cleaning. This is to improve resist adhesion [73]. The cleaned and dehydrated sample was placed onto the spinner, on top of an appropriately sized chuck, where the chuck is slightly smaller than the sample⁸. A photosensitive resist was deposited by pipette on to the surface, avoiding bubble formation. The sample was then spun to obtain a uniform thickness of resist of approximately $1 \text{ }\mu\text{m}$. The acceleration, speed and time of the spin are varied depending on the desired thickness of resist and the sample size and geometry. The uniformity and thickness of resist are heavily dependent on the rotational speed as the centrifugal force pushes the majority of the resist across the sample and off the edge, thinning the remaining resist. The duration of the spin required to create a uniform thickness is dependent on the size of the sample, whilst acceleration

⁸ The size of chuck ensures a maximum vacuum between the sample and the spinner.

assists in creating a uniform covering, particularly with rough surfaces, as additional torque allows the resist to overcome large features [73, 74].

The spin coating parameters are also dependent on the resist used, where a series of optimal parameters can be found in the relevant data sheets. However, it is often necessary to adjust these slightly. Often having a high acceleration ensures the uniformity of the resist, but may also result in sample damage if the strength of the vacuum holding the sample to the spinner is lower than required. The spin speed is optimal above a certain value and increasing the speed further makes little difference to the thickness of resist. In the case of a sample with poor vacuum (most likely from a rough back or small size), it is necessary to explore the spin recipe parameters to minimise the force on the sample without compromising the resist thickness or uniformity.

Due to the grid grooves on the spinner that are intended to improve vacuum, the LOR3A can often deposit on the back of the sample when spun. Therefore, before spinning the S1813, the back of the sample must be cleaned using remover and a cleanroom swab, otherwise the vacuum between the sample and the spinner may become compromised.

The sample coated with resist was then soft-baked on a hot plate to harden the resist, using a thermocouple to ensure the correct temperature is reached⁹. Once cooled to room temperature the resist coating was exposed to UV light through a purpose-made mask. Depending on whether the resist is positive or negative tone, it will become more or less soluble in developer respectively. Generally positive tone resist was used in this work. It is important when exposing to UV light to have a good contact between the mask and the sample; as such the edge bead, created by excess resist at the edge of the sample must be removed as an intermediate step before device lithography [75].

An edge bead is the thicker layer of resist that is present on the perimeter of a sample due to the centrifugal force moving resist away from the centre, but the surface tension of the resist stopping the excess resist from being removed from the sample. If the speed of the spinner is increased, the edge bead thickness is decreased but this must be balanced with having too thin a layer at the centre of the sample. If the edge bead is not removed a blurred and slightly misshaped lithography pattern is produced, or an uneven resolution in pattern from one side of the sample to the other if the sample to mask distance varies. On particularly small devices the resolution of the mask must be considered, which will either be defined during the mask creation process, or more importantly during usage by

⁹ Hot plates after frequent use lose their uniformity due to resist spillage and often have 'hot' or 'cold' spots. For repeatability it is useful to directly measure where the sample is baked.

the separation between the mask and the sample. The resolution defined by a contacting gap is given by equation 4.1 [76],

$$MFS = \sqrt{(g + d) \lambda} \quad 4.1$$

where MFS is the minimum feature size possible for a given gap between the resist and the mask, g . Here d is the resist height, and λ is the wavelength of the light (in this case 365 nm). For the samples presented here, the MFS is 0.7 μm when the gap is assumed to be zero. This is more than suitable for the Hall bar device features which have a minimum feature size of 9.3 μm . The minimum feature sizes present on the mask are the exposure test line patterns, with each line width equalling 2 μm , therefore the gap must be kept below 10 μm in order to achieve a well-defined exposure test. As there is contact between the resist on the sample and the mask, after frequent usage the mask may have some resist deposited onto it, this is easily cleaned using acetone and then dried using a circular motion high pressure nitrogen gas. To check the contact between the mask and sample, the microscope may be used, if both the mask and the sample are in focus simultaneously, then they are suitably in contact.

Once the sample and resist have been exposed for an appropriate amount of time, the sample is then developed. Exposure test patterns are placed on all samples for examination under a microscope [76]. Varying results of these exposure tests are shown in Figure 4.2, where over and under exposure cause the same result on an exposure test as over and under development respectively. Finally, the developer is quenched with a stream of deionised (DI) water. The final step of this is very important as residual developer will continue to develop on the surface. The lithography recipe should be checked at the beginning of each processing run (see Table 4.1).

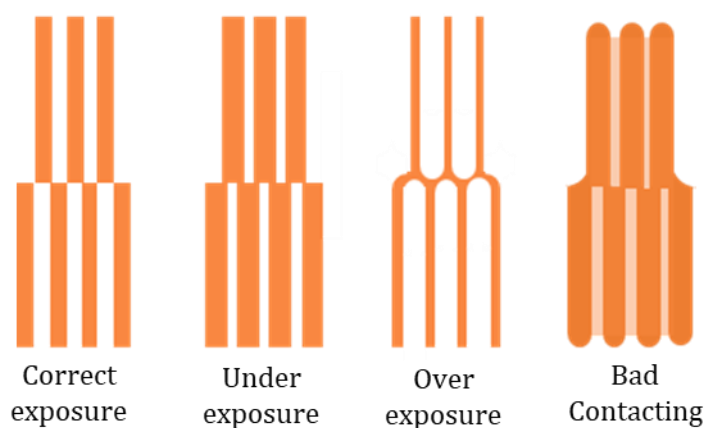


Figure 4.2: A figure showing the various results of exposure test, the correct or intended exposure test, under exposure (or under development), over exposure (or over development) and bad contacting.

The full lithography recipe is stated below in Table 4.1 for both contact and mesa patterning, the parameters of which were fine-tuned through various trials. There are many non-optimal results which can be obtained when fabricating devices.

Table 4.1: The standard lithography recipe used in this work for both contacts and mesa masks, where the acceleration is the initial acceleration until the speed is reached.

Contacts

Resist	Spin Recipe:			Bake Recipe:	
	Time (s)	Acceleration (rpm/s)	Speed (rpm)	Temperature (°C)	Time (min)
LOR3A	7	500	500	180	5
	45	4000	3000		
S1813	30	4000	6000	115	3
Mask pattern		Exposure duration (s)		Develop duration (s)	
Edge bead		3.0		80	
Hall bar contact		2.4		80	

Mesa

Resist	Spin Recipe:			Bake Recipe:	
	Time (s)	Acceleration (rpm/s)	Speed (rpm)	Temperature (°C)	Time (min)
S1813	30	4000	6000	115	3
Mask pattern		Exposure duration (s)		Develop duration (s)	
Edge bead		3.0		80	
Hall bar mesa		2.4		80	

The contacting recipe shown in Table 4.1 includes an initial layer of LOR3A, used to create an undercut as this resist develops faster than S1813. This undercut aids lift-off of residual metal deposited on the resist and results in a more stable and well-defined structure for the contacts. If just S1813 were used, the contact may produce an unstable overhang when the resist was removed (see Figure 4.3).

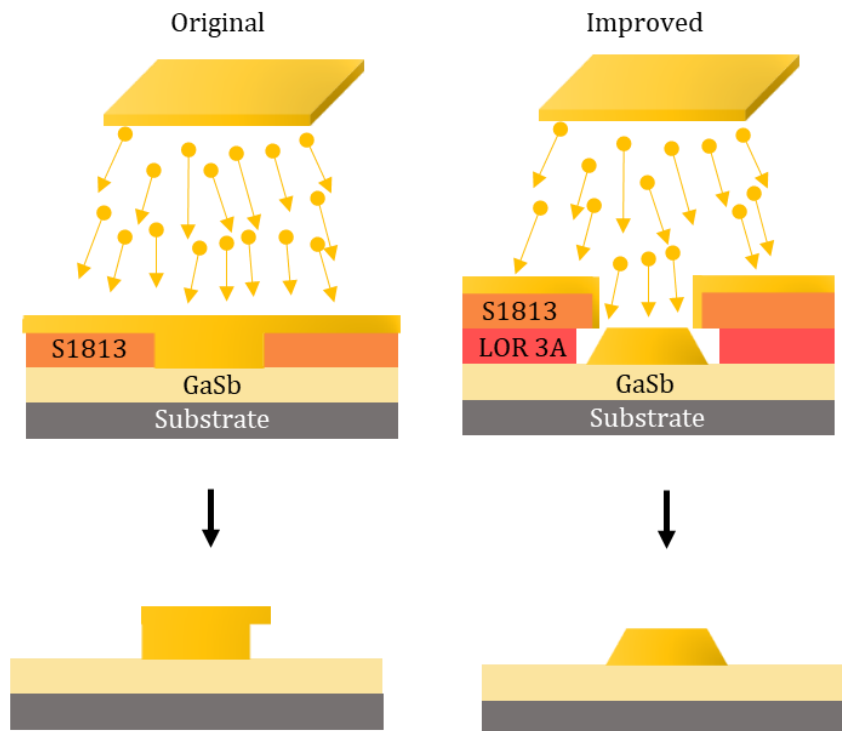


Figure 4.3: A diagram indicating the improved formation of a contact after lift off with the use of a bi-layer resist.

The result of good optical lithography is a well-defined pattern across the sample. This is most easily investigated in the smallest features, such as the exposure tests and alignment marks. The alignment marks are designed to create micron level precision when placing a pattern on top of already defined features, such as aligning the mesa mask to the already defined contacts[77]. If the lithography is unsatisfactory for any reason it can easily be repeated after thorough cleaning, provided no further steps have been taken (such as thermal evaporation). Cleaning of S1813 on top of LOR3A involves bathing the sample in acetone, then developer and finally deionised (DI) water before drying, ensuring to always inspect the surface before starting further processing. The option of cleaning is only preferable for cleanroom tests or if there is a limited amount of material available as complete removal of resist can be challenging.

4.3 Thermal Evaporation

Thermal evaporation is a standard process used for depositing contacts on semiconductor devices. The sample is first prepared for evaporation by further removing any resist in the exposed area by using the plasma asher, where any residual resist is removed and pumped. The sample is then etched to remove any oxide, where this is achieved with a mixture of HCl: H₂O (1: 1) for 35 s before being quenched with water. After preparation,

the sample is placed directly in the evaporation chamber, minimising the time exposed to air. The metal for evaporation is placed within a tungsten wire basket in a chamber below the sample, which is taped to a plate, with a shutter between them. The chamber is shut and pumped to a high vacuum at a pressure of approximately 1×10^{-6} mBar to create a clean environment for evaporation. For deposition of the metal, a current is passed through the wire basket until the metal is hot enough to evaporate, and once a steady current is achieved the shutter is opened until the desired thickness of material is deposited. The appropriate current depends on the density of the material. The shutter is then closed, and the current is reduced[78]. Very low evaporation rates can be recorded purely by the heat of the chamber and so only steady deposition rates above 1 \AA/s should be considered reliable. This is often a consideration with palladium which requires a high current for evaporation. The process is repeated until the desired contact layer combination is obtained. It is often important to allow cooling time between evaporations of different materials to prevent over heating of the resist, where this would distort features made in the lithography phase and potentially over bake the resist preventing easy lift off [73].

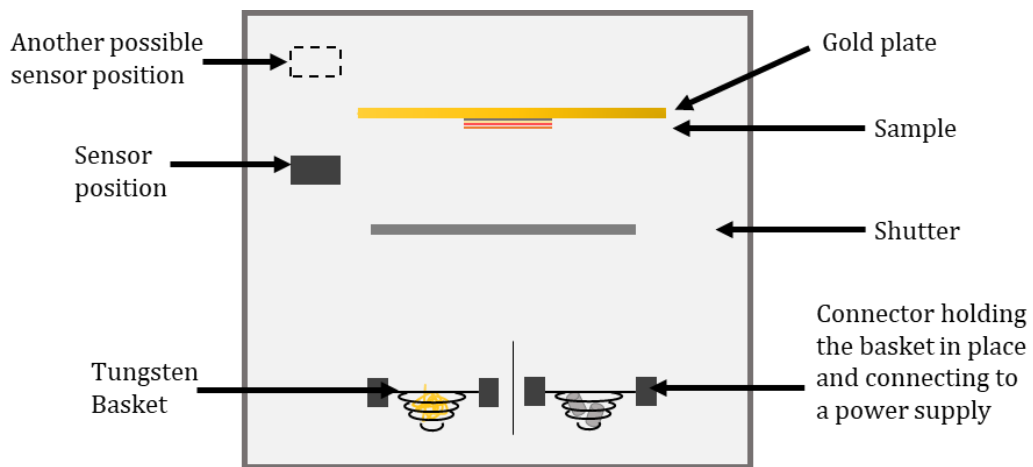


Figure 4.4: A schematic diagram of a thermal evaporator indicating the relevant components for metal evaporation as well as the sensor position.

The evaporation rate and thickness are calculated given the metal parameters (such as density) and tooling in a program which is fed sensor information. The metal parameters are standard values known for most metals and can be found in many databases. The tooling factor, however, is particular to the individual machine and material and was calibrated for each material in this study. Separate tungsten baskets were used for all metals except gold where an alumina coated basket was used, with each basket having

been burnt in before use¹⁰. The evaporation of gold was completed at a high rate for a brief time to prevent significant heating of the resist and sample.

The tooling factor is a parameter that is usually determined by the distance between sensor and the sample, but can also take into account many other factors. The sensor is made up of a quartz crystal between electrodes. An AC voltage is applied across the electrodes and the crystal oscillates, the frequency will then change when material is deposited onto the crystal, thus allowing a measurement of thickness. This correction factor adjusts for the thickness of material deposited on the sample rather than the sensor. In order to accurately measure this parameter a series of 100 nm depositions must be made and measured using a surface profiler. The tooling parameter may be obtained using equation 4.2, where T_{New} is the resultant tooling percentage, T_{Initial} is the original tooling percentage, h_{Measured} is the measured contact height and h_{Target} is the target contact height.

$$T_{\text{New}} = T_{\text{Initial}} \frac{h_{\text{Measured}}}{h_{\text{Target}}}. \quad 4.2$$

In the case of indium, a slightly altered approach was taken, as deposited pure indium is malleable and will be scribed by the surface profiling needle, obscuring any results. Consequently, 20 nm of previously calibrated gold was deposited on top of the indium.

Three trials were performed for each material, in each case resulting in a tooling percentage of $(120 \pm 2) \%$ for indium and $(90 \pm 3) \%$ for palladium.

Once the metal was deposited, the samples were removed from the evaporator and placed in acetone for 5 minutes to remove the excess unwanted metal. The majority of the excess gold and resist were seen as flakes in the beaker. To remove any remaining excess gold, a pipette was put in the beaker and squeezed releasing bubbles, encouraging further removal. The sample was then taken and placed in developer for 60 s and finally quenched with DI water and blow-dried with nitrogen.

The contacting recipe used for *n*-type GaSb in this work was Pd/In/Pd/Au with thicknesses of 5/40/5/100 nm, following the work of Robinson *et al.* [79]. Gold is often used as an upper metal layer as it doesn't easily oxidise and is inert in reactions with many chemicals, it is also ductile and easy to bond to [80] [16, 73].

¹⁰ "Burning in" is a process where a basket is heated to evaporation temperatures without any material in it before being used for evaporation. This essentially burns off any unwanted debris on the surface of the basket.

Annealing is a process by which contacts are heated to improve the contacting quality by inter-diffusing the metal with the semiconductor allowing for further adhesion and in certain cases, lightly doping the surface of the semiconductor [80]. The intermixing of metals can be controlled using multilayer contacts by the varying of thicknesses of each layer, as well as by controlling annealing times and temperatures. A more thorough description of the contact deposition and the effects of annealing will be given in the next chapter.

4.4 Etching

Etching in this work was mainly used for electrical isolation of devices. Hydrofluoric acid (HF) was used with a HF:H₂O₂:H₂O:C₆H₈O₇ (1:10:67:300) recipe which had an etch rate of 1 μm/min. The use of HF acid was limited to specially trained users due to the associated dangers of this acid and as such was in general carried out by Dr Adam Craig and was only observed by myself. The samples were each checked using the surface profiler to monitor etch depth with the main concern during etching not to completely separate the legs of the contacts from the body of the Hall bar.

Initially, the citric acid (C₆H₈O₇) was mixed by adding 70 g of citric acid powder to 70 ml of DI water, thoroughly stirring the mixture until the powder is completely dissolved. HF in the form of buffer oxide etch (BOE) was used where HF is 20 % of the BOE. All equipment that is in contact with HF must be plastic as HF will dissolve glass, and in general the acid should always be added to the water or to the more dilute solution to avoid excess heating.

A mixture of HCl: H₂O₂: H₂O (1: 1: 5) could also be used to etch GaSb. While this may be a safer option, it provides an unreliable etch rate and creates rough surfaces.

Finally, the Hall bars are cleaned of resist and cleaved. The cleaving was done by hand using a scribing pen and a magnifying glass with the aid of the metal guidelines which were placed on the perimeter of each chip, shown on the mask in Figure 4.6.

4.5 Bonding

The Hall bar samples were packaged and bonded to a standard 28 contact chip carrier shown in Figure 4.5. This was achieved by dotting conducting silver paint to the base of the chip carrier and carefully placing the sample on top. To bond fine gold wires to the

sample once the paint is set, equal weights of epoxy part A and epoxy part B were mixed on a glass slide to produce a viscous liquid. Fine gold wire was held in place on top of a Hall bar contact pad and epoxy was applied to attach the end of the wire to the contact. This was repeated for all contacts. The wires were then shaped to reach the chip carrier pads and the gold wire pressed into the pad, creating a mechanical bond. The epoxy or silver paint was then used to seal this bond.

A similar method was also used for any samples measured using the van der Pauw method that were measured in the cryostat. The cleaned wafer was first dotted in each corner using indium solder and a fine tipped soldering iron. Gold wire was then placed over the solder which is then reheated, submerging the wire. There are only four contacts in the van der Pauw formation and all need to be functioning, so to allow for some redundancy, two gold wires were bonded to each indium dot.

In the case of the bulk study van der Pauw samples that were only studied at room temperature, a chip board was used instead of a chip carrier, and indium solder was used on both the sample and the board.

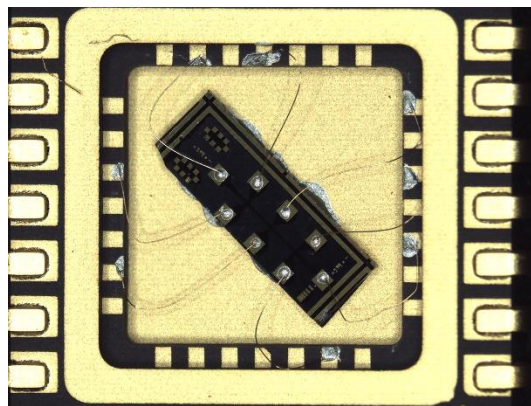


Figure 4.5: A picture showing the chip carrier for a Hall bar used in the temperature dependent set up, shown to aid the bonding description.

4.6 Mask Creation

The Hall bar mask used for photolithography was designed in KLayout and the patterns defined in chromium on a plate made of quartz [81]. The mask is split into four sections, with two contacting mask patterns and two mesa mask patterns.

The contacting mask consists of the contact pad definitions for the various size Hall bars, TLM patterns for contact resistance measurements and guidelines defining the perimeter of each chip. The size of the chips were defined by the chip carriers and had to be comfortably under 5 mm in either direction. The chip carriers also have 28 contact pads

and so each chip was designed to contain three devices (so 24 contacts). Finally, the alignment marks were subtly changed depending on which pattern would be defined first to allow for easier alignment in the subsequent photolithography step.

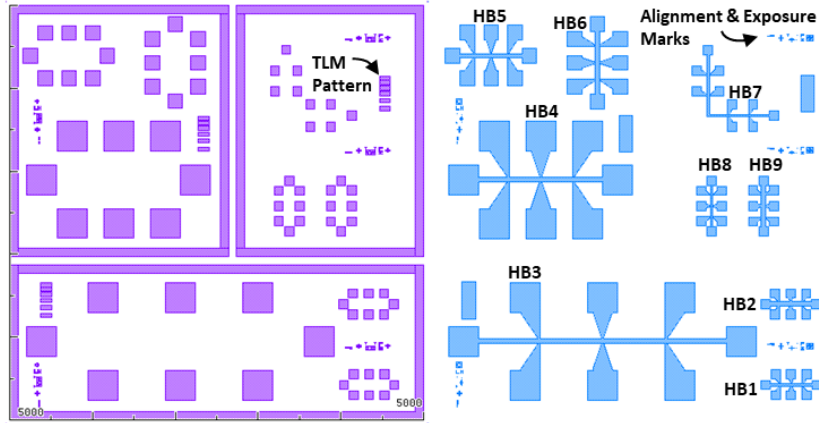


Figure 4.6: Contact and mesa mask unit cell design. The cell has three chips, each with three Hall bars surrounded by gold guidelines. The total repeated pattern has an area of 5 mm^2 . The Hall bars and certain other features have been annotated for reference in this work in black.

The mesa mask defines all the semiconductor area to be isolated, where anything not protected by the mask will be etched to the insulating substrate. All features on the mask must allow for an etching buffer, where for example if a $5 \mu\text{m} \times 5 \mu\text{m}$ square shape is desired, but an isolation etch of $1 \mu\text{m}$ depth is required, the square on the mask must be made $7 \mu\text{m} \times 7 \mu\text{m}$.

Several Hall bar designs were created, consisting of various sizes, aspect ratios and directions, in order to investigate distinctions in carrier properties with respect to geometrical factors. The full list of designs is given in Table 4.2. Contact pads were made suitably large on all devices to allow for bonding.

Table 4.2: Dimensions of all Hall bar designs created on the Hall bar mask, labelled following the mask shown in Figure 4.6. The smallest aspect ratio is defined as the aspect ratio between neighbouring contacts.

	Length (mm)	Width (μm)	Orientation	Smallest Aspect Ratio
HB1	0.50	25	Horizontal	5.2
HB2	0.50	50	Horizontal	2.7
HB3	3.00	50	Horizontal	15.2
HB4	1.50	50	Horizontal	7.7
HB5	0.75	50	Horizontal	3.9
HB6	0.75	50	Vertical	3.9
HB7	1.50	25	L-shape	5.0
HB8	0.50	25	Vertical	2.7
HB9	0.50	50	Vertical	5.2

4.7 Summary

Each sample to be processed was initially cleaved to an appropriate size and then cleaned using acetone and IPA. The sample at each step was investigated optically to monitor the progress of the fabrication. The samples were first spin coated with bi-layer resist, each layer is spun and baked, then the edges were exposed for removal of the edge bead. The sample was then developed and again exposed in the Hall bar mask contact pattern and then again developed. Once the lithography was deemed suitable, the sample was prepared for thermal evaporation. The sample was exposed to an oxygen plasma to further remove any resist and then the sample was etched using HCl and H₂O to remove any oxide. The sample was placed in the thermal evaporator and the contacting metal was deposited. The sample was then removed from the evaporator, where it was then placed in a beaker of acetone for lift off. The resist was removed and just the desired pattern remains. The sample is again spin coated, this time with a single layer resist where the resist is then baked. The sample edges are exposed and developed to again remove edge bead and then is exposed in the mesa mask pattern and developed. Finally, the sample was etched to the substrate and cleaned before being removed from the clean room and bonded for measurement.

“There is no problem so bad that you can’t make it worse.”

- Chris Hadfield

Chapter 5

Characterising Metal-Semiconductor Interfaces

Fundamentally, metal-semiconductor interfaces govern the integration of any semiconductor structure into a circuit where it is then electrically measured. This is not only of significance for electrical measurement but for the application of electrical, optical and excitonic devices (e.g. LEDs, lasers and more). Metallisation recipes tend to be classified as either Schottky, where there is a barrier between the metal-semiconductor junction, or ohmic where there is not; each of which have their uses. Schottky contacts can be used if there is a need for applying a voltage but no current, whereas ohmic contacts allow current to pass. Currently in n -GaSb (and its alloys) the metallisation recipes are indeterminate and there appears to be no standard for ohmic contacts.

In this chapter the theory behind contacting is discussed and a literature review of the current status will be given. Following this, a description of the metallisation study performed on n -Al_{0.2}Ga_{0.8}Sb is given, where the aim was to produce a low resistance (ideally ohmic) interface, which could be used in this work to accurately determine the transport properties.

5.1 Contacting Theory

For many devices, ideally, the current would flow freely through the contact as if through a resistor, with the current directly proportional to the constant contact resistance R_c of an ohmic contact. A Schottky barrier, however, behaves much like a diode, only allowing free current flow in one direction [82]. The differences between these two very different behaviours are commonly described by the Schottky model and are due to the interface of

the metal and the semiconductor, and the energy interactions between them. On the metal side of the interface the important parameter is the work function, ϕ_m , which is the energy required to completely free an electron from the metal to free space [51]. For the semiconductor side of the interface, the electron affinity, χ_s , the energy difference between the conduction band and free space, is considered [27].

As the metal and semiconductor are brought together, the Fermi level of the semiconductor is aligned to the Fermi level of the metal. This occurs due to electron exchange between the two materials, where the metal electron energy levels are seemingly unchanged due to the high concentration of electrons. In the semiconductor, the width affected by this transfer of charge becomes a depletion region[83].

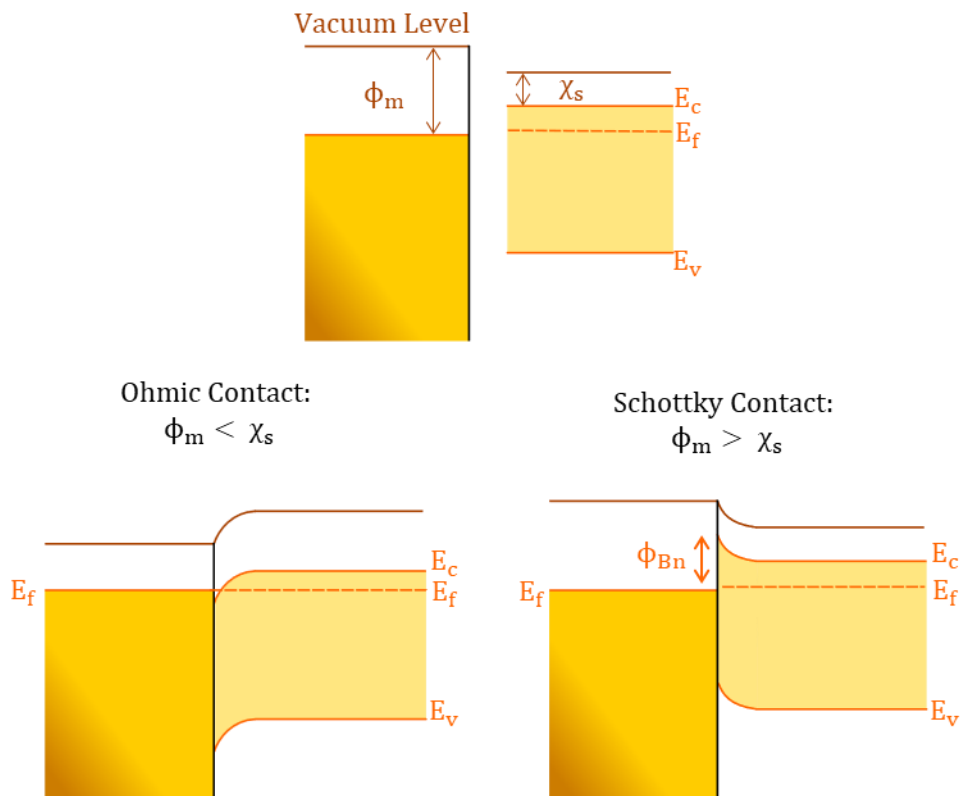


Figure 5.1: A figure showing a separate metal and semiconductor, then the band structure alignment after the joining of these two materials when $\phi_m < \chi_s$ and when $\phi_m > \chi_s$.

In the case where the electron work function is larger than the electron affinity, the electrons in the semiconductor will flow into the metal creating a negatively charged metal and a positive charge in the semiconductor. The barrier height between the Fermi level of the semiconductor and the top of the conduction band, ϕ_{Bn} is a Schottky barrier and can be described by equation 5.1, giving

$$\phi_{Bn} = \phi_m - \chi_s \quad 5.1$$

When practically measuring across a Schottky barrier, a forward bias acts to reduce the barrier of the Schottky contact whereas a reverse bias acts to increase it [84]. In the opposing case where the work function is small, the opposite occurs, with a negative band bending, see Figure 5.1, where this forms an ohmic contact, allowing electrons to flow freely in both directions across the interface [85].

Though this Schottky model very simply describes the formation of a Schottky barrier, it is not always accurate at predicting the barrier heights that are experimentally measured [51, 80]. Instead the Bardeen model and the unified defect model should be considered for more accurate predictions [16, 51]. The unified defect model states that the heat of joining a metal to a semiconductor breaks bonds and creates native point defects at the surface of the semiconductor [86]. The electronic states associated with these native point defects pin the Fermi level at the surface, making the Schottky barrier height independent of the choice of metal. The Bardeen model is then used to predict the pinning, and states that surface states of a semiconductor will pin the Fermi level at $E_g/3$, creating a barrier height of $\phi_{Bn} = 2E_g/3$, texts such as *“Surface states and barrier height of metal-semiconductor systems”* and *“microelectronic materials”* discuss the finer details of the Bardeen and unified defect models [51, 87]. In general, covalently bonded semiconductors such as GaSb and GaAs have high electronic surface state concentrations and so Schottky barrier heights are quite invariant to the work function of the metal. More ionically bonded semiconductors, however, have a lower electronic state concentration and so there is (theoretically) no Fermi level pinning and the Schottky model is used [84].

This, however, indicates that for any covalently bonded semiconductor, a Schottky barrier is inevitable. With this Bardeen model, GaSb would be expected to have a barrier height of ~ 0.48 eV at room temperature. There are a few methods of reducing the effect of this high barrier, such as by reducing the barrier height, encouraging thermionic emission (conduction over the top of the barrier), or thinning of the barrier, encouraging quantum tunnelling (through the barrier). The experimental barrier height of any interface will in reality also depend on a number of external factors including the oxide on the surface of the semiconductor [88] [51].

Considering the effect of temperature on the barrier height, the Fermi level pinning will occur for all temperature, implying that as the energy gap changes with temperature (see equation 2.6, in section 2.1.2), the barrier height will also change. To make an estimation of the resistance change expected for this temperature dependence would involve making assumptions based on the type of current flowing through the barrier, and even if purely

thermionic current is assumed, there is a complicated temperature relationship. This relationship also does not include other temperature dependent components such as the energy gap and the effective mass. The depth of this analysis is out of the scope of this PhD but would be of interest to all *n*-GaSb devices. Though a good ohmic contact and associated properties would be preferable, this study aims to merely produce a metallisation recipe that produces measurable transport devices at low temperatures.

Initially the contacting recipe used for *n*-type GaSb contacts fabricated in this work consisted of Pd/In/Pd/Au, 5/40/6/100 nm as deposited (not annealed), where Pd is deposited first, following the work of Robinson *et al.* [79]. The Hall bar contacts of this recipe fabricated for transport measurements proved insufficient and unmeasurable at low temperature, with these contacts found to be of high resistance with a non-consistent I-V trace. Transmission line tests, described in section 5.3, were carried out, and when tested against temperature, the contacts became highly resistive, limiting further measurements below 150 K. This temperature is insufficient for the measurements required to extract the transport properties of the bulk GaSb and GaSb/AlGaSb structures as described in Chapter 7. Thus, an investigation into various metallisation recipes and the underlying theory was carried out. Several different metallisation's were investigated, with and without annealing, the results of which are explained in section 5.4.

5.2 A Review of Contacting Materials for *n*-GaSb

There have been vast numbers of works investigating the ohmic properties of contacts on *n*-type GaSb, with reports often stating non-reliable or rectifying contact behaviour, with few yielding reliable, low resistance ohmic contacts. Many of the recently reported ohmic contacting recipes involve multilayer contacts with the inclusion of impractical metals such as platinum¹¹. Platinum is often used as a buffer or blocking layer between gold and the sample, required as gold can form reaction layers between 100-850 nm into the semiconductor depending on annealing conditions, which can lead to an unstable device [89]. Indium can be used to reduce the barrier height by creating an InGaSb layer which has a lower band gap than pure GaSb. It has been reported by Yang *et al.* that layers such as these can extend to 100 nm or more into the sample [90].

¹¹The boiling point of platinum is approximately 3825 °C and the melting point of tungsten, which is used as the metal crucible for evaporation, is 3422 °C. Therefore, the tungsten basket will likely melt before the platinum evaporates. Even with the reduced pressure in the evaporator this is a fine line.

Dopant can be used to thin the barrier, and often the same dopant that was used in the growth stage would be used [79]. Tellurium dopant was used by Villemain *et al.*, and has previously shown some success in contacting [91]. Villemain *et al.* investigated Te/Au recipes with varying thicknesses, using secondary-ion mass spectrometry (SIMS) measurements to evaluate the intermixing with annealing time and temperature. They illustrated that, after an initial anneal of 350 °C for 1 hour, the tellurium had diffused into the sample. After a further anneal of 450 °C for 2 s, interface alloying was achieved with significant Ga and Sb measured in the contact at the interface. It was this alloying that they believe lead to low contact resistances.

Subekti *et al.* reported ohmic contacts achieved for contact metal mixtures of AuGe and AuNiGe, as well as AuNiGe/Au (i.e. with a subsequent layer of Au deposited) [92]. These were ohmic provided that the annealing temperature was above 150 °C, and the specific contact resistance had a minimum at an annealing temperature of ~300 °C for the first contact and 200 °C for the final two contacts. In this work, Subekti *et al.* also analysed the specific contact resistances to extract the Schottky barrier height. This analysis resulted in a barrier height of ~0.49 eV for the as deposited recipe, which is the expected barrier height for GaSb using the Bardeen model. They suggest that the exchange between germanium and gallium is the key to the rapid decrease in specific contact resistance with annealing temperature, but do not suggest a reason why further annealing then increases the specific contact resistance.

Khvostikov *et al.* [88] also investigated recipes containing gold and nickel, all of which were tried for two doping concentrations ($4 \times 10^{17} \text{ cm}^{-3}$ and $1 \times 10^{18} \text{ cm}^{-3}$), and with a variety of annealing profiles. For both doping concentrations, the specific contact resistance improved with increased annealing temperature from 230°C to 300°C. Further, the higher doping concentration gave a lower specific contact resistance at each annealing temperature, however the difference in resistance between the two doping levels diverged at higher annealing temperatures (i.e. the higher doped sample improved more from 270°C to 300°C than the lower doped sample). The lowest specific contact resistance was achieved for high doping and Au/Ni/Au at 300°C.

Yang *et al.* [93] investigated a contact combination of indium and tellurium with a recipe of Pd/Te/Pd/In/Au, which attempted to simultaneously lower the barrier by creating InGaSb, using Te to *n*-dope the surface, and using the Au-Ga interaction to create Ga sites for Te to dope within the surface. Despite this complicated recipe, simpler recipes with

fewer metals also gave comparable results, as discussed below. Huang [94] and Vogt [95] also tried similar multilayer recipes but included a platinum blocking layer.

Robinson *et al.* [79] investigated a variety of palladium-based recipes, with increasing complexity and was the initial recipe trialled in this work for contacts for the measurement of transport properties of *n*-AlGaSb/GaSb heterostructures. However, of the many recipes attempted by Robinson, only the many layered recipes resulted in deposited ohmic contact, and of these, the preferred contacting recipe (lowest contact resistance) was found to be Pd/In/Pd/Pt/Au (4/40.3/5.7/50/100 nm). For this recipe, annealing was found to greatly improve the resistance, with the palladium believed to act as a blocking layer, partially limiting the amount of indium diffusing through the contact. Robinson *et al.*'s original recipe also contained a platinum layer to prevent an Au/GaSb reaction layer, however when recreated for our study, due to limitations of the evaporator and the impracticality of depositing platinum, this layer was removed.

When considering the variation between contact resistances obtained in this work, and those reported in the literature, some of the variation may be due to the literature values, in general, reported for contacts to *n*-type GaSb with carrier concentrations as high as $1 \times 10^{18} \text{ cm}^{-3}$. The samples studied here are not as severely doped at the surface and so may not yield the same numerical result.

5.3 Determining Contact Resistance

Many parameters can be very easily determined from seemingly simple electrical measurements, such as the contact resistance, the sheet resistance and the transfer length, with the measurement of these values unlocking a large wealth of information. The following sections discuss these parameters and the methods used to determine them.

Whenever the resistance of a semiconductor sample, R_{Total} , is measured through a 2-probe measurement, the resistance measured is given by the equation

$$R_{\text{Total}} = 2R_c + R_s, \quad 5.2$$

where R_c is the contact resistance (simplified here to encompass the resistance of the metal as well as the metal-contact interface) and R_s is the resistance of the semiconductor. When a resistance is measured under different conditions (e.g. as a function of temperature), it is important to determine whether the changes in resistance measured are due to the semiconductor or to the contact. The resistance of the semiconductor is a

function of the sheet resistance, R_{\square} , and the aspect ratio of the current path, see Figure 5.2, where S is the separation length between the contacts and W_c is the width of the current carrying path (often the width of the contacts)[96]. This ratio determines the number of “squares” in the semiconductor being measured, with the semiconductor resistance then given by

$$R_s = R_{\square} \frac{S}{W_c}. \quad 5.3$$

The specific contact resistance, ρ_c is a parameter used for comparing the quality of contacting materials [97]. The standard method for determining specific contact resistance is through transmission line measurements (TLMs). A set of equally sized identical contacts, in this case $50 \mu\text{m} \times 130 \mu\text{m}$, are spaced at varying separations from each other, with the resistance measured between each pair of contacts, and plotted against the separation, S . A simple combination of equations 5.2 and 5.3 results in the straight line seen in Figure 5.2, where at the y -intercept, the separation is zero, giving twice the contact resistance [98, 99].

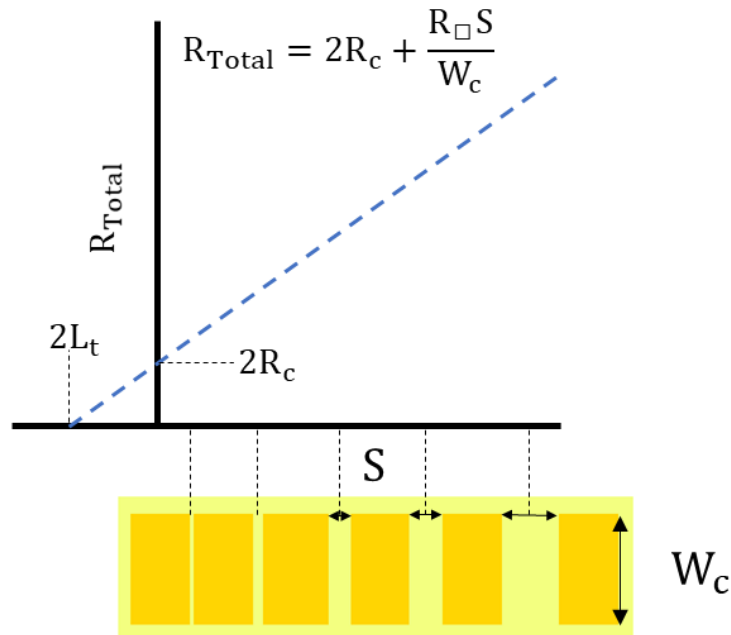


Figure 5.2: A demonstration of transmission line measurement geometry and the graphical analysis that can be conducted.

The specific contact resistance, ρ_c , can then be found by extrapolating to the x -intercept to find the transfer or transmission length, L_t , and using equation 5.4, giving

$$\rho_c = L_t R_c W_c. \quad 5.4$$

Current will mainly flow through the shortest path (to the closest edge of the contact), however there will be some current paths flowing further through the semiconductor

before entering the contact. This current distance relationship follows an exponential drop off, where the decay constant is the reciprocal transfer length. Alternatively, the transfer length is also often defined as the average length a carrier will move underneath the contact before flowing up into the contact [96].

Another way of measuring the specific contact resistance is by comparison to a 4-probe measurement, where a 4-probe measurement can be considered to be a direct measurement of the sheet resistance. Thus, by comparing to equation 5.2, the contact resistance can be found, where the contacts are considered identical.

5.4 Characterization of Metal Contacts on n-GaSb

Using the TLM method explained above, various metallisation recipes for *n*-GaSb were characterised. However, it became apparent that the assumption of the contacts all having ohmic behaviour was not always the case. This resulted in a re-evaluation of the objectives for this study, where these are outlined in the following section, after which the results and analysis will be discussed.

5.4.1 Aims for Contact Resistance

The measurements required to study the transport properties of *n*-AlGaSb/GaSb devices require a constant current supplied between two contacts, and voltage measured through two others. Therefore, there are two applications for the contacts created, and as these are 4-point measurements, in theory it is irrelevant whether these are ohmic or Schottky, provided they are low enough resistance that the measurement can be achieved.

Initial measurements of Hall devices yielded unsuccessful results which were deduced to be limited by the contact resistance. Though measurable (but still high resistance) at room temperature, the total resistance measured drastically increased as the temperature decreased, and below 150 K the samples were unmeasurable, with resistances of the order of 1000 k Ω 's. The same wafer was successfully measured using the van der Pauw method with indium dotting, confirming that a lack of carriers was not the cause of the high resistances observed. Though this method allowed the measurement of these samples, In dotting is impractical on the scale of the Hall bars. The samples were also inspected to ensure the devices were not over etched, and that there was a clear current path for the current contacts, and the legs to the voltage contacts were also still intact. It is believed that due to the high resistance of the contacts, the small constant current was unable to be maintained at lower temperatures.

The AC set up uses a lock-in amplifier which sets a voltage V_{Ref} and is put in series with a large resistor, R_L (typically $1\text{ M}\Omega$), so that the majority of the voltage drop is across this resistor, such that the current through the sample is assumed to be V_{Ref}/R_L . This assumption can no longer be made once the sample and contacts make up a significant fraction of the large resistor. The size of the large resistor in series could be increased to ensure this assumption is correct, however, the current path is still of question.

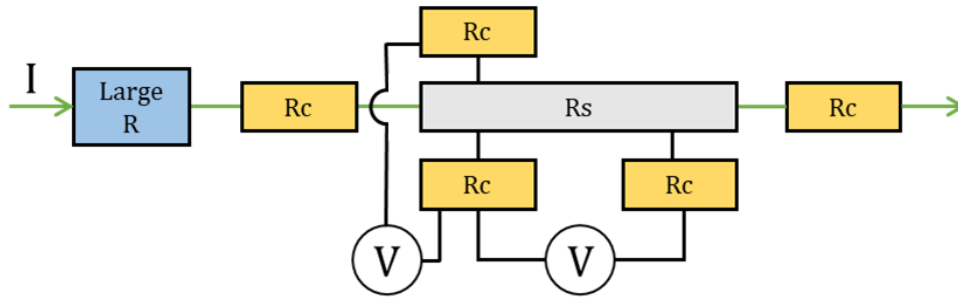


Figure 5.3: A schematic diagram of the resistances involved in measuring a Hall bar for the determination of transport properties. The ideal current path is shown in green.

The input impedance of the lock-in measuring the voltage is $10\text{ M}\Omega$, so again, once the resistance of the sample and contacts (and variation between contacts) is of a significant fraction of the impedance, the current could be split across this path. Therefore, the assumption that there is negligible current flowing through the voltmeter, a standard assumption in electrical measurement, is no longer necessarily true. Even if a higher impedance voltmeter is used such as a Keithley Nanovoltmeter, the current paths at such high resistance are unpredictable. If a Keithley were to be used, the advantage of the high signal-to-noise ratios given by an AC lock-in amplifier would be lost, increasing the uncertainty in an already sensitive measurement.

The objective of this study is to enable measurement of devices, though a low specific contact resistance is preferable, it is not necessary. As such any recipe which yields a low enough resistance at low temperature to maintain a constant current of $\sim 1\text{ }\mu\text{A}$ is sufficient.

5.4.2 Recipes Tested

A few recipes were trialled to find a suitable ohmic contact for use with confined $n\text{-AlGaSb/GaSb}$ systems to be measured at low temperatures, given as stated above the initial test was unsuccessful with a recipe of Pd/In/Pd/Au as deposited.

Four recipes were investigated, each annealed and as deposited, and in each case the processing procedure was the same. Using the same Hall bar mask, TLM pad designs were produced through lithography following the process steps given in section 4.2, where the

TLM pads were each $50\ \mu\text{m} \times 130\ \mu\text{m}$ with increasing spacings of $5\ \mu\text{m}$, $10\ \mu\text{m}$, $20\ \mu\text{m}$, $30\ \mu\text{m}$ and $50\ \mu\text{m}$. All samples were processed in the same processing run and on the same wafer. The samples were then placed in a PlasmaEtch Asher with an oxygen plasma for 1 min to rid the surface of any remaining resist, in preparation for the contacts. The samples were then etched using a recipe of HCl:H₂O (1:1) for 45 s to remove the oxide from the surface, quenched with water, and placed into the evaporator immediately (within a few mins), preventing further oxide forming. Each metallisation was carried out using the same evaporator with a base pressure of $\sim 1 \times 10^{-6}$ Torr. Upon completion of the recipe, lift off was achieved in all cases easily, following the procedure as described in section 4.2. Each recipe was tested as deposited onto MBE grown doped n-AlGaSb of $2\ \mu\text{m}$, where the sample chuck for evaporation of the metal is not at all heated. Annealing was achieved using an Allwin AW610 Rapid Thermal Annealer, where samples were placed in the centre of a heated chamber and once the heating cycle was complete, left to cool in situ in nitrogen gas. Between each sample the chamber was left to cool to ensure a full heat cycle for each sample. The annealing times and temperatures were set as an automatic profile and were also measured in real time; there was no significant deviation seen between the two during any of the processes. A full table of the recipes trialled is given below.

Table 5.1: A table showing the contact recipes tested and their associated annealing recipes.

Materials	Thicknesses (nm)	Annealing Time	Annealing Temperature (°C)
In	400	10 s	290
In/Au	100/100	10 s	290
Au/Ni/Au	10/50/200	2 min	300
Pd/In/Pd/Au	4/41/6/100	10 min	300

A pure indium recipe was used for testing initial growth material using the van der Pauw method using indium solder. These yielded low resistance contacts and the samples were measurable at low temperatures, however this was not feasible on the small scale of Hall bar devices. The pure indium metallisation recipe was an attempted recreation of that process, where the annealing temperature is the temperature of the soldering iron. In/Au was a recreation of the In recipe but including a layer of Au to give an easier surface to bond to as the indium was visibly rough on the surface after lift-off. Au/Ni/Au and Pd/In/Pd/Au were trialled following recipes given in the literature by Khvostikov *et al.*

[88] and Robinson *et al.* [79] respectively. Khvostikov *et al.* was chosen as they displayed successful results for multiple doping concentrations.

Each sample was measured using a 2-probe probe-station with a 2450 Keithley source meter. The probe station also has the capability of being cooled to 77 K using liquid nitrogen, with the sample placed in a vacuum chamber capable of reaching a pressure of $\sim 1 \times 10^{-6}$ Torr. Probes were placed on each TLM pad pair, with an applied voltage swept between ± 2 V with the current measured. After initial testing at room temperature the samples were cooled to 77 K and the temperature was stabilised. The samples were then measured and heated using the chuck, with measurements across temperature only performed when the set temperature had stabilised. Each TLM pad pair was measured 3 times by re-probing the contacts.

In all cases annealing reduced the resistance of the contacts for each recipe by more than an order of magnitude, though in all cases the I-V traces are clearly non-ohmic to varying degrees. Figure 5.4 shows an example of each of the I-V traces at room temperature, and how they varied from as deposited to annealed; the reader should note the change in scale of the y axis on each graph, particularly from the as deposited recipes (left) to the annealed equivalent (right). An average trace was picked for each case though in some cases there was variation in the characteristics and resistances between TLM pad pairs.

The resistance was taken for each recipe for each TLM pad pair for comparison, where this was determined from the higher voltage range where the Schottky contacts are in forward bias mode, and where the electrons are freely flowing and the barrier has been overcome. The resistance was taken to be the reciprocal gradient in this region. When linear fitting, a fitting parameter called the coefficient of determination or R^2 can be used as an estimation of the linear fit. R^2 it is a value between 0 and 1 that is a ratio of the controlled (predicted) variation of your data over the total variation of your data. A value of $R^2 = 1.0$ indicates that all the variation in y is predicted by the fit. The R^2 value in this case gives an estimation of how ohmic the contacts behave once the barrier is overcome, and, in most cases, the R^2 value is close to 1.0 in the annealed case.

The In and In/Au recipes, once annealed, created quite well defined back to back Schottky contact I-V traces, whereas Au/Ni/Au recipe trace is not clearly either ohmic or Schottky. The Pd/In/Pd/Au trace, though not perfectly ohmic, appears to be a more easily overcome Schottky barrier. The unusual Au/Ni/Au trace may be due to an uneven diffusion of Ni and Au, creating a combination of ohmic and Schottky contacts in parallel and series, with varying resistances and current densities, creating an undefined I-V trace. All the as

deposited metallisation recipes created unideal Schottky pairs of significant resistance in comparison to the annealed recipes, so they will be dropped from this study from this point. The reader should note that they were still measured and continued to be of high resistance, and as such, the results will not be presented here.

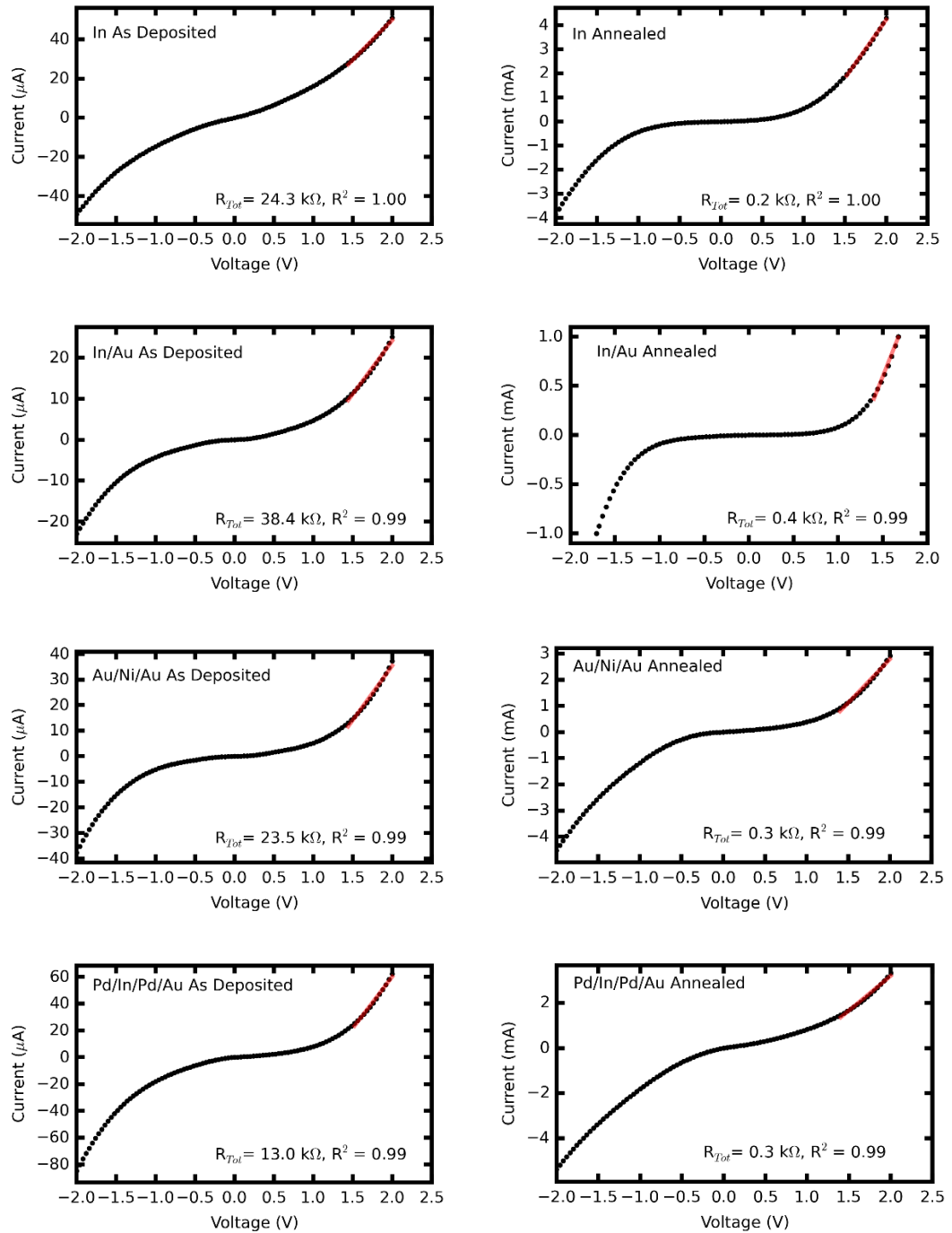


Figure 5.4: Example I-V characteristics for each metal recipe investigated shown at 300K. Black points indicate the measured points from a current voltage sweep and the red line indicates the fit line used to extract a resistance (see the text for further details).

This work shows that it is not merely the diffusion of indium that creates a low resistance contact. The palladium blocking layer allowing only a certain amount of indium to diffuse must be key to this process. The drastic difference in the contact resistance depending on the amount of indium diffused into the semiconductor may in part be due to indium diffusing under the contact, lowering the conduction band edge locally, but obviously giving no change in any region where there is no contact. This would therefore create a junction between these semiconducting regions which may also create a barrier, particularly if a significant proportion of In has been diffused. As an example of the difference diffusing indium into GaSb may make, using Vegard's law (equation 2.24) the difference in band gap between GaSb and (e.g.) even $\text{In}_{0.1}\text{Ga}_{0.9}\text{Sb}$ is 60 meV at 300 K. This is more than $2kT$ and would create a significant barrier between the regions under the contact and the rest of the device.

5.4.3 Ohmicity

As seen above, the contacts produced are non ohmic, but to varying degrees. If a contact were ohmic, the resistance would be invariant across voltage. As a test of the ohmicity of the contacts, the resistance was determined using a few methods, and the similarity of the resistances should shed light on how ohmic or non-ohmic the contact is.

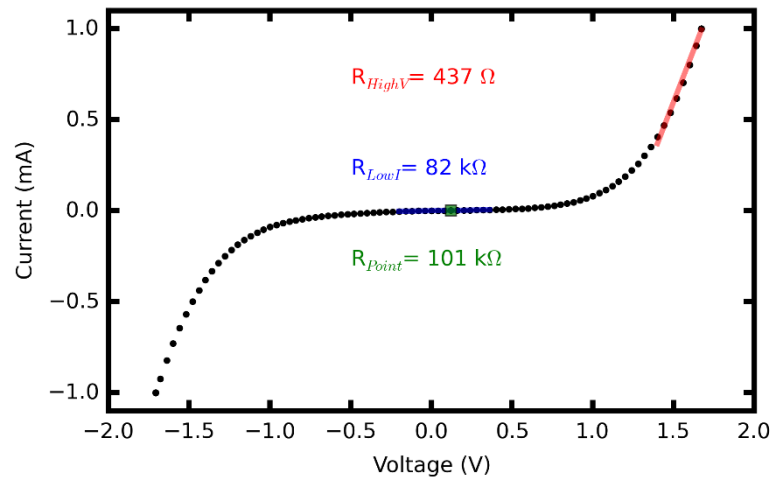


Figure 5.5: A graph of voltage against current for a Schottky contact indicating the significant variation in resistance when it is taken from differing regions of the traces, whereas in a perfectly ohmic case all resistances are equal.

The first method as shown above is the high voltage method, measuring only once the Schottky barrier was overcome, where this method will give more similar values when comparing to the literature. However, in the measurement set up used in this work, a constant current of $1 \mu\text{A}$ is maintained and thus, given the non-ohmic nature of the

contacts, taking the resistance from high voltage range is not satisfactory for the objective in this study. The two other methods of determining the resistance are taking the resistance at a current of 1 μA , and taking the local resistance around 0 (i.e. the resistance in a low current range on the order of $\pm 2\mu\text{A}$).

Table 5.2: A table showing resistance calculated over different ranges for each contacting recipe to 2 significant figures, and the ratio $R_{\text{Point}}/R_{\text{HighV}}$, to 1 decimal place. All values taken at 300 K.

Contact Types	High voltage range Resistance (Ω)	Low current range $\pm 2\mu\text{A}$ Resistance (Ω)	Point Resistance (Ω)	$\frac{R_{\text{Point}}}{R_{\text{HighV}}}$
In	240	9300	9300	38.8
In/Au	440	82000*	100000	203.5
Au/Ni/Au	300	6300	6500	21.5
Pd/In/Pd/Au	260	530	520	2.0

* The trace even on this small range was not linear.

Unsurprisingly the low current resistance and the point resistance are similar and are both of higher resistance than the high voltage range resistance. The ratio of the high resistance range and the point resistance indicates the extent of the non-ohmic behaviour.

Indium in the high voltage range gave the lowest resistance however the high voltage resistance is not representative of the desired measurement set up. In/Au, given that it created a well-defined Schottky, predictably is the least ohmic and even on the small scale of $\pm 2\mu\text{A}$ had a low R^2 value of 0.96. From Table 5.2 it can be seen that the recipe of Pd/In/Pd/Au, for this trace, gave a more ohmic contact and was the lowest resistance in the region used for measurement.

5.4.4 Determination of Contact Resistance

The resistance measured from a current voltage sweep is the total resistance of the sample and contacts, though as stated above, a TLM pattern can be used to determine the contact resistance. However, this assumes the metal-semiconductor interface is ohmic, which is clearly not the case.

The low current resistance was measured for each TLM pair and plotted against separation (Figure 5.6), with a straight-line fit used to extract the specific contact

resistance. However, it became evident that where contacts are non-ohmic, the resistances measured were inconsistent and as such the TLM extracted values become unphysical.

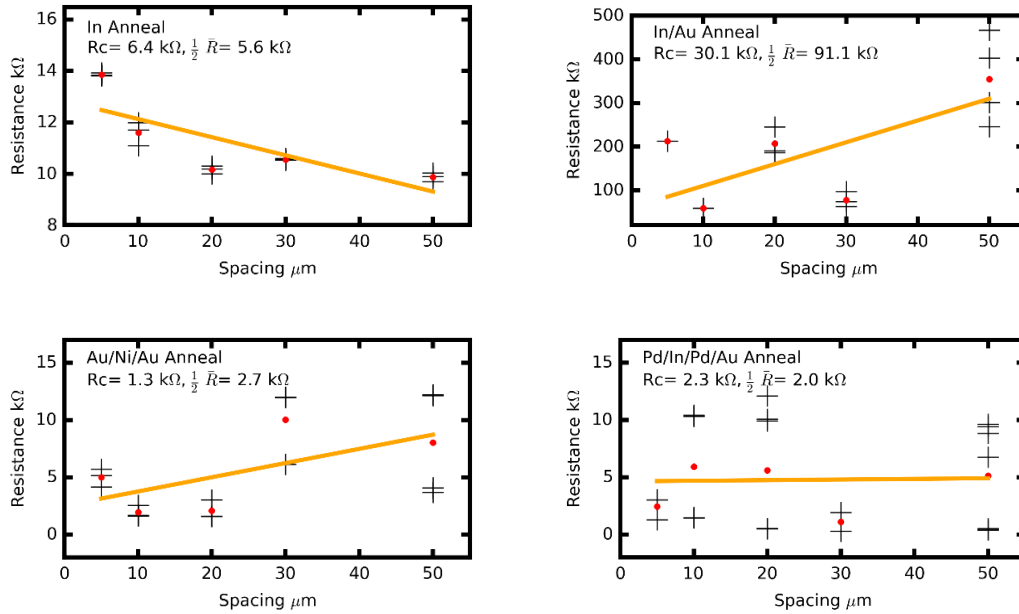


Figure 5.6: Transmission line measurements for each annealed recipe using the low current region of each trace. The black crosses indicate the measured points, the red dots indicate the average of each spacer and the orange line is a linear fit. Each graph is annotated with the contact resistance, taken from half the y intercept of the fit line, and the halved average of all the points ($\frac{1}{2} \bar{R}$).

Though trends and values could be extracted they are with little confidence as there is not a clear trend in the data points for either the TLM resistance taken from the low current region or those taken from the high voltage region, where these produced unphysical results. For example, the TLM for In suggests a higher resistance for a smaller region of semiconductor and the transfer length cannot be extracted from this, and thus a specific contact resistance cannot be found. Despite this, indium gives the most consistent resistance with all pad pairs falling within $\pm 2.7 \text{ k}\Omega$ of the average. This consistency could be due to the simplicity of the recipe, with only one layer being deposited there will naturally be less opportunity for variation of the contacts produced. Au/Ni/Au has a linear trend as expected from a TLM, however this is not feasible as a TLM as the highest two resistance points could reasonably share a contact pad with a particularly high resistance (see Figure 5.6).

The reason for these unphysical TLMs may be due to variation in the contacts that have been created or high resistance reaction layers. The set up currently can be thought of as two TLM pads, which in this case are two Schottky contacts, in series with a resistor (the

semiconductor) where the resistance will increase with spacer. An increasing spacer (or series resistance) would likely not be sufficient to significantly affect the voltage at which the barrier is overcome. However, if uneven diffusion has created regions of parallel conduction this may change the characteristics of the trace (see Figure 5.7). The theory used to extract the contact resistances from TLMs also assumes that all TLM pads (for each recipe) are exactly equal in resistance, which may not be the case.

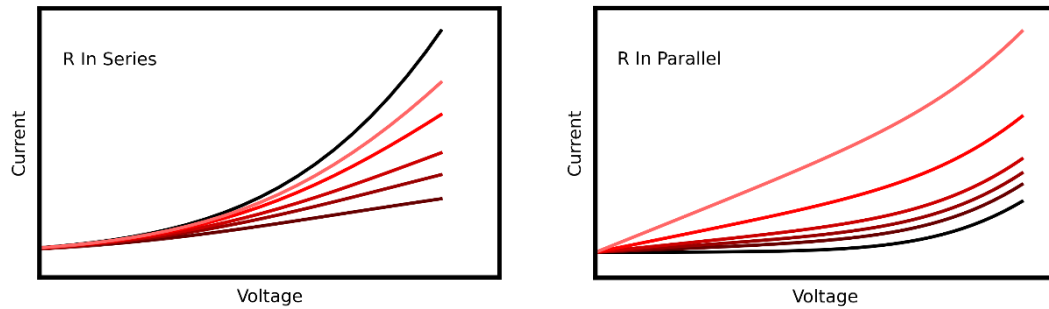


Figure 5.7: A plot indicating how a current voltage measurement would change when two Schottky contacts are placed in series (left) and in parallel (right) with varying size resistors, the changing darkness of red signifies the increased magnitude of the resistor with the black line indicating no resistor in series.

For a Schottky pair with a resistor in series, as the magnitude of the resistance increases, the contribution to the resistance of each Schottky will diminish and so the trace will look more ohmic in nature, as shown by Figure 5.7 left. For a Schottky pair in parallel with a resistor, as the resistor increases in resistance the Schottky becomes the preferred current path and so the I-V trace has Schottky characteristics, but with a slightly altered trace, as shown by Figure 5.7 right.

By comparing the curvature of the below traces to Figure 5.7, it could be speculated that the dominating factor in the In recipe is a resistor in series with a varying resistance. In the case of Pd/In/Pd/Au, the trace shows characteristics of resistors in parallel, where this could be due to Au spiking or uneven diffusion of indium through the Pd layer.

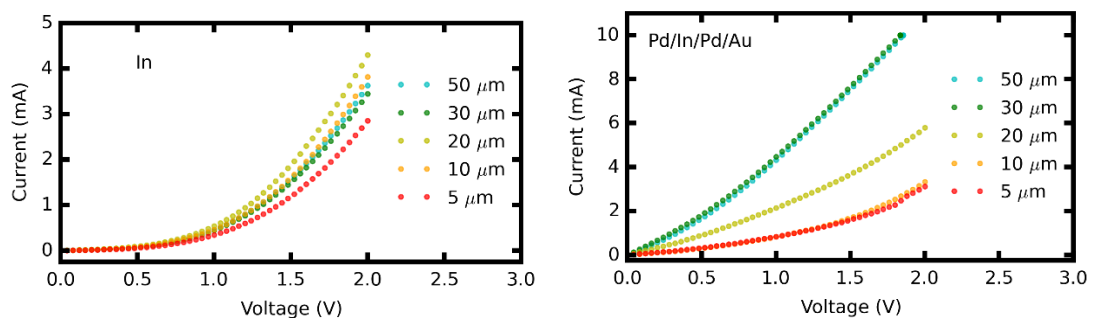


Figure 5.8: A series of traces for In (left) and Pd/In/Pd/Au (right) for varying spacers (represented by varying colours), giving an indication that the indium recipe characteristic is governed by an in series varying resistance, and Pd/In/Pd/Au by an in parallel resistance.

Again, taking the resistance at a low current range is more representative of the physical Hall measurement, but for TLMs this low resistance gives seemingly non-physical results where the high contact resistance also means a sheet resistance cannot be determined.

Usually the contact resistance is found by extracting the half the intercept of the TLM (as there are 2 contacts in any given measurement). However, for the traces observed here, these would be extracted based on questionable results. Instead, as a comparison between different contacting recipes, the average resistance of all points will be taken and halved as an estimation of the contact resistance, as the total resistance is dominated by the contact. This is shown by $\frac{1}{2}R$ in Figure 5.6. This will of course be an over-estimation and not an actual measure of contact resistance, however, it is sufficient for this work given each recipe is being compared like for like.

In the case of Pd/In/Pd/Au a particularly flat TLM can be seen (Figure 5.6), mainly due to bimodal data points, with a combination of high resistance and low resistance contact resistances at each spacer. Upon further investigation it was found that the low contact resistances are also more ohmic in nature, where using the R^2 fitting parameter, this can be seen in Figure 5.9. These figures amplify that though lower contact resistances are possible, the contacts for this recipe are not consistent. The inconsistency could be due to a number of factors such as the variation of material thicknesses in the deposited layers, and the variation in diffusion upon annealing of the multiple layers.

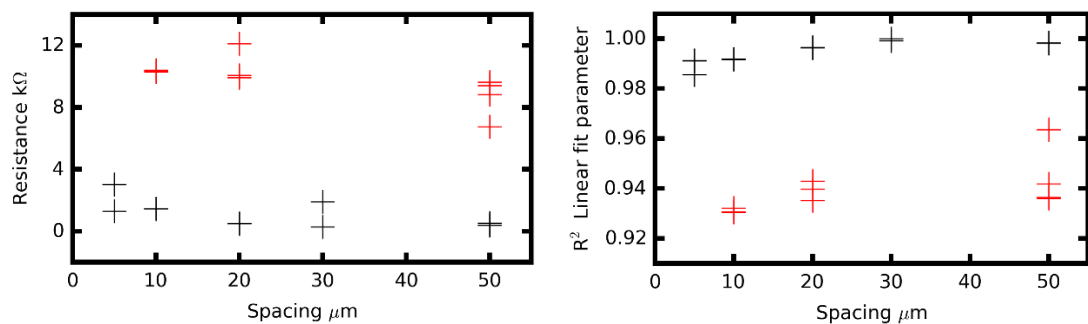


Figure 5.9: **Left:** The resistance of annealed Pd/In/Pd/Au TLM pairs against spacer indicating the bimodal resistances. All contact pairs with a high resistance are indicated by red crosses, whilst those with lower resistance are indicated by black crosses. **Right:** R^2 against spacer indicating the ohmicity of each trace. These two plots together indicate there are two types of contacts created, relatively low resistance ohmic contacts, and high resistance Schottky contacts.

Analysing the low resistance (ohmic region) results in a halved average resistance, of 600Ω , whereas the high resistance region results in a halved average resistance of $4.8 \text{ k}\Omega$.

Table 5.3: A table showing the extracted TLM contact resistances and the halved average resistances for each metallisation recipe at 300 K, given in k Ω .

Contact Types	Extracted R _c	$\frac{1}{2}R$
In	6.4	5.6
In/Au	30.1	91.1
Au/Ni/Au	1.3	2.7
Pd/In/Pd/Au	2.3	2.0

Comparing all the recipes in Table 5.3 Pd/In/Pd/Au and Au/Ni/Au show the most promise at 300 K, and so these contacts were then measured using the same procedures at low temperature.

5.4.5 Resistance Variation with Temperature

Previous measurements on Hall bar devices showed a drastic increase in resistance with a decrease in temperature, and a low temperature resistance should be investigated to ensure any contact recipe maintain their measurability. Following a metallisation study, successful recipes have been found for 300 K and will now be further investigated across temperature. Resistance variation with temperature of contacts could in part be due to the changing barrier height with the band gap, following the Bardeen model, and is most likely due to thermionic emission changes with temperature. Investigating the origin of the temperature dependence of each recipe is out of the scope of this thesis.

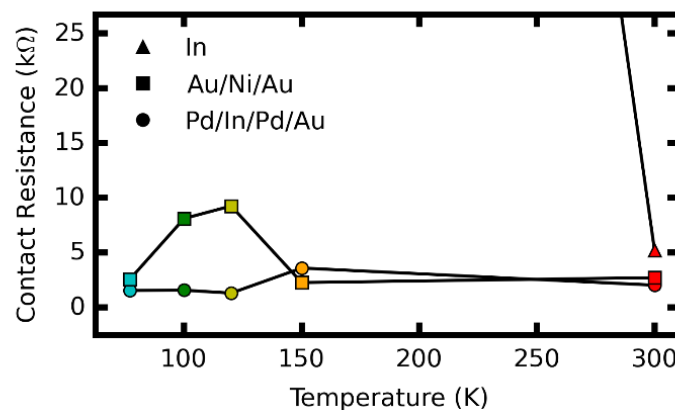


Figure 5.10: Contact resistance against temperature for each contacting recipe (all annealed) down to 77 K, where two recipes were highly resistive below 150 K, and two remained of reasonable resistance down to 77 K.

At room temperature the pure indium deposited was of comparable resistance to the lower resistance recipes. However, once the temperature decreased, as is the case with all the as deposited recipes, the contact resistance drastically increased and showed no trend. In/Au was also measured but the resistance at low temperature was too large to show in Figure 5.10. The Pd/In/Pd/Au resistance appears to be relatively invariant in temperature and sufficiently small enough in contact resistance to be suitable for measurement, whilst Au/Ni/Au also appears to be suitable. The Pd/In/Pd/Au annealed recipe was used throughout the rest of this work as it gave the lowest resistance at low temperature and appeared the most temperature invariant. This recipe was subsequently successfully used in the transport measurements of *n*-AlGaSb/GaSb Hall bars at low temperature (3 K).

5.5 Conclusions

Investigations into the contacting material used were carried out due to significantly high resistance and difficulty in measurement of devices at low temperatures. From the recipes considered in this work obtaining a low resistance contact without annealing was unachievable, however annealing in each case improved the resistance by over an order of magnitude. Four contacting recipes were investigated through I-V measurement of TLMs, all of which produced non-ohmic contacts to varying degrees. In the case of In/Au, a well-defined Schottky contact was created, pure indium produced a less distinct Schottky contact and Au/Ni/Au produced an undefined non-ohmic contact. Pd/In/Pd/Au was inconsistent and produced some contacts which were low resistance and approximately ohmic, and some which were high resistance and Schottky like. Due to the variation across contacts and the questionable ohmicity of contacts, the ohmic behaviour was further defined by investigating the resistance at different regions of the I-V trace. The resistances were then compared where, in a perfect ohmic case, they would be invariant. The R^2 fitting parameter was also used with a linear fit to give another qualifier of ohmicity. The low current region was used as the main comparison between contacts as this is the region that would be used in transport measurements. Pd/In/Pd/Au gave the most ohmic contact and the lowest resistance at the current required for transport measurements. There was, however, more variation with this contact than the other contacting recipes; the low resistance contacts were of $\sim 600 \Omega$ resistance with the higher resistance contacts being 4.8 k Ω . The variation of this recipe may be due to the sensitivity of the contact resistance to the thickness of the Pd blocking layer, or to gold spiking into the semiconductor. Using TLMs to extract the contact resistance was determined to give

unphysical results, and thus the overestimation of averaging the total resistance measured and halving it (due to a pair of contacts being used in any measurement) was implemented. Both Au/Ni/Au and Pd/In/Pd/Au remained low resistance to 77 K, and the latter was selected as the contacting recipe as it had the lowest resistance, was the least temperature variant, and achieved the most ohmic contacts.

Chapter 6

Designing Heterostructures Through Simulation

Prior to growth and measurement of $\text{Al}_{0.2}\text{Ga}_{0.8}\text{Sb}/\text{GaSb}$ heterostructures (heterojunctions and square quantum wells), various structures were simulated to investigate their band structures and their transport properties. Schrödinger-Poisson and transport model simulations were completed in order to predict the optimal structure for high quality transport devices.

In the case of a heterojunction, the electrons are confined in a triangular well. The triangular well is created from the movement of electrons from the dopant atoms (usually situated in the barrier material), to the lower band gap material. Thus, the confinement of electrons is dependent on the donor concentration, a complicated topic in GaSb based systems. The initial step is to simulate the confinement of a given structure. This investigation will yield whether there is a sufficient doping concentration to create a quantum well (in heterojunctions). Alternatively, it is possible to over dope, resulting in a multiband structure, or parallel conduction where there is conduction in the doped region. The native defects in GaSb must also be considered to achieve an accurate representation of the band structure.

Once a band structure has been simulated and confinement is achieved, a transport model is used to investigate the scattering mechanisms and resultant mobility. The scattering mechanisms considered include phonon scattering, interface roughness scattering, and ionised impurity scattering, including from the native defects. The predicted mobility obtained for various structures is then compared, with the structures corresponding to the best mobilities grown and fabricated into devices to be measured.

The simulations in this work were calculated using a simulation software called nextnano [100]. This software is self-described as “software for the simulation of electronic and optoelectronic semiconductor nanodevices”[100]. The simulations are completed by interacting with nextnanomat (the interface), where a coded input template is required, examples of which are found in the tutorials on the nextnano website. The input supplies the software with the relevant parameters and commands from which it can calculate a variety of physical processes requested. The output is given in the form of text files. Though the calculations and code are hidden, a wealth of information on how the software works can be found on the website and in the literature published by nextnano. Their in-built parameter database is used where a parameter hasn't been specified in the input file, and this database is also available to any user. It is important to understand the physics behind the calculations and which parameters are required for each calculation. The main calculations used for this work and performed in nextnano are briefly outlined in this chapter.

This chapter will start with an overview of the flow of calculations occurring in nextnano. Following this, a detailed summary of the theory and numerical implementation of a Schrödinger-Poisson solver is given. The resulting band structures that have been simulated will then be discussed before moving onto the transport model. The theory of the transport model is then outlined, followed by the resulting mobility calculations for each structure.

6.1 Input and Calculation Flow in nextnano

The investigation of the band structure using a self-consistent Schrödinger-Poisson solver, and the mobility using a transport model, are the main calculations considered in this work. The operation of these are explained in detail in the following sections. However, alongside these calculations a number of other physical calculations are also taking place. For example, the ionisation energy is an input parameter which can then be used to contribute to the band structure calculation.

When calculating a structure in nextnano, initially the semiconductor structure is created in the form of a point by point mesh of parameters. These include material composition and doping concentration as a function of depth. Though the thickness of each sample was set to 2 μm , the step size varied over the course of the sample. The step size sets the resolution of the calculation, and thus the step size is larger in the regions where there

was minimal change in the sample, speeding up the calculation. The active regions of the sample were set to a highly resolved step size of 0.1 nm while 500 nm into the sample the step size was changed to 5 nm.

With the structure defined as a mesh, the temperature dependent parameters are calculated at the initial set temperature stated in the input file, and thus an initial band structure is formed. The change in the conduction band with temperature is calculated as described by the Varshni equation 2.6. The doping concentrations are calculated from the activation energy and input into the self-consistent Schrödinger-Poisson (S.P.) solver. The band structure for the whole sample is then iteratively calculated until a solution has converged. In this case convergence is defined where the change in the solution of the Schrödinger equation from one iteration to the next is minimal.

The results of the S.P. solver include the Γ , L and X conduction bands across depth (though only the Γ band is generally considered), and the light and heavy hole valance bands. Along with the band structures are solutions to the Schrödinger equation for the given band structures, which include the wave functions, and their associated energy levels. In these simulations the Fermi level is set to 0 eV, where all energies are changed with reference to this. From the energy states calculated, with aid of the Fermi distribution and the 2D density of states, a carrier concentration is also calculated.

The carrier concentration is fed into the transport model where it is used to calculate the Fermi wave vector, k_f . The Fermi wave vector is a factor required for the calculation of certain scattering mechanisms such as ionised impurities and interface roughness. The carrier concentration can also be manually set. However, there are other parameters of the structure which are compulsory for the calculations in the transport model which include the spacer and the quantum well width. These parameters must be manually set in the input file.

In the case of a triangular well, this quantum well width is not well defined. Following an S.P. solver tutorial for AlGaAs/GaAs given in nextnano, where a heterojunction with a triangular well is formed, the well was initially approximated to be 25 nm. The value was then adjusted to a more accurate value upon inspection of the conduction band, where the width of the triangular well was determined by the position where the gradient of the confining band structure becomes sufficiently flat. Whilst there is uncertainty in this width, the width is only used in the acoustic phonon scattering mechanism in nextnano, and as such is only significant at higher temperatures.

This section covered a brief overall view of the calculations in nextnano, whilst the following section gives a detailed introduction to the theory and numerical implementation of the Schrödinger-Poisson solver.

6.2 Schrödinger-Poisson Modelling Theory

In this section, for clarity, the example of a square quantum well with modulation doping will be used to describe how a band structure evolves through a Schrödinger-Poisson calculation. It will be assumed for simplicity that this square quantum well has one confined energy state.

The Schrödinger equation is used to describe the quantum state of a particle throughout space. In a quantum mechanically confined system, such as a quantum well, the solution for a single electron is found to be a wave function (eigenvector), ψ , and a confined energy (eigenvalue), E . The modulus of the wave function, when squared and normalised, results in a probability density for the position of that electron [101]. However, when there is more than one electron, as is the case with most semiconductor structures, this probability density can be used to describe a spatial charge density. The quantum well is defined by the potential, $V(z)$, which is a profile of the conduction band edge of that structure as a function of the depth of the structure, z . The Schrödinger equation is then given by

$$-\frac{\hbar^2}{2m^*} \frac{\partial^2}{\partial z^2} \psi(z) + V(z) \psi(z) = E \psi(z), \quad 6.1$$

where m^* is the effective mass. As there is a higher charge density (a higher number of electrons) at the peak of the probability density, this region is negatively charged with respect to the edges of the wave function, resulting in a non-uniform electric field [102-104]. In the case where the structure is modulation doped, the dopant electrons will reside in the well, whereas the positive atoms will still be in the dopant plane. This local imbalance in charge neutrality also results in an electric field. The potential associated with these electric fields causes a change in the quantum structure. The perturbation to the potential can be solved using Poisson's equation,

$$\nabla \cdot \mathbf{E} = -\nabla^2 V = \frac{\rho}{\epsilon}, \quad 6.2$$

where \mathbf{E} is the electric field, V represents the potential, ϵ is the material dependent dielectric constant and ρ is the charge density distribution [105]. From the inclusion of electric fields due to the charge distribution, the band will bend.

Once the new structure is calculated, the original wave function is no longer accurate as the shape of the potential well has changed. Thus, Schrödinger's equation has to be solved again. Both Schrödinger's and Poisson's equations are solved iteratively until they converge upon a wave function and band structure that satisfy both equations to a desired accuracy [106].

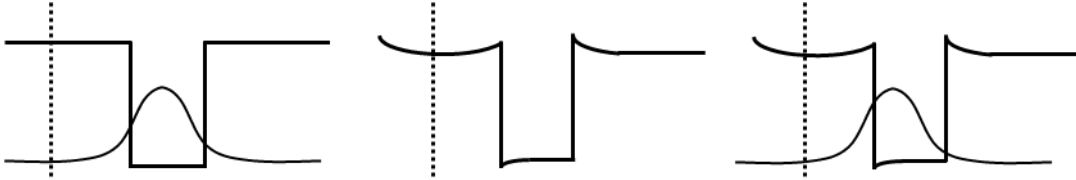


Figure 6.1: A schematic diagram indicating the changes that occur during a Schrödinger-Poisson calculation. **Left:** A simple well with its associated first wave function, the dashed line indicating a dopant plane. **Middle:** Poisson's equation solution for a simple well with a dopant plane. **Right:** The resulting Schrödinger solution of the changed well and the shifted wave function.

The conduction band is solved numerically by estimating a confinement energy for the state in the quantum well and solving the Schrödinger equation to find the electron distribution for a given potential profile (a heterojunction or quantum well). This is done until the estimate is refined and is within a given threshold, where the solution has iteratively converged on this condition [106].

6.2.1 Schrödinger's Equation and Numerical Implementation

Schrödinger's equation can be solved numerically using a combination of the shooting method and the Newton-Raphson method. In order to implement the shooting method an iterative version of the Schrödinger equation must be obtained. To approximate the solution for derivatives in Schrödinger's equation the finite difference method is used, as shown below,

$$\frac{df}{dz} \approx \frac{f(z + \delta z) - f(z - \delta z)}{2\delta z}, \quad 6.3$$

$$\frac{d^2f}{dz^2} \approx \frac{f(z + 2\delta z) - 2f(z) + f(z - 2\delta z)}{4\delta z^2}, \quad 6.4$$

where $f(z)$, is any function, z is a variable of the function f , and δz is, in theory, the infinitesimal change in z , but in practice the step size of the mesh [107]. By substituting the finite difference method into the Schrödinger equation and rearranging to find $\psi(z + \delta z)$, equation 6.5 can be found, where

$$\psi(z + \delta z) = \left[\frac{2m^*}{\hbar^2} (\delta z)^2 (V(z) - E) + 2 \right] \psi(z) - \psi(z - \delta z). \quad 6.5$$

In the above equation, $\psi(z + \delta z)$, $\psi(z)$ and $\psi(z - \delta z)$ are different points of the wave function in the mesh and can be relabelled ψ_{i+2} , ψ_{i+1} and ψ_i respectively. With the generic

starting boundary conditions that $\psi_0 = 0$ and $\psi_1 = 1$ the shooting method predicts ψ_2 by using equation 6.5. The potential, $V(z)$, represents the conduction band profile and this equation assumes an initial guess of the confinement energy. The shooting method is continued along the structure to obtain the full wave function across all z [106]. The numerical values of the wave function at each point are then normalised once the wavefunction across the entire structure is found. If the solution has not converged (has an exponential tail) it is not a suitable solution for confinement and thus a different confinement energy is trialled until the wavefunction is confined.

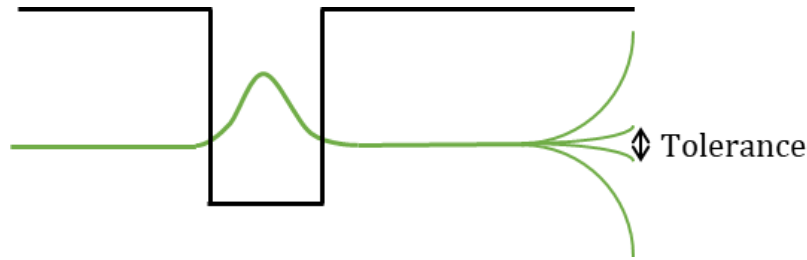


Figure 6.2: A schematic diagram indicating the condition in which a trial wave function is accepted as a solution.

The wave function solution is defined as having reached confinement when the last point of the wave function is equal to 0, or in practice ≈ 0 within a set tolerance. An approximate guess of the confined energy is trialled and is made significantly more accurate with each iteration by the Newton-Raphson method [106]

$$E^{(n+1)} = E^{(n)} - \frac{f(E^{(n)})}{f'(E^{(n)})}, \quad 6.6$$

where $f(E)$ is a value in the wave function profile calculated by the shooting method at an energy E , and $f'(E)$ is the notation for the differential of $f(E)$ with respect to E . Once a more accurate eigenenergy is calculated [108], it is substituted into equation 6.5 to calculate the wave function, and if the last value of the wave function is not approximately zero to a given accuracy, the process is repeated. If the last value of the wave function is approximately zero, then a confined state has been found.

6.2.2 Poisson's Equation and Numerical Implementation

The numerical implementation of Poisson's equation is achieved by breaking down the equation for ease of calculation, starting with the charge density.

The charge density at each point, $\sigma(z)$, is calculated, taking into account both the dopant ions and electrons distributed at each point. The electrons are distributed by the probability density function (taken from the wave function) calculated by the Schrödinger solver described above. Though the summation over the entire structure would be zero

due to charge neutrality, at each point the local charge density will be different. The charge density is given by

$$\sigma(z) = q(N\psi^*(z)\psi(z) - d(z))\delta z, \quad 6.7$$

where q is the charge of the carriers, δz is the step size, $d(z)$ is the volume density of the dopant, $\psi(z)$, is the wave function and N is the number of carriers per unit area, which can be defined by dopant concentration. As quantum wells are assumed to be infinite planes in this calculation, the 3D charge density can be thought of as an areal charge density σ with a width of δz .

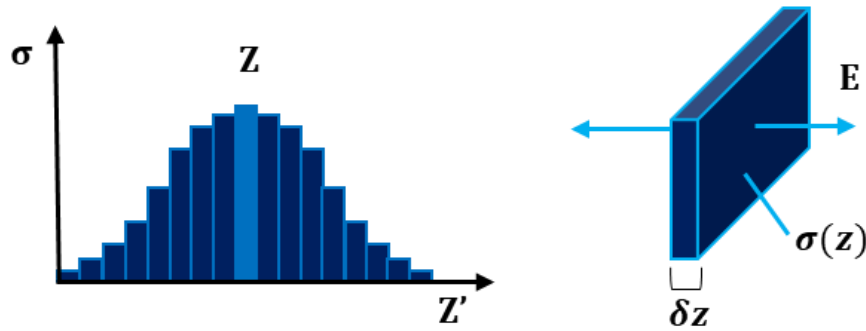


Figure 6.3: **Left:** The charge distribution in the form of a histogram, where Z' is the depth into the structure. **Right:** A diagram illustrating the electric field strength from an infinite sheet of charge.

Each charge density block of width δz can be considered to be a sheet of charge with an associated electric field strength E . The electric field strength for a single block is constant for all distances from that block. The summation of the contribution from each sheet at each depth away from to z (z'), results in a total electric field strength at each point, z ,

$$E(z) = \sum_{z'=-\infty}^{\infty} \frac{\sigma(z')}{2\epsilon} \text{sign}(z - z'), \quad 6.8$$

where E is the electric field strength, ϵ is the permittivity and the sign function equals +1 if $z - z'$ is positive, -1 if $z - z'$ is negative, and 0 if $z = z'$. The sign function is used to express the vector nature of the electric field strength[106].

From this result the additional potential (in addition to the potential given by the band structure) due to the electron distribution is easily found via Poisson's equation, where in 1 dimension

$$V_{\rho}(z) = - \int_{-\infty}^z E dz. \quad 6.9$$

To make this calculation self-consistent with the Schrödinger solution, the calculations of both Schrödinger's and Poisson's equations are iterated until both the Schrödinger

solution and Poisson solution have converged to a set tolerance. At this point the wave function and confinement energy are then solutions of the Schrödinger equation, with the associated charge density a solution of the Poisson equation.

6.3 Simulated Confinement in GaSb Heterostructures

The initial outline for the structures simulated is given in Figure 6.4, a simple heterojunction with slab modulation doping in the $\text{Al}_{0.2}\text{Ga}_{0.8}\text{Sb}$ top cap which will form a triangular well at the GaSb junction. The structure design is limited partially by strain, where a Matthews and Blakeslee model calculated for this structure (see section 2.3.5) resulted in a top cap that can not exceed 120 nm.

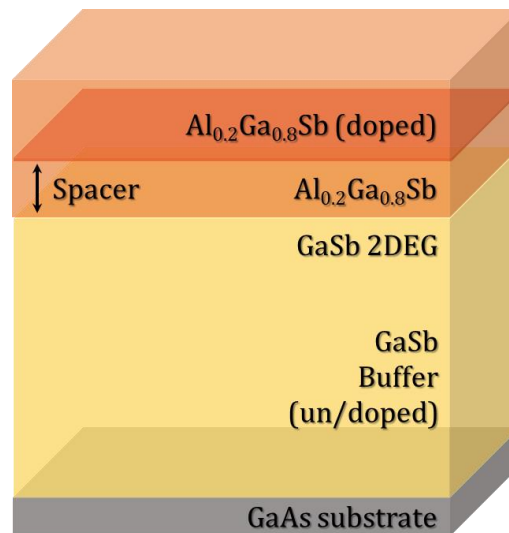


Figure 6.4: The initial $\text{Al}_{0.2}\text{Ga}_{0.8}\text{Sb}/\text{GaSb}$ heterojunction structure proposed to achieve electron confinement, noting the doped and undoped (unintentionally doped) regions.

The other variables that were investigated with the Schrödinger-Poisson solver include the spacer thickness, which is the undoped region between the GaSb layer and where the doping starts in the top cap, and the concentration of donors, required to obtain good confinement.

The structures investigated in this chapter were all calculated with the same set of material dependent parameters, a number of which are given in Table 6.1. The majority of band parameters are taken from Vurgaftman [13] unless stated otherwise.

Table 6.1: A table indicating the parameters used in the S.P. solver calculations for $\text{Al}_{0.2}\text{Ga}_{0.8}\text{Sb}$ /GaSb structures. In the table α and β represent the material parameters for a change in band gap with temperature, and ϵ_r represents the relative permittivity.

Input Parameter	Value
α (eV/K)	4.2×10^{-4}
β (K)	140
m^* (m_e)	0.039
ϵ_r (ϵ_0)	15.69 [27]
Bowing parameter $\text{Al}_{0.2}\text{Ga}_{0.8}\text{Sb}$ (eV)	0.2

6.3.1 The Effect of Defects on Heterostructure Design

The growth study completed in chapter 3 investigated a range of growth conditions, and thus the resultant acceptor defect concentration achieved in unintentionally doped samples. This study showed that the defect density will likely fall within the range of $3.0 \times 10^{16} \text{ cm}^{-3} - 8.0 \times 10^{16} \text{ cm}^{-3}$, and, as such, the structures in this chapter have been simulated with an average defect concentration of $5.0 \times 10^{16} \text{ cm}^{-3}$ unless otherwise specified. It is worth noting, however, that the change in defect concentration from one side of this range to the other may impact the band structure simulated. This is due to differing electron distributions, and thus the confinement of electrons, particularly in the heterojunctions. As such, the effect of this variation was considered and simulated, where an example of the effects of increased defects can be seen below.

Figure 6.5 shows an example of the variation of the band structure across the defect range expected from the growth study, with only the defect concentration varied. In Figure 6.5, the heterojunction is n -type doped either side of the well with a concentration of $1 \times 10^{17} \text{ cm}^{-3}$, leaving the junction undoped with a spacer either side. The quantum well is a similar structure with doping either side of the well, and the well undoped, with a quantum well width of 25 nm.

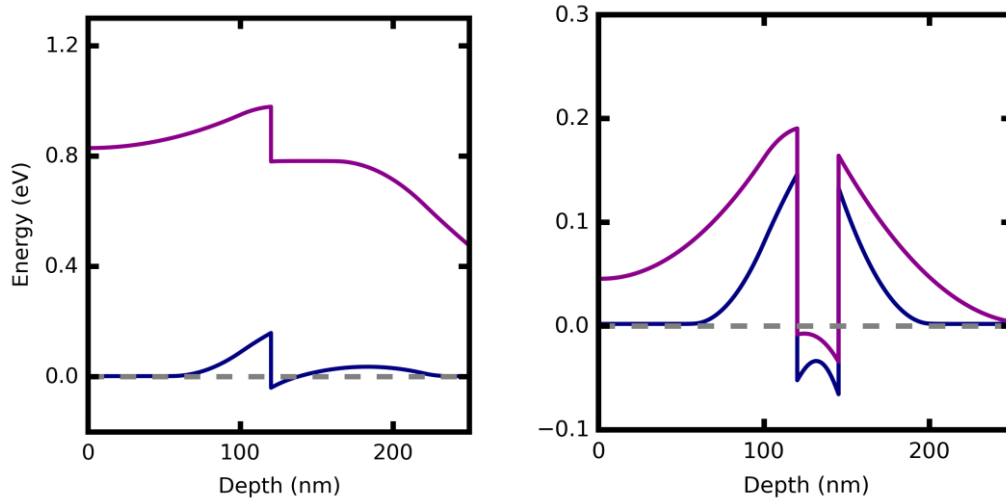


Figure 6.5: The same structures simulated with low and high defect concentration (blue and purple lines respectively). **Left:** A heterojunction with doping in the top and bottom barriers with an undoped well, where the RHS barrier is reduced due to doping. **Right:** A quantum well with n -type doping of concentration $1 \times 10^{17} \text{ cm}^{-3}$ in the top and bottom barriers and an undoped well. Both structures have spacers either side of the well.

The obvious statement is that the increase in acceptor defects creates a structure that appears less doped. The Fermi level (0 eV) is further into the forbidden gap towards the valence band for the increased defect concentration and the triangular well is seen to be unoccupied when a large number of defects are present. This of course stems from the Fermi distribution where the Fermi level in this case is 0 eV. When the ratio of $(E_1 - E_f)/k_bT$ equals 1, the probability of occupation from the Fermi distribution is $f(E) = 0.27$ and if the ratio increases to 2 then $f(E) = 0.12$. This shift is approximately the same for the heterojunctions and the quantum wells, however the quantum wells are essentially immune to any differences in confinement made by the defect concentration changes.

6.3.2 Doping the Barrier of a Triangular Well

In a heterojunction, the confinement of the 2D electron gas (2DEG) comes from the movement of charge introduced from the donors in the barrier moving into the lower band-gap material. This movement introduces band bending (as described in section 6.2.2). The doping concentration needs to be carefully chosen, however, as over doping in the barrier can lower the local (AlGaSb) conduction band edge below the Fermi level, leading to occupied states with wave functions in the dopant plane. The presence of these states gives rise to parallel conduction in a region with a large number of scattering centres, reducing the mobility of the carriers. Conversely, under-doping won't create a triangular well and thus confinement (e.g. Figure 6.5 left), as there is not enough charge

movement to the well to create the necessary band bending and perhaps not enough dopant to allow n -type conduction. Therefore, a fine balance of doping concentration is required, and hence the need for the detailed simulations performed in the following sections. For GaSb/AlGaSb heterostructures this is complicated by the defect acceptor states.

To investigate any structure assumptions must be made. In this section we will assume that all structures have an accepting defect concentration of $5 \times 10^{16} \text{ cm}^{-3}$ across the entire structure. It is also assumed that this is equal in the $\text{Al}_{0.2}\text{Ga}_{0.8}\text{Sb}$ and GaSb layers. Previously analysed transport results for MBE grown bulk $\text{Al}_{0.2}\text{Ga}_{0.8}\text{Sb}$ and GaSb epilayers confirm that the defect concentration does not change with this fraction of aluminium.

Initially, the aim is to produce confinement by avoiding doping the quantum well, leaving the well unintentionally doped with the native defects in GaSb. Dopants in the quantum well would act as scattering centres, where this increase in scattering centres would reduce the mobility. In the initial simulations, only the barrier was doped, and the doping concentration was in the range $(1 \times 10^{17} - 3 \times 10^{18}) \text{ cm}^{-3}$. The upper limit originates from the saturation of Te in GaSb, where an increase in Te flux during growth does not lead to an increase in incorporated dopant in the structure. An example of the resultant band structures and associated wave functions for a typical structure with a spacer equalling 30 nm are shown in Figure 6.6 for under- and over-doped samples, produced using the nextnano Schrödinger-Poisson solver.

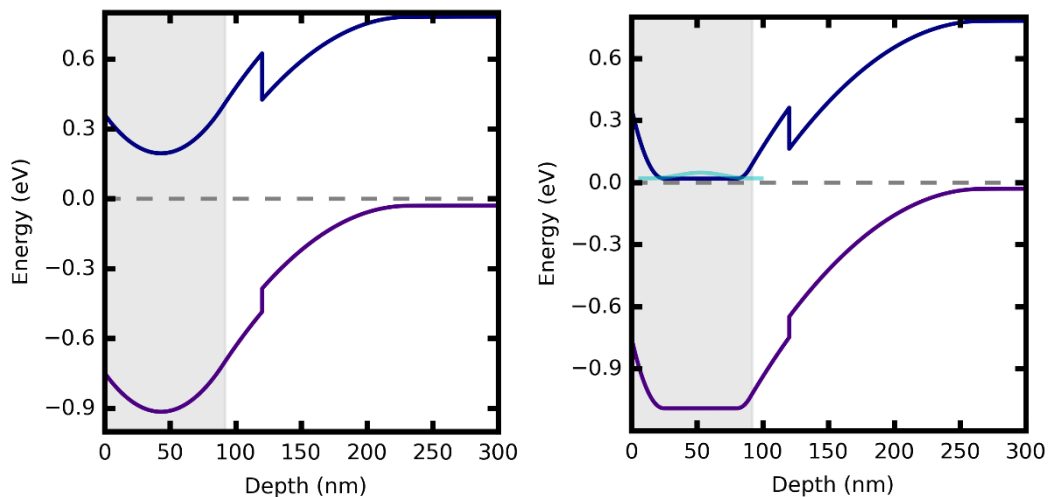


Figure 6.6: Band diagrams for a $\text{Al}_{0.2}\text{Ga}_{0.8}\text{Sb}/\text{GaSb}$ structures doped only in the top cap with the Fermi level (dashed) set at 0 eV. The doped region is shaded grey. **Left:** Doping is too low, resulting in a sample that is p -type. **Right:** Doping is too high, where doping the top cap results in wave functions and occupied states in the barrier.

The band structures for the full range of doping considered showed lower doping concentrations (below $4 \times 10^{17} \text{ cm}^{-3}$) resulted in the Fermi level lying deep in the forbidden gap, as seen in Figure 6.6 left. However, once the doping concentration has increased enough for the Fermi level to lie in the conduction band, the ground-state wave functions are positioned in the barrier. Once the conduction band is comparable to the Fermi level, the wavefunctions will reside wherever in the structure the lowest minimum of the conduction band edge is. This will not necessarily be at the junction and the wavefunctions will follow the band edge minimum. This change in the structure is of course due to the alignment of the Fermi levels of the *p*-type and *n*-type regions. Even in a highly doped case, the addition of donors in the barrier just aided in a local shift in the conduction band of the doped region (as Fermi level is set to 0 eV). The conduction band in the quantum well region is then energetically higher and thus electrons will not move to the intended confinement region.

Therefore, no concentration of doping will result in the desired confinement profile for this particular structure when there is just doping in the barrier material. This is true across all temperatures.

A reduced spacer may increase the chances of obtaining a confined region and thus this was the next investigation. Reducing the spacer is slightly more complicated as this will also affect the transport properties. A small spacer results in more ionised impurity scattering from the dopant and therefore reduces the mobility. However, for now this consequence will be neglected.

The band structure simulations performed above were repeated for spacers in a range of (5–30) nm in 5 nm steps. Reducing the spacer further made little difference to the position of the wave function across doping range except for at the highest doping concentration and a low spacer of 5 nm. With these conditions, at low temperature, the wave function lies in the well, however, as the temperature increases, the peak position deviates to the barrier.

Therefore, to practically achieve this structure, the doping concentration would have to be exact and in the limit of what is practically achievable. If this doping concentration was achieved, the small spacer would cause concerns for undesirably high remote ionised impurity scattering, which is discussed in the transport section.

Doping the $\text{Al}_{0.2}\text{Ga}_{0.8}\text{Sb}$ barrier alone thus is an impractical and very limited design due to the inherent p -type nature of GaSb. A table summarising the variable ranges and results of this section is shown in Table 6.2.

Having calculated the full range of doping concentrations practically available using MBE for the barrier, and for a range of spacers, only one set of conditions gave a confinement possibility. This one set of conditions would likely result in a low mobility. Therefore, a new structure is proposed where the bottom buffer of GaSb is also doped.

Table 6.2: A table indicating the summarised Schrödinger-Poisson results from the confinement study for an $\text{Al}_{0.2}\text{Ga}_{0.8}\text{Sb}$ /GaSb heterojunction with a doped barrier and an undoped buffer, where each structure has a background acceptor concentration of $5 \times 10^{16} \text{ cm}^{-3}$ due to native defects.

Set Parameters		Variables		Concluding Result
Spacer	30 nm	Dopant	$(1.0 \times 10^{16} - 3.5 \times 10^{17}) \text{ cm}^{-3}$	Fermi level in the gap
Spacer	30 nm	Dopant	$(4.0 \times 10^{17} - 3.0 \times 10^{18}) \text{ cm}^{-3}$	States in the barrier
Dopant	$< 10^{18} \text{ cm}^{-3}$	Spacer	(5 – 25) nm	Same as 30 nm spacer
Dopant	$3 \times 10^{18} \text{ cm}^{-3}$	Spacer	(5 – 25) nm	E_1 in the well at 5 nm
Dopant	$3 \times 10^{18} \text{ cm}^{-3}$	Temp	(3 – 300) K	E_1 moves to the doped barrier @ 10 K
Spacer	5 nm			

The doping concentration in the buffer is only required to be high enough to overcome the p -type defects. A greater increase may encourage states to reside in the bulk. There is now a conflict. Having a large concentration of Te atoms in the quantum well would drastically reduce the mobility but having an undoped buffer does not result in a GaSb 2DEG. Tellurium atoms are also known to drag during growth of other material systems such as InSb. Therefore, another spacer is required between the junction where the 2DEG will lie, and the doped GaSb buffer region. Though there have been no investigations into tellurium dragging in GaSb, other works have investigated this effect in InSb [109]. During growth, a percentage of the tellurium does not initially incorporate into the structure but instead sits on top of the uppermost atomic layer and gradually incorporates over the coming layers. This occurs even after the Knudsen cell valve has been closed.

Works by Orr *et al.* [109] show from SIMS measurements that 25 nm after the intended Te deposition where the shutter has been closed, there is still Te, although the concentration

has dropped to a small fraction of the original concentration. This decrease is exponential, therefore in this work we will consider a spacer of above 50 nm from the $\text{Al}_{0.2}\text{Ga}_{0.8}\text{Sb}/\text{GaSb}$ junction to the doped GaSb region. The concern here is that the Te concentration may drop, but if there is still a small number in the well then Te complexes may be created, again reducing the mobility.

6.3.3 Doping the GaSb Buffer in the Triangular Well

The structure now includes a doped buffer region which will have its own spacer (leaving the well undoped), and doping concentration that can be varied. For the sake of ease, the spacers will initially be fixed at 20 nm in the $\text{Al}_{0.2}\text{Ga}_{0.8}\text{Sb}$ barrier and 50 nm in the GaSb buffer. This will however be modelled as an instant shut off of dopant unlike the reality where an exponential tail would be obtained.

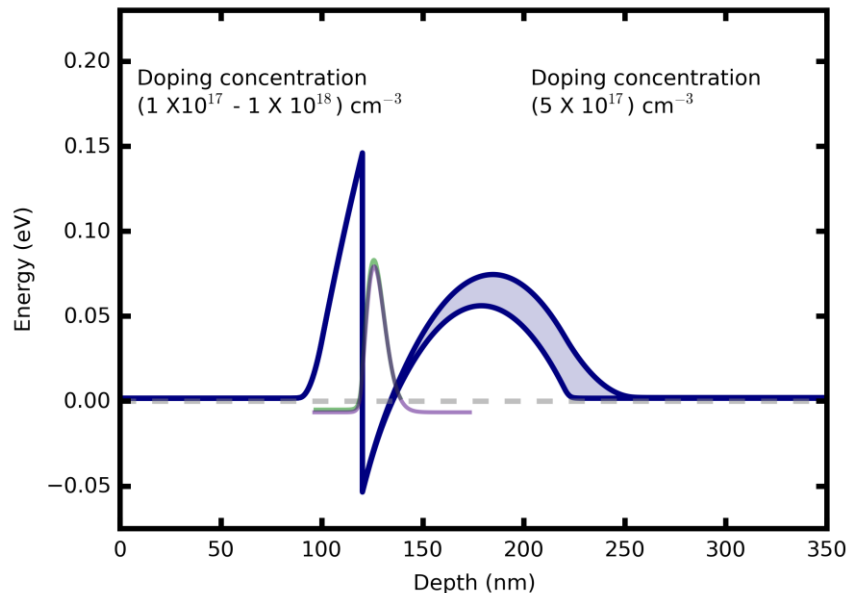


Figure 6.7: Band diagrams for an $\text{Al}_{0.2}\text{Ga}_{0.8}\text{Sb}/\text{GaSb}$ structure at 3 K with doped buffer and barrier regions. Outlined are the highest and lowest conduction band edge energies for the doping range investigated, shaded to indicate the variation of results between them. Similarly, the ground state wave functions for each structure with the highest and lowest doping are outlined. The dashed grey line at 0 eV indicates the Fermi level.

The doping ranges investigated were from $(1 \times 10^{17} - 3 \times 10^{18}) \text{ cm}^{-3}$ in the top barrier and $(5 \times 10^{16} - 5 \times 10^{17}) \text{ cm}^{-3}$ in the buffer, with both symmetrical and asymmetrical doping being investigated. However, only a range of $(1 \times 10^{17} - 1 \times 10^{18}) \text{ cm}^{-3}$ in the top barrier and a concentration of $5 \times 10^{17} \text{ cm}^{-3}$ in the buffer produced wavefunctions confined in the well.

A number of doping concentrations investigated resulted in the ground state wave functions in the desired positions (confined in the well) at low temperatures, unlike in the structures shown in Figure 6.6. In Figure 6.7 it can be seen that a “hump” has appeared in the conduction band where the undoped (unintentionally doped) region is located. This is due to the Fermi level alignment of the p and n regions and helps define the triangular well shape for the lowest doping concentration for the buffer. The second energy level E_2 in all cases was many $k_b T$ above the Fermi level and thus would not be expected to be occupied, resulting in single carrier conduction as anticipated. However, as the temperature is increased the wave function peak instead changes to reside in the bulk GaSb or in the barrier.

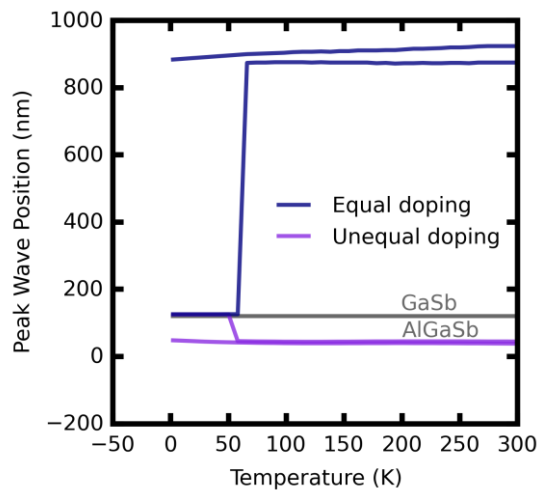


Figure 6.8: Simulation results of the peak wave function position (depth into the heterojunction) against temperature. Only a few select doping concentrations are displayed for clarity. The dark blue lines indicate where the doping is equal in the barrier and buffer and the purple indicates where the barrier doping is greater than the buffer. The grey line shows the separation of the barrier and the well and thus approximately where the 2DEG should reside.

Figure 6.8 shows that although some of the wave functions started in the 2DEG at 3 K, at high temperature, if the doping concentration is unequal, somewhat unsurprisingly, the energy levels would lie where the higher doping concentration resides (in the barrier). If the doping concentrations were equal the states would instead lie in the bulk at high temperature.

The “hump” shape created by the undoped region may seem like it would create better confinement, though the triangular well can become sharp and therefore too narrow at higher temperature. The reduced width of the triangular well pushes the energy state upwards past the point of confinement and thus the state is lost to the bulk.

If the top spacer is increased, the well becomes too flat and shallow at low temperature thus there are no confined states in the low doping case. With increased doping, with increased spacer, a similar result as Figure 6.8 above is found where the states are confined, however, they move to bulk at ~ 100 K. For a spacer of 10 nm above the well the same again is found, and as expected, a thinner spacer results in a lower confinement energy level. As this structure does not result in confined states across temperature, a doped well was simulated to consider all structural options.

6.3.4 Doping the Triangular Quantum Well

The final option to create confinement in heterojunctions is to dope the well, where this will mean a lower mobility due to Te atoms in close proximity to the charge carriers. This will also result in a less well-defined triangular quantum well but will certainly result in n -type conduction. The same simulations were repeated as above with the whole structure doped. The barrier was doped with a range of concentrations of $(1 \times 10^{17} - 3 \times 10^{18}) \text{ cm}^{-3}$ and the GaSb was doped with a range of concentrations of $(5 \times 10^{16} - 1 \times 10^{18}) \text{ cm}^{-3}$, with both equal and unequal doping being investigated. Low temperature resulted in all structures giving confinement in the correct position, at the junction.

As above, the energy levels were below the Fermi level however the characteristic “hump” of the undoped region was lost. As temperature is increased the majority of the wave functions stayed in the GaSb. Only the structures with the highest doping concentrations in the barrier compared to the GaSb resulted in states in the barrier. However, unequal doping did result in wave functions straying to the bulk with temperature.

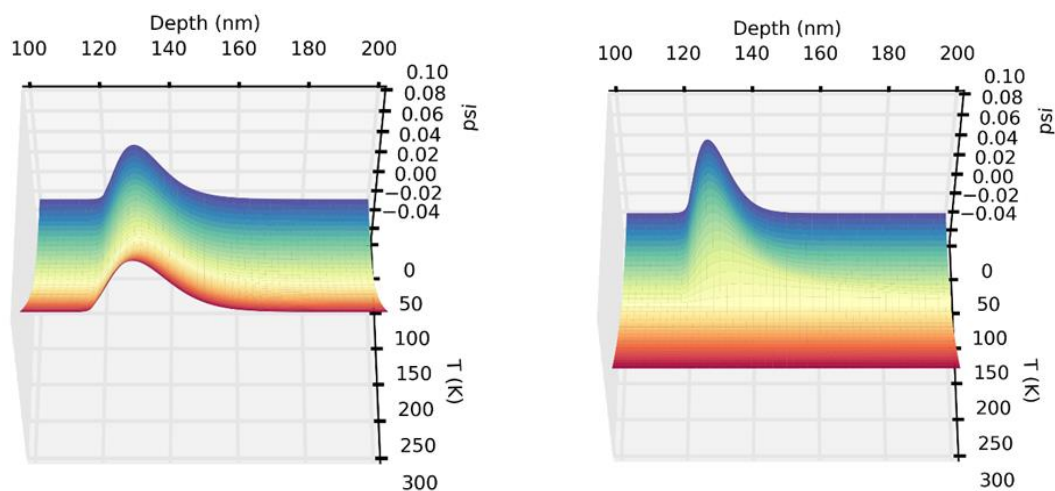


Figure 6.9: The ground-state wave functions against temperature for symmetrically doped heterojunctions with a doped well. These figures show the broadening of the wave function with higher doping levels. The junction is located at a depth of 120 nm. **Left:** Symmetric doping of $1 \times 10^{17} \text{ cm}^{-3}$. **Right:** Symmetric doping of $1 \times 10^{18} \text{ cm}^{-3}$.

The structures which resulted wavefunctions straying to the bulk were all neglected for the rest of the study and only equal doping concentrations are shown below. Still, whilst for many structures the wave functions were confined, this confinement was not uniform across temperature, with some wave functions more sharply defined than others. Figure 6.9 shows the variation of the wave functions across temperature for two examples, one of lower doping ($1 \times 10^{17} \text{ cm}^{-3}$) and one of high doping ($1 \times 10^{18} \text{ cm}^{-3}$).

It can be seen that for equal but lower doping concentrations ($1 \times 10^{17} \text{ cm}^{-3}$) the state stays confined against temperature. Whereas for higher doping concentrations, though the state is confined (the wave function is still defined and the peak is close to the junction), the wave function spreads. Thus, there is higher chance of conduction for a wide portion of the GaSb layer. This changing shape of the wave function can also have a complicating effect on the resultant mobility [36], where, for example, a shift in carriers away from the interface will potentially reduce any scattering from interface roughness. This will also simultaneously change the parameters required to be input into the transport model at each temperature, increasing the complexity of the modelled and measured mobilities.

It can be seen here that provided that doping concentration is low enough, the state will remain sharply defined (well localised). There is now a feasible design option where the whole structure is doped with equal doping throughout. This is once again attributed to the shape of the well. In the high doping case, the native defects will have little effect and as there is no undoped region aiding the confinement shape, so the triangular well is shallow. As the temperature increases the well gets shallower and the wave function broadens.

Seemingly, the doping of the entire GaSb epilayer opens up some possible structures to be grown. When the entire GaSb layer is doped including the well, the structures give better confinement. Though at high doping concentrations, the Te in the well will contribute to scattering, lowering the mobility, and so low doping is preferable. It is clear that obtaining a well-confined heterojunction is difficult, particularly across a full range of temperatures, though low temperature simulations show that for many of the structures, obtaining a measurable device should be feasible. Consequently, the investigation was expanded to include square quantum well structures, where the barriers either side are doped.

6.3.5 Square Quantum Well Design Investigation

A range of heterojunction structures were simulated but only a few obtained confinement of the wave function across a full temperature range. The square quantum well will guarantee confinement, yet, this structure has two barrier interfaces. The barrier interfaces can result in lower mobility due to interface roughness, which will be discussed further in section 6.4.3. The square quantum wells studied in this section consist of a GaSb well between two layers of $\text{Al}_{0.2}\text{Ga}_{0.8}\text{Sb}$.

The square quantum wells were again investigated using S.P. modelling as above. The GaSb well is undoped, with the spacers above and below the well equalling 20 nm and 50 nm respectively. The second spacer is greater to prevent Te dragging into the well. Doping was investigated with the quantum well width investigated initially set at 25 nm, the doping concentration range was $(1 \times 10^{17} - 1 \times 10^{18}) \text{ cm}^{-3}$. The simulations resulted in, unsurprisingly, the ground state wave function being confined to the well across the full temperature range, for most structures simulated. The band structure in Figure 6.10 shows how the bands bend to be energetically low towards the bulk (RHS) of the structure. The band structures are shown for the doping range $(1 \times 10^{17} - 1 \times 10^{18}) \text{ cm}^{-3}$. The low-lying band in the *n*-type $\text{Al}_{0.2}\text{Ga}_{0.8}\text{Sb}$ region is aligned at a similar energy to the states in the well. This is due to the undoped region around the well being inherently *p*-type, and again the Fermi level of this region aligning with the *n*-type regions.

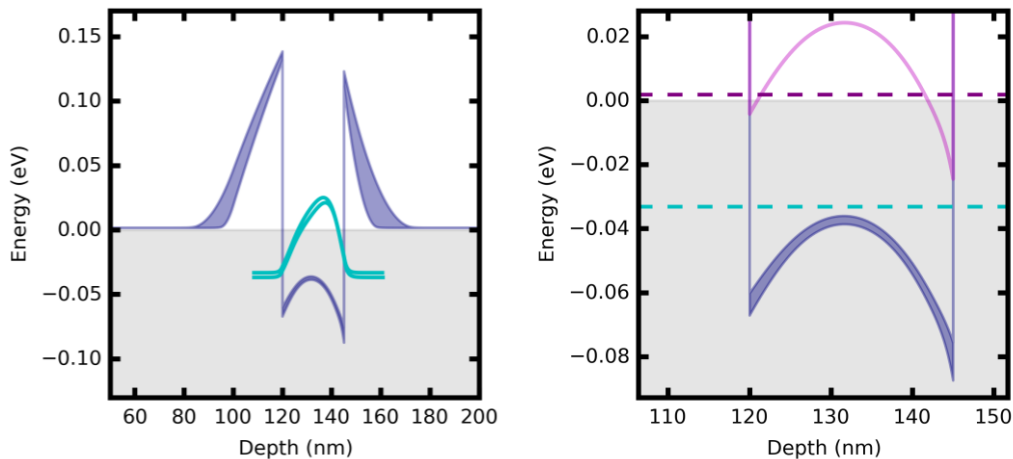


Figure 6.10: **Left:** The band structure for an $\text{Al}_{0.2}\text{Ga}_{0.8}\text{Sb}/\text{GaSb}$ 25 nm quantum well with either side doped in the doping range $(1 \times 10^{17} - 1 \times 10^{18}) \text{ cm}^{-3}$ with spacers of 20 nm and 50 nm either side of the well. The shaded grey area indicating the region below the Fermi level. **Right:** A focus on the quantum well showing the ground state energy (light blue dashed) the second energy state (purple dashed) and the L band (pink solid).

For the majority of the doping range this design was successful with the quantum well easily solving the issue of confinement that was brought about with the heterojunctions.

However, these structures resulted in a different issue, the second wave function. In Figure 6.10 it can be seen that at low temperature there are multiple states below the Fermi level in which conduction can take place, not technically creating a 2DEG (which would only have one electronic state). Though this is not preferable, a reduction in doping to somewhere below $5 \times 10^{16} \text{ cm}^{-3}$ would result in a non-conducting or *p*-type sample, particularly if there is a slight increase in defect concentration. These states are however at an energy below the L-band, where this is preferable as accessible states in the L band can cause interband scattering between the bands. Also, the effective mass in the L band is much larger than the effective mass in the Γ band and so the mobility would be heavily reduced for the carriers in that band. The second state being below both the L-band and the Fermi level is consistent across doping levels.

The first and second wave functions are well separated, with the second energy state only contributing 18.4 % of the carrier density for the higher doped case and 5.9 % for the lower doped case. As the temperature increases, the second energy state resides in the bulk.

Alternatively, the well width could be varied. Narrowing the well would push the second state further up though a narrow well could also introduce a significant increase in scattering due to the potential interface roughness. The simulations for quantum well structures with the doping ranges above were repeated for a number of quantum well sizes (10 – 30) nm. When this was investigated, the simulations showed that in the quantum wells the states were below the Fermi level with a 10 nm well, where the separation in energy levels had increased as expected, however the second level resided in the bulk. The second wave functions were lost to the bulk at higher temperatures as is the case for the larger well widths.

Though the quantum wells solve the confinement issue, they are likely to be two carrier, therefore each design option yields its own advantages and disadvantages.

6.3.6 Schrödinger-Poisson Summary

From the structures investigated, it became clear that a 2DEG confinement is hard to achieve through a single heterojunction structure. Confinement appears unachievable with just the barrier being doped. The full range of doping in the MBE's capability for GaSb was explored ($1 \times 10^{17} - 3 \times 10^{18}$) cm^{-3} . The simulations showed that there were structures with energy states low enough to be below the Fermi level, however, these resided in the barrier. This effect was due to the aligning of the Fermi level of the *p*-type and *n*-type regions. Thus, doping of the buffer was also investigated.

The doping range in the buffer was $(1 \times 10^{16} - 5 \times 10^{17}) \text{ cm}^{-3}$, whilst the well was left undoped to avoid unnecessary scattering of the electrons with the dopant atoms. This design resulted in confinement of the ground state wave function at low temperatures. As the temperature increased past 60 K the first energy level was lost to the buffer in all cases, and so the structure would have bulk conduction (in equally doped structures). Alternatively, the first energy level was confined to the barrier (in unequally doped structures). There were many structures which gave a single, confined wave function as desired in the low temperature region but a confined state across temperatures would be preferable, thus doping the well was also investigated.

Doping the triangular well opened up many options for confinement provided the doping was symmetric. At higher doping ranges $> 8 \times 10^{17} \text{ cm}^{-3}$ the wave function spread as temperature increased. An increased doping concentration is again a disadvantage for scattering as there is a larger concentration of scattering centres. This structure design, though unpreferable for transport due to the increased scattering from Te ions being present in the well, gave many confined structures and thus is a design option for growth.

As confinement was inherently difficult using the heterojunction design, a square quantum well was investigated. The square quantum well structures gave confinement for the ground state wave function across temperature for symmetric doping.

Table 6.3: A table summarising the design options to be investigated using the transport model.

Type	Doping profile	Doping concentration ($\times 10^{17} \text{ cm}^{-3}$)	Spacer (nm)
Heterojunction	All doped symmetrically	1 – 5	-
Heterojunction (low T)	Barrier and buffer doped symmetrically	1 – 10	25, 50
Quantum Well	Barriers doped symmetrically	1 – 7	25, 50

At low temperature secondary energy states were also present in all cases below the Fermi level, and thus they are not single carrier. As temperature was increased the secondary wave functions resided in the bulk as the $\text{Al}_{0.2}\text{Ga}_{0.8}\text{Sb}$ barrier has a low-lying conduction band edge. Reducing the well size did not significantly change the results of the Schrödinger-Poisson simulation, and would lower the mobility due to interface roughness scattering, discussed further in section 6.4.3.

Both the heterojunction and the square quantum well structures have their advantages and disadvantages so are worth exploring further. In the low temperature region of interest then the heterojunction with an undoped well but doped buffer, should give a high mobility device. These structures will be further investigated using the transport model in the next section.

6.4 Transport Model Theory

Movement of charge carriers due to an electric field is modelled through a transport model. This transport model assumes a charge carrier will move in a straight line (ballistically) until something deflects that movement in a different direction (a scattering mechanism). Desired movement of an electron in any structure is from one side of a sample or device to another to give rise to conduction. In the structures studied here the transport or conduction occurs through a GaSb quantum well.

There are various scattering mechanisms, some of which are heavily dependent on the sample structure and others that are primarily dependent on the material. The following sections explore the theory of transport modelling and how structural differences affect each scattering mechanism. Finally, the transport simulations of the structures examined in the previous section are discussed.

Each scattering mechanism has a scattering rate $1/\tau$ which can be converted to a mobility μ using [110]

$$\mu = \frac{e\tau}{m^*}. \quad 6.10$$

Here, e represents the magnitude of the charge of the charge carrier (1.6×10^{-19} C) and m^* is the effective mass. The individual scattering rates of each scattering mechanism can then be combined by Matthiessen's Rule, equation 6.11 [19, 110], to give a total scattering rate ($1/\tau_{tot}$), where

$$\frac{1}{\tau_{tot}} = \sum_{i=0}^n \frac{1}{\tau_i}. \quad 6.11$$

In the model described here and implemented in nextnano, there are five prominent scattering mechanisms considered: optical phonons, acoustic phonons, charged background impurities (including the unintentional native defects which were discussed earlier), remote ionized impurities (including the intentional dopants) and interface roughness. Interface roughness scattering is the scattering from non-uniform growth of

the interface and can be significant in thin quantum well structures. It has, however, been suggested by several groups, that this effect is not significant for the single interface heterojunctions [111, 112]. Scattering may also occur due to the low-lying L-band, where high energy electrons may exchange between the bands, giving an associated change of momentum. S.P. simulations show this is unlikely, however, so this form of scattering has not been considered. It is assumed that there is only one energy level and that it resides in the well.

6.4.1 Impurity Scattering

Charged impurities are generally the main limitation of mobility at low temperatures for many semiconductor structures [113-116]. Although the background charged and remote ionized impurity scattering rates can be vastly different, they both stem from the same principles. Impurity scattering is not directly temperature dependent but does contain temperature dependent parameters that contribute to the scattering rate. On average, a conducting electron will travel for a certain length of time unscattered (the quantum lifetime), before then being deflected by a charged ion. After this Coulomb interaction the momentum of the electron will change. However, due to conservation of energy, the magnitude of the wave vector before the scattering event, k , must equal the magnitude of the wave vector after the event, $k + q$, and it is only the direction of the wave vector that is changed through a scattering angle, θ . This is shown schematically in Figure 6.11.

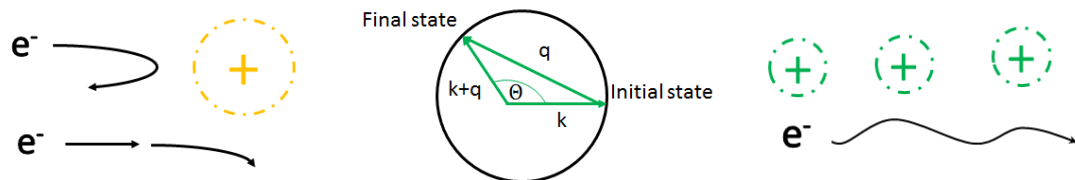


Figure 6.11: **Left:** A charged impurity scattering electrons. **Middle:** The conservation of energy for a scattering event with a scattering angle of θ [36]. **Right:** The scatter due to a charged plane of dopant ions.

Fermi's Golden rule allows the calculation of the rate of transition from an initial momentum state to a final state. This is dependent on the perturbation in the potential of the crystal that the electron moves through; this perturbation is given by the potential energy of the ion. This can also be thought of as the probability that for a given scattering event, a particular momentum will be exchanged. However, the description above is just a scattering rate due to a single electron and a single impurity, a more general form suitable for a whole system must be considered[21, 117].

To determine the scattering rate for a whole system, first consider that there are many possible final states (many differences in momentum due to a collision). The scattering

rate will then be given by the integral of the individual scattering rates for each electron wave vector, k . The large number of impurities can then be considered by simply multiplying the single impurity scattering rate by the impurity concentration per area (n_{imp}^{2D}), assuming the scattering from each impurity is independent. A weighting with angle is also included as a shallow angle scattering would have much less of a perturbation effect on the transport of electrons than backscatter. The general case for impurity scattering $1/\tau_{tr}$ is therefore [36]

$$\frac{1}{\tau_{tr}} = n_{imp}^{2D} \frac{m^*}{2\pi\hbar^3 k_f^3} \int_0^{2k} |\tilde{V}(q)|^2 \frac{q^2 dq}{\sqrt{1 - \left(\frac{q}{2k_f}\right)^2}}. \quad 6.12$$

Here $\tilde{V}(q)$ is the matrix element, a function of the potential energy perturbation, q is the wave vector associated with the change in momentum due to the scattering event, defined as $q = 2k \sin(\theta/2)$, and k_f is the Fermi wave vector defined as $k_f = (n_{2D} 2\pi)^{0.5}$.

Remote impurity scattering for doping can be described as the scattering brought about by ions that are introduced into the system through modulation doping. The matrix element for this case is the unscreened Coulomb potential for the plane of ions, scaled by the Thomas-Fermi dielectric function, where it is assumed that the 2DEG is of a δ width. A form factor is then used to account for the shape of the wave function given by $\left(\frac{b}{b+q}\right)^3$ [36]. This form factor is required as a triangular shaped well is strictly too rigid a structure and this accounts for the band bending and broadness of the wave function. Similarly, a form factor (G) is needed to modify the Thomas-Fermi dielectric function, resulting in a matrix element of:

$$V_{Scr}(q) = \left(\frac{e^2}{2\varepsilon_0\varepsilon_s} \frac{\exp(-q|d|)}{q} \right) \left(\frac{1}{1 + \frac{q_{TF}}{q}} \right), \quad 6.13$$

and scattering rate,

$$\frac{1}{\tau_{ion}} = n_{imp}^{2D} \frac{m^*}{2\pi\hbar^3 k_f^3} \left(\frac{e^2}{2\varepsilon_0\varepsilon_s} \right)^2 \int_0^{2k} \frac{\exp(-2q|d|)}{(q + q_{TF}G(q))^2} \left(\frac{b}{b+q} \right)^6 \frac{q^2 dq}{\sqrt{1 - \left(\frac{q}{2k_f}\right)^2}}, \quad 6.14$$

where,

$$G(q) = \frac{1}{8} \left(2 \left(\frac{b}{b+q} \right)^3 + 3 \left(\frac{b}{b+q} \right)^2 + 3 \left(\frac{b}{b+q} \right) \right). \quad 6.15$$

Here, b is the Fang Howard parameter which is defined by material parameters such that $b = \left(\frac{33m^*e^2n_{2D}}{8\hbar^2\epsilon_0\epsilon_s} \right)^{1/3}$ [118]. The distance from the dopant plane to the 2DEG is given by d , and the relative permittivity is given by ϵ_s and the Thomas-Fermi screening wave vector is given by q_{TF} . A more rigorous mathematical derivation is provided in (e.g.) Ref [36] pp 353-358.

The mathematical transition to the background impurity scattering (a 3D distribution of impurities including impurities in the 2DEG) is small. The same expression can be used by treating the structure as an infinite number of layers with constant n_{imp}^{3D} throughout the structure (and so by integrating over d), the scattering rate, $1/\tau_{Bkg}$, is given by

$$n_{imp}^{2d} e^{-2q|d|} \rightarrow n_{imp}^{3D} \int_{-\infty}^{\infty} e^{-2q|d|} dd = \frac{n_{imp}^{3D}}{q}, \quad 6.16$$

$$\frac{1}{\tau_{Bkg}} = n_{imp}^{3D} \frac{m^*}{2\pi\hbar^3 k_f^3} \left(\frac{e^2}{2\epsilon_0\epsilon_s} \right)^2 \int_0^{2k} \frac{1}{(q + q_{TF})^2} \frac{qdq}{\sqrt{1 - \left(\frac{q}{2k_f} \right)^2}}. \quad 6.17$$

6.4.2 Phonon Scattering

A phonon is a quantised lattice vibration, which causes a displacement of the atoms within the lattice and can be thought of as a wave or a colliding particle much like a photon.

At 0 K in an ideal crystal, there is no thermal kinetic energy within the crystal lattice and so the atoms are (theoretically) not displaced from equilibrium. As the temperature and kinetic energy increases, the masses that make up the lattice are displaced. This vibration has a quantised energy in units of $\hbar\omega$. As the phonons move the ionic cores, magnetic and electric fields are induced which scatter the electrons [119]. Alternatively, due to their quantised nature, a phonon can be thought of as a particle with a momentum of $\hbar\mathbf{k}$, where \mathbf{k} is the phonon's wave vector. When the phonon collides with an electron it exchanges its momentum [120-122].

There are two types of phonon considered here, the acoustic phonon and the optical phonon, where both are temperature dependent. Both reduce the mobility significantly at higher temperatures.

The vibration from an optical phonon causes the neighbouring charged masses to move out of phase, producing an electric field that deflects the travelling electron, this occurs in all III-V semiconductors [36].

The optical phonon scattering rate ($1/\tau_{op}$) is determined by equation 6.18 and is dependent on the number of phonons $N(\omega_0)$ according to

$$\frac{1}{\tau_{op}} = \sqrt{\left(\frac{2m^*\omega_0}{\hbar}\right)} \frac{e^2 N(\omega_0)}{8\varepsilon_p \hbar}. \quad 6.18$$

In equation 6.18, $\varepsilon_p^{-1} = \varepsilon_\infty^{-1} - \varepsilon_s^{-1}$.

Bose-Einstein statistics can be used to find the number of phonons at a particular temperature (as phonons do not obey the Pauli Exclusion Principle they can be mathematically treated as bosons [36]), giving the number as

$$N(\omega_0) = \left[\exp\left(\frac{\hbar\omega_0}{k_b T}\right) - 1 \right]^{-1}, \quad 6.19$$

where ω_0 is the frequency of the phonon and k_b is the Boltzmann constant.

Though this is the scattering rate used by nextnano, as suggested by Price *et al.* [123], another scattering rate has been used in other works (e.g. [36, 109]) which has a quantum well width, w , dependence, as suggested by Ridley *et al.* [124]. This scattering rate is given in equation 6.20, such that

$$\frac{1}{\tau_{op}} = \frac{e^2 \omega_0 N(\omega_0) m^* w}{4\pi \varepsilon_p \hbar^2}. \quad 6.20$$

The differences between the two resultant scattering rates are discussed later in section 6.5.1, whilst the full differences in the derivation are discussed in ref [125].

Analogous to a sound wave, the longitudinal acoustic phonon compresses and expands the lattice structure, with neighbouring lattice atoms moving coherently [36]. The deformation of the lattice structure can lead to a small energy shift of the local band edge. The deformation potential, Ξ , is a function of the crystal characteristics describing this lattice dilation [126] and associated energy change. The acoustic scattering rate is then found with equation 6.21 [109], such that

$$\frac{1}{\tau_{ac}} = \frac{3m^* \Xi^2 k_b T}{2\hbar^3 \rho_d v_s^2 w}, \quad 6.21$$

where ρ_d is the density of the lattice and v_s is the longitudinal sound velocity in the crystal [110].

6.4.3 Interface Roughness

In transport modelling, the quantum well in a heterostructure is generally approximated to an infinite square well. The lower potential is physically described as a layer of material with a lower lying conduction band (and often a lower band gap) and with a width w . The energy levels in the well are then given by E_n , where the ground state energy is given by $n = 1$, such that

$$E_n = \frac{n^2 \pi^2 \hbar^2}{2m^* w^2}. \quad 6.22$$

These heterostructures are grown using MBE, layer upon layer, and although this growth process is accurate, it is difficult to create a perfectly flat and smooth layer and thus an atomically flat quantum well [127, 128]. Thus, the variation in the quantum well width will affect the trajectory of the electron [129, 130], as the wavefunction will firstly shift its peak position, and secondly, the energy state the electron is at. Figure 6.12 shows the variation in the ground state energy against well width. This, of course, is a simple inverse square relationship as seen above.

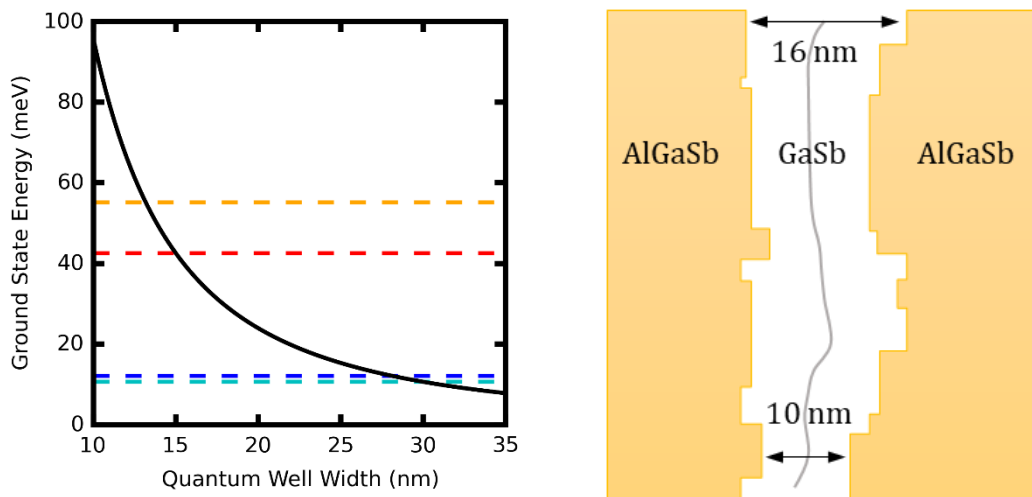


Figure 6.12: **Left:** The variation in the ground state energy for a quantum well with a subtraction of 3 monolayers (orange dashed) from a well width of 15 nm (red dashed) and the same variation for a 30 nm well width (light and dark blue dashed) **Right:** A schematic diagram showing an extreme case of how the well width can vary across a structure with a line indicating the approximate midpoint of the well and thus likely the wave function peak.

However, Figure 6.12 highlights the significant change in ground state energy at lower well widths for only a few monolayers of variation. At a width of 30 nm the change in energy for a 3 monolayer variation is 1.4 meV, whilst at a width of 15 nm, the

corresponding change in energy is much larger at 12.6 meV. Each variation of well width causes the ground state energy to change with a perturbation of \hat{V} , which can be used to find the scattering rate for interface roughness, where \hat{V} is given by

$$\hat{V} = \frac{\pi^2 \hbar^2}{m^* w^3} \Delta(\mathbf{r}). \quad 6.23$$

In the equation above, $\Delta(\mathbf{r})$ is the interface roughness function describing the probability that the roughness, Δ , has the same value at different distances from a given point (see Figure 6.13).



Figure 6.13: A diagram that describes the different parameters of interface roughness. L is the roughness extent, Δ is the rms average roughness and $\Delta(\mathbf{r})$ the probability function [110].

The vector \mathbf{r} is a two-dimensional position vector in the (x, y) plane [131]. As the magnitude of \mathbf{r} increases, the probability of the roughness being the same decreases, such that

$$\Delta(\mathbf{r}) \approx \Delta^2 \exp\left(-\frac{r^2}{L^2}\right), \quad 6.24$$

where L represents the roughness extent. The scattering rate for the interface roughness is then described by equation 6.25, with a particularly strong dependence on well width (w^{-6}), giving

$$\frac{1}{\tau_{int}} = \frac{\pi^4 \hbar \Delta^2 L^2}{2m^* w^6 k_f^3} \int_0^{2k_f} \exp\left(-\frac{q^2 L^2}{4}\right) \frac{q^2 dq}{\sqrt{1 - \left(\frac{q}{2k_f}\right)^2}}. \quad 6.25$$

This strong well width dependence is the reason why, in general, thin well widths were avoided in the Schrödinger-Poisson simulations.

6.5 Simulation of GaSb Heterostructure Transport Properties

Each of the scattering mechanisms above are calculated in nextnano across temperature, with the total mobility also calculated. There are many parameters used in the transport model; the material dependent parameters are stated in Table 6.4, indicating the reference for the value. Other parameters used vary with the structure and so will be

stated where relevant. The native defects were assumed to have a p -type density of $5 \times 10^{16} \text{ cm}^{-3}$ for all of the structures.

Table 6.4: A table to indicate the parameters used for the transport model, including the reference each value was acquired from.

Scattering Mechanism	Input Parameter	Value	Reference
Optical phonon, Remote ionised impurities, Background impurities	ϵ_s	$15.7 \epsilon_0$	S. M. Sze and K. Ng <i>et al.</i> [27]
Optical phonon	$\hbar\omega_0$	29.8 meV	Basinski <i>et al.</i> [132]
	ϵ_∞	$14.5 \epsilon_0$	Patrini <i>et al.</i> [133]
Acoustic phonon	ρ_d	$5.614 \times 10^3 \text{ kg/m}^3$	Dutta <i>et al.</i> [9]
	v_s	$3.24 \times 10^3 \text{ m/s}$	Dutta <i>et al.</i> [9]
	Ξ	9 eV	Adachi <i>et al.</i> [134]

It is seen here that the dielectric constant is present in multiple scattering mechanisms. Scattering from phonons tends to be dominant at room temperature whereas the other scattering mechanisms are dominant at lower temperature. The dielectric constant is present in both phonon ($\mu_{Op} \propto \epsilon_p$) and impurity scattering ($\mu_{Rii,Bkg} \propto \epsilon_s^2$), thus, it is prominent across temperature. Having a large dielectric constant as is the case in GaSb, makes the material preferable to others for high mobility devices. This assumption is a simplification of the many factors at play required to create high mobility devices. Other factors must be considered such as background impurity concentration. This factor in particular is significant in the case of GaSb.

The interface roughness parameters, the rms average roughness Δ and the roughness extent L , are not known for these samples. As such, the interface roughness scattering mechanism will be used as a fitting parameter to match the measured data to the modelled mobility in the subsequent chapter. The rms average roughness would be expected to be no more than a few monolayers for MBE grown samples. The roughness extent is harder to estimate though tends not to be more than a few nanometres [135]. For now, parameters will be assumed to be on the higher end of a reasonable range of $\Delta = 1.5 \text{ nm}$ (~ 5 monolayers) and $L = 5 \text{ nm}$, as to not overestimate the predicted mobility [135]. The interface roughness scattering rate is approximately proportional to $(\Delta L)^2$,

however the harsher dependency is on the well width (w^{-6}) which will have a greater effect. This is logical as 4 monolayers of change has a greater proportional change on the width of smaller well, and also causes a greater change in the energy states of that well.

6.5.1 Structural Variations in the Transport Model

The structures simulated by the S.P. solver showed that there are multiple design options that can lead to 2DEGs in GaSb. There are many structural parameters considered in the transport model, with each potentially changing the resulting mobility. Therefore, changes in mobility due to a change in the overall structure makes it hard to determine which structural change is the most significant. Discussions of the effect of changing structural parameters are given below, highlighting the complexities of the relationships which result in the total mobility. The effect of variations in the well width, the spacer and the carrier density are discussed.

The well width is present in the acoustic phonon scattering rate, in the Ridley model for the optical phonon [124], and in the interface roughness, and thus is prominent across temperature. The mobility in a quantum well as a function of well width ranging from 10 nm to 30 nm with both barriers doped has been simulated, with the results shown in Figure 6.14. For this simulation, a doping concentration of $1 \times 10^{17} \text{ cm}^{-3}$ on either side of the well was assumed, with a spacer of 20 nm above the well and 50 nm below the well. The defect concentration was assumed to be $5 \times 10^{16} \text{ cm}^{-3}$ and the carrier density was set to be $6 \times 10^{11} \text{ cm}^{-2}$, as predicted by the S.P. modelling. The interface roughness parameters Δ and L were set at 1.5 nm and 5 nm respectively.

For each scattering mechanism, the corresponding mobility is added inversely to determine the total mobility. As such, the largest contribution will come from the scattering mechanism with the lowest mobility (largest scattering rate). This is considered the limiting scattering rate.

It can be seen from Figure 6.14, that the acoustic phonon mobility increases with well width. At room temperature this increase is from $7.0 \times 10^4 \text{ cm}^2/\text{Vs}$ to $2.0 \times 10^5 \text{ cm}^2/\text{Vs}$ for an increase in well width from 10 nm to 30 nm respectively.

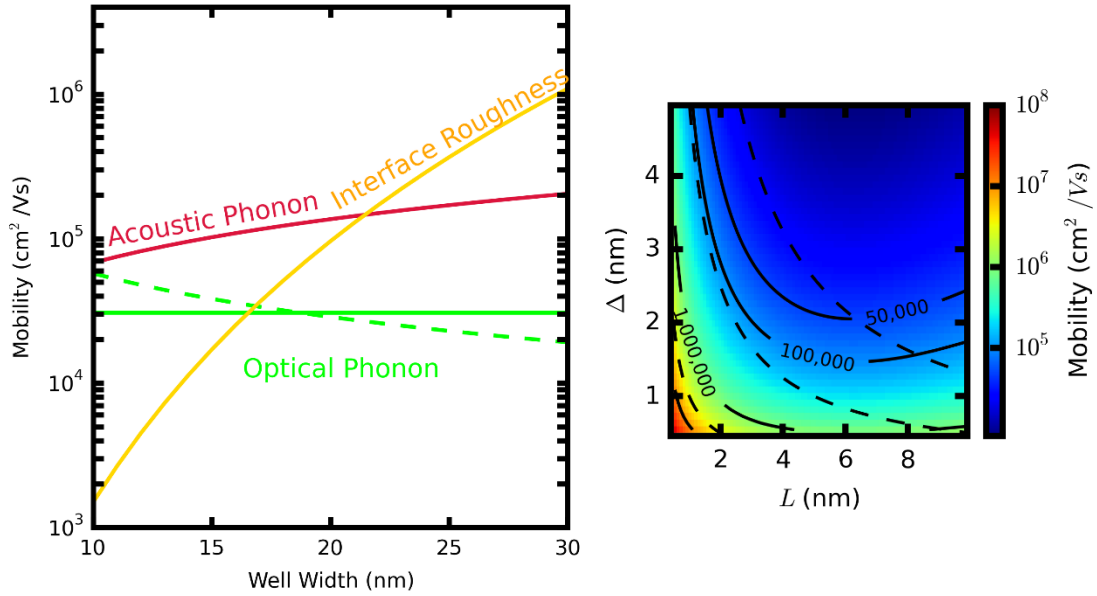


Figure 6.14: Left: The mobility for each well width dependent scattering rate against well width at 300 K for a GaSb quantum well. The green dashed line indicates the optical phonon scattering rate used by Ridley *et al.* [124] and the green solid line is the optical phonon as calculated by nextnano. **Right:** A graph showing the mobility due to the interface roughness variation with the roughness parameters at a well width of 20 nm. The colours represent the mobility and the scale is shown on the colour bar. The solid lines show contours of constant mobility and the dashed lines are lines of constant ΔL .

Below 20 nm, the acoustic phonon scattering is the least significant of the scattering rates (it is not the limiting factor) and the lowest contribution to the total mobility when only these mechanisms are considered. Above 20 nm, it falls below the interface roughness scattering rate but still considerably higher than the optical phonon. The optical phonon scattering rate given by Ridley *et al.* has the inverse relationship with well width and as such changes from $5.5 \times 10^4 \text{ cm}^2/\text{Vs}$ to $2 \times 10^4 \text{ cm}^2/\text{Vs}$ as the well width increases. It is observed that at a well width of 18 nm the nextnano optical phonon scattering rate (Price *et al.*[123]) and the Ridley *et al.* solutions match.

The interface roughness drastically changes across well width. Below a well width of 16.5 nm it becomes the limiting scattering rate, whereas above a well width of 24 nm it becomes an order of magnitude higher than the optical phonon.

As temperature decreases the phonon scattering rate will reduce. Of these scattering mechanisms, the interface roughness will be the dominant scattering mechanism at lower temperatures. Therefore, when designing a sample structure, this scattering rate should be as low as possible to achieve the largest (low temperature) mobility possible. As such, in the case of interface roughness scattering, the larger the well the better. However, in

terms of solutions to the Schrödinger equation, as the well width gets larger there is a decrease in energy at which each state lies, and the spacing between states decreases, allowing for scattering to occur between states. This is a careful balance that needs to be considered, especially as the well width has a greater effect on the interface roughness than the rms roughness and roughness extent. For a quantum well of 20 nm, to achieve a mobility contribution of the interface roughness of $5 \times 10^4 \text{ cm}^2/\text{Vs}$ it would require a rms roughness of 8 or more monolayers (2.5 nm), as seen in Figure 6.14 Right. Whereas the same contribution can be achieved by a reduction in well width of 2 nm, as seen in Figure 6.14 left.

In the case of varying the spacer, it would be expected that an increase of the spacer would reduce the scattering of the charge carriers by simply moving the remote ionised impurities further away from the well. This would reduce the electric field which perturbs the electron's path. However, a more realistic picture would require the carrier concentration in the well to also be varied as a result of the change in the spacer. This knock-on effect would then in turn change k_f and thus both the impurity scattering rate and the interface roughness scattering rate. Thus, a variation in spacer cannot be considered independently. The same can be said for the defect concentration, which would not only change the background impurity scattering but the carrier density and again k_f . To account for this, self-consistency with the Schrödinger-Poisson simulations must be considered.

6.5.2 Transport Properties of Simulated $\text{Al}_{0.2}\text{Ga}_{0.8}\text{Sb}/\text{GaSb}$ Structures

In this section, the above transport model is implemented for the structures simulated through S.P. modelling in section 6.3 that showed viable confinement. The predicted mobilities are then compared. These structures consisted of a limited range of heterojunction designs achieving confinement across temperature. The heterojunction structure design doped both above and below the well (but with an undoped well) resulted in unconfined wavefunctions above a temperature of $\sim 80 \text{ K} - 120 \text{ K}$, however this is dependent on the doping concentration. Consequently, the transport-model-predicted behaviour in this temperature range should not be considered representative of what would be physically observed. From this point onwards this structure will be referred to as the “undoped-well”, with the other heterojunction structure doped throughout the structure being referred to as the “doped-well” structure. This doped-well structure resulted in the wave-function being confined across temperature, however this is expected to produce significant scattering which is discussed further in this section.

The transport model for the undoped well heterojunctions is shown in Figure 6.15 with varying doping concentrations. These structures consist of two doped regions and two spacers (one above and one below the well) and thus two distinct contributions to the remote ionised impurity scattering rate. These structures are also assumed to contain a concentration of background impurities associated with the native acceptor defects. The predicted mobility results are produced across temperature with the effect of the movement of the wave-function to bulk neglected (the structure is always considered 2D in the transport model). The graph is shaded, however, to indicate the likely temperature range where the states would reside in the bulk, and so where the results should be interpreted with caution.

Often, when a transport model is implemented to characterise the observed mobility trends in a sample, the corresponding measured carrier density is used. As the transport modelling performed here is being used as a predictive method to aid in the choice of which structure designs to grow and fabricate, the carrier density output from low temperature S.P simulations is used instead, as the low temperature regime is of greatest interest. The low temperature regime is where the mobility will be largest, and the structures will be confined (not necessarily true at temperatures above 100 K).

The level of the doping concentration range considered in these structures ($1 \times 10^{17} \text{ cm}^{-3} - 5 \times 10^{-17} \text{ cm}^{-3}$, equal in the buffer and barrier) will have a couple of effects on the mobility. It will not only directly impact the scattering from the remote ionised impurities via the impurity density, but will also affect the carrier density. This will indirectly impact the other, non-phonon, scattering rates (i.e. the background impurity scattering rate and the interface roughness scattering considered for the quantum wells). Specifically, the remote ionised impurity scattering rate is directly proportional to the doping concentration, but the scattering rate is also proportional to the carrier density via the relationship $1/\tau_{ion} \propto 1/k_f^3$, where k_f is proportional to the carrier density. Combining these relationships, the mobility was shown by Hayne *et al.* [115] to be proportional to $n_s^{1.5}/N$, where n_s is the carrier density and N is the density of dopants. Qualitatively, this can be understood by considering that as the doping concentration is increased, the remote ionised impurity scattering would also be expected to increase. However, as the doping level is increased, the screening from the carrier density increase will have a reducing effect on the scattering, where this has a stronger relationship. This would imply that a large doping concentration would be preferable. However, the doping concentration does not simply equal the carrier concentration. As the doping concentration is increased, the carrier concentration will increase, but some carriers may

be lost to the surface and thus they are not necessarily increasing at the same rate. This is also an oversimplification which assumes the band structure profile does not change with doping concentration, which is not the case. As was seen in the S.P. simulation results in section 6.3, an increase in doping concentration in certain structures can lead to states lying outside of the confined region.

A doping concentration range was investigated self-consistently with the Schrödinger-Poisson carrier density to produce Figure 6.15 left, where the variation shows how the increased carrier density changes each scattering mechanism. An independent study of remote ionised impurity scattering was also completed. This indicates how an increase in doping concentration will affect the remote ionised impurity scattering mobility if the carrier density is set. This is shown in Figure 6.15 right.

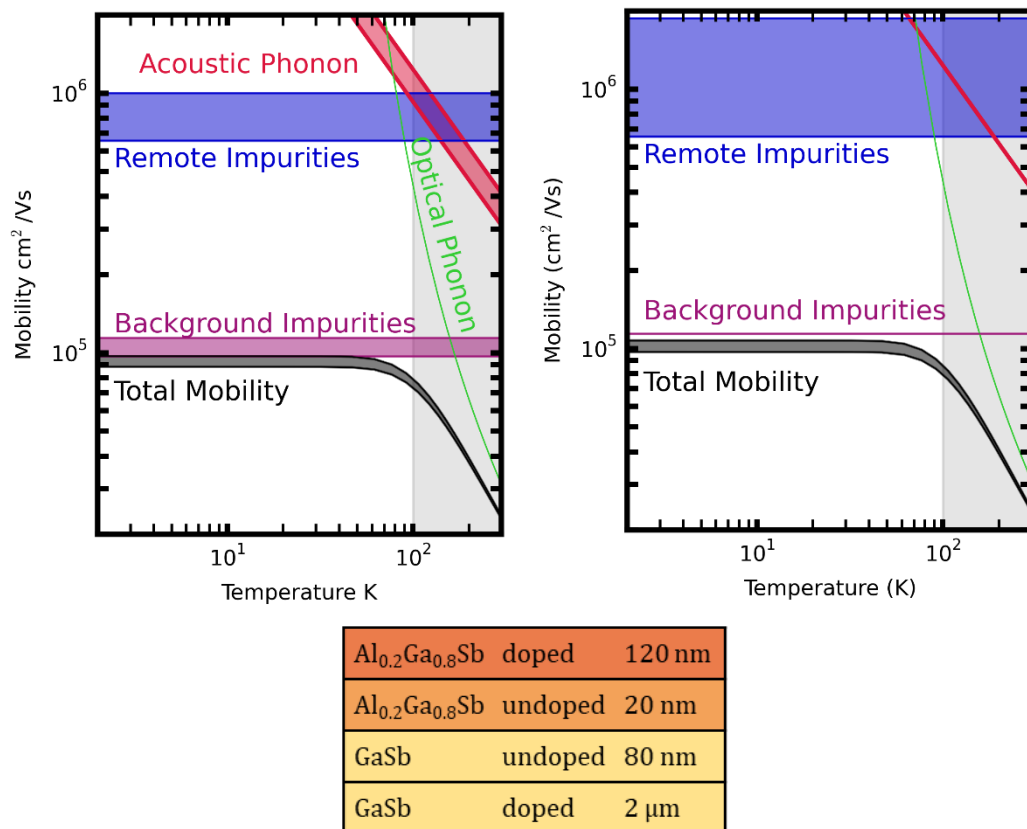


Figure 6.15: Left: A standard transport model for a undoped heterojunction indicating how changing the doping concentration in the range $1 \times 10^{17} \text{ cm}^{-3}$ to $5 \times 10^{17} \text{ cm}^{-3}$ affects each scattering rate, and the associated mobility, directly and indirectly (through carrier density and k_f). Each scattering mechanism is labelled, and regions are shaded to signify the change with doping concentration. The RHS is shaded to indicate the temperature at which the S.P. solver showed that the states deviated to the bulk. **Right:** A transport model isolating the effect of a change in the remote ionised impurity density using only the remote ionised impurity scattering rate, investigating the effect on the total mobility with carrier density and well width fixed. **Bottom:** A schematic of the structure simulated.

The figure above shows a typical transport model. Here it can be seen that the phonon scattering contribution to the total mobility is significant at higher temperatures (above $\sim 50\text{K}$). In the case of the undoped well, the background impurity scattering for a background charge density of $5 \times 10^{16} \text{ cm}^{-3}$ is by far the limiting scattering rate up to 150 K. This value of background impurity density level is reasonable, though as the growth study performed in Chapter 3 shows, it could be an overestimation. This overestimation would likely be slight, and even a reasonable lower limit estimate of defects results in a background-scattering-limited structure. This is as well as significant contribution the defect concentration makes through the variation of the band structure itself as seen in section 6.3.1.

Figure 6.15 right shows that the decrease in the doping concentration from $5 \times 10^{17} \text{ cm}^{-3}$ to $1 \times 10^{17} \text{ cm}^{-3}$ (neglecting any associated change in carrier density) results in a decrease in remote ionised impurity scattering, as expected. This reduction in scattering has an associated increase in mobility from $6.5 \times 10^5 \text{ cm}^2/\text{Vs}$ to $1.89 \times 10^5 \text{ cm}^2/\text{Vs}$. However, as this is not the limiting scattering rate, the total mobility is only changed by 17 %. Similarly, if the carrier density change associated with the change in doping concentration is also considered, the overall mobility changes by only 9 %.

The next design consideration from the S.P. simulations was the doped heterojunction structure. This structure drastically improved confinement across temperature, however this requires doping the well with a concentration of $\sim 1 \times 10^{17} \text{ cm}^{-3}$. As can be seen in Figure 6.15 above, the mobility is limited by the background impurities at the $\sim 5 \times 10^{16} \text{ cm}^{-3}$ level of the native acceptor concentration, with the higher dopant concentration of $\sim 1 \times 10^{17} \text{ cm}^{-3}$ here only reducing the mobility further. As the doping is no longer remote, the 3D doping concentration will be implemented in the same way as background impurity concentration. This will be in addition to the native defects.

Figure 6.16 shows a comparison of the doped well and undoped well heterojunctions with doping concentrations of $5 \times 10^{17} \text{ cm}^{-3}$. The undoped well structure has scattering contributions from the remote ionised impurities and the background impurity concentration resulting in a mobility of $9.7 \times 10^4 \text{ cm}^2/\text{Vs}$ at low temperatures. The doped well structure is again ionised impurity limited across temperature, where this is unsurprising with such a significant increase in the 3D impurity concentration. The total mobility at low temperature for the doped well structure is $7.2 \times 10^3 \text{ cm}^2/\text{Vs}$.

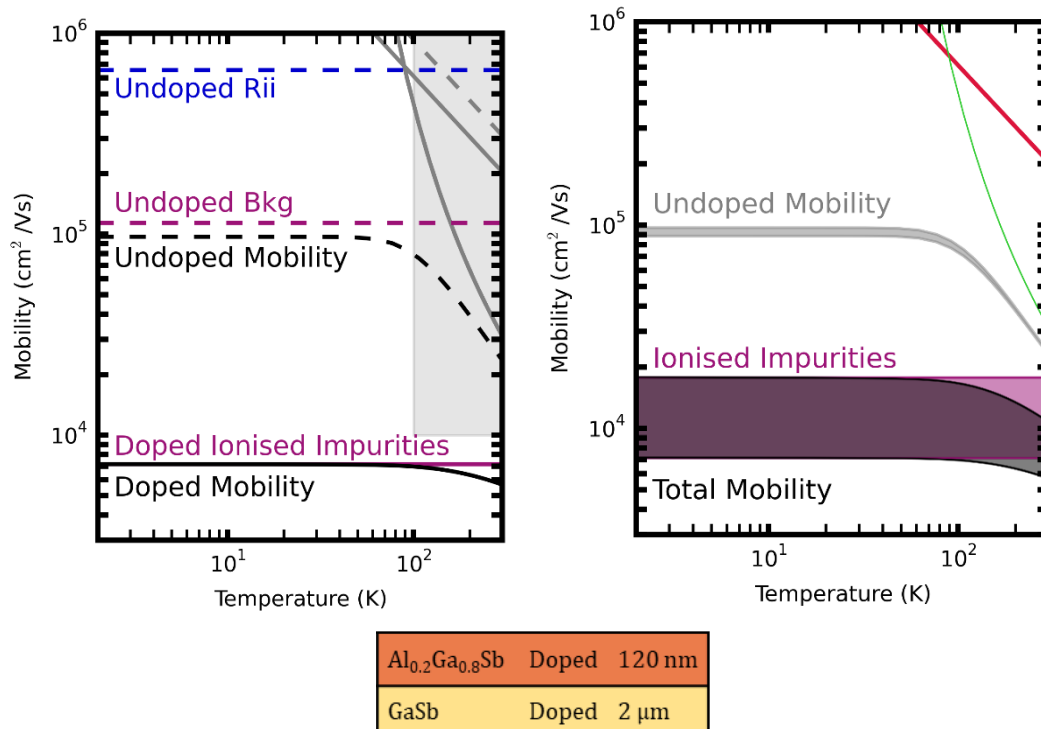


Figure 6.16: **Left:** The calculated mobilities for a heterojunction with a doped (solid line) and undoped (dashed) well with doping concentration $5 \times 10^{17} \text{ cm}^{-3}$. The grey shaded region at high temperature is to signify the region where the undoped well may have bulk states (i.e. not confined to the well). **Right:** The transport model for the full range of doping considered ($1 \times 10^{17} \text{ cm}^{-3}$ to $5 \times 10^{17} \text{ cm}^{-3}$) for a uniformly doped structure indicating the significance of the ionised impurity scattering. The range of calculated mobilities for the equivalent undoped well structures is shown in grey. **Bottom:** A schematic diagram of the structure simulated where the doped region varies as described above.

Comparing the predicted mobilities at a doping level of $5 \times 10^{17} \text{ cm}^{-3}$ maybe somewhat of an extreme comparison as this is a significant doping level at the higher end of the range considered, and therefore a high impurity concentration to lie in the well. The full doping range for the doped triangular well is shown in Figure 6.16 right.

This figure shows the calculated mobility for the doping range of $1 \times 10^{17} \text{ cm}^{-3}$ to $5 \times 10^{17} \text{ cm}^{-3}$ for the doped well structures, as well as the undoped well total mobility for the same range. It can be seen for all ranges of doping, the doped well structure is approximately an order of magnitude lower in mobility at low temperature as compared to the undoped well. The decrease in mobility towards room temperature is shallower in the doped well structures due to the phonons having a reduced contribution to the total mobility as compared to the previous heterojunction design.

Whilst the doped well ensures confinement, this also introduces a significant change in mobility compared to the undoped well. Thus, square quantum well structures were also investigated to give confinement whilst still enabling remote doping.

The square quantum wells examined previously were designed with an undoped well of width 25 nm. The spacers above and below the well are 20 nm and 50 nm respectively, the latter chosen to prevent Te dragging into the well during growth. An extended doping range of $1 \times 10^{17} \text{ cm}^{-3}$ to $7 \times 10^{17} \text{ cm}^{-3}$ was considered in the S.P. simulations, with all doping levels resulting in confined structures and, therefore, only the extremes of the doping range will be considered here. Interface roughness scattering will also be included in these calculations with the parameters $\Delta = 1.5 \text{ nm}$ (~ 5 monolayers) and $L = 5 \text{ nm}$ used as the upper of the reasonable range considered previously.

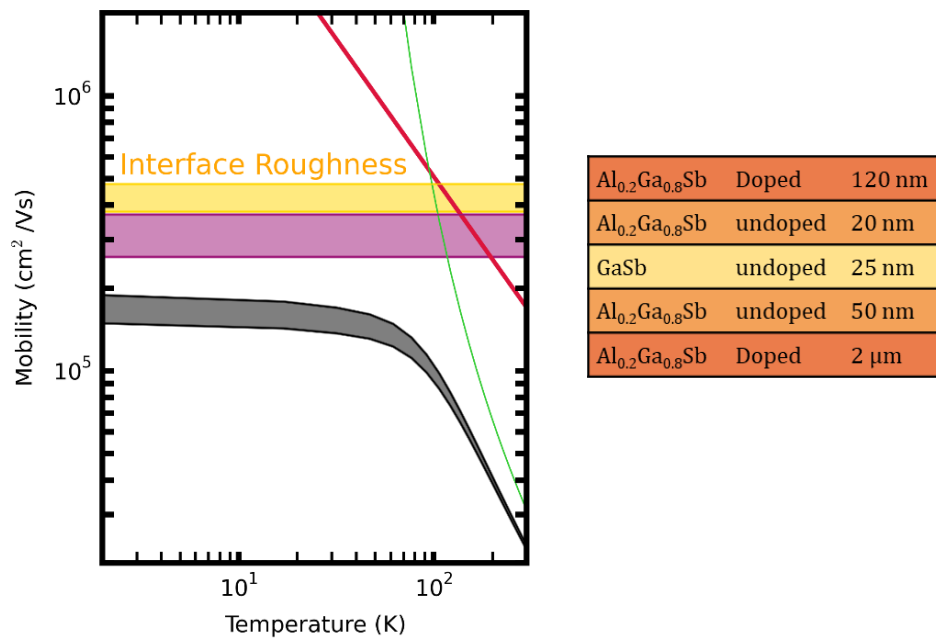


Figure 6.17: Left: A standard transport model indicating how changing the doping concentration in the range $1 \times 10^{17} \text{ cm}^{-3}$ to $7 \times 10^{17} \text{ cm}^{-3}$ affects the mobility of a square quantum well. Regions are shaded to signify the change with doping concentration. The mobility due to scattering from remote ionised impurities is not visible on this scale. Right: A schematic diagram of the structure that was simulated where the doped region varies as described above.

It is seen from Figure 6.17 that the background impurities are again the limiting scattering mechanism at low temperature. The mobility due to scattering from remote ionised impurities is not visible on this scale. This is due to the increase of the carrier density by an order of magnitude compared to the triangular well case, leading to a large increase in screening through the Fermi wavevector. This increase in carrier density may be due to

the dopant in both barriers supplying the well with electrons. In the heterojunction case, electrons are only being supplied from one barrier.

A similar effect is seen in the background-impurity-scattering-related mobility, which has increased from the heterojunction case by a factor of 3 in Figure 6.17. This is the same factor as for the mobility due to the remote ionised impurities. The inclusion of interface roughness decreases the low temperature total mobility further by a factor of ~ 0.6 as compared to the ionised impurities alone. However, despite this decrease due to the interface roughness, the total mobility is still improved as compared to the heterojunction structures, as is seen below.

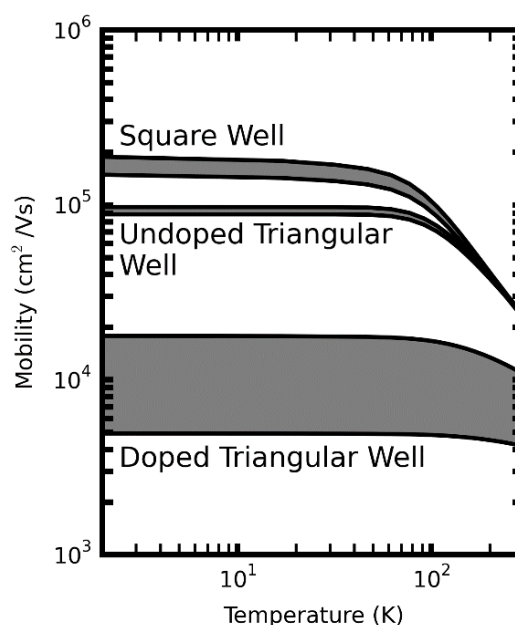


Figure 6.18: The total mobility for each structure design with the full doping range shown.

The doped triangular well is seen here as the lowest mobility option. Though, from the Schrödinger-Poisson simulations, it was shown that this doping structure was necessary for a single heterojunction to be confined across temperature. Therefore, if this structure is to be investigated, the lowest doped option is preferable.

The undoped triangular well shows little variation in the total mobility across the doping range considered. This structure is almost an order of magnitude higher mobility than its doped counterpart, however, the band structure simulations show a potential for the wave functions to be lost to the bulk.

The square well eliminates this problem, whilst also achieving a higher mobility at low temperature as compared to the heterojunctions. The primary concern with this structure

however is the potential two-carrier nature and the associated potential inter-subband scattering that can occur, which was not considered in the transport model.

6.6 Conclusion

Various designs of GaSb/Al_{0.2}Ga_{0.8}Sb heterostructures were investigated using a Schrödinger-Poisson solver in order to determine the confinement in the structures. It was found that heterojunctions could not simply be doped in the barrier. This is due to the alignment of the Fermi level of the *n*-type region and the unintentionally doped region, meaning the states would reside in the barrier not at the junction, or the Fermi level would be in the band gap. Heterojunctions were further investigated with the buffer doped to compensate out the *p*-type background. A spacer was left to prevent Te dragging into the well causing significant scattering. This design with an intentionally undoped region forming the triangular well resulted in confinement at low temperatures but the confined states strayed into the buffer or into the barrier as temperature increased.

A fully doped structure was also investigated, with this resulting in confinement, however the Te atoms present in the well will cause significant scattering and thus lower mobility. This was shown in the transport model with this structure having a consistently lower mobility than the undoped well structure. Due to the difficulty of achieving confinement in single heterojunctions, square quantum wells were also investigated. These structures eliminated the difficulty of achieving confinement, though introduced a new issue in the form of two confined states in the well.

Once the structures were confirmed to have confinement, a variations in these structures were further examined using the described transport model. The transport model revealed that the square quantum wells resulted in the highest mobility of all the structures investigated. The doped well heterojunction resulted in the lowest mobility in all cases. The difference in mobility for the square well and the heterojunction with an undoped triangular well is due to the increase in carrier density in the square well for comparable doping levels. This increase in carrier density increases the screening from the remote ionised impurity scattering and the background impurity scattering. This model does not consider inter-subband scattering where this could reduce the mobility further.

As a result of these simulations, it was decided to grow and measure a selection of these designs as these structures have many differences, with both advantages and disadvantages. Further allowing the simulations to be verified by measurement. A summary of the structures that were physically realised is shown in the figure below.

Doped Triangular Quantum Well

$\text{Al}_{0.2}\text{Ga}_{0.8}\text{Sb}$	doped	120 nm
GaSb	doped	2.2 μm
GaAs Semi-insulating Substrate		

Undoped Triangular Quantum Well

$\text{Al}_{0.2}\text{Ga}_{0.8}\text{Sb}$	doped	120 nm
$\text{Al}_{0.2}\text{Ga}_{0.8}\text{Sb}$	undoped	20 nm
GaSb	undoped	80 nm
GaSb	doped	2.2 μm
GaAs Semi-insulating Substrate		

Square Quantum Well

$\text{Al}_{0.2}\text{Ga}_{0.8}\text{Sb}$	doped	120 nm
$\text{Al}_{0.2}\text{Ga}_{0.8}\text{Sb}$	undoped	20 nm
GaSb	undoped	25 nm
$\text{Al}_{0.2}\text{Ga}_{0.8}\text{Sb}$	undoped	50 nm
$\text{Al}_{0.2}\text{Ga}_{0.8}\text{Sb}$	doped	2.2 μm
GaAs Semi-insulating Substrate		

Figure 6.19: The final structures to be grown and measured informed by the simulations performed in the chapter.

Chapter 7

Measurement of GaSb Transport Properties

The transport properties (mobility and carrier density) of various semiconducting materials have been of great interest for decades. The fundamental understanding of how to achieve high mobility devices stems from the Hall effect, where resistivity is measured against magnetic field. The mobility can then be further analysed using a transport model, giving understanding of the limiting scattering mechanisms, and allowing for improvements to be made in the structure to produce higher mobility devices. The determination of the mobility and the carrier density is generally performed through relatively low field B -field measurements. In the high field regime, though the set up does not change, different physical processes occur in the sample. This chapter will give an overview of the theory and implementation of both the low-field and high field regime in which the $\text{Al}_{0.2}\text{Ga}_{0.8}\text{Sb}/\text{GaSb}$ samples were measured.

Confined $\text{Al}_{0.2}\text{Ga}_{0.8}\text{Sb}/\text{GaSb}$ structures that have been simulated in the previous chapter, Chapter 6, and have been grown using the optimal growth conditions ($T_g = 475^\circ\text{C}$, $V/\text{III} = 1.3$) found in Chapter 3. The structures were then fabricated into Hall bars following the procedure described in Chapter 4, using the optimal metallisation recipe found in Chapter 5 of Pd/In/Pd/Au, 5/40/6/100 nm, which was then annealed for 10 min at 300°C . The experimental procedure for the characterisation of the transport properties of these structures will be stated here. The longitudinal and transverse resistances as a function of temperature and magnetic field will be presented, and a two-carrier fit extracting the transport properties of the majority carrier will be displayed. The resultant mobility of which will be analysed by the transport model. The transport model will aid describing the predominant scattering mechanisms within these structures. This will

outline any unforeseen factors that would require further thought and analysis in order to optimize these structures for any potential future repeat growths or measurements.

7.1 Measurement Theory of Transport Properties

The theory behind the measurement and analysis methods used to determine a carrier density and mobility for these samples will be outlined in this chapter. From exploitation of the Hall effect, the carrier density and the mobility of charge carriers can be found. This is achieved by measuring the resistance of a sample in particular orientations with respect to the B -field and current direction. However, this measurement will merely reveal the total transport properties across the sample with little indication of how many kinds of carriers there are. The profile of the resistances against magnetic field can indicate whether the sample is single or multi-carrier. Therefore, a two-carrier fit is performed in order to extract relevant transport property information for each carrier species. The details of both the single carrier and multi-carrier analysis methods are outlined below, with a brief description of how the carriers then behave at high enough fields that the simple (non-quantised) Hall effect is no longer suitable.

7.1.1 Measuring 2D Transport Properties

The Hall effect was used to measure the transport properties of $\text{Al}_{0.2}\text{Ga}_{0.8}\text{Sb}/\text{GaSb}$ structures where, unlike the cases described in previous chapters, the sheet carrier density, n_s , is 2D (measured in cm^{-2}) with a 2D resistivity. Therefore, an adjustment is made to the equations that relate the measured values to the transport properties.

The Hall voltage, V_H , produced from the charge separation across the sample, now becomes

$$V_H = \frac{I_x B_z}{en_s}, \quad 7.1$$

with I_x representing the set current through the sample, and B_z representing a magnetic field perpendicular to the current [136]. The carrier mobility, μ , can be extracted from a measurement of the Hall voltage and a longitudinal voltage, V_{xx} , or associated resistivity ρ_{2D} , and is given by

$$\mu = \frac{V_H}{B_z I_x \rho_{2D}}. \quad 7.2$$

It is also useful to note that for all confined structures, a Hall bar geometry was used. The resistivity in this case is found from the resistance measured and adjusted by the aspect ratio L/W . W is the width of the Hall bar and L is the distance between the two contacts that are used to measure the longitudinal voltage, giving

$$\rho_{2D} = R_{xx} \frac{W}{L}. \quad 7.3$$

The 2D resistivity is measured in Ω/\square . The Hall bars were non-gated, 8-pad geometry Hall bars [137]. A variety of sizes were created, though the Hall bars measured in this chapter all had had an aspect ratio of 3.9.

By combining equation 7.2 and 7.3, it can easily be seen that the conductivity, and so the resistivity is given by

$$\sigma = \rho^{-1} = ne\mu. \quad 7.4$$

However, this is a simplification and there can be complications with this measurement when considering B -fields, as technically, the conductivity where $\sigma = \rho^{-1}$ is given by the tensor

$$\boldsymbol{\sigma} = \begin{pmatrix} \sigma_{xx} & \sigma_{xy} \\ -\sigma_{xy} & \sigma_{xx} \end{pmatrix}. \quad 7.5$$

Here it is seen that the total conductivity is dependent on the conductivity in each direction, where the subscripts xx and xy indicate longitudinal and transverse respectively. Therefore, the resistivity in each direction is given by

$$\rho_{xx} = \frac{\sigma_{xx}}{\sigma_{xx}^2 + \sigma_{xy}^2}, \rho_{xy} = \frac{-\sigma_{xy}}{\sigma_{xx}^2 + \sigma_{xy}^2}. \quad 7.6$$

Thus, if there are geometrical offsets in the voltage contacts, inaccuracies can occur in measurement. The Hall bar structure is designed symmetrically, with the intention of not having to address this issue in measurement [28, 138]}[139].

When the sheet carrier density and the mobility are extracted with the equations above, it is assumed that the samples are single carrier, however this is not always the case.

7.1.2 Multi-Carrier Fitting of Conduction

For a number of reasons many samples can be multi-carrier. In this case, any sample with carriers that have different mobilities to each other appear as multicarrier. Different mobilities can originate from a variety of reasons, it may be due to having a different effective mass (e.g. from travelling in the L-band or in the doped $\text{Al}_{0.2}\text{Ga}_{0.8}\text{Sb}$ region) or different energy (e.g. from travelling in the second subband).

An indication of a multicarrier sample is a curving of the expected linear resistivity against field relationship in both the longitudinal and transverse case. To accurately determine the transport properties of each of these carriers a two-carrier fit is employed.

The carrier densities and mobilities of the two carriers are now entwined in the resistivities measured, and thus equations 7.7 and 7.8 are more applicable:

$$\rho_{xx} = \frac{1}{n_1 e \mu_1 + n_2 e \mu_2}, \text{ and} \quad 7.7$$

$$\rho_{xy} = \frac{n_1 e \mu_1^2 + n_2 e \mu_2^2}{e(n_1 \mu_1 + n_2 \mu_2)^2} B_z. \quad 7.8$$

In these equations n_i is the carrier density of carrier i , where $i = 1$ or 2 , and μ_i represents the mobility [140]. It should be noted that these equations are a low field approximation. Within the low field regime, it is seen that where the conductivity contribution ($\sigma = ne\mu$) from one carrier is much greater than the other, both resistivities are dominated by that carrier. It should also be pointed out that ρ_{xx} is invariant to the magnetic field, and ρ_{xy} has a linear relationship. As high fields are approached these equations would no longer be suitable. Instead the resistivities are given by

$$\rho_{xx} = \frac{\frac{n_1 e \mu_1}{1 + B_z^2 \mu_1^2} + \frac{n_2 e \mu_2}{1 + B_z^2 \mu_2^2}}{\left(\frac{n_1 e \mu_1}{1 + B_z^2 \mu_1^2} + \frac{n_2 e \mu_2}{1 + B_z^2 \mu_2^2}\right)^2 + \left(\frac{n_1 e \mu_1 B_z}{1 + B_z^2 \mu_1^2} + \frac{n_2 e \mu_2 B_z}{1 + B_z^2 \mu_2^2}\right)^2}, \text{ and} \quad 7.9$$

$$\rho_{xy} = \frac{\frac{-n_1 e \mu_1^2}{1 + B_z^2 \mu_1^2} + \frac{-n_2 e \mu_2^2}{1 + B_z^2 \mu_2^2}}{\left(\frac{n_1 e \mu_1}{1 + B_z^2 \mu_1^2} + \frac{n_2 e \mu_2}{1 + B_z^2 \mu_2^2}\right)^2 + \left(\frac{n_1 e \mu_1^2 B_z}{1 + B_z^2 \mu_1^2} + \frac{n_2 e \mu_2^2 B_z}{1 + B_z^2 \mu_2^2}\right)^2} B_z. \quad 7.10$$

A full derivation is given in ref [140].

Figure 7.1 shows an example of how each resistivity would vary for a set mobility and carrier density, with a corresponding second carrier of a lower conductivity. It can be determined that when there are two carriers, there is a field dependence in the longitudinal resistance that will make the resistivity stray at high fields. The linear dependence of the transverse resistivity with field also becomes curved. Conversely from above, if a resistivity is measured and assumed single carrier, the high mobility carrier will be underestimated in mobility.

When these non-linear trends are seen, least-squares fitting can be used to apply equations 7.9 and 7.10. These equations can be simultaneously fitted to match the longitudinal and transverse resistivities as a function of B -field, determining a carrier

density and mobility for each carrier type. The figure below shows how the longitudinal resistance becomes more curved as the lower mobility carrier increases in mobility (it is assumed here that the carrier densities were equal). The second graph shows how the transverse resistivity becomes non-linear with a two-carrier sample.

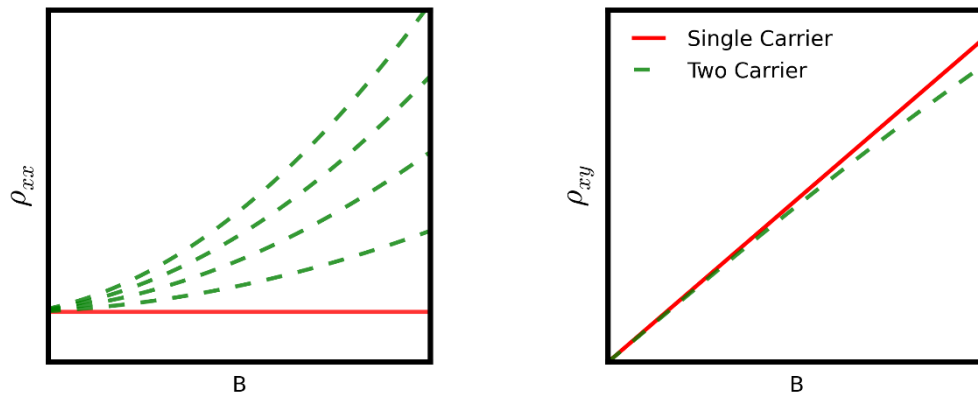


Figure 7.1: The behaviour of each resistivity (ρ_{xx} and ρ_{xy}) when a sample has a single carrier of mobility μ_1 and carrier density n_1 (red solid), and when the sample has two carriers with equal density and the second carrier has a lower mobility (green dashes). **Left:** longitudinal resistivity against magnetic field. **Right:** transverse resistivity against magnetic field.

7.1.3 Carrier Dynamics at High field

The simple Hall effect gives an accurate description of a charged carriers behaviour at low magnetic fields. As the field strength increases the charge carriers path tightens until eventually the circular path is small enough that a carrier can maintain a circular trajectory with a frequency ω_c , the cyclotron frequency, see Figure 7.2. This is of course, just the classical picture.

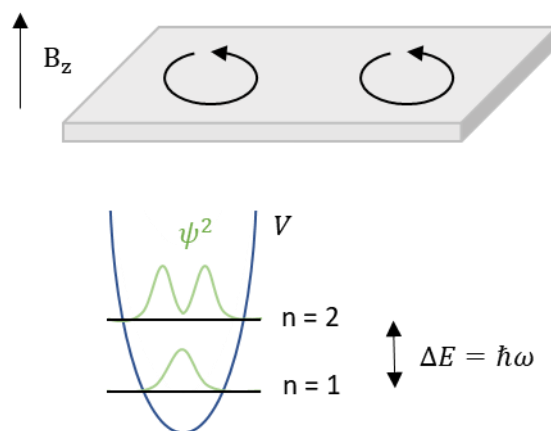


Figure 7.2: A diagram indicating the physical effects that occur at high fields depicted both classically and quantum mechanically.

Each circular orbit, quantum mechanically, can be thought of as a physical position where a series of states exist in a parabolic potential [141]. Much like a parabolic quantum well, there are quantised states within this potential, and the states are equally separated by an energy $\hbar\omega_c$ [141, 142]. These are called Landau levels. The cyclotron frequency is dependent on the magnetic field B and is given simply by [143]

$$\omega_c = \frac{eB}{m^*}. \quad 7.11$$

This cyclotron frequency is also present in the standard Hall effect, however the radius of the orbit is large and so a full orbit isn't complete. There is a large overlap between adjacent Landau levels meaning many quantum mechanical effects present and higher fields are not discernible at lower fields. It is the presence of these Landau levels, or more specifically, the filling of these Landau levels, that causes some unusual behaviour in the conduction of electrons, and thus the resistivity, as a function of magnetic field.

These Landau levels, due to scattering in the samples, are not distinct levels, but instead have a broadness in energy. The separation between Landau levels is increased with B field according to 7.11 and once the separation is comparable to the broadness of the levels, characteristic effects in resistance can be observed. The broadness of the levels is related to the quantum lifetime, τ_q , where these effects become observable at $\omega_c\tau_q \gg 1$, thus materials with reduced scattering produce oscillations at lower magnetic fields [144]. It is important to note that the quantum lifetime, τ_q , is not the same as the scattering lifetime (the transport lifetime). The quantum lifetime is the time between any scattering event and thus is equally sensitive to long range scattering and short-range scattering [145]. Thus, if long range scattering is dominant (remote ionised impurity scattering), these lifetimes can be quite different, with the resultant quantum lifetime being significantly smaller [28]. The broadness parameter can be calculated by

$$\Gamma = \frac{\hbar e B_{SDH}}{m^*} \quad 7.12$$

where B_{SDH} is the magnetic field value at the onset of observable oscillations[146]. The precise definition of the field value at which the oscillations become observable is open to interpretation.

The density of these states changes as the field increases. Where the magnetic field is low, the separation of the Landau levels is small and so the states are still continuous. As the Landau levels move through the Fermi level, the electrons will behave differently in terms of conduction.

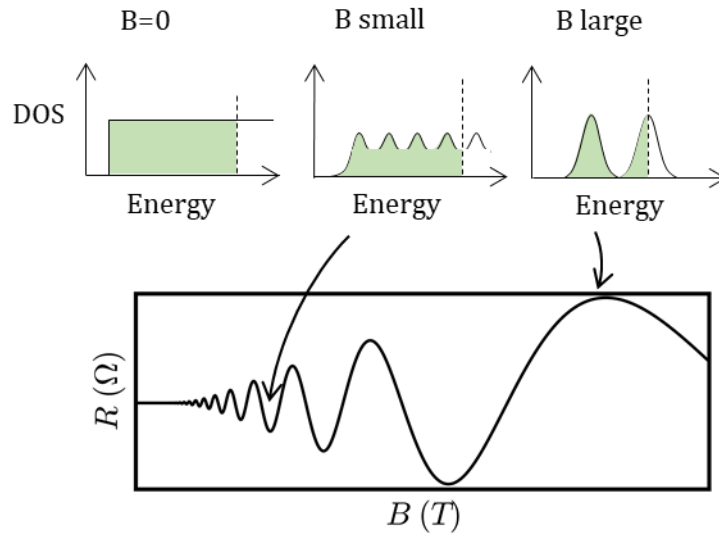


Figure 7.3: A diagram indicating the physical effects that occur at high fields which result in an oscillating resistance trace, there these oscillations are periodic in $1/B$.

Qualitatively, and to a first approximation, where the Fermi level is at a peak, there are energy states available above it. Therefore, an electron can scatter from one state to another, and thus, the resistivity is high. Where the Fermi level is between Landau levels, there are no states available immediately above it, and thus, the electrons do not scatter and resistivity is low [28]. A more full and thorough explanation would require treatment of localised and extended states though this does not alter the results presented here.

The longitudinal resistivity is seen to oscillate with increasing magnetic field (periodic in $1/B$) and the transverse resistivity shows quantised plateaus with increasing magnetic field. These phenomena are called the Shubnikov-de Haas effect (SdH) and the integer quantum Hall effect (IQHE). However, in the case where there are two carriers conducting in parallel, a significant background is observed in the oscillating ρ_{xx} and the IQHE becomes less distinct and thus unobservable [24, 147].

The Shubnikov-de Haas effect is caused by the oscillation in the density of states at the Fermi energy. This phenomenon is often used to study confined systems and is not present in 3D systems, thus is a confirmation of a confined system [148]. The oscillatory behaviour can be used to determine the carrier density in the 2DEG which, when coupled with temperature dependence, can be used to determine an effective mass and a quantum lifetime. The carrier density, n_{2D} , can be determined by

$$n_{2D} = \frac{2eB_F}{h}, \quad 7.13$$

where the peak frequency B_F (the frequency of SdH oscillations in $1/B$), can be found from a Fourier transform of an ideal single carrier sample. It can also be found from a fan diagram plotting the Landau level index against the magnetic field associated with the maxima and minima of the oscillations [24].

When observing ρ_{xx} , using the dampening of the peak amplitude with temperature, a quantum lifetime can be extracted using [149]

$$\frac{\Delta R}{R_0} = 4\chi e^{-\frac{\pi}{\omega_c \tau_q}}. \quad 7.14$$

Here, χ is the thermal dampening factor and is given by $\chi = A/\sinh(A)$ and $A = 2\pi^2 k_B T / \hbar \omega_c$, ΔR is the amplitude of the resistance oscillation and R_0 is the zero-field resistance. The quantum lifetime τ_q can thus be extracted using this equation.

A Dingle plot can be created where the Dingle parameter, D_p , is plotted against $1/B$, where the gradient is then dependent on the quantum lifetime [149]. The Dingle parameter is given by

$$D_p = \frac{\Delta R}{R_0} (4\chi)^{-1}. \quad 7.15$$

The gradient of this Dingle plot is then given by $\pi m_e^* / e \tau_q$. Performing a similar analysis, the effective mass can also be extracted from a plot of the thermal dampening factor, χ , as a function of T . As χ is only dependent on fundamental constants and the cyclotron frequency, and as the cyclotron frequency is dependent on effective mass, the thermal dampening can be fitted to extract an m^* .

7.2 Equipment and Set Up for Magnetotransport

The electrical equipment used to measure longitudinal and transverse resistances in this work is shown in Figure 7.4. This circuit, coupled with a helium cryostat and a superconducting magnet, allowed the measurement of transport properties and magnetoresistance up to a field of 15 T and down to a temperature of ~ 3 K.

To pass a current through the device, a low-frequency alternating voltage was supplied by a Stanford Research 830 lock-in amplifier across a large resistor (1 M Ω) in series with the device. The large resistor in series allows the current to be calculated with the assumption that the resistor is the dominating resistance in the circuit. This lock-in amplifier was also

used to measure one orientation of voltage, with a second lock-in amplifier measuring the other required voltage.

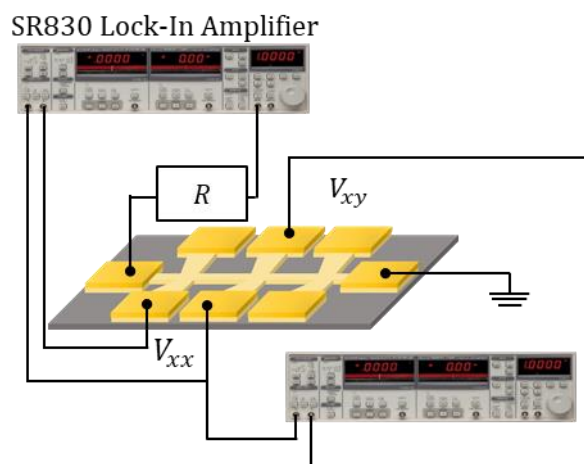


Figure 7.4: A schematic diagram of the set up for a Hall measurement on a Hall bar using two lock-in amplifiers. The left lock-in amplifier supplies a low frequency oscillating voltage across a large resistor R to generate a current, and measures the longitudinal voltage. The right lock-in measures the transverse voltage.

All the equipment was connected to a switch box which allowed for simple multi-device and multi-configuration measurement. All the equipment was controlled by purpose-made LabView programs allowing, for example, measurement of the longitudinal and Hall resistances with a magnetic sweep at many temperature steps, remotely. The set up in its entirety was assembled by Dr. Leonid Ponomarenko, who also created the programs to control the measurements.

The sample is placed at the centre of the field created by a superconducting magnet in an Oxford Instruments helium bath cryostat allowing for a temperature measurement range of (3-400) K, and a magnetic field up to 15 T. The extraction of the transport properties (mobility and carrier concentration) only requires a low field sweep (up to ~ 1 T), with each sample being measured down to 3 K.

The samples were attached to a chip carrier with 28 connections. Hall bar devices were electrically bonded to the chip carrier using silver epoxy, applied with a fine pointed toothpick, and fine gold wire. On the contact pad of the chip carrier the gold was pressed to the contact pad to produce a mechanical bond, before then being sealed with silver paint.

The chip carrier fits into a socket on the end of a purpose-made insert and is surrounded by a cup which is vacuum sealed and protects the sample from direct exposure to helium. The insert is pumped down to approximately 1×10^{-5} mbar prior to insertion into the

cryostat. Once inside the cryostat, the sample is connected to the switch box in preparation for measurement.

The cryostat consists of the sample space, surrounded by a helium bath, which is itself surrounded by a nitrogen bath. In order to regulate temperature in the sample space, a needle valve is opened allowing the flow of helium, whilst the sample space is pumped to encourage this flow of helium passing over the sample, cooling it. There is also a heater and thermometer in this chamber connected to a Mercury integrated temperature controller (iTC) used to increase the temperature and maintain set temperatures. Initially, it is important to cool the sample space by opening the pump valve and then the needle valve, and balancing the flow of helium so as not waste helium which the heater would then have to compensate for. Once a good flow is obtained and a consistent temperature is obtained, the cryostat is ready for a measurement sweep across temperature. In order to obtain a steady temperature in the sample space, ample time is left between the steady reading of the iTC and the start of a measurement. The superconducting magnet was in general used for low field measurements, however, it is also capable of reaching fields up to 15 T. The magnet is controlled by a Mercury integrated power supply (iPS) which powers the leads connected to the magnet, and also the switch heater which allows a change in current path to create a steady magnetic field in persistent mode.

7.3 Transport Measurements of $\text{Al}_{0.2}\text{Ga}_{0.8}\text{Sb}/\text{GaSb}$ Heterostructures

The transport properties of three types of $\text{Al}_{0.2}\text{Ga}_{0.8}\text{Sb}/\text{GaSb}$ heterostructures were investigated, one quantum well structure and two heterojunctions. The two heterojunction structures consisted of one with the confined region (the interface) doped, and the other where the confined region was left undoped. The “undoped” triangular well, will of course have an uncompensated, high p -type background due to the high concentration of native defects in GaSb. This is also the case with the square quantum well structure. The specific structural details of these are given in Chapter 6. Hall bars with an 8-pad geometry were created for each sample.

The longitudinal and Hall resistances were measured against B -field, with a set current of 2 μA . In the low field measurement regime, the field was swept to ± 0.6 T, and in the high field regime, the magnetic field was taken up to 14.0 T. The temperature range for the measurements was (3-300) K. The results for these measurements are analysed and discussed in this section.

7.3.1 Magnetic Field Dependence of Resistance

The longitudinal resistance, R_{xx} , and the transverse or Hall resistance, R_H , against magnetic field were inspected and analysed for each sample at each temperature. Equations 7.9 and 7.10 were then used along with a least-squares fitting routine to extract transport properties (mobility and carrier density) for 2 carrier types.

7.3.1.1 Multi-Carrier Extraction for a Square Quantum Well

Figure 7.5 shows the resistivities from a square quantum well sample against field at multiple temperatures. From the longitudinal resistance, the structure can be determined to be multi-carrier at low temperature. For a single carrier structure, it would be expected that this graph would give an unchanging resistance across B -field (to a first approximation). This is neglecting other possible magnetic field dependent effects such as localisation or (potentially) more significant effects such as geometric magnetoresistance, though in these samples, this is expected to be minimal due to the aspect ratio being larger than 3 in all cases [137].

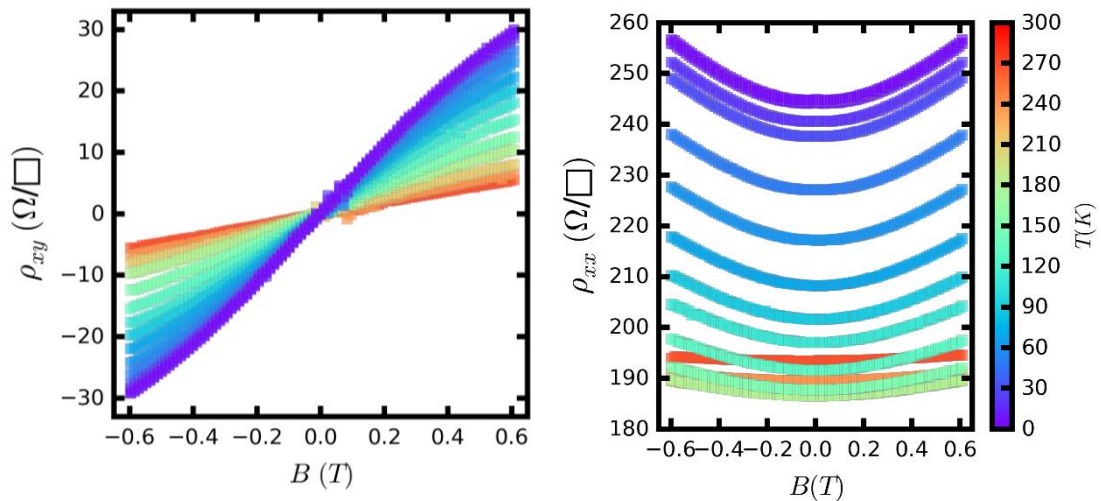


Figure 7.5: The longitudinal and transverse resistivities measured against magnetic field for a square quantum well structure.

ρ_{xx} is more sensitive to the contributions from multiple carriers than ρ_{xy} , and thus the effect is often harder to observe but still present in ρ_{xy} . However, in this case, multi-carrier characteristics are seen in both resistivities.

The two-carrier model gives an accurate fit to the data, confirming that this structure is multicarrier. This procedure was carried out for all structures measured and the transport properties of the carrier of interest were found (typically for the highest mobility carrier) and compared against the other structures. Shown below are the two-carrier fits for a

selection of temperatures with a reduced number of points, from which you can see the accuracy of the fits.

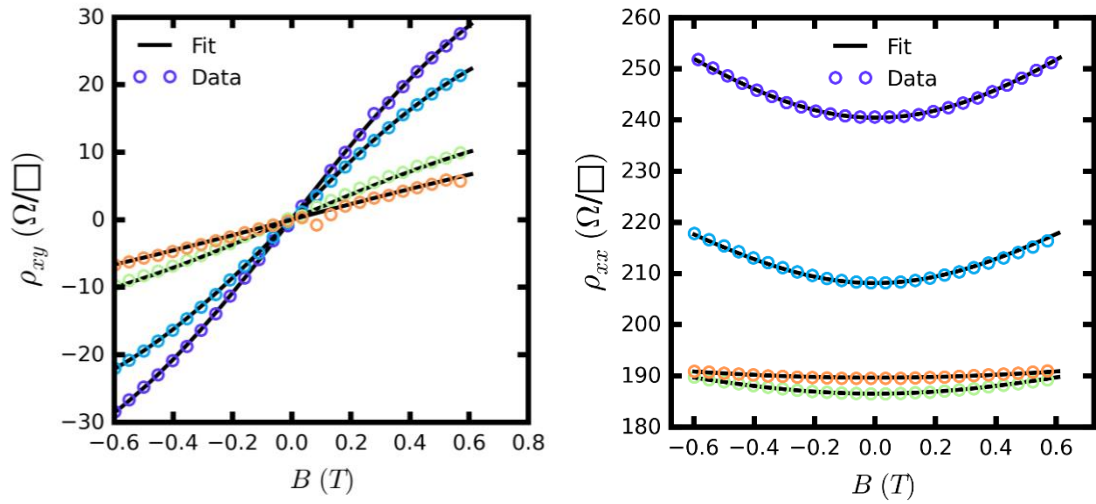


Figure 7.6: The measured longitudinal and transverse resistivities for a square quantum well (open circles), and a fit to the data using the two-carrier fit equations given in the previous section (lines). For clarity only a small selection of temperatures are shown, with a reduced number of points for each temperature.

The extracted carrier densities in all cases were significantly higher than anticipated when compared to the previous S.P. simulations which showed carrier densities up to but not above $6 \times 10^{11} \text{ cm}^{-2}$. The lowest carrier concentration extracted from the two-carrier fitting equalled $7.4 \times 10^{11} \text{ cm}^{-2}$ for the square quantum well sample.

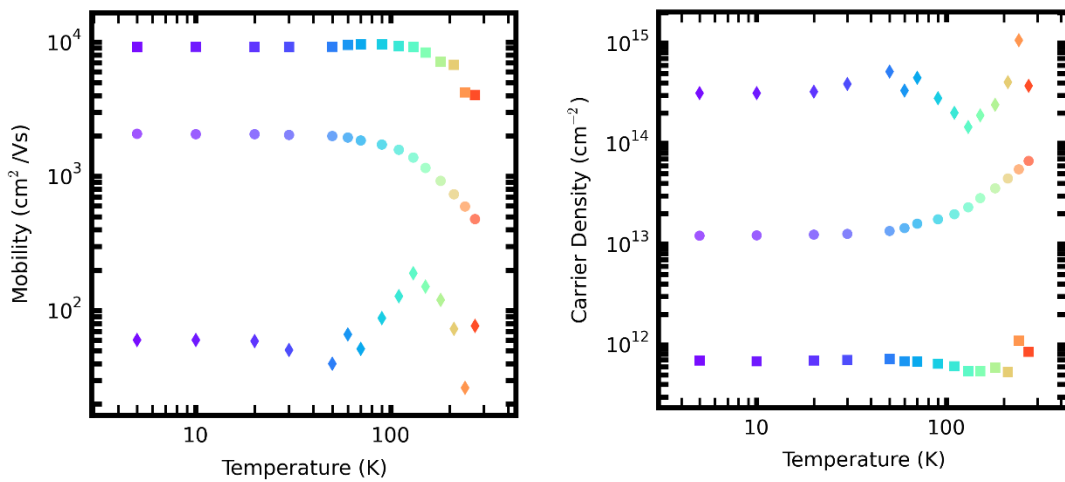


Figure 7.7: The mobility and carrier density for a square quantum well structure where a single carrier is assumed (dots) and where a two carrier fit was carried out (diamonds and squares). The high mobility carrier (squares) was assumed to be the carrier in the ground state of the QW (the 2DEG).

The extracted transport properties for each carrier for the quantum well structure, as well as those that would be extracted if it were assumed single carrier, are shown in Figure 7.7. Though two carriers are extracted, the main interest here is in extracting the high mobility 2DEG carrier transport properties, which is presumed to be the highest mobility carrier of the structure.

It is seen that the lower carrier density carrier (square symbols) is relatively invariant with temperature below 200 K, having a carrier density of $7 \times 10^{11} \text{ cm}^{-2}$ at 5 K. The mobility of this carrier is increased from the assumed single carrier case, rising to a value of $9030 \text{ cm}^2/\text{Vs}$ at 5 K, significantly higher than the second carrier mobility. This relative invariance of the carrier density with temperature, as well as the plateauing of the mobility, is characteristic of transport properties observed in two-dimensional systems. A summary of the carrier densities and mobilities extracted from two carrier fitting of the quantum well and heterojunction samples is given in Table 6.1 at the end of the following section.

The origin of the second carrier is unknown, however, such a reduced mobility could be speculated to be either L-band electrons or electrons in the dopant plane (or both), as these would have both a heavier effective mass ($0.95 m_0$) and a higher total scattering rate. The S.P. simulations suggested that a 2-carrier structure was likely in the quantum well case, though this was expected to be a second sub-band in the well.

The filling of each state in the quantum well (in both the Γ and the L bands) can be approximately determined by considering the energies of the states (using 6.22) and the density of states (equation 2.28). In combination, these give the location and number of states, and at 0 K, as the Fermi function is a step function, the occupancy of states (i.e. the carrier density) can be determined. Figure 7.8 shows the first 3 sub-bands in the Γ –band in blue, and the first 5 in the L band in purple (the L band is not shown but assumed to be offset from the gamma band edge by 80 meV).

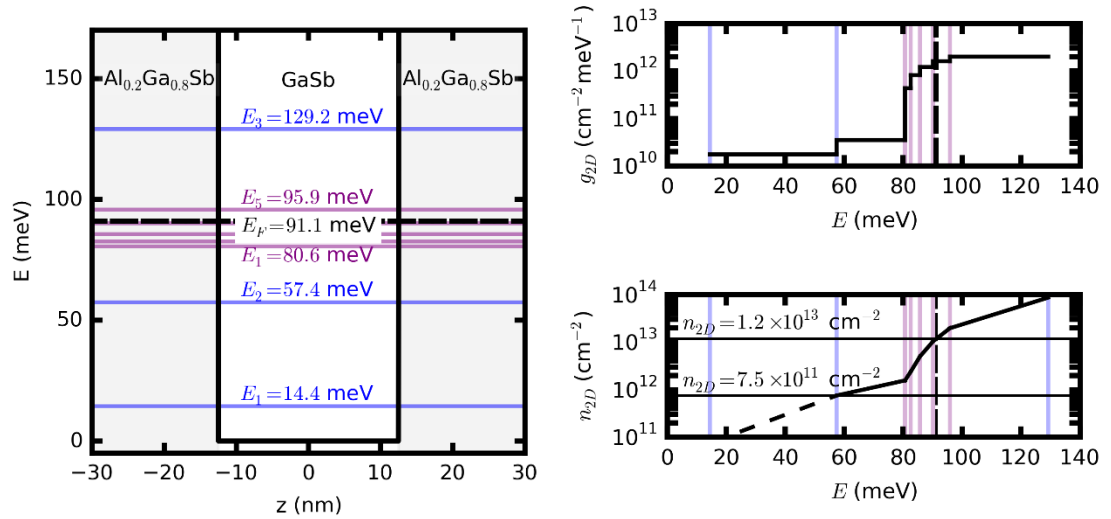


Figure 7.8: Schematic diagrams showing the increase in carrier density with energy level. **Left:** A GaSb/AlGaSb quantum well with calculated energy levels using an infinite square well approximation. Blue lines indicate levels in the Γ -band with purple lines indicating levels in the L-band. The dashed black line indicates the Fermi level which was calculated from the measured carrier density. **Right:** The density of states (top) and carrier density (bottom) against energy with faint lines indicating the energy of the states. The carrier density in the first state just before the onset of occupancy in the second state, and at the calculated Fermi level, are labelled.

Alongside the energy states and the quantum well, the density of states is shown, showing the initial small increase in states due to the low Γ band effective mass, followed by the rapid increase due to the increased L band effective mass. At the level just below the second sub-band in the well, an approximate carrier density of $7.5 \times 10^{11} \text{ cm}^{-2}$ would be expected, in excellent agreement with the two-carrier fitting for the high mobility, low carrier density sample. To calculate the Fermi energy and so the occupancy level at the extracted density of $1.2 \times 10^{13} \text{ cm}^{-2}$, E_F would be at 91 meV, implying the first 2 Γ subbands and 4 L subbands are occupied. The determination of E_F is drawn from a simple approximation as it assumes the carrier density from the single carrier case, and therefore cannot be used to draw quantitative conclusions, but it shows how the carrier properties cannot be assumed simple in these samples. This neglects any carrier density contribution from the doped region or the bulk, though is at least indicative of the complex nature of the filling of energy levels observed, and is an indication as to the complexity of 2 carrier fitting.

7.3.1.2 Multi-Carrier Extraction for Triangular Wells

The two carrier fitting equations were also used for the two heterojunctions, with the results for the doped heterojunction shown in Figure 7.9 below. It is seen here that for this

structure the transverse resistivity is linear at low temperature. The longitudinal resistivity shows a curvature at all temperatures.

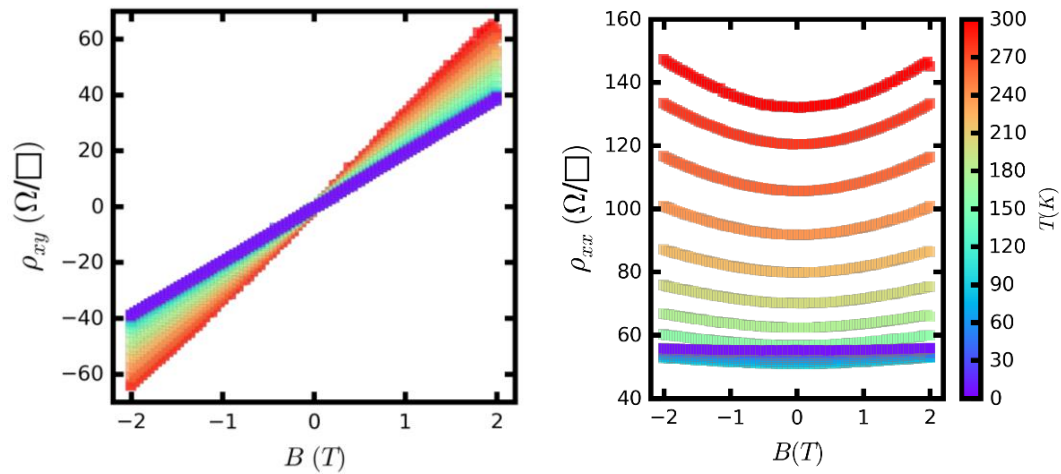


Figure 7.9: The longitudinal and transverse resistivities measured against magnetic field for a doped heterojunction structure.

As with the square quantum well, the doped triangular well resulted in a carrier with a characteristic mobility of a confined structure. The second carrier had the mobility resembling the characteristic of an ionised impurity limited bulk structure with a decreasing mobility at low and high temperature. The carrier with the highest mobility was assumed to be in the 2DEG for continuing analysis.

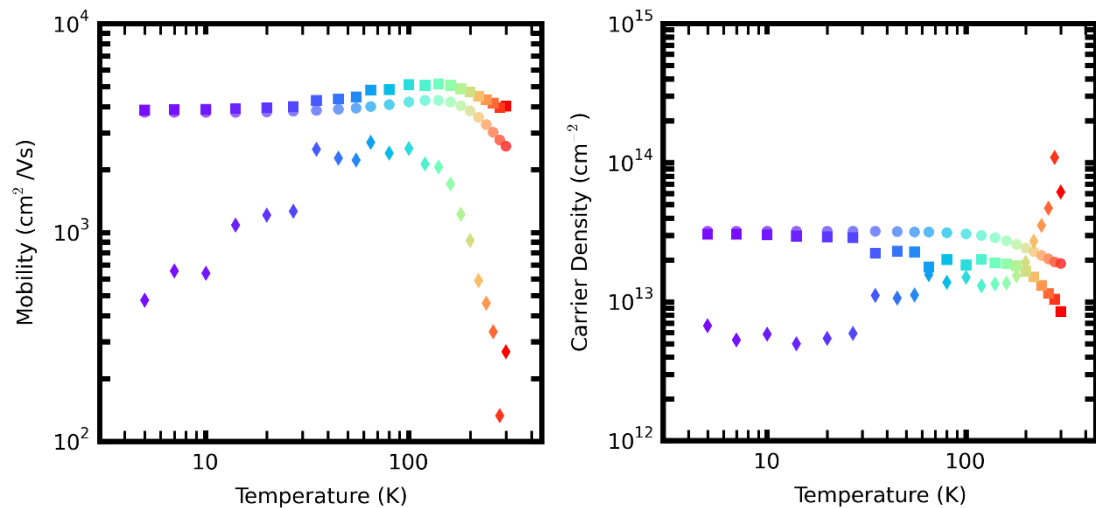


Figure 7.10: The mobility and carrier density for a doped heterojunction structure where a single carrier is assumed (dots) and where a two carrier fit was carried out (diamonds and squares). The high mobility carrier (squares) was assumed to be the carrier in the ground state of the QW (the 2DEG).

As the electron wavefunctions in a heterojunction are less well-confined, there could be a change in confinement of the wavefunction where the wavefunction moves to the buffer (bulk). From the simulations in the previous chapter it was shown that this is likely in the higher temperature case for undoped heterojunctions, though this is unexpected in the fully doped structure. The 2nd carrier could alternatively be a 2nd sub-band carrier or carriers in the barrier, as well as potential carriers in the bulk.

The same procedure was performed to extract a carrier density and mobility for the undoped well sample. It was found that, as opposed to the doped well heterojunction, the properties of the second carrier determined from the fit of the undoped triangular well were unphysical and unstable across temperature, despite a good fit to the data. It is indicated this is due to the sample being primarily dominated by a single carrier, where other factors could be affecting the two-carrier fitting. Though fitting the resistivities in this manner is an useful tool, there are always assumptions that must be made in order to create a model. One in this case, is that the transport properties are independent of magnetic field. The model is also limited by the assumptions of the inputs, specifically the number of carriers and approximate mobility and carrier density for each carrier must be given. From these inputs, a least squares fit method is used to fit the data, where, as shown by Gui *et al.* for a HgCdTe sample [139], the results can be non-unique, giving a good fit to the data for 2 or even 4 carrier species, thus results have to carefully interpreted.

For this work, the simple case of a dominating single carrier is assumed. With this single carrier assumption, the doped and undoped heterojunctions were of very comparable mobility and carrier density, and although the undoped triangular well is of slightly higher mobility as would be expected, ($4000 \text{ cm}^2/\text{Vs}$ at 5 K rather than $3500 \text{ cm}^2/\text{Vs}$), the small difference is surprising. The doped triangular well is expected to be subject to significant scattering due to the tellurium atoms residing in the well and so the small difference may be due to the tellurium dragging through the well in undoped case. Due to the similarity of the extracted mobilities and carrier densities, and due to the unstable nature of the fit to the undoped well, for the purpose of the next section (transport modelling) comparisons will only be made between the quantum well and the doped heterojunction, though the results should also extend to the undoped heterojunction.

A table summarising the transport results from this section is shown below.

Table 7.1: A table indicating the low temperature transport properties for each structure measured in this work, the carrier shown below is the high mobility carrier in all cases.

Structure	Carrier Density (cm⁻²)	Mobility (cm⁻²/Vs)
Square Quantum Well	7.5×10^{11}	9030
Doped Triangular Quantum Well	3.2×10^{13}	3500
Undoped Triangular Quantum Well	4.9×10^{13}	4000

The quantum well structure at low temperature has a carrier density of $7.5 \times 10^{11} \text{ cm}^{-2}$ and a mobility of $9030 \text{ cm}^2/\text{Vs}$. Whereas the doped heterojunction is assumed to be dominated by a single carrier and has a significantly higher carrier density of $3.2 \times 10^{13} \text{ cm}^{-2}$, and mobility of $3500 \text{ cm}^2/\text{Vs}$. The larger carrier density for the undoped quantum well is unexplained, however this may be related to a different shape of the well. The triangular quantum wells will have multiple occupied states, much like the square quantum well, including states in the L band, however, these are likely to be bulk states for the heterojunctions. The doped heterojunction has a shallower well than the undoped case, as shown in the S.P. results in the simulation chapter, and thus a different distribution of states, all of which leads to a complex situation that would require further theoretical and experimental analysis to unravel further.

7.3.2 Transport Properties of GaSb Heterostructures

The transport model was implemented as described in Chapter 6, however the carrier density measured at low temperature was input as a set parameter. Using the same, expected, parameters as before, Figure 7.11 left was obtained for the 25 nm square quantum well sample, though this model required some adjustments to obtain a fit to the measured data as seen in Figure 7.11 right. The expected parameters used to produce Figure 7.11 left, included a remote ionised impurity concentration of $5 \times 10^{17} \text{ cm}^{-3}$, representative of the intended doping concentration, a background concentration of $7 \times 10^{16} \text{ cm}^{-3}$ (higher end of the range), representative of the expected native defect concentration from the growth study, and interface roughness parameters of $\Delta = 1.5 \text{ nm}$ and $L = 5 \text{ nm}$.

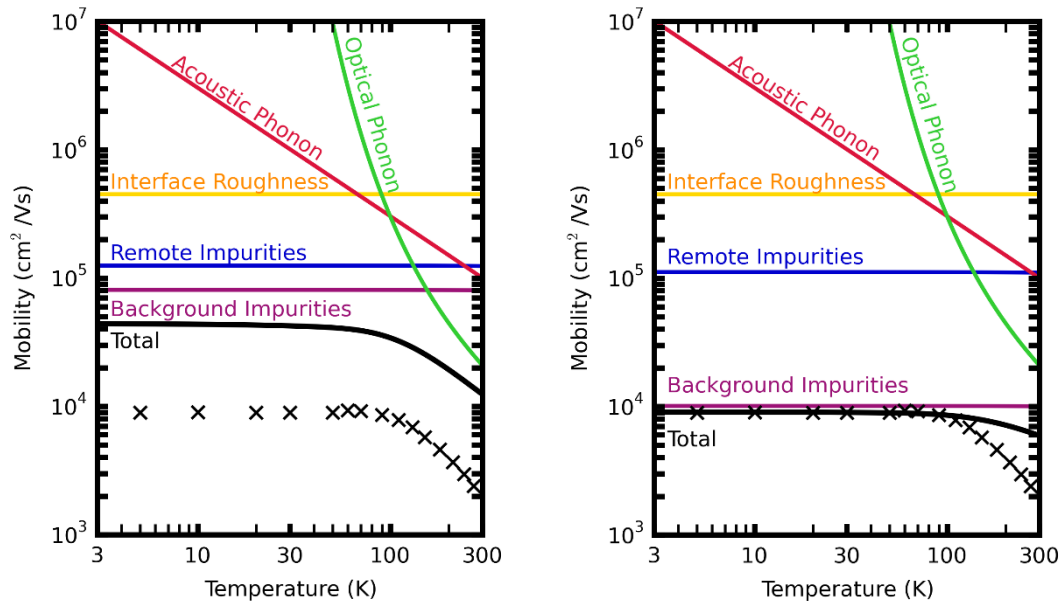


Figure 7.11: The transport model for a 25 nm square quantum well structure where each line is labelled and the total mobility (black) is expected to align with the data which is shown for comparison (crosses). **Left:** The transport model using expected parameters. **Right:** The transport model where the parameters have been adjusted to ensure a fit to the low temperature data.

There are many unknown parameters in the transport model that could be varied to fit the structure. It should be noted that inter-subband scattering has not been included in this model, however, and is likely to have an effect due to the large carrier density. Despite this, determining the range of reasonable scattering rates required to match the data for the scattering rates considered gives a reasonable upper range on the parameters involved in the calculations (e.g. background impurity scattering concentration). As this mobility is expected to be background impurity limited at low temperature the simplest solution to fit the data is to vary just the background impurity concentration. This would have to be increased to a concentration of $5.5 \times 10^{17} \text{ cm}^{-3}$ to match the measured mobility, with this shown in Figure 7.11 right. This concentration is higher than would be expected for an undoped well, even with a large number of accepting native defects which are all ionised. However, to reduce this number slightly to $5.0 \times 10^{17} \text{ cm}^{-3}$ whilst maintaining an accurate fit to the mobility, requires significant changes in all the other parameters, such as increasing the rms roughness to 3.8 nm, see Table 7.2. One possibility could be the tellurium from the doped region below the well dragging into the well. Though there was a spacer implemented to prevent this, the value of background impurity concentration is comparable to the concentration of slab doping in the barrier. A more accurate representation would be a remote ionised concentration that decays through the “spacer”, allowing a lower but comparable background impurity concentration through the well.

Table 7.2: A table showing the model parameters required to fit the mobility of an undoped square quantum well, at low temperature, in a transport model. It is shown that unphysical changes to parameters other than background impurity concentration are required to fit the data given the expected background impurity concentration. Fit 2 was used to fit the data in Figure 7.11.

	$n_{imp}^{2D} (\text{cm}^{-3})$	$n_{imp}^{3D} (\text{cm}^{-3})$	Spacer (nm)	Δ (nm)	L (nm)
Fit 1	5.0×10^{17}	6.0×10^{17}	100	1.5	5
Fit 2	5.5×10^{17}	5.5×10^{17}	1	1.5	5
Fit 3	5.0×10^{17}	5.0×10^{17}	1	3.8	5

Despite the improved fit to the mobility at low temperatures, the high temperature region of the transport model still does not fit, indicating some unknown affect occurring. Variation of other parameters were trialled in an attempt to achieve a fit, however, the parameter values required to attain a good fit were all unreasonable. There could also be another scattering mechanism not explored in the current transport model, such as inter subband scattering or $\Gamma - L$ interband scattering, though this was not explored further in this work. A table showing a comparison for the fits is given above.

The transport model was also implemented for the heterojunctions. The carrier density measured for the heterojunctions however was significantly higher at $3.2 \times 10^{13} \text{ cm}^{-2}$. The effect of this high carrier density in the transport model was substantial screening. The resulting transport model using the expected parameters for the doped triangular well is given by Figure 7.12 left. Despite a large background impurity concentration applied in the model, the dominant scattering mechanisms across almost all temperatures are the phonons. This is due to the high carrier concentration acting as screening from the dopant ions. This is clearly unrepresentative of the measured mobility as not only is the mobility predicted to be higher, but there is no similarity in the trend.

In order to obtain a fit to the mobility at low temperature, a significant ionised impurity concentration must be included ($6.5 \times 10^{19} \text{ cm}^{-3}$). Even with the a doped well, this value is unrealistic, and the predicted high temperature mobility is not representative of the measured trend. As the carrier density is significant, non-parabolicity could have an effect and thus was implemented. Non-parabolicity increases the effective mass and so decreases the modelled mobility data. Accounting for this non-parabolicity, the resultant trend in mobility at higher temperature still did not match the measured mobility, as is seen in Figure 7.12 right below. In the case of the square quantum well structure the change due to non-parabolicity is not significant at the extracted carrier density and so therefore wasn't included.

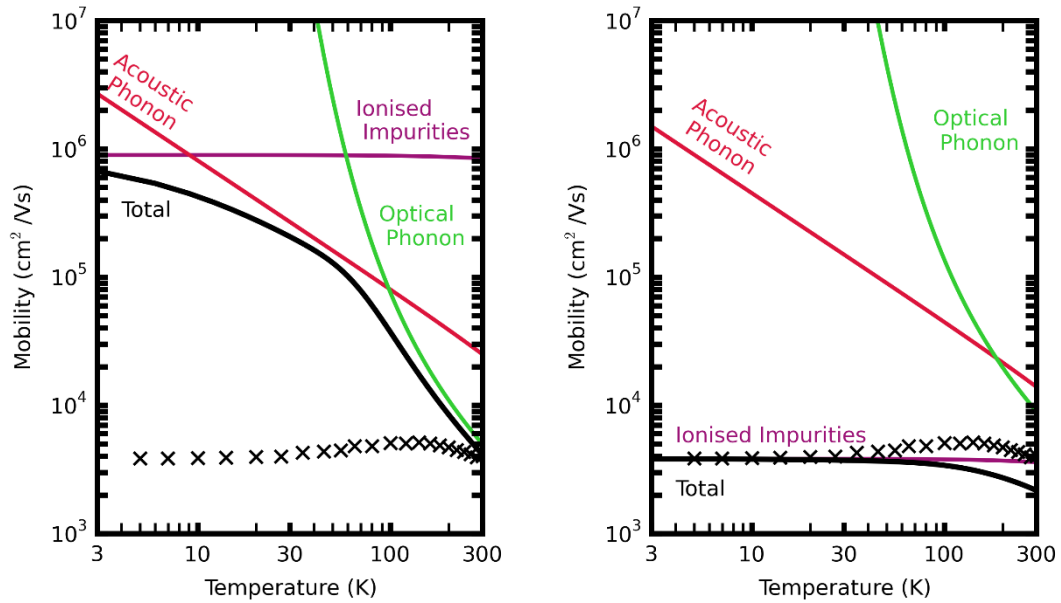


Figure 7.12: The transport model for a doped heterojunction where each line is labelled and the total mobility (black) is expected to align with the data which is shown for comparison (crosses). **Left:** The transport model using expected parameters. **Right:** The transport model where the parameters have been adjusted to ensure a fit to the low temperature data.

Including interface roughness again did not improve the quality of the transport model fit to the mobility. Therefore, it can be concluded that other scattering mechanisms, such as inter-subband scattering or electron-electron interactions, are likely to be a significant factor, though the specific scattering mechanism of which will not be considered here.

Alternatively, and more likely, the low mobility and high carrier density extracted from the two-carrier fitting for the doped heterojunction, was a poor physical representation of the sample's conduction. Though the two carrier fit equations resulted in a reasonable fit to the measured data, the extracted parameters required unreasonable measures to explain this low mobility and high carrier density. The extracted properties from the two-carrier fitting may be inaccurate in part, due to many carriers contributing to the transport properties, where only a two-carrier fit was used to extract the data. Investigating a larger field may also assist in resolving the contributions from the multi-carriers.

As many of the scattering mechanisms are dependent on carrier density (directly or indirectly), a change of the carrier density compared to that extracted would result in a potentially significant change in the mobility predicted by the transport model. Therefore, it is reasonable to investigate the carrier density that would be required to match the extracted mobility given reasonable values for the other scattering rates. For the

measured mobility of the doped heterojunction, a carrier density of $3.3 \times 10^{11} \text{ cm}^{-2}$ is required to fit the data with reasonable parameters.

Further, given that the structure is a single heterojunction, with a strong confining potential on one side of the well and only a weakly confining triangular potential on the other, the confinement of the structure comes into question. This is particularly the case due to the complicated doping in GaSb systems as there is an inclusion of native accepting defects, with the added possibility of significant bulk contributions. For such a high carrier density and the associated discrepancy with the transport model, as well as due to all the added complications mentioned, it is possible that there is no triangular well formed. However, this structure was measured at high B -fields, resulting in Shubnikov–de Haas oscillations up to 100 K. These results and their analysis will be discussed in the next section. The presence of the Shubnikov–de Haas oscillations confirm the presence of a 2DEG in this n -type doped $\text{Al}_{0.2}\text{Ga}_{0.8}\text{Sb}/\text{GaSb}$ triangular well.

7.3.3 High Field Measurements and Analysis

High-field, low-temperature measurements were achieved resulting in the observed Shubnikov-de Haas (SdH) results shown below.

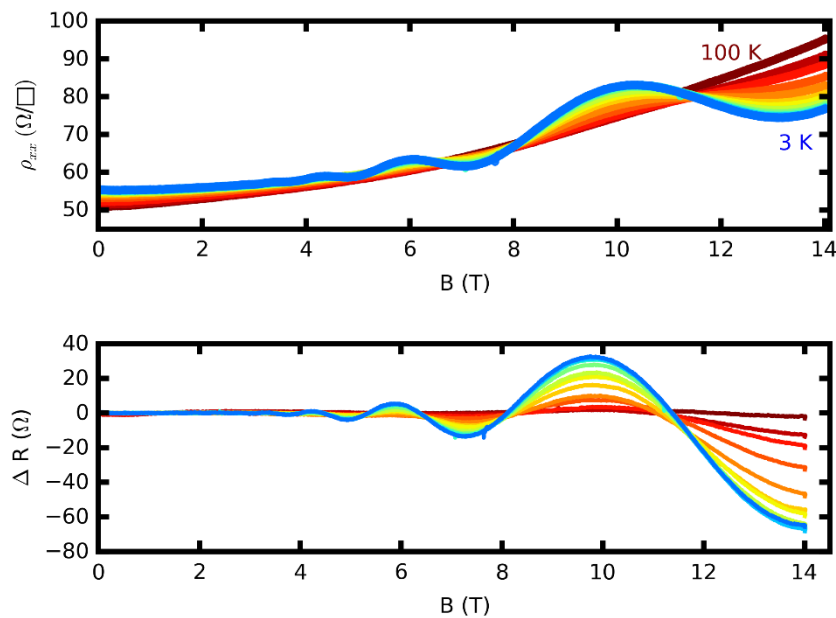


Figure 7.13: Top: Measured longitudinal resistivity for the doped heterojunction against magnetic field, across measurement temperature. **Bottom:** The longitudinal resistance against magnetic field, with a parabolic background subtracted.

The results presented come from the doped triangular well sample, confirming confinement at low temperatures. All the following analysis is from this measurement.

The oscillations decrease with temperature as expected, though they can still be seen up to 100 K. The Hall resistance R_{xy} was also measured however no quantised steps were observed, though this can be attributed to the high carrier concentration obscuring the effect in this orientation [24]. There was a significant background on the oscillations which was removed by fitting a parabola to the first 3 T of data. This parabola is attributed to parallel conduction, where the other conducting states are in the bulk. As no beating in the oscillations is observed, it can be interpreted that there is only one confined state (a single 2D carrier). The parabolic fit was then removed from the data to give the results seen in Figure 7.14.

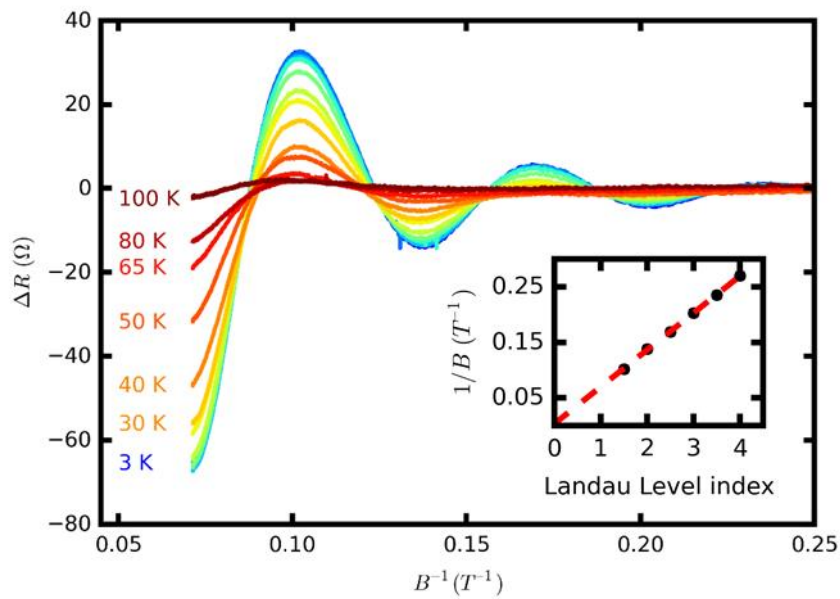


Figure 7.14: Shubnikov-de Haas oscillations observed from the doped heterojunction plotted against $1/B$ to show the periodic nature of the oscillations. **Inset:** Fan diagram where the peaks and troughs of the oscillations (half integer and integer indexes respectively) are plotted against $1/B$ to find the peak frequency or fundamental field, B_f .

By examining the low field data with the background subtracted (Figure 7.13 bottom) the broadness parameter of the Landau levels was obtained using equation 7.12, resulting in a broadness of 6.9 meV. This broadness is within a range seen in other material systems such as InSb (3-8 meV) [28]. By obtaining the period of the oscillations in $1/B$ and thus the frequency B_f , a 2D carrier density can be found using equation 7.13. The period of the oscillations was determined from a fan diagram of the Landau level index [149] against $1/B$ at the values of the peaks and troughs of the SdH oscillations. The gradient of the fan diagram then gives a value of $B_f = 15.1 \pm 0.1$ T, giving a 2D carrier density for the heterojunction of $7.3 \times 10^{11} \text{ cm}^{-2}$. Similarly, the frequency of the oscillations in $1/B$ can also be determined using a Fourier transform, with this giving a 2D carrier density for the

heterojunction of $7.4 \times 10^{11} \text{ cm}^{-2}$. These two values are in very close agreement, and both are similar to the value calculated previously for the filling of the ground state in an infinite square well. Whilst this scenario is not directly comparable, it does add confidence to this extracted carrier density, despite the disagreement with the two-carrier fitting, and again gives further confidence that the assumed well width of 25 nm is of the approximately correct scale. When this carrier density is set parameter in the two-carrier model, a good fit to the data could not be achieved.

Further analysis of the SdH oscillations included an investigation of the dampening of the peak resistances as a function of temperature to determine the effective mass. The temperature damping factor is given by $\chi_T = A / \sinh(A)$, where A is dependent on B , T and m^* via ω_c . The damping factor can be fit to the modified SdH resistance values at a set B -field across temperature, where the values taken are at the extrema points of the resistance, and where a finite temperature normalisation is required to scale the damping factor to equal 1 at 0 K. Figure 7.15 shows the extracted damping factor data and associated fit for three values of B -fields corresponding to maxima and minima in resistance. From these fits a comparable effective mass was extracted at each B -field value, with an average effective mass calculated of $(0.042 \pm 0.001) m_0$. This is within the range of electron effective masses given in the literature and below what would be expected if the carriers were conducting in the barrier, which would be approximately an increase of 40 % ($0.056 m_e$).

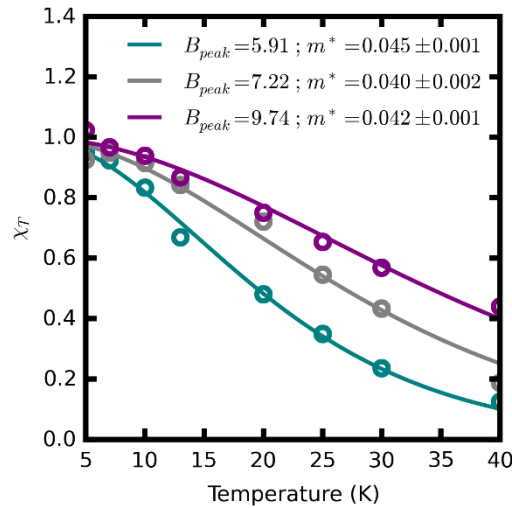


Figure 7.15: A plot of Shubnikov-de Haas oscillation amplitude dampening against temperature for different B -field values corresponding to resistance peaks and minima for the doped heterojunction. The dampening factor was fit to the extracted points and an effective mass was obtained and given in the legend.

Further to analysing the dampening with temperature, the dampening in $1/B$ can be analysed by the Dingle parameter (equation 7.15), and thus by examining the decay of the oscillations with inverse magnetic field, the quantum lifetime is found. The effective mass found from the thermal damping is used here. Figure 7.16 left, shows Dingle plots for a range of temperatures, where a quantum lifetime can be extracted from the gradient at each temperature. The plot shown below offsets the data extracted at each temperature vertically by a value of 1 for clarity. The data was fit to a straight line where the parameters were free fit (solid) and where the intercept was set to equal 0 (dotted), as equation 7.15 would predict. Figure 7.16 right, shows the extracted quantum lifetime and the associated error in the fit for both cases. The mean value for the free fitted quantum lifetime is 31.7 ± 3 fs whilst for the forced intercept it is 28.1 ± 1 fs, where the forced fit falls within the error of the free fit at all temperatures. The forced intercept quantum lifetimes do not appear to have any temperature dependence, consistent with a temperature independent scattering mechanism such as from the background impurities. However, the free fitted quantum lifetime does appear to have some slight temperature dependence, though the scale of this is below the associated errors, and as such a conclusion cannot be drawn from this possible trend.

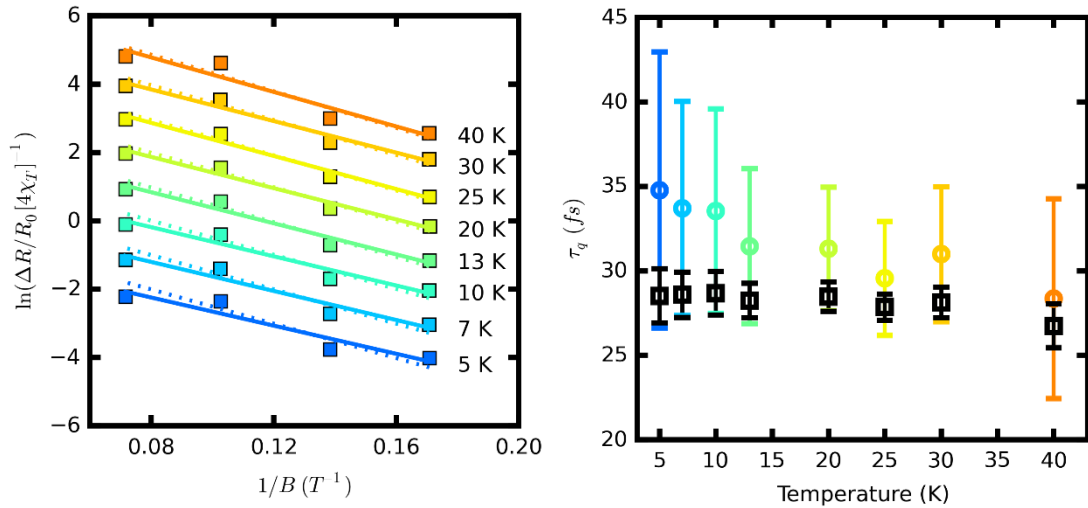


Figure 7.16: Left: Dingle plots the doped heterojunction at various temperatures where the data is free fit (solid line) and fit with a set intercept of 0 (dotted), each line is offset by 1 for clarity. **Right:** The quantum lifetime against temperature where the coloured circles indicate the free fitted lines from the Dingle plot, with the associated error from the fitting. The black squares indicate the quantum lifetime extracted from the Dingle plot when the intercept is set to 0.

From the extracted mobility, the transport lifetime (τ_s) was found to be 84 fs for the doped heterojunction, giving the ratio of the two lifetimes τ_s/τ_q in the range 2.7-3.0. This ratio

for the heterojunction is small compared to other values reported in the literature [149]. This indicates that short range scattering such as from the background impurities is, unsurprisingly, dominant in these structures [150].

7.3.4 Revision of the Transport Model

The high field analysis uncovered some properties which can be used to update and improve the transport model for this structure. As the 2D carrier density was extracted from the high field measurements, this could be input not only into the transport model, but used as a set value in the two-carrier fitting for one of the carriers. Thus, the carrier density extracted from the SdH measurements was used in the transport model and the mobility extracted is a lower limit of the 2DEG mobility (the single carrier case $3500 \text{ cm}^2/\text{Vs}$). With variation of parameters such as well width (as it is a triangular well) and ionised impurity concentration, the transport model was again fit to the data at low temperatures using the SdH determined carrier density. However, yet again, an unreasonably high background impurity concentration ($1.5 \times 10^{18} \text{ cm}^{-3}$) is required to achieve a fit (for a well width of 30 nm) and the high temperature trend does not match. This fit was achieved accounting for non-parabolicity and neglecting interface roughness due to the single interface of the heterojunction. If interface roughness is included using the same roughness values as used in the quantum well, the background impurity concentration can be reduced to $3 \times 10^{17} \text{ cm}^{-3}$ (a more reasonable value) though this also requires reducing the well width to 11.5 nm, and including the well width dependence in the optical phonon to give a worst case mobility. These values are, however, unrealistic and as such, the origin of the reduced mobility is as yet still unknown.

It is clear that there are still many unknown quantities required for these samples to fully explain the values observed using standard transport modelling. Other scattering mechanisms may still be a factor such as electron-electron interactions, inter-subband scattering or scattering between the Γ and L-band, these scattering mechanisms will not be considered or analysed further here.

7.3.5 Conclusions

Confined $\text{Al}_{0.2}\text{Ga}_{0.8}\text{Sb}/\text{GaSb}$ structures that were simulated in Chapter 6 were grown using the optimal growth conditions found in Chapter 3. The structures were then fabricated into Hall bars following the procedures described in Chapter 4, using the optimal metallisation recipe found in Chapter 5. Once complete, the longitudinal and transverse resistances were measured against magnetic field and temperature. This was carried out in two regimes, low-field (up to 0.6 T) and high field (up to 14 T). The low field

regime was analysed using a two-carrier fit model and yielded transport properties of carrier density and mobility against temperature for the square quantum well sample and both the doped well and undoped well heterojunctions.

The square quantum well structure gave a clear two-carrier behaviour across temperature with a high mobility carrier concentration of $7.5 \times 10^{11} \text{ cm}^{-2}$, and mobility of $9030 \text{ cm}^2/\text{Vs}$ at 3 K. The transport model was then used to further analyse the scattering in the 2DEG where it was found that a high background impurity scattering concentration higher than $5.0 \times 10^{17} \text{ cm}^{-3}$ was required to fit the mobility. This would indicate that despite the spacer below the well, the Te atoms dragged into the well, limiting the mobility of the carriers in the 2DEG with background impurity scattering. Tellurium dragging is known in other materials such as InSb, however the extent of the dragging is expected to change with different materials and growth temperatures. It could be particularly relevant in this case given the structure has a large bulk doped tellurium region. The tellurium in this case would not incorporate over microns of growth to finally deposit in the undoped region. Alternatively, it could mean that the electrons are scattering into the L-valley, this is a possibility given the large carrier density measured.

Heterojunctions, both doped and undoped in the triangular well, were also investigated using two carrier fitting. They gave very similar results to each other, both resulting in high mobility carriers with a mobility comparable to the mobility extracted if the samples were assumed single carrier. The mobilities for the doped and undoped triangular well at 3 K were $3500 \text{ cm}^2/\text{Vs}$ and $4100 \text{ cm}^2/\text{Vs}$ respectively. These are surprisingly comparable, and it is assumed that, similar to the square quantum well, Te also dragged in the heterojunction case and thus just the doped triangular well was analysed further. With the assumption of just a single carrier, the parameters required in the transport model to match the measured mobilities were unreasonable. This was primarily due to a high measured carrier density of $3.2 \times 10^{13} \text{ cm}^{-2}$, from which there is a large screening effect, increasing the predicted mobility for several of the scattering rates. As such, this carrier density was clearly an unreasonable parameter to be used in the transport model. A further investigation of this sample would require measurements at greater fields or a more accurate extraction of the carrier density. The longitudinal resistivity suggests a multi-carrier sample however extracting two carriers within a reasonable range was not achievable, therefore there may be more than two carriers conducting. The data can be fit using a many carrier model, however, arguably the model will more closely fit the data simply due to more free parameters for the fit.

This structure was then measured in the high field regime (up to 14 T) across temperature and Shubnikov-de Haas oscillations were observed, confirming the presence of a 2DEG up to 100 K. Quantum Hall plateaus were not observed, where this is believed to be due to the high carrier density. The oscillation frequency in $1/B$ was determined, which was then used to find a carrier density, where this resulted in a much more reasonable carrier concentration of $7.4 \times 10^{11} \text{ cm}^{-2}$ for the 2DEG. The effective mass was also extracted from the thermal dampening of the oscillations via a fit of the thermal damping factor. An effective mass of $(0.042 \pm 0.001) m_0$ was obtained. This is very comparable to literature values and confirms the confinement is in fact in the GaSb layer and not in the $\text{Al}_{0.2}\text{Ga}_{0.8}\text{Sb}$ barrier as this would result in an electron effective mass of $0.056 m_0$. A Dingle plot was then created, and from the gradient, the quantum lifetime was found to be between $(28.1 - 31.7)$ fs. The transport lifetime is <3.0 times that of the quantum lifetime. The low ratio indicates that as expected, short range, small angle scattering is dominant in these samples which is consistent with background doping impurity scattering.

With the new carrier density found from the high field regime, the transport model was revisited, however, the fit to the data was still unreasonable. This may be due to the lower limit mobility being used for the fit. If this is in fact the mobility of the 2DEG, it is likely there is another scattering mechanism not explored in this work which is further reducing the mobility.

The initial measurements and analysis of confined $\text{Al}_{0.2}\text{Ga}_{0.8}\text{Sb}/\text{GaSb}$ show promising results with a mobility of $9030 \text{ cm}^2/\text{Vs}$, similar to the early measurements of confined GaAs the mid 1970s [14]. There is still much to be understood about these samples and much to be optimised in future samples. The Te dragging is clearly an issue that needs resolution if higher mobility devices are to be achieved. The measured carrier density is also inexplicably higher than expected. To investigate this further, the next iteration of samples should consist of similar structures with reduced doping concentrations in order to further understand the relationship of doping concentration to carrier concentration in the 2DEG. If a method to reduce Te dragging in GaSb to avoid a doped well is found, or an alternative method of n -doping GaSb is implemented, higher mobility devices would certainly be a possibility.

Chapter 8

Conclusions and Further Investigations

Transport in confined *n*-type GaSb has been investigated both practically and theoretically in this work. With a high dielectric constant and low effective mass, GaSb should theoretically be preferable to GaAs for high mobility devices. However, the practical realisation of the samples has shown complications in many aspects.

This work investigated the growth of GaSb with the aim of reducing the native *p*-type defects, and included a growth study and *n*-type doping calibrations with Te, which also complexes to create further *p*-type defects when incorporated in low concentrations. With the knowledge from this growth study, nextnano, a physical simulation software, was used to investigate the band structure and thus confinement of GaSb/Al_{0.2}Ga_{0.8}Sb heterojunctions and square quantum wells for a range of doping concentrations. A transport model was also used to estimate the mobility for each structure. A small subset of the structures investigated were then grown and processed using standard processing techniques. The metallisation of contacts introduced a further source of uncertainty due to the lack of a standard *n*-type GaSb ohmic contact recipe, and initial trials yielded extremely high resistance contacts which increased in resistance as temperature decreased. It was found that the key to an improved contact was annealing in combination with a multilayer contact. This method resulted in reduced resistances and allowed samples to be measurable at low temperatures. The transport measurements of these samples provided insight that Te dragging was significant, increasing the challenge of selectively doping to compensate the *p*-type background. High-field measurements confirmed the presence of a 2DEG in an Al_{0.2}Ga_{0.8}Sb/GaSb heterojunction through observation of Shubnikov-de Haas oscillations. Analysis of the quantum lifetime revealed that, unsurprisingly, the mobility is limited by short-range, large-angle scattering. This is further confirmed by the transport model concluding that background (3D) impurity

scattering limits this structure. This is somewhat unsurprising given the concentration of native defects, tellurium complexes and tellurium atoms in the well.

More detailed conclusions of each chapter will be given below followed by a discussion of the future possibilities for this work.

8.1 Conclusions

The transport properties of $\text{Al}_{0.2}\text{Ga}_{0.8}\text{Sb}/\text{GaSb}$ 2DEG heterojunctions and square quantum wells have been investigated. Predictions from Takeda *et al.* [15] indicate a mobility comparable (though improved) to that of GaAs systems should be achievable. This prediction was mainly due to the high relative permittivity of $15.7 \epsilon_0$ and low electron effective mass of $0.042 m_0$ in GaSb that led Takeda *et al.* to suggest that the remote ionised impurity scattering (a limiting factor in GaAs) would be reduced in this material. It was stated that this relative permittivity coupled with a lower electron effective mass, boded well for high mobility AlGaSb/GaSb systems. Though these predictions were made following simulations, these considered just the remote ionised impurity scattering mechanism at low temperatures as this is the limiting scattering mechanism for AlGaAs/GaAs systems. What was not considered in their work was the high concentration of native defects in GaSb. These *p*-type native defects occur irrespective of growth method used and are well reported in literature. These defects primarily consist of a gallium atom in an antimony site in the lattice (a gallium antisite defect, Ga_{Sb}), though other defect types such as gallium and antimony vacancies ($V_{\text{Ga}}, V_{\text{Sb}}$), and antimony antisites (Sb_{Ga}) could also occur. The native defects are often expressed as unintentional doping and have a *p*-type concentration typically between $(10^{16} - 10^{17}) \text{ cm}^{-3}$. These will act as a significant scattering mechanism and thus treating the remote ionised impurity scattering rate as the only contribution at low temperature is inaccurate in the case of GaSb.

These defects can in some degree be controlled by growth conditions and thus a growth study was completed in order to control and reduce their occurrence. All samples were grown via MBE on semi-insulating GaAs substrates with $2.2 \mu\text{m}$ of GaSb. An IMF was used to minimise the strain and therefore the resulting dislocations. The full investigated substrate temperature range was $(380\text{-}520) \text{ }^\circ\text{C}$ for a V/III ratio of 1.3, where at the extremes of this temperature range, samples had a milky, rather than shiny, surface. The V/III ratio was also varied to 1.6 and 2.2 at temperatures of $505 \text{ }^\circ\text{C}$ and $475 \text{ }^\circ\text{C}$. These samples were electrically measured using the van der Pauw method in combination with the Hall effect to deduce the carrier density and the mobility at room temperature, and as a function of temperature. Mobility in this case was used as a material quality factor and

the bulk scattering mechanisms were not further investigated. An optimum growth condition which included a reduction of the p -type concentration was found at a substrate temperature of 475 °C and a V/III ratio of 1.3. This resulted in a reduction of the defect generated carrier density to a minimum of $5 \times 10^{16} \text{ cm}^{-3}$, and an increase in mobility to a peak of 460 cm^2/Vs . There did not seem to be a consistent trend with growth temperature, but rather a set of optimum conditions, with higher growth temperature growth dominated by more Ga_{Sb} antisite defects, and lower temperature growth dominated by multiple defect types. The presence of these Ga_{Sb} antisite defects causes issues not just in scattering of electrons, but also for donor doping.

In the case of heterojunctions, doping is used to create the confinement with tellurium used as the n -type dopant. The tellurium must not only compensate (neutralise) the accepting nature of any p -type defects, but also create the confinement of the electrons through band bending. A doping calibration was performed where it was found that low doping of Te in GaSb results in further p -type defects, then, as the Te cell temperature was increased (and so the doping level increased), the GaSb became n -type at a cell temperature of 238 °C, with an electron concentration of $3 \times 10^{16} \text{ cm}^{-3}$. This cell temperature would typically result in a carrier concentration of ~ 10 times this value in InSb, the material used to calibrate the doping. The Te is believed to complex with the native Ga_{Sb} antisite defect found in GaSb, creating a triply accepting defect. The inclusion of Te will thus initially increase the acceptor concentration before then reducing it through compensation, where individual tellurium atoms act as standard donors. The stark difference in doping concentrations achieved for a given Te cell temperature between InSb to GaSb was found to be a combination of the high defect concentration in GaSb, coupled with a low activation energy of Te in GaSb compared to InSb. It was also revealed that in any n -GaSb sample, an acceptor concentration of approximately $1.3 \times 10^{17} \text{ cm}^{-3}$ would likely be present, which is a combination of Te complexes and native defects. The tellurium complexes are dependent on the number of native defects, which act as sites for the tellurium to complex with.

Following this, the temperature dependence of the measured bulk n -type GaSb carrier concentration was investigated. An unusual behaviour of a decreasing Hall coefficient with decreasing temperature was observed. This behaviour was explained using a model by Sagar *et al.*[10], suggesting that the low-lying L-band in GaSb is populated, giving low mobility carriers. As the Hall coefficient is a function of both the mobility and carrier density of the two carrier species, when these two carriers are measured this unusual effect is observed. If a single carrier is wrongly assumed, a rising carrier density with

decreasing temperature is observed. In this case, for these samples, when the temperature is reduced, the carriers all reside in the Γ -band and once this occurs, the Hall coefficient and carrier concentration are invariant with temperature.

As there are many defects inherent in *n*-type GaSb which could affect any intended confinement, the band structure of various GaSb/Al_{0.2}Ga_{0.8}Sb heterostructures were investigated. To achieve this, the Schrödinger-Poisson solver and the transport model in nextnano were used. These together simulated the band structure, wave functions, confinement energy, carrier density and the individual scattering mechanisms and subsequent mobility across temperature.

Investigating various doping profiles in the heterojunction structures (i.e. the number of doped regions, doping levels, spacers) to achieve confinement, it was found that it would require doping in the quantum well region to ensure confinement across temperature. The difficulty of achieving confinement was mainly due to the *p*-type nature of the “undoped” region and the alignment of the Fermi level between this region and the doped region. The doped well, however, resulted in a drastic drop in predicted mobility due to the close proximity of the electron charge carriers and the ionised dopant atoms. Thus, a square quantum well structure was also investigated. The square quantum well resolved the confinement concerns, however, in these structures there will likely be two occupied energy levels, and thus not technically creating a 2DEG. When there are two energy levels the electrons will likely scatter between the subbands, further reducing the mobility. The transport model revealed that the square quantum wells resulted in the highest predicted mobility compared to both the doped and undoped heterojunctions despite the potential interface roughness. This is due to well region remaining undoped, as well as the expected increase in carrier density from the heterojunction case, causing screening in the impurity scattering mechanisms. As each structure had its own advantages and disadvantages, each were grown with a subset of them measured.

After each structure was grown, they were then processed using standard techniques to create Hall bar devices as discussed in chapter 4. However, there is no standard metallisation recipe for *n*-GaSb contacts, and initial trials resulted in significantly high contact resistances. This sparked a brief study into metallisation recipes. The primary focus was to minimise the contact resistance so that devices could be electrically measured across temperature, whilst preferably creating an ohmic contact. The recipes investigated included In, In/Au, Pd/In/Pd/Au and Au/Ni/Au, where both annealed and unannealed contacts were tested. In each case, annealing improved the resistance by over

an order of magnitude, however, all produced non-ohmic contacts to varying degrees. The resistance in the low-current region was used as the main comparison between contacts as this is the region that would be used in transport measurements. Pd/In/Pd/Au 4/41/6/100 nm, with an annealing recipe of 300 °C for 10 mins, gave the most ohmic contact (the most linear relationship between current and voltage), and the lowest resistance at the current required for transport measurements. There was more variation with Pd/In/Pd/Au contacts than the next best contact recipe, Au/Ni/Au however. The lowest resistance Pd/In/Pd/Au contacts typically had a contact resistance of $\sim 600 \Omega$, whilst the higher resistance contacts were typically $\sim 4.8 \text{ k}\Omega$, where the variation in resistances achieved from this recipe may be due to the sensitivity of the contact resistance to the thickness of the Pd blocking layer, or to gold spiking into the semiconductor. Both Au/Ni/Au and Pd/In/Pd/Au remained low resistance to 77 K. The latter was selected as the contacting recipe of choice as it had the lowest resistance, had the least variation with temperature, and achieved the most ohmic contacts.

Finally, the $\text{Al}_{0.2}\text{Ga}_{0.8}\text{Sb}/\text{GaSb}$ structures were measured, utilising the Hall effect to investigate the transport properties. The longitudinal and transverse resistances were measured against magnetic field and temperature, where two regimes were investigated, low-field (up to 2 T) and high-field (up to 14 T).

The square quantum well structure gave a clear two-carrier result across temperature with a high mobility carrier concentration at low temperature of $7.5 \times 10^{11} \text{ cm}^{-2}$, and mobility of $9030 \text{ cm}^2/\text{Vs}$. The transport model revealed that a high background impurity concentration (higher than $5.0 \times 10^{17} \text{ cm}^{-3}$) was required to fit the mobility. This would indicate that despite the spacer below the well, the Te atoms dragged into the well, limiting the mobility of the carriers in the 2DEG with background (3D) charged impurity scattering.

Two carrier fitting of both of the heterojunctions resulted in high-mobility carriers with a mobility comparable to the mobility extracted if each sample were assumed single carrier, indicating that the conduction in these samples is likely dominated by a single carrier, though the curvature of the longitudinal resistance indicates the presences of multi-carrier behaviour. These two structures had comparable mobilities to each other, $3500 \text{ cm}^2/\text{Vs}$ and $4100 \text{ cm}^2/\text{Vs}$ for the region with the triangular well doped and undoped respectively. From the similarity of these two mobilities, and with the undoped square quantum well having a similar spacer below the well, it is assumed the Te also dragged into the well in the undoped well sample. When a single carrier is assumed, the resultant

low temperature carrier density extracted was $1.2 \times 10^{13} \text{ cm}^{-2}$. When this value was input into the transport model, it was clear that the model's result was unrepresentative of the data when reasonable values were used for the scattering mechanisms, and only extreme unphysical parameters could fit the data. However, given the high carrier densities, inter-subband scattering is likely.

The doped heterojunction was then measured in the high field regime (up to 14 T), and across temperature. Shubnikov-de Haas oscillations were observed up to a temperature of 100 K, confirming the presence of a 2DEG. The corresponding quantum Hall plateaus were not observed, which is believed to be due to the high carrier density.

From the SdH oscillations, the carrier density, effective mass and quantum lifetime were found to be $7.4 \times 10^{11} \text{ cm}^{-2}$, $(0.042 \pm 0.001) m_0$ and $(21.6 \pm 0.1) \text{ fs}$ respectively. This carrier density is very comparable to carrier density calculated from the occupancy of states, and the effective mass very comparable to literature values. The ratio of quantum lifetime to transport lifetime was found to be <3.0 . This low ratio indicates that, as expected, short-range, large-angle scattering such as background impurity scattering is dominant in these samples. However, even with these new parameters, transport modelling still indicated that an unknown scattering mechanism was a large contributor to the limitation of the mobility across temperature. However, it must be noted that the lower limit of the mobility was being investigated (i.e. single carrier assumption) and thus the measured mobility may not be a true representative of the mobility of the carriers in the 2DEG.

The initial measurements and analysis of confined $\text{Al}_{0.2}\text{Ga}_{0.8}\text{Sb}/\text{GaSb}$ structures show promising results with a mobility of $9030 \text{ cm}^2/\text{Vs}$ for the square quantum well sample, similar to the early measurements of confined GaAs [14], as described in chapter 1. There is still much to be understood about these samples and much to be optimised in future samples. The Te dragging is clearly an issue that needs resolution if higher mobility devices are going to be achieved. The measured carrier density is also inexplicably higher than expected. Further investigations into preventing Te dragging through the well and the unexpectedly high carrier concentration that is measured are required. However, despite significant concentrations of scattering centres and carrier concentrations, high mobility devices are still a possibility, if a solution to Te dragging can be found.

In short, $\text{GaSb}/\text{Al}_{0.2}\text{Ga}_{0.8}\text{Sb}$ structures were investigated, the practical obstacles included native *p*-type defects and an unknown metallisation recipe. Both heterojunctions and square quantum well structures were investigated theoretically to ensure confinement

with an optimum mobility, and from these possible candidates, three structures were chosen to be grown. The structures were grown at a growth temperature and V/III ratio of 475 °C and 1.3 respectively, which a growth study showed to be the optimum growth conditions investigated. These growth conditions are believed to give a *p*-type concentration of $5 \times 10^{16} \text{ cm}^{-3}$ due to the native defects in GaSb. The structures were grown on semi-insulating GaAs at 1 ML/s with an IMF between the GaAs and GaSb. They were processed into Hall bars which were contacted with Pd/In/Pd/Au and etched to isolation with HF. The longitudinal and transverse resistances of the Hall bars were then measured across magnetic field and temperature. Once measured it was discovered that the main limitation to the mobility was the Te dragging in the well in combination with the native defects. The square quantum well resulted in a mobility and carrier density of $9030 \text{ cm}^2/\text{Vs}$ and $7.5 \times 10^{11} \text{ cm}^{-2}$ at low temperature (3 K). Shubnikov-de Haas oscillations were observed up to 100 K for a doped triangular well structure, from which various parameters were extracted. The effective mass was found to be $(0.042 \pm 0.001) m_0$ and the 2DEG carrier density was found to be $7.4 \times 10^{11} \text{ cm}^{-2}$. The quantum lifetime to transport lifetime ratio was found to be <3.0 which indicates that short range scattering limits the mobility. To achieve higher mobility devices, the doping must be prevented from entering the well in following generations of samples.

8.2 Further Work

There is still much work to be completed on the topic of transport in confined *n*-GaSb. The creation and initial transport and high field measurements of these quantum well structures are just the tip of the iceberg; these structures and the analysis of the measurements have much room to be developed. Though the metallisation recipe was found to result in some measurable devices at low temperature, there was still a considerable number of high resistance devices leading to difficulty in measurement. The measured carrier density was very high, indicating a disjoint between the simulated relationship from doping concentration to carrier concentration and the physical reality. The Te was also found to drag through the well, resulting in mobility limited by background impurity scattering, and thus dragging should be resolved if high mobility devices are to be created. Finally, the Shubnikov-de Haas measurements at high temperature prove to be an interesting discovery, particularly when the number of scattering centres in GaSb is considered[151].

The metallisation recipe investigation could be expanded to include an annealing investigation as there is a drastic difference between the unannealed and annealed resistances of the Pd/In/Pd/Au recipe. For the work in this thesis, the resistance was only required to be sufficiently low to allow devices to be measurable. However, many other applications and devices could easily be limited by the still high contact resistances or the non-ohmic nature of the contacts. Having a practical solution, where consistently low resistance ohmic contacts to *n*-type GaSb can be realised would therefore be very advantageous. To achieve this would require a more thorough and more detailed investigation of the metallisation of GaSb, including a variation in annealing time and temperature. For example, a set annealing temperature can be defined (e.g. 300 °C) and the annealing time can be increased, tracking the nature of the contact after multiple exposures. A more detailed analysis would be required to compliment this. An understanding of the underlying trends would then include TLM measurements specifically to investigate at which annealing temperature or time the contact resistance reduces, and whether this is due to gold spiking or the amount of indium that is diffused.

To understand the relationship between doping and carrier density, another generation of samples with similar structures to this work could be produced with reduced doping. Preferably, to a point where the structure turns *p*-type or in the case of heterojunctions no confinement, thus defining the limitations of the doping and structures. This will allow for more understanding, and thus, more control over the carrier density produced. This could be further investigated with a Schrödinger-Poisson model to understand this relationship. Alternatively, or as well as, gated structures could be created where the carrier density could be reduced as a function of gate bias. This could relate scattering to carrier density, though in the current structures, the scattering would still likely be limited by the Te in the quantum well.

Methods to reduce the dragging of Te into the well should also be investigated. In the structures in this work a spacer was put in place and the required width of this spacer was estimated from the exponential decrease of Te found in InSb. However, the Te dragging may be different in GaSb and it may drag further. This could be due to growth temperature difference between the two materials. A bulk Al_{0.2}Ga_{0.8}Sb structure could be grown with the top 300 nm left undoped, with SIMS then measuring the Te at the surface and the characteristics of the dragging in AlGaSb. From this an appropriate spacer can be put in place to ensure no Te drags into the well. There could also be an investigation into growth rate and whether a reduction in growth rate allows for more Te to be incorporated in each layer after the flux has stopped. Other prevention methods could include growing

alternating doped and undoped regions under the well, where this may prevent Te accumulation on the surface of the structure. It is found that Te drags significantly in GaSb the doping could be graded such that the flux is reduced steadily upon the approach to the well, allowing more Te to incorporate, again with an undoped spacer beneath the well.

The initial measurements and analysis of confined $\text{Al}_{0.2}\text{Ga}_{0.8}\text{Sb}/\text{GaSb}$ samples showed Shubnikov-de Haas oscillations up to 100 K, a unusually high temperature to observe such oscillations even given the low effective mass. These oscillations could be investigated further focussing on the limitations at high temperature and the relation between quantum lifetime and transport lifetime. Simulations of the Landau broadening can be achieved using gaussian or Lorentzian fits, allowing for more understanding of the high field measurements across a temperature range. This would allow an explanation for the appearance these oscillations at high temperature in GaSb or pinpoint an area of further investigation. Further work could be achieved to produce many multi carrier fits to better extract transport properties, where the measurements for these fits would be taken to higher fields.

Transport measurement of confined n -GaSb is still a relatively unexplored field, and thus there are many directions that could be explored, all aiding towards mapping the electrical nature of confined n -GaSb.

References

- [1] D. Benyahia *et al.*, "Optimization of the interfacial misfit array growth mode of GaSb epilayers on GaAs substrate," *J Cryst Growth*, vol. 483, pp. 26-30, 2018/02/01/ 2018, doi: <https://doi.org/10.1016/j.jcrysgro.2017.11.015>.
- [2] D. Wang *et al.*, "Optical properties improvement of GaSb epilayers through defects compensation via doping," *Journal of Luminescence*, vol. 197, pp. 266-269, 2018/05/01/ 2018, doi: <https://doi.org/10.1016/j.jlumin.2018.01.050>.
- [3] J. Tong, L. Y. M. Tobing, Y. Luo, D. Zhang, and D. H. Zhang, "Single Plasmonic Structure Enhanced Dual-band Room Temperature Infrared Photodetection," *Scientific Reports*, vol. 8, no. 1, p. 1548, 2018/01/24 2018, doi: 10.1038/s41598-018-20028-6.
- [4] G. Knebl *et al.*, "Optical tuning of the charge carrier type in the topological regime of InAs/GaSb quantum wells," *Phys Rev B*, vol. 98, no. 4, p. 041301, 07/16/ 2018, doi: 10.1103/PhysRevB.98.041301.
- [5] K. Shibata *et al.*, *Electric-field-induced two-dimensional hole gas in undoped GaSb quantum wells*. 2019, p. 232102.
- [6] Q. Xie, J. E. Van Nostrand, R. L. Jones, J. Szelove, and D. C. Look, "Electrical and optical properties of undoped GaSb grown by molecular beam epitaxy using cracked Sb 1 and Sb 2," *J Cryst Growth*, vol. 207, no. 4, pp. 255-265, 1999, doi: 10.1016/S0022-0248(99)00379-6.
- [7] A. Bosacchi *et al.*, "Electrical and Photoluminescence Properties of Undoped Gasb Prepared by Molecular-Beam Epitaxy and Atomic Layer Molecular-Beam Epitaxy," (in English), *J Cryst Growth*, vol. 150, no. 1-4, pp. 844-848, May 1995, doi: Doi 10.1016/0022-0248(95)80058-K.
- [8] M. Lee, D. J. Nicholas, K. E. Singer, and B. Hamilton, "A photoluminescence and Hall-effect study of GaSb grown by molecular-beam epitaxy," *J Appl Phys*, vol. 59, no. 8, pp. 2895-2900, 1986/04/15 1986, doi: 10.1063/1.336948.
- [9] P. S. Dutta, V. Prasad, H. L. Bhat, and V. Kumar, "Carrier compensation and scattering mechanisms in p-GaSb," *J Appl Phys*, vol. 80, no. 5, pp. 2847-2853, 1996/09/01 1996, doi: 10.1063/1.363135.
- [10] A. Sagar, "Experimental investigation of conduction band of GaSb," *Physical Review*, vol. 117, no. 1, pp. 93-100, 1960, doi: 10.1103/PhysRev.117.93.
- [11] P. S. Dutta, H. L. Bhat, and V. Kumar, "The physics and technology of gallium antimonide: An emerging optoelectronic material," (in English), *J Appl Phys*, vol. 81, no. 9, pp. 5821-5870, May 1 1997, doi: Doi 10.1063/1.365356.
- [12] C. J. McIndo, "Transport Effects In InSb Quantum Well Heterostructures," PhD, Physics Department, Cardiff Physics, 2019.
- [13] I. Vurgaftman, J. R. Meyer, and L. R. Ram-Mohan, "Band parameters for III-V compound semiconductors and their alloys," (in English), *J Appl Phys*, vol. 89, no. 11, pp. 5815-5875, Jun 1 2001, doi: Doi 10.1063/1.1368156.
- [14] V. Umansky, M. Heiblum, Y. Levinson, J. Smet, J. Nübler, and M. Dolev, "MBE growth of ultra-low disorder 2DEG with mobility exceeding $35 \times 10^6 \text{cm}^2/\text{Vs}$," *J Cryst Growth*, vol. 311, no. 7, pp. 1658-1661, 2009/03/15/ 2009, doi: <https://doi.org/10.1016/j.jcrysgro.2008.09.151>.
- [15] T. Yoshikazu, I. Masaya, and S. Akio, "Predicted Extremely High Mobilities of Two-Dimensional Electrons in AlGaSb/GaSb and AlInAsSb/InAs Single Heterostructures," *Japanese Journal of Applied Physics*, vol. 24, no. 6A, p. L455, 1985. [Online]. Available: <http://stacks.iop.org/1347-4065/24/i=6A/a=L455>.

- [16] F. Alshaeer, "A Study of Current Transport in Schottky Diodes Based on AlInSb/InSb-QW Heterostructures," Ph.D., School of Physics and Astronomy, Cardiff University, 2018.
- [17] B. R. Bennett, M. G. Ancona, J. B. Boos, C. B. Canedy, and S. A. Khan, "Strained GaSb/AlAsSb quantum wells for p-channel field-effect transistors," *J Cryst Growth*, vol. 311, no. 1, pp. 47-53, 2008/12/15/ 2008, doi: <https://doi.org/10.1016/j.jcrysgro.2008.10.025>.
- [18] K. W. Böer, *Handbook of the Physics of Thin-Film Solar Cells [electronic resource]*. 2013.
- [19] C. Kittel, *Introduction to solid state physics*, 5th ed. ed. Wiley, 1976.
- [20] P. Hofmann, *Solid State Physics: An Introduction*. Wiley, 2011.
- [21] P. Yu and M. Cardona, *Fundamentals of Semiconductors: Physics and Materials Properties*. 1997.
- [22] R. Enderlein and N. J. M. Horing, *Fundamentals of semiconductor physics and devices*. Singapore ; London: World Scientific, 1997.
- [23] J. Singleton, *Band theory and electronic properties of solids*. Oxford University Press, 2001.
- [24] A. Gilbertson, "Spin and Magnetotransport Properties of Narrow Gap Semiconductors," Doctor of Philosophy, Physics Department, Imperial College London, 2009.
- [25] S. M. Sze, *Physics of semiconductor devices*, 2nd ed. ed. New York ; Chichester: Wiley, 1981.
- [26] B. G. Yacobi, *Semiconductor Materials: An Introduction to Basic Principles*. Kluwer Academic/Plenum Publishers, 2003.
- [27] S. M. Sze, *Physics of semiconductor devices*. New York ; London: Interscience, 1969.
- [28] G. Smith, "The Characterisation of 30nm InSb Quantum Well Heterostructures by Electrical Measurement," PhD, Physics Department, Cardiff University, 2018.
- [29] B. V. Zeghbroeck. "<https://ecee.colorado.edu/~bart/book/>." (accessed 2019).
- [30] R. A. Smith, *Semiconductors*. University Press, 1961.
- [31] E. H. Putley, *The Hall effect and semi-conductor physics*. New York: Dover Publications, 1968, pp. viii, 263 p.
- [32] S. L. Murray *et al.*, "MOCVD growth of lattice-matched and mismatched InGaAs materials for thermophotovoltaic energy conversion," *Semiconductor Science and Technology*, vol. 18, no. 5, pp. S202-S208, 2003/04/07 2003, doi: 10.1088/0268-1242/18/5/309.
- [33] A. G. Milnes and A. Y. Polyakov, "Gallium antimonide device related properties," *Solid State Electron*, vol. 36, no. 6, pp. 803-818, 1993/06/01/ 1993, doi: [https://doi.org/10.1016/0038-1101\(93\)90002-8](https://doi.org/10.1016/0038-1101(93)90002-8).
- [34] K. K. Schuegraf, *Handbook of thin-film deposition processes and techniques: principles, methods, equipment, and applications*. Noyes Publications, 1988.
- [35] C. E. Dreyer, A. Janotti, and C. G. Van de Walle, "Effects of strain on the electron effective mass in GaN and AlN," *Appl Phys Lett*, vol. 102, no. 14, p. 142105, 2013/04/08 2013, doi: 10.1063/1.4801520.
- [36] J. H. Davies, *The physics of low-dimensional semiconductors : an introduction*. Cambridge: Cambridge University Press, 1998, pp. xviii, 438 p.
- [37] T. P. Pearsall, *Strained-layer superlattices : materials science and technology* (Semiconductors and semimetals,, no. 33). Boston ; London: Academic Press, 1991, pp. ix, 431 p.
- [38] A. P. Craig, "Lattice Mismatched Infrared Photodetectors," PhD Thesis, Physics, Lancaster University, Lancaster, a, 2015. [Online]. Available: m
- [39] J. W. Matthews and A. E. Blakeslee, "Defects in Epitaxial Multilayers .1. Misfit Dislocations," (in English), *J Cryst Growth*, vol. 27, no. Dec, pp. 118-125, 1974, doi: [Doi 10.1016/0022-0248\(74\)90424-2](https://doi.org/10.1016/0022-0248(74)90424-2).

- [40] B. J. Sasan Fathpour, *Silicon Photonics for telecommunications and Biomedicine*. Boca Raton: CRC Press, 2012.
- [41] S. Wang, *Technology and applications Lattice Engineering*. Singapore: Pan Stanford Publishing, 2012.
- [42] S. Huang, G. Balakrishnan, and D. L. Huffaker, "Interfacial misfit array formation for GaSb growth on GaAs," *J Appl Phys*, vol. 105, no. 10, 2009, doi: 10.1063/1.3129562.
- [43] R. People and J. C. Bean, "Calculation of Critical Layer Thickness Versus Lattice Mismatch for Gexsi1-X/Si Strained-Layer Heterostructures," (in English), *Appl Phys Lett*, vol. 47, no. 3, pp. 322-324, 1985, doi: Doi 10.1063/1.96206.
- [44] H. J. Gossmann, G. P. Schwartz, B. A. Davidson, and G. J. Gualtieri, "Strain and critical thickness in GaSb(001)/AlSb," *Journal of Vacuum Science & Technology B: Microelectronics Processing and Phenomena*, vol. 7, no. 4, pp. 764-766, 1989/07/01 1989, doi: 10.1116/1.584641.
- [45] M. A. Herman, *Molecular beam epitaxy : fundamentals and current status*, 2nd, rev. and updated ed. ed. Springer, 1996.
- [46] M. Razeghi, "Compound Semiconductors and Crystal Growth Techniques," in *Fundamentals of Solid State Engineering*, M. Razeghi Ed. Boston, MA: Springer US, 2002, pp. 349-386.
- [47] Z. Y. Fan, G. Rong, N. Newman, and D. J. Smith, "Defect annihilation in AlN thin films by ultrahigh temperature processing," *Appl Phys Lett*, vol. 76, no. 14, pp. 1839-1841, 2000, doi: 10.1063/1.126185.
- [48] J.-i. Nishizawa, "Stoichiometry control for growth of III-V crystals," *J Cryst Growth*, vol. 99, no. 1, pp. 1-8, 1990/01/01/ 1990, doi: [https://doi.org/10.1016/0022-0248\(90\)90477-3](https://doi.org/10.1016/0022-0248(90)90477-3).
- [49] R. A. Stradling, P. Klipstein, T. Imperial College of Science, M. Medicine . Dept. of, T. Imperial College of Science, and P. Medicine . Dept. of, *Growth and characterisation of semiconductors : papers contributing to a short course*. Hilger, 1990.
- [50] D. R. Olander and A. T. Motta, "Light Water Reactor Materials, Volume 1 - Fundamentals," ed: ANS (American Nuclear Society).
- [51] C. R. M. Grovenor, *Microelectronic materials*. Hilger, 1989.
- [52] J. A. Van Vechten, "Simple Theoretical Estimates of the Enthalpy of Antistructure Pair Formation and Virtual-Enthalpies of Isolated Antisite Defects in Zinc-Blende and Wurtzite Type Semiconductors," *Journal of the Electrochemical Society*, vol. 122, no. 3, pp. 423-429, 1975, doi: 10.1149/1.2134227.
- [53] N. Segercrantz, J. Slotte, F. Tuomisto, K. Mizohata, and J. Räisänen, "Instability of the Sb vacancy in GaSb," *Phys Rev B*, vol. 95, no. 18, p. 184103, 05/03/ 2017, doi: 10.1103/PhysRevB.95.184103.
- [54] H. Bracht, S. P. Nicols, W. Walukiewicz, J. P. Silveira, F. Briones, and E. E. Haller, "Large disparity between gallium and antimony self-diffusion in gallium antimonide," *Nature*, vol. 408, no. 6808, p. 69, 2000, doi: 10.1038/35040526.
- [55] N. Segercrantz, "Optoelectronic properties of III-V compounds and alloys," PhD, Department of Applied Physics, Aalto University 2017.
- [56] M. Hakala, M. J. Puska, and R. M. Nieminen, "Native defects and self-diffusion in GaSb," *J Appl Phys*, vol. 91, no. 8, pp. 4988-4994, 2002, doi: 10.1063/1.1462844.
- [57] J. Kujala, N. Segercrantz, F. Tuomisto, and J. Slotte, "Native point defects in GaSb," (in English), *J Appl Phys*, vol. 116, no. 14, Oct 14 2014, doi: Artn 143508
10.1063/1.4898082.
- [58] W. Lewandowski, M. Gajewska, B. Pastuszka, and M. Bugajski, "Growth and luminescence properties of GaSb single crystals," *Acta Physica Hungarica*, vol. 57, no. 3, pp. 303-308, 1985, doi: 10.1007/BF03158901.

- [59] R. D. Baxter, F. J. Reid, and A. C. Beer, "Electron mobility in GaSb at 77°K," *Physical Review*, vol. 162, no. 3, pp. 718-727, 1967, doi: 10.1103/PhysRev.162.718.
- [60] J. Allegre, M. Averous, R. Jourdan, and A. Joullie, *Photoluminescence studies on GaIn_{1-x}Sb alloys*. 1976, pp. 339-347.
- [61] C. C. Ling, S. Fung, C. D. Beling, and W. Huimin, "Defect study of Zn-doped p-type gallium antimonide using positron lifetime spectroscopy," *Physical Review B - Condensed Matter and Materials Physics*, vol. 64, no. 7, pp. 752011-752017, 2001, doi: 10.1103/PhysRevB.64.075201.
- [62] W. Hu, Z. Wang, B. F. Su, Y. Dai, S.-J. Wang, and Y. Zhao, *Gallium antisite defect and residual acceptors in undoped GaSb*. 2004, pp. 286-290.
- [63] H. Wang *et al.*, "The influence of growth temperature and input V/III ratio on the initial nucleation and material properties of InN on GaN by MOCVD," *Semiconductor Science and Technology*, vol. 24, no. 5, p. 055001, 2009/03/27 2009, doi: 10.1088/0268-1242/24/5/055001.
- [64] C. Pelosi *et al.*, "The role of the V/III ratio in the growth and structural properties of metalorganic vapor phase epitaxy GaAs/Ge heterostructures," *Journal of Electronic Materials*, vol. 24, no. 11, pp. 1723-1730, 1995/11/01 1995, doi: 10.1007/BF02676841.
- [65] A. Jasik *et al.*, "The influence of the growth rate and V/III ratio on the crystal quality of InGaAs/GaAs QW structures grown by MBE and MOCVD methods," *J Cryst Growth*, vol. 311, no. 19, pp. 4423-4432, 2009/09/15/ 2009, doi: <https://doi.org/10.1016/j.jcrysgro.2009.07.032>.
- [66] L. J. V. d. Pauw, "A Method of Measuring the Resistivity and Hall Coefficient on Lamellae of Arbitrary Shape," *Philips Technical Review*, vol. 20, pp. 220-224, 1958.
- [67] A. Salhi, S. Alshaibani, M. Alhamdan, H. Albrithen, A. Alyamani, and M. El-Desouki, "Effects of Sb incorporation in GaAsSb-capping layer on the optical properties of InAs/GaAs QDs grown by Molecular Beam Epitaxy," *Superlattices and Microstructures*, vol. 101, pp. 138-143, 2017/01/01/ 2017, doi: <https://doi.org/10.1016/j.spmi.2016.11.021>.
- [68] M. Ichimura, K. Higuchi, Y. Hattori, T. Wada, and N. Kitamura, "Native defects in the Al_xGa_{1-x}Sb alloy semiconductor," *J Appl Phys*, vol. 68, no. 12, pp. 6153-6158, 1990/12/15 1990, doi: 10.1063/1.346904.
- [69] S. K Ma *et al.*, *Electron irradiated liquid encapsulated Czochralski grown undoped gallium antimonide studied by positron lifetime spectroscopy and photoluminescence*. 2004, pp. 6205-6212.
- [70] S. Subbanna, G. Tuttle, and H. Kroemer, "N- type doping of gallium antimonide and aluminum antimonide grown by molecular beam epitaxy using lead telluride as a tellurium dopant source," *Journal of Electronic Materials*, vol. 17, no. 4, pp. 297-303, 1988/07/01 1988, doi: 10.1007/BF02652109.
- [71] M. Kasap and S. Acar, *The temperature dependence of electron and magneto transport properties in Te-doped InSb*. 2004, pp. 3113-3120.
- [72] A. Bignazzi *et al.*, "Low temperature photoluminescence of tellurium-doped GaSb grown by molecular beam epitaxy," *J Cryst Growth*, vol. 169, no. 3, pp. 450-456, 1996/12/01/ 1996, doi: [https://doi.org/10.1016/S0022-0248\(96\)00441-1](https://doi.org/10.1016/S0022-0248(96)00441-1).
- [73] O.Tizmo, "Design, fabrication and characterisation of a novel memory device based on III-V semiconductors."
- [74] R. K. Y. a. D. S. Soane, "Model for spin coating in microelectronic applications," *J Appl Phys*, vol. 72, no. 2, pp. 725-740, 1992, doi: 10.1063/1.351859.
- [75] M. Feldman, *Nanolithography: The Art of Fabricating Nanoelectronic and Nanophotonic Devices and Systems*. Elsevier Science, 2014.
- [76] C. Mack, *Fundamental Principles of Optical Lithography: The Science of Microfabrication*. Wiley, 2008.

- [77] B. W. Smith, K. Suzuki, and J. R. Sheats, *Microlithography: Science and Technology*. Taylor & Francis, 1998.
- [78] M. Ohring, *Materials science of thin films*. Elsevier, 2001.
- [79] J. A. Robinson and S. E. Mohny, "An improved In-based ohmic contact to n-GaSb," (in English), *Solid State Electron*, vol. 48, no. 9, pp. 1667-1672, Sep 2004, doi: 10.1016/j.sse.2004.02.022.
- [80] D. V. Morgan and K. Board, *An introduction to semiconductor microtechnology*. Chichester [West Sussex] ; New York: Wiley, 1983, pp. xii, 167 p.
- [81] "KLayout - High Performance Layout Viewer And Editor." <https://www.klayout.de/> (accessed 12/09/18, 2018).
- [82] D. V. Morgan and K. Board, *An introduction to semiconductor microtechnology*. J. Wiley, 1990.
- [83] B. L. Sharma, *Metal-Semiconductor Schottky Barrier Junctions and Their Applications*. Springer US, 2013.
- [84] I. P. Batra, *Metallization and metal-semiconductor interfaces*, First edition. ed. (Proceedings of a NATO ARW held at the Technical University of Munich, Garching, Germany, August 22-26, 1988). 1989.
- [85] A. G. Milnes, *Heterojunctions and Metal Semiconductor Junctions*. Elsevier Science, 2012.
- [86] W. E. Spicer, I. Lindau, P. Skeath, and C.-y. Su, *Unified defect model and beyond*. 1980, pp. 1019-1027.
- [87] A. M. Cowley and S. M. Sze, "Surface States and Barrier Height of Metal-Semiconductor Systems," *J Appl Phys*, vol. 36, no. 10, pp. 3212-3220, 1965, doi: 10.1063/1.1702952.
- [88] V. P. Khvostikov *et al.*, "High-efficiency (49%) and high-power photovoltaic cells based on gallium antimonide," *Semiconductors*, vol. 40, no. 10, pp. 1242-1246, 2006/10/01 2006, doi: 10.1134/S1063782606100216.
- [89] E. K. A. PIOTROWSKA, T. PIOTROWSKI, S. KASJANIUK, and M. GUZIEWICZ, "Interaction of Au with GaSb and it's impact on the formation of the ohmic contacts," *ACTA PHYSICA POLONICA A*, vol. 87, no. 2, p. 419, 1995.
- [90] P. H. H. a. L. C. W. Z. C. Yang, "Au/In/Pd/Te/Pd ohmic contact to n-GaSb," *Electronics Letters*, vol. 32, no. 25, pp. 2348-2349, 1996, doi: 10.1049/el:19961589.
- [91] S. G. E. Villemain, M. Rolland, A. Joullie, "Characterization of ohmic contacts on n- and p-type GaSb," *Materials Science and Engineering: B*, vol. Volume 20, no. 1-2, pp. 162-164, 1993.
- [92] A. Subekti, V. W. L. Chin, and T. L. Tansley, "Ohmic contacts to n-type and p-type GaSb," *Solid State Electron*, vol. 39, no. 3, pp. 329-332, 1996/03/01/ 1996, doi: [https://doi.org/10.1016/0038-1101\(95\)00144-1](https://doi.org/10.1016/0038-1101(95)00144-1).
- [93] P. H. H. a. L. C. W. Z.C. Yang, "Au/In/Pd/Te/Pd ohmic contact to n-GaSb," *ELECTRONICS LETTERS*, vol. 32, no. 25, p. 2349, 1996.
- [94] R. K. Huang, C. A. Wang, C. T. Harris, M. K. Connors, and D. A. Shiau, "Ohmic contacts to n-type GaSb and n-type GaInAsSb," *Journal of Electronic Materials*, vol. 33, no. 11, pp. 1406-1410, 2004/11/01 2004, doi: 10.1007/s11664-004-0171-1.
- [95] A. Vogt *et al.*, "Ohmic contact formation mechanism of the PdGeAu system on n-type GaSb grown by molecular beam epitaxy," *J Appl Phys*, vol. 83, no. 12, pp. 7715-7719, 1998/06/15 1998, doi: 10.1063/1.367943.
- [96] D. K. Schroder, *Semiconductor Material and Device Characterization*. Wiley, 2006.
- [97] A. G. Baca and C. I. H. Ashby, *Fabrication of GaAs Devices*. 2005.
- [98] H. S. Rathore, G. C. Schwartz, R. A. Susko, E. S. Dielectrics, and I. Division, *Proceedings of the Symposia on Reliability of Semiconductor Devices and Interconnection and Multilevel Metallization, Interconnection, and Contact Technologies*. Electrochemical Society, 1989.

- [99] S. Kasap, P. Capper, and C. Koughia, *Springer Handbook of Electronic and Photonic Materials*. Springer, 2006.
- [100] S. Birner. "nextnano"
 " (accessed 2017-2019, 2019).
- [101] J. Singh, *Physics of semiconductors and their heterostructures* (McGraw-Hill series in electrical and computer engineering Electronics and VLSI circuits). New York ; London: McGraw-Hill, 1993, pp. xxiv, 851 p.
- [102] D. A. Fleisch, *A Student's Guide to the Schrödinger Equation*. Cambridge University Press, 2019.
- [103] A. C. Phillips, *Introduction to Quantum Mechanics*. Wiley, 2013.
- [104] D. J. Griffiths, *Introduction to Quantum Mechanics*. Cambridge University Press, 2017.
- [105] J. Oatley and C. W. Oatley, *Electric and Magnetic Fields*. Cambridge University Press, 1976.
- [106] P. Harrison, *Quantum wells, wires and dots : theoretical and computational physics of semiconductor nanostructures*, 3rd ed. Chichester: Wiley, 2009, pp. xxvi, 538 p.
- [107] D. S. Naqvi and U. o. R. M. S. A. Group, *Poisson's Equation : Finite Difference Grid Refinements and Transfinite Transformations*. Mathematical Sciences Applications Group, 1986.
- [108] C. D. Cantrell, *Modern Mathematical Methods for Physicists and Engineers*. Cambridge University Press, 2000.
- [109] J. M. S. Orr *et al.*, "Electronic transport in modulation-doped InSb quantum well heterostructures," (in English), *Phys Rev B*, vol. 77, no. 16, Apr 2008, doi: ARTN 165334
 10.1103/PhysRevB.77.165334.
- [110] J. Orr, "Low Dimensional Transport Measurements in InSb Heterostructure Devices," PhD Thesis, School of Electrical and Electronic Engineering Universtiy of Manchester, Manchester, 2007.
- [111] M. G. Greally, M. Hayne, A. Usher, G. Hill, and M. Hopkinson, "Low-temperature mobility of two-dimensional electrons in (Ga,In)As-(Al,In)As heterojunctions," (in English), *J Appl Phys*, vol. 79, no. 11, pp. 8465-8469, Jun 1 1996, doi: Doi 10.1063/1.362481.
- [112] W. Walukiewicz, H. E. Ruda, J. Lagowski, and H. C. Gatos, "Electron-Mobility in Modulation-Doped Heterostructures," (in English), *Phys Rev B*, vol. 30, no. 8, pp. 4571-4582, 1984, doi: DOI 10.1103/PhysRevB.30.4571.
- [113] K. F. Brennan, *The Physics of Semiconductors: With Applications to Optoelectronic Devices*. Cambridge University Press, 1999.
- [114] P. Das, D. Wickramaratne, B. Debnath, G. Yin, and R. K. Lake, "Charged impurity scattering in two-dimensional materials with ring-shaped valence bands: GaS, GaSe, InS, and InSe," *Phys Rev B*, vol. 99, no. 8, p. 085409, 02/08/ 2019, doi: 10.1103/PhysRevB.99.085409.
- [115] M. Hayne, A. Usher, J. J. Harris, V. V. Moshchalkov, and C. T. Foxon, "Remote impurity scattering in modulation-doped GaAs/Al_xGa_{1-x}As heterojunctions," (in English), *Phys Rev B*, vol. 57, no. 23, pp. 14813-14817, Jun 15 1998, doi: DOI 10.1103/PhysRevB.57.14813.
- [116] J. L. Boland *et al.*, "Towards higher electron mobility in modulation doped GaAs/AlGaAs core shell nanowires," *Nanoscale*, 10.1039/C7NR00680B vol. 9, no. 23, pp. 7839-7846, 2017, doi: 10.1039/C7NR00680B.
- [117] C. Hamaguchi, *Basic Semiconductor Physics*. Springer Berlin Heidelberg, 2009.
- [118] L. Challis, L. J. Challis, and O. U. Press, *Electron-phonon Interactions in Low-dimensional Structures*. Oxford University Press, 2003.

- [119] X. L. Lei, "Dynamical Screening and Carrier Mobility in GaAs-GaAlAs Heterostructures," (in English), *J Phys C Solid State*, vol. 18, no. 20, pp. L593-L597, 1985, doi: Doi 10.1088/0022-3719/18/20/005.
- [120] J. Bardeen and W. Shockley, "Deformation Potentials and Mobilities in Non-Polar Crystals," *Physical Review*, vol. 80, no. 1, pp. 72-80, 10/01/ 1950, doi: 10.1103/PhysRev.80.72.
- [121] A. C. Anderson and J. P. Wolfe, *Phonon Scattering in Condensed Matter V: Proceedings of the Fifth International Conference Urbana, Illinois, June 2–6, 1986*. Springer Berlin Heidelberg, 2012.
- [122] L. Challis, *Phonon Scattering in Solids*. Springer US, 2012.
- [123] P. J. Price, "Two-dimensional electron transport in semiconductor layers. I. Phonon scattering," *Annals of Physics*, vol. 133, no. 2, pp. 217-239, 1981/05/01/ 1981, doi: [https://doi.org/10.1016/0003-4916\(81\)90250-5](https://doi.org/10.1016/0003-4916(81)90250-5).
- [124] B. K. Ridley, "The electron-phonon interaction in quasi-two-dimensional semiconductor quantum-well structures," *Journal of Physics C: Solid State Physics*, vol. 15, no. 28, pp. 5899-5917, 1982/10/10 1982, doi: 10.1088/0022-3719/15/28/021.
- [125] V. K. Arora and A. Naeem, *Phonon-scattering-limited mobility in a quantum-well heterostructure*. 1985, pp. 3887-3892.
- [126] D. Long and R. J. Hager, "Electrical Properties and Resonance Scattering in Heavily Doped N-Type GaSb and Related Semiconductors," (in English), *J Appl Phys*, vol. 36, no. 11, pp. 3436-&, 1965, doi: Doi 10.1063/1.1703012.
- [127] G. Margaritondo, *Electronic Structure of Semiconductor Heterojunctions*. Springer Netherlands, 2012.
- [128] G. Agostini and C. Lamberti, *Characterization of Semiconductor Heterostructures and Nanostructures*. Elsevier Science, 2013.
- [129] H. S. Nalwa, *Handbook of Surfaces and Interfaces of Materials, Five-Volume Set*. Elsevier Science, 2001.
- [130] S. Oktyabrsky and P. Ye, *Fundamentals of III-V Semiconductor MOSFETs*. Springer US, 2010.
- [131] D. K. Ferry, S. M. Goodnick, and J. Bird, *Transport in Nanostructures*, 2 ed. Cambridge: Cambridge University Press, 2009.
- [132] J. Basinski, D. J. E. Demars, and J. C. Woolley, "Low electron mobility in GaSb," *Journal of Physics C: Solid State Physics*, vol. 7, no. 4, pp. 716-726, 1974/02/21 1974, doi: 10.1088/0022-3719/7/4/009.
- [133] M. Patrini *et al.*, "Optical functions of bulk and epitaxial GaSb from 0.0025 to 6 eV," *Solid State Communications*, vol. 101, no. 2, pp. 93-98, 1997/01/01/ 1997, doi: [https://doi.org/10.1016/S0038-1098\(96\)00541-8](https://doi.org/10.1016/S0038-1098(96)00541-8).
- [134] S. Adachi, P. Capper, S. Kasap, and A. Willoughby, *Properties of Semiconductor Alloys: Group-IV, III-V and II-VI Semiconductors*. Wiley, 2009.
- [135] C. Bocchi, L. Lazzarini, M. Minelli, L. Nasi, and E. K. Mukhamedzhanov, "Interfaces in AlGaSb/GaSb multiquantum well structures," *J Appl Phys*, vol. 96, no. 6, pp. 3110-3116, 2004/09/15 2004, doi: 10.1063/1.1779950.
- [136] R. S. Popovic, *Hall Effect Devices*. CRC Press, 2003.
- [137] E. H. Putley, *The Hall Effect and Related Phenomena*. Butterworth, 1960.
- [138] *Standard Test Methods for Measuring Resistivity and Hall Coefficient and Determining Hall Mobility in Single Crystal Semiconductors*. Beuth, 2008.
- [139] J. Chu and A. Sher, *Physics and Properties of Narrow Gap Semiconductors*. Springer New York, 2007.
- [140] M. A. Reed, W. Kirk, and P. S. Kobiela, *Investigation of Parallel Conduction in GaAs/Al_xGa_{1-x}As Modulation-Doped Structures in the Quantum Limit*. 1986, pp. 1753-1759.

- [141] R. M. Nieminen, "Electronic Properties of Two-Dimensional Systems," *Physica Scripta*, vol. T23, pp. 54-58, 1988/01/01 1988, doi: 10.1088/0031-8949/1988/t23/009.
- [142] O. Pooley, "Electron Transport in InSb/AlInSb Semiconductor Heterostructures," PhD, School of Electronic and Electrical Engineering, University of Manchester, 2011.
- [143] Z. F. Ezawa, *Quantum Hall Effects: Recent Theoretical and Experimental Developments Third Edition*. World Scientific Publishing Company, 2013.
- [144] T. Ihn, *Semiconductor Nanostructures: Quantum States and Electronic Transport*. OUP Oxford, 2010.
- [145] J. J. Harris *et al.*, "Relationship between classical and quantum lifetimes in AlGaIn/GaN heterostructures," *Semiconductor Science and Technology*, vol. 16, no. 5, pp. 402-405, 2001/04/12 2001, doi: 10.1088/0268-1242/16/5/321.
- [146] Coleridge, Zawadzki, and Sachrajda, "Peak values of resistivity in high-mobility quantum-Hall-effect samples," *Physical review. B, Condensed matter*, vol. 49, no. 15, p. 10798, 1994, doi: 10.1103/PhysRevB.49.10798.
- [147] D. V. Morgan, R. H. Williams, and I. o. E. Engineers, *Physics and Technology of Heterojunction Devices*. P. Peregrinus Limited, 1991.
- [148] R. E. Prange *et al.*, *The Quantum Hall Effect*. Springer New York, 2012.
- [149] D. G. Hayes *et al.*, "Electron transport lifetimes in InSb/Al_{1-x}In_xSb quantum well 2DEGs," *Semiconductor Science and Technology*, vol. 32, no. 8, p. 085002, 2017/07/04 2017, doi: 10.1088/1361-6641/aa75c8.
- [150] C. Weisbuch, C. W. B. Vinter, and B. Vinter, *Quantum Semiconductor Structures: Fundamentals and Applications*. Elsevier Science, 1991.
- [151] R. Krishna Kumar *et al.*, "High-temperature quantum oscillations caused by recurring Bloch states in graphene superlattices," *Science (New York, N.Y.)*, vol. 357, no. 6347, p. 181, 2017, doi: 10.1126/science.aal3357.

Appendix A: Growth Rate Conversion Calculations

This appendix expands on the brief description of growth rates given in Chapter 3, describing the understanding between the conversion from a calibrated growth rate on one material, to an expected growth rate in another.

When growing III-V semiconductors, it is the growth of the group III element that controls the growth rate, and so in the case of GaAs or GaSb, this is controlled by the gallium. The group III growth rate is then controlled via the cell temperature, controlling the elemental flux on to the substrate. To relate this cell temperature to a growth rate, repeated growth trials are performed on a calibration material (in the case of gallium, this is calibrated on GaAs), where for a given cell temperature, the number of oscillations in the intensity of the RHEED pattern over a given time are counted. Each oscillation in intensity corresponds to the growth of a single monolayer, and so by dividing the number of oscillations observed by the length of time grown for, a growth rate in ML/s can be determined. As this calibration is performed on GaAs, if the growth rate for (e.g.) GaSb is desired at the same gallium cell temperature, a conversion must be performed. This appendix describes the theory behind this conversion.¹²

To understand the derivation of this conversion, a simple starting point is to consider the flux of atoms arriving at the surface of the sample per unit area per second, n_a . This will be dependent on the temperature of the cell (in this case the gallium cell), and not dependent on the crystal material being grown. For a surface of a given area, A , there will be a fixed number of lattice sites which these incoming atoms can bond to and incorporate into the lattice, where each of these sites is spaced at the material dependant lattice constant, a_0 , apart. The density of sites per m^2 is then given by a_0^{-2} . For GaSb, these lattice sites will be spaced further apart than in GaAs, reducing this number. This spacing not only affects the number of sites in the given area, but will also affect how fast the material will grow as the monolayer thickness is increased. This reduction in sites (proportional to $(a_{GaAs}/a_{GaSb})^2$) means that the constant flux of incoming atoms will fill these sites at the equivalent proportionally increased rate, i.e. $(a_{GaSb}/a_{GaAs})^2$. Therefore, if a flux of n_a corresponds to a certain monolayer growth rate of GaAs per second, R_{GaAs} , found by dividing n_a by the density of sites such that

¹² Strain is neglected here, where an epilayer may be strained to match the substrate grown on.

$$R_{\text{GaAs}} = \frac{n_a}{a_{\text{GaAs}}^{-2}},$$

then in GaSb, this monolayer growth rate will now be given by

$$R_{\text{GaSb}} = \frac{n_a}{a_{\text{GaSb}}^{-2}} = R_{\text{GaAs}} \frac{a_{\text{GaAs}}^{-2}}{a_{\text{GaSb}}^{-2}} = R_{\text{GaAs}} \left(\frac{a_{\text{GaSb}}}{a_{\text{GaAs}}} \right)^2,$$

or more generally,

$$R_A = R_B \left(\frac{a_A}{a_B} \right)^2.$$

Further, this increase in lattice constant will not just affect the density of sites in the growth plane, but will also increase the monolayer spacing in the growth direction. This increase in spacing increases the growth rate, measured in μm per hour, by the ratio of the lattice constants $a_{\text{GaSb}}/a_{\text{GaAs}}$, giving the conversion of the thickness grown per unit time, t , from GaAs to GaSb as

$$t_{\text{GaSb}} = t_{\text{GaAs}} \left(\frac{a_{\text{GaSb}}}{a_{\text{GaAs}}} \right)^3,$$

or again more generally,

$$t_A = t_B \left(\frac{a_A}{a_B} \right)^3.$$

Understanding these simple conversions allows for the possibility of precisely determining growth rates for many material systems whilst only having to perform the calibration for a small subset of base elements.